Assessment of Damages in Concrete Parking Structures

N. Assendelft

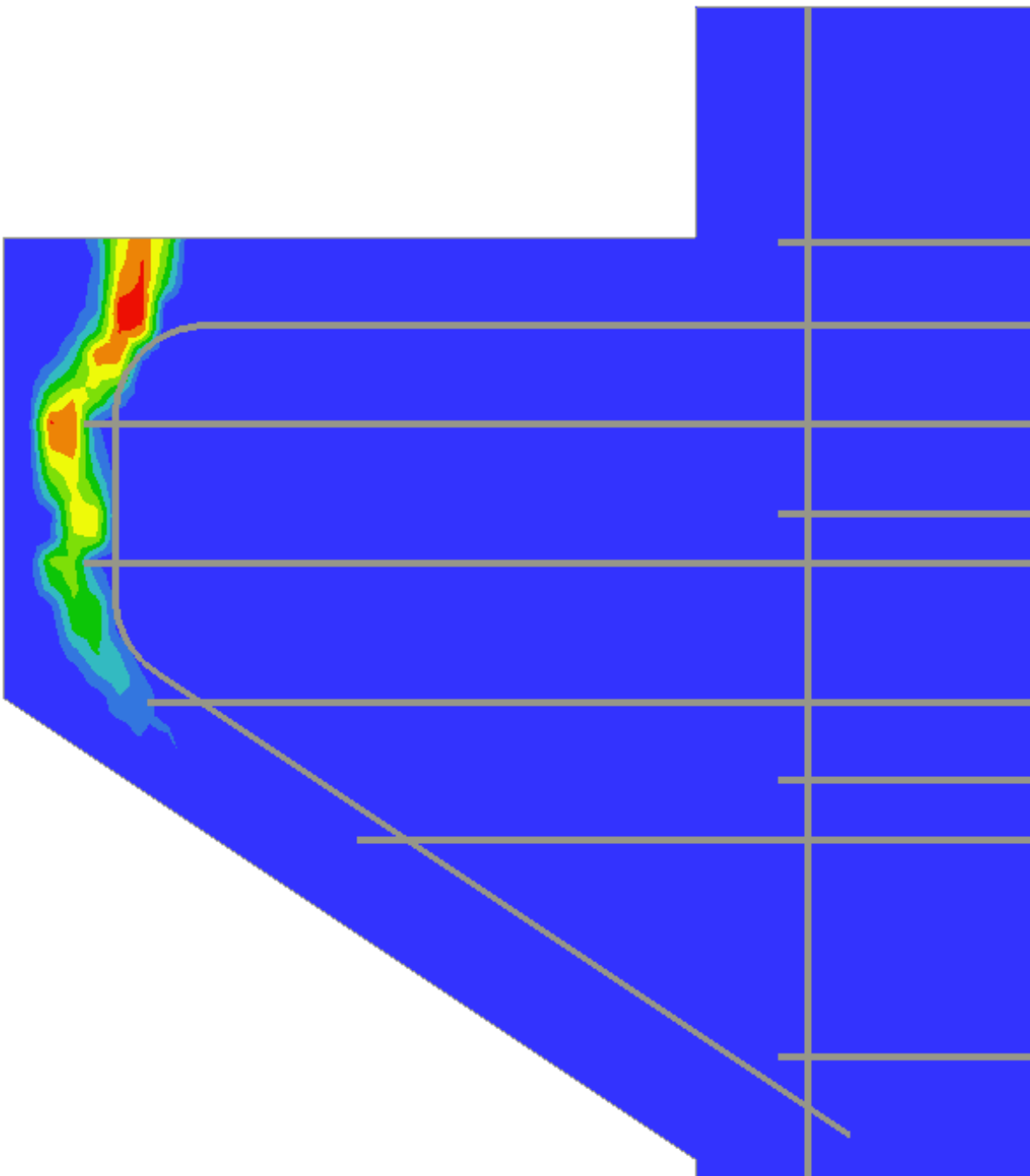

Assessment of Damages in Concrete Parking Structures

by

Niels Assendelft

MSc Thesis

31-10-2024

Delft University of Technology, Department of Engineering Structures

Student number: 4777212

Thesis Committee:

Prof. dr. ir. E. O. L. Lantsoght (Chair)	TU Delft & USFQ
Prof. dr. ir. M. A. N. Hendriks	TU Delft
Ir. H. Alkisaei	TU Delft
Dr. ir. D. A. Hordijk	Adviesbureau Hageman

TU Delft

ADVIESBUREAU HAGEMAN

Acknowledgements

This thesis was accomplished as the concluding part of the Master track Structural Engineering at Delft University of Technology. The research was realised in collaboration with the engineering consultancy firm Adviesbureau Hageman.

First and foremost, many thanks to the members of my graduation committee, from TU Delft, for all their efforts and time during this research. Especially to the chair of the committee, Prof. dr. ir. E. O. L. Lantsoght, for her counsel and interest during the past months.

Secondly, I am grateful for the opportunity given by Adviesbureau Hageman for this collaboration and all the colleagues for their enthusiasm, interest, and knowledge provided. I am indebted to, in particular, Dr. ir. D. A. Hordijk and Ir. J. J. Meester for all their constructive feedback, enthusiasm, but especially for making it an incredibly educational journey.

Finally, I would like to share my gratitude to all my friends and family who supported me throughout my educational career. Special thanks to my parents, for their unwavering support and encouragement.

Niels Assendelft
Rijswijk, 2024

Summary

Unfortunately, parking structures are a reoccurring subject in the Dutch forensic engineering industry, as damage is frequently observed. In the past seven years, there even have been three partial collapses.

The aim of this research is to gather an overview of the frequently reoccurring types of damage in parking structures in The Netherlands, and assess the behaviour of such damage. In the first part of this research (Chapters 1 to 7), the following research question is answered: *"How can frequently occurring damage in concrete parking structures in The Netherlands be related to its causes?"*.

An initial overview of potential damages in parking structures is made based on prior research (Chapter 2). A more concise overview is obtained by a data analysis on 145 forensic reports on damage in parking structures, provided by the Dutch consultancy firm Adviesbureau Hageman (Chapter 4). The results of the data analysis suggest that most of the frequently occurring damages are reoccurring and caused by faults in design or execution, based on the observed types of damage and the age of a structure at observation. Additionally, it is indicated that the frequency of observed types of damage differs between above- and underground structures.

Based on the findings of the data analysis, a damage catalogue is made in which the types of damage are categorized by the element of occurrence (Chapter 5). The damage catalogue describes the characteristics, causes, and mitigating measures, emphasizing important design parameters and can be used as an identification tool of damage.

In part II of this research (Chapters 8 to 16), an exploratory study is carried out on the behaviour of the support end failure, to provide an answer to the following research question: *"To what extent can the behaviour of the support end failure be assessed by a parametric study using a finite element model?"*.

Numerical analyses are conducted on various corbel configurations in which the occurrence, initiation, and propagation of the support end failure was studied. First, a two-dimensional finite element model is made and validated by experimental results, available in the literature, in which the support end failure was studied (Chapter 10). A comparison between results of the model and experiment show that the support end failure could be accurate replicated with a two- dimensional model. Although, the support end failure is only captured for mesh sizes smaller than or equal to 10x10 mm^2 and when using a fixed crack model.

The behaviour of a corbel designed according to the Eurocode is investigated, which showed a safety margin of factor 2 between design and capacity of the corbel (Chapter 11). In Chapter 12, three numerical experiments are conducted to explore the contribution of the dimensions and location of a support and an applied horizontal load. The results indicated that the loading conditions and dimensions of the support contribute to the support end failure, and influence the propagation and initiation of the support end failure cracks. The results showed that for a

vertical load, the support end failure crack initiates below the surface of the corbel, while for a horizontal load, the crack initiates at the surface. While the support end failure occurred in the numerical experiments, a significant load had to be applied before the failure mechanism was initiated. Additional studies on the influence of grouted continuity reinforcement and a non-uniform applied load could provide an explanation for the frequent occurrence of this failure mechanism in practice.

An analytical method was proposed to approximate if support end failure would occur for a given situation (Chapter 13). A comparison of the analytical results and numerical experiments show that the analytical model does not accurately predict the initiation of the support end failure, for a failure plane spanning the entire height of the corbel. Further research is required to study the effectiveness of the analytical model on a diagonal support end failure crack plane.

The findings of the research provide a deeper understanding of the frequently occurring damages in concrete parking structures; it emphasizes important design aspects and mitigation measures for future structures.

Contents

Part I

An overview of types of damage in concrete parking structures

Part II

A study of the support end failure behaviour in concrete corbels

Part I

An overview of types of damage in concrete parking structures

1 Introduction

1.1 Background

Parking structures are a vital part of the infrastructure in The Netherlands, as an estimated four- to five hundred public parking structures have been built (Ministerie van Infrastructuur en Waterstaat, 2021, Bos et al., 2020). Unfortunately, these structures are a reoccurring subject in the Dutch forensic engineering industry, as damage is frequently observed. There have even been several recent partial collapses of parking structures: Eindhoven in 2017, Wormerveer in 2018, and Nieuwegein in 2024 (NOS, 2017; NOS, 2018; NOS, 2024).

Damage is frequently observed in both older existing and newly constructed parking structures, with various causes. Older structures suffering from deterioration initiated damage is to be expected, yet damage is commonly found in new parking structures, either due to faults in design- or execution. Internationally, parking garage damage has been an existing issue for the past decades. Liitvan and Bickley (1987) stated this problem in the 1980's in Canada, and Tighe and Van Volkinburg (1989) spoke of a "Parking garage crisis" in the 1980's in America. The engineering faults made in The Netherlands are commonly reoccurring mistakes, seen across various parking structures (Nuiten & Rinsma, 2021). Although damage as a result of the faults is not always detrimental to the structural capacity or integrity, it could cause unnecessary maintenance or repair costs, visual discomfort or unnerving feelings from users, or even hazardous situations.

1.2 Scope and objectives

This research focusses on both non-structural and structural damage in parking structures located in The Netherlands. Predominantly damage of concrete systems are analysed, thus excluding reoccurring damages in steel structures. However, an exception is made for water retaining sheet pile walls, as these could also play an important role for massive concrete structures. Subsequently, no distinction is being made between private and public parking structures.

The aim of this study is to gather an overview of the frequently reoccurring types of damage in Dutch parking structures. Respective causes of the types of damage are included in the overview to emphasize important factors which should be taken into account when designing a parking structure. Additionally, a visual representation of the type of damage is integrated in order to identify existing damage in a parking structure, based on damage characteristics, structural element, and influential factors.

1.3 Research question

To create an overview of the types of damage and causes in these structures, it is essential to distinguish possible relations between them. Consequently, the main research question to be addressed in part I of this study is:

"How can frequently occurring damage in concrete parking structures in The Netherlands be related to its causes?"

The main research question is answered with the use of several sub-questions, encompassing:

1.1 What are the causes and types of damage in parking structures?
1.2 In which elements does damage occur in parking structures?
1.3 How does elapsed time influence damage in parking structures?
1.4 How can the occurring damage be prevented or mitigated?

1.4 Outline

This research is divided into two parts in order to ensure clarity and coherence. Part I of this research provides the breadth of this study, by studying the types of damages within parking structures. Subsequently, Part II studies the behaviour of one of these types of damage in further detail, which provides the depth of this research. A visualisation is given by a T-shaped diagram in Figure 1.1.

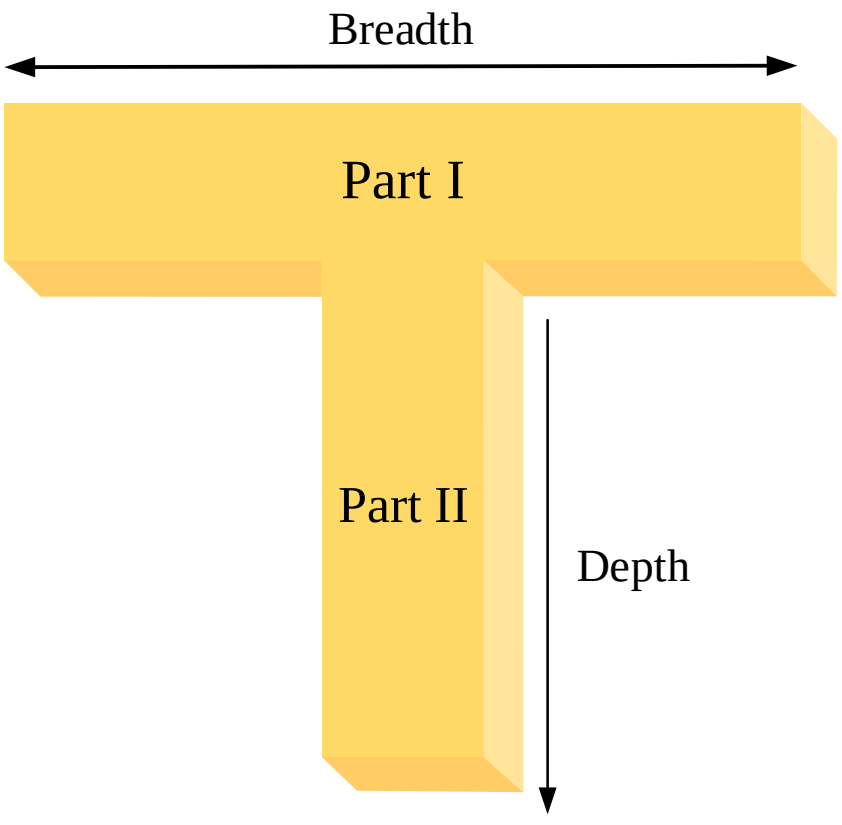

Figure 1.1 T-Shaped overview of Parts I and II of the research.

Following is a breakdown of the chapters in Part I of this research.

In Chapter 2 an overview of typical structural components and elements used in parking structures located in The Netherlands is made. Subsequently, an initial overview of potential damage in parking structures is created based on both international and Dutch literature.

The methodology of data collection in Part I and its limitations are elaborated in Chapter 3. It explains which parameters are relevant for the dataset and the approach for the data collection.

Chapter 4 provides an analysis of the collected data. The analysis comprises of a brief overview of the encountered types of damage followed by their respective causes, and the occurrence of the damage in each element. Lastly, the influence of the elapsed time on the types of damage is presented.

The results of the data analysis were used to create a "damage catalogue", found in Chapter 5. In the damage catalogue the characteristic, causes and mitigations of the observed damages are presented.

Lastly, a discussion and conclusion of the results are presented in respectively Chapters 6 and 7.

A flowchart of the research outline is presented in Figure 1.2.

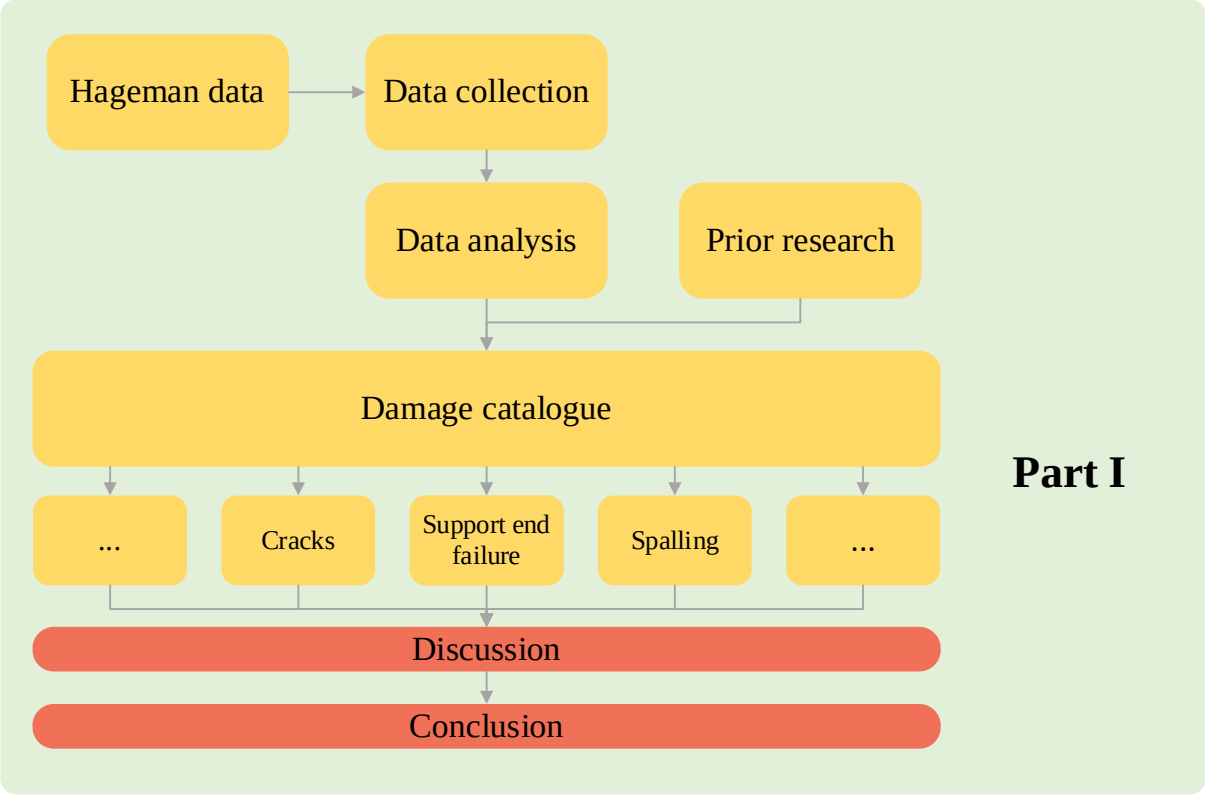

Figure 1.2 Flowchart of Part I of the research.

2 Literature study

2.1 General

The state-of-the-art is researched to give an initial insight into the past and current research on damage in parking garages. First, a short overview of structural elements used in Dutch parking garages is given in Section 2.2. Subsequently, an overview of types and causes of parking garage damage is given, based on both international and Dutch literature, elaborated in Section 2.3.

2.2 Structural systems

2.2.1 Wall elements

Underground and aboveground parking structures differ in use of wall elements. In aboveground structures wall elements are mainly applied as support element of floors or to provide stability to a structure. In underground structures, wall elements are a key element in sufficing the water retaining capabilities of the structure (De Boer & Van Haastert, n.d.). Generally, four distinct wall elements are applied in underground structures, encompassing:

- Retaining walls
- Diaphragm walls
- Sheet pile walls
- Cast in-situ walls

Retaining walls
Retaining walls are applied in underground parking structures, generally for singular layered parking layers. Often these elements are prefabricated in a factory, guaranteeing efficiency on the construction site. These L- or T- shaped elements utilize the retained soil as a method to stabilize the element, as seen in Figure 2.1.

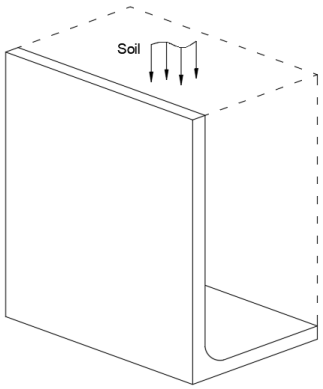

Figure 2.1 Schematisation of retaining wall.

Diaphragm walls

Diaphragm walls are large in-situ cast walls which are applied for multi-level underground parking structures as these are able to withstand large lateral loads and efficiently retain soil and water. The construction of diaphragm is a specialized process in which initially guide elements are installed, followed by excavation of the entrapped area which is filled with bentonite, to prevent the walls from caving in. Subsequently, reinforcement is lowered into the bentonite slurry, after which the bentonite is tremieed in, replacing the bentonite. After hardening of the wall element the adjacent element is constructed in the same manner, creating joints in between wall elements. These construction stages are portrayed in Figure 2.2.

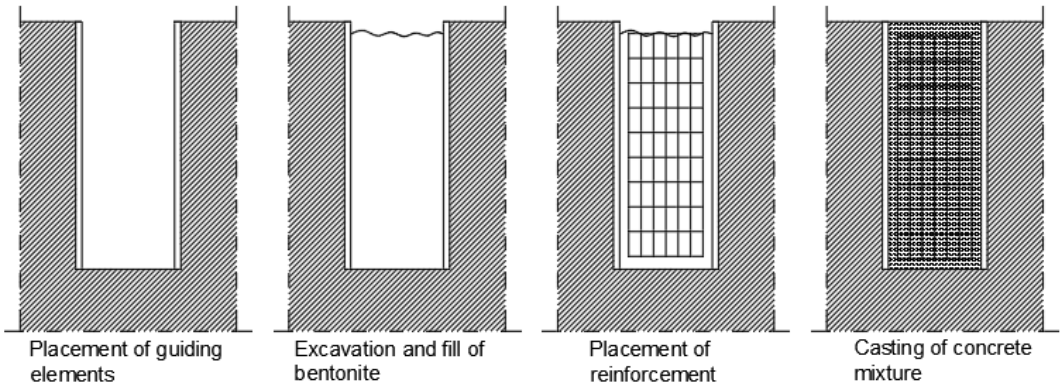

Figure 2.2 Construction phases of diaphragm walls.

Diaphragm walls are advantageous for multi-level underground parking structures as large depths can be reached. Furthermore, the bottom floors can be integrated into the wall elements to improve watertightness. To connect floor systems to diaphragm walls gains are integrated into the wall element, which act as continuity reinforcement with the cast in-situ concrete floor. Moreover, the installation process can be executed efficiently with minimal- to no nuisance.

Steel sheet pile walls
Sheet piles are frequently applied as water retaining walls. The U- or Z- profiled elements utilize slotted connections to form a continuous water impermeable wall, as seen in Figure 2.3. The steel individual elements are pushed into the soil using vibrations. After construction of floor and additional wall elements they can either be retrieved or kept in place.

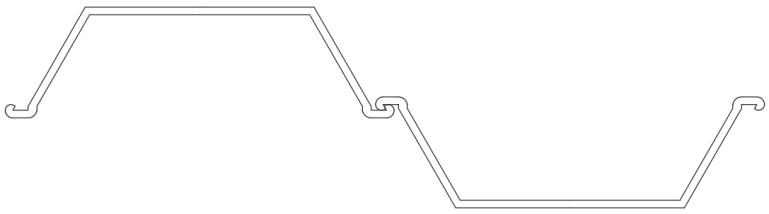

Figure 2.3 Cross-section of a U-profiled sheet pile wall element.

Sheet pile walls can also be used as supports for floor elements either by supporting the floor element directly on top of the sheet pile wall or by connecting it to the sheet pile wall with continuity reinforcement, as displayed in Figure 2.4 (De Boer & Van Haastert, n.d.).

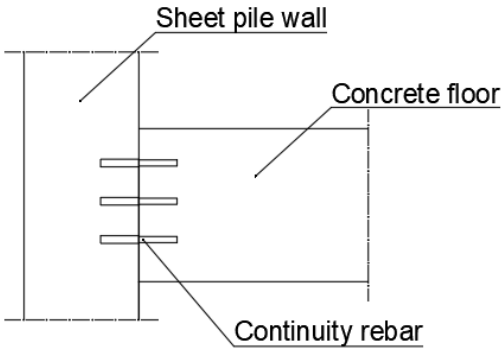

Figure 2.4 Connection between sheet pile wall and concrete floor, using continuity rebar.

Cast in-situ walls
Cast in-situ walls, alike retaining walls, are commonly used for singular layered parking garages. For the construction of these walls the soil is excavated, after which a concrete floor is installed on top of a foundation. Following the hardening of the concrete floor the concrete walls are casted on top of the floor. A schematization of this connection can be found in Figure 2.5.

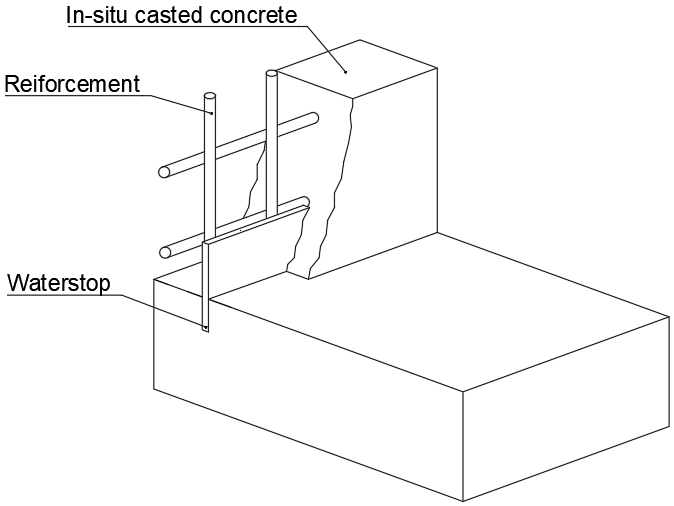

Figure 2.5 Schematisation of in-situ casted wall elements.

2.2.2 Floor systems

Three types of prefab floor systems are generally used for both underground and aboveground parking structures in The Netherlands. These systems are TT slabs, hollowcore slabs, and filigree slabs (Van Den Broek, 2021, De Boer & Van Haastert, n.d.). Moreover, in-situ casted monolithic, both reinforced or post-tensioned, concrete floors are commonly applied.

The floor systems (hollowcore and TT slabs are commonly integrated with an additional concrete compressive top layer to create monolithic behaviour of the floor. The monolithic behaviour ensures that horizontal loads can be transferred from the floor element to the stability systems of the parking structure. Moreover, it creates a water impermeable layer on the prefabricated floor elements.

TT slab
TT slabs are prefabricated prestressed concrete floor slabs (Figure 2.6). They are implemented either with or without an additional compressive layer. Without use of concrete topping watertightness needs to be ensured; this is usually achieved by applying sealant between joints (De Boer & Van Haastert, n.d.). In case compressive layers are used for TT slabs these are usually 60-80 mm thick (Van Den Broek, 2021).

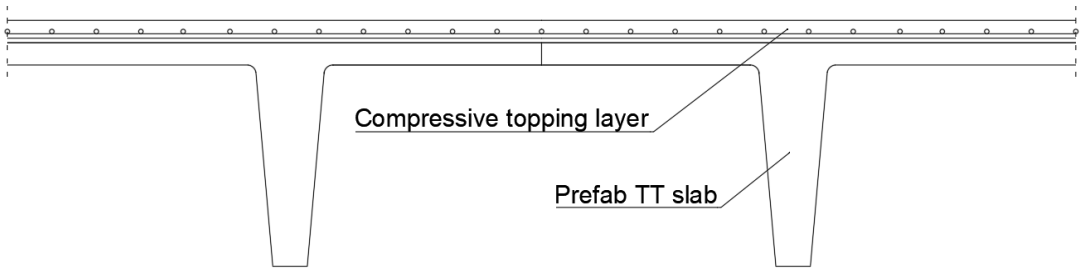

Figure 2.6 Schematisation of TT-slab configuration with compressive topping layer.

Hollowcore slab

Hollowcore slabs are generally, alike TT slabs, prefabricated prestressed concrete floor slabs. The slabs span up to 16 m with a standard width of 1.2 m. Hollow shafts are inserted at the core of the slab element to reduce the elements' weight (Figure 2.7). These slabs are generally paired with an in-situ casted topping layer as the elements by itself is not water impermeable (Van Den Broek, 2021).

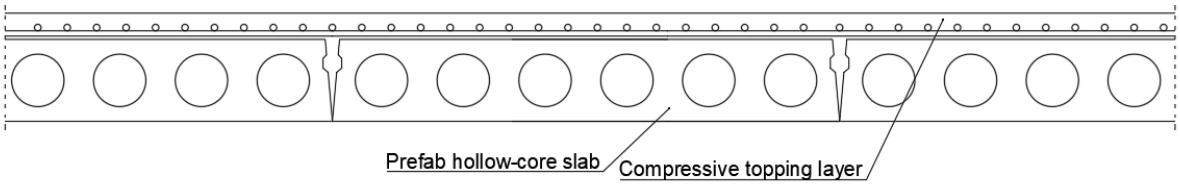

Figure 2.7 Schematisation of hollowcore slab configuration with compressive topping layer.

Filigree slab

Filigree slabs, in Dutch called "breedplaatvloeren", are partially prefabricated reinforced concrete slabs. A prefabricated slab element acts as a base of the floor. Integrated in the slab are steel trusses which act as longitudinal and shear reinforcement, as shown in Figure 2.8. Situated in between the floor elements are optional weight-reduction measures such as polystyrene cubes or plastic voids. The slab elements are installed on site and propped before casting of an integral concrete layer. Additionally, coupling reinforcement is added between adjacent floor elements to transfer shear forces between adhering slabs. Filigree slabs utilize a precast layer of 50 - 80 mm with integrated rebar on top of which concrete is cast, creating a monolithic floor (De Vree, n.d.).

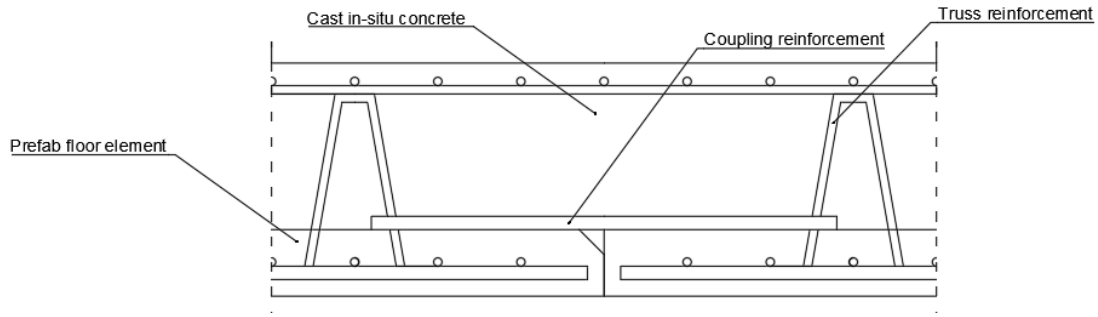

Figure 2.8 Schematisation of filigree-slab cross-section of joint.

Monolithic floors

Monolithic floors are in-situ casted concrete floors forming a singular element. Reinforced monolithic floors are commonly applied in underground parking garages to create a water impermeable bottom floor. Moreover, post-tensioned monolithic floors are occasionally used in both underground and aboveground systems.

2.2.3 Support systems

Three types of support methods are frequently applied for prefabricated connections in parking garages. These systems encompass: corbels, half-joint connections (dapped end), and L- or inverted T- beams (De Boer & Van Haastert, n.d.). Corbel connections are integrated in column elements to support concrete beams. The connection of a beam element on a corbel is commonly achieved by dapped ended connections, as depicted in figures 2.9 and 2.10. To reduce floor height, thus maximize effective height, L-beams or inverted T-beams are used as support for concrete floor elements.

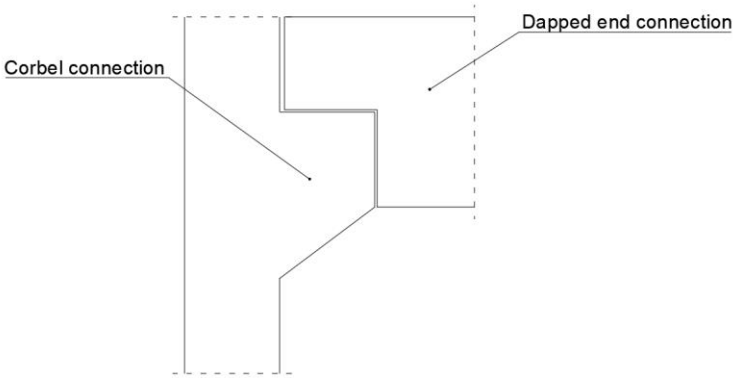

Figure 2.9 Schematisation of connection between corbel and dapped-ended beam.

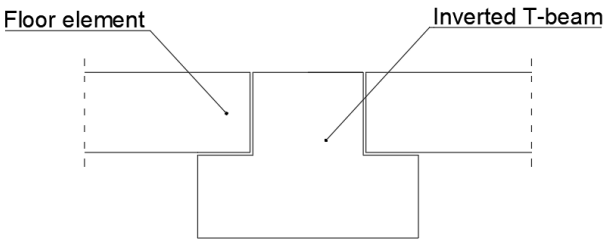

Figure 2.10 Schematisation of connection between floor elements and support beam.

2.3 Damage mechanisms

Causes of damage in parking structures effectively stem from three origins:

- Deterioration mechanisms
- Faults in design
- Faults in execution

The deterioration of the structures is mainly related due to environmental factors and aging, whereas damage due to flaws in design or execution are generally caused by human errors. Research mentions the most occurring types of damage in Dutch garages being corrosion, cracking, local spalling, and leakage (Concept Ingenieurs, n.d.; SGS Intron, 2019; Nuiten & Rinsma, 2021) These four types of damage are also frequently found in parking structures internationally (Donnelly et al., 2006; ACI Committee 362, 2000; StructureCare, n.d.). However, the causes of the types of damage vary to a certain extent.

De Jong (1992) presented an overview of common types of damage in concrete structures based on 30 years of in-practice experience at Adviesbureau Hageman, between approximately 1960 and 1990, encompassing:

1. Crack caused by restrained shrinkage
2. Crack caused by different causes
3. Concrete damage due to insufficient cover
4. Chloride induced damage
5. Casting related issues
6. Poor concrete surface
7. Support end failure
8. Delamination
9. Insufficient bearing capacity of floors
10. Insufficient reinforcement

From this overview it is suggested that the majority of the observed damage is caused by faults in design or execution, as just chloride induced damage is related to degradation. In the following subsections an elaboration is given for potential damages in parking structures.

2.3.1 Degradation mechanisms

Corrosion is a re-occurring degradation mechanism for parking structures. Chlorides, originating form de-icing salts, are the most common cause for corrosion (SGS Intron, 2019; SGS Intron, 2017; Concept Ingenieurs, n.d.; StructureCare, n.d.; Donnelly et al., 2006; ACI Committee 362, 2000). Besides, wrong exposure classes of concrete, too little cover, or stress corrosion pose for additional contribution (SGS Intron, 2017).

Corrosion
Corrosion is found in three forms: uniform corrosion, non-uniform corrosion, and pitting corrosion. The main causes of corrosion of rebar in concrete structures is due to carbonation or chloride ingress (Ahmad, 2003; Hansson et al., 2012; Jabed et al., 2023). Parking structures are exposed to chlorides from de-icing salts creating a chlorine environment. Studies proved that chloride induced corrosion outweigh the effect of carbonation in these environments (Choi et al., 2006; Malhotra et al., 2000). Chlorine induced corrosion can result from different stages of the lifetime, which can also be distinguished as internal and external chlorides. Internal chlorides involve chloride ingress in the fresh stage of concrete, whereas external chlorides are exposed to the concrete in the hardened stage. Pradhan and Bhattacharjee (2011) stated that external chlorides are the main cause of corrosion in parking structures.

Chlorides induce local corrosion pits in the concrete rebar. This is caused by degradation of the passivation layer of the rebar by chlorides, called depassivation (Darmawan, 2010). Depassivation takes place once the chloride threshold level (CTL) is exceeded (Darmawan, 2010; Ryou & Ann, 2008).

Pitting corrosion is known for two types: wide-shallow pits and narrow-deep pits (Zhao et al., 2020). Pitting corrosion of rebar has several effects on the structural behaviour of an element. Corrosion leads to a significant decrease of the cross-sectional area, volume expansion, resulting in cracking, delamination, or even spalling of concrete (Broomfield, 2003; Lin et al., 2019, Zhao; Stewart, 2009). The latter showing potential of bond degradation. This greatly depends on concrete cover depth and orientation of longitudinal reinforcement (Fu et al., 2021). The reduction of cross-sectional area can even cause a change from ductile to brittle failure, changing steel properties significantly (Sheng & Xia, 2017).

Corrosion enhanced cracking is often a result from external chloride ingress in already existing cracks. The allowed crack width for chlorine environments is 0.2 mm (Nederlands Normalisatie Instituut, 2020). However, faulty assumptions in the exposure class in concrete design have been observed in practice, with exceedance of the permitted crack width as result (SGS Intron, 2017). This could be impactful regarding chloride penetration or diffusion, however studies are conflicting on this impact (Win et al., 2004; Lai et al., 2020; Jang et al., 2011). Furthermore, studies have mentioned their doubts regarding the scientific background of the regulated crack width of 0.2 mm in chlorine environments (Šavija & Schlangen, 2011).

Freeze-thaw

Various sources in literature claim that freeze-thaw is the most common degradation induced cause for cracking (StructureCare, n.d.; Donnelly et al., 2006; ACI Committee 362, 2000). Freeze-thaw poses two possible damage mechanisms: scaling due to de-icing salts or cracking due to expansion. Cracking or spalling due to entrapped water in concrete pores results in induced forces to the concrete. The entrapped water expands in cold climates and exerts pressure in the concrete, resulting in cracks (De Schutter, 2017). But mostly, freeze-thaw in combination with de-icing salts is a common cause for scaling, or salt-scaling, of concrete surface. Valenza and Scherer (2007) proposed the so-called “glue spall” mechanism, seen as the primary mechanism of salt scaling. De-icing salts cause salt solution on the surface of the concrete, which upon cooling turns into a solid layer. The thermal expansion coefficient differs from these layers, with a larger thermal expansion coefficient for the ice layer of roughly factor five. During cooling the ice layer contracts more than the concrete layer. The concrete surface restraints the ice layer and thus causes tensile forces in the ice layer. As result, the ice layer cracks and scales parts of the concrete surface with it. Research has shown that freeze-thaw enlarges chloride migration coefficient (Keßler et al., 2016). Keßler et al. (2016) argued that especially concrete with a water/cement ratio of 0.55, without use of air entraining agents, is not suitable for a freeze-thaw and chlorine environment. Air entraining agents could mitigate this effect, however these showed a larger initial chloride migration coefficient.

Corrosion and freeze-thaw are frequently mentioned degradation mechanisms of damage in parking garages. However, Donnelly et al. (2006) mentioned that degradation mechanisms such as alkali-silica reaction (ASR) and sulphate attack include possible causes for damage.

2.3.2 Faults in design and execution

Crack formation is mentioned in literature as a frequently re-occurring damage. Amongst the causes is restrained concrete shrinkage, specifically: plastic-, thermal, and drying- shrinkage (Nuiten & Rinsma, 2021; Donnelly et al., 2006; ACI Committee 362, 2000). Additionally, leakage and interaction between damage mechanisms frequently occur (Nuiten & Rinsma, 2021; ACI Committee 362, 2000).

Restrained shrinkage

Concrete naturally shrinks. Aforementioned in-situ concrete elements such as floors, walls, or concrete topping layers are especially subject to shrinkage, due to larger continuous spans. If the casted element becomes constrained, for example by adherence of adjacent elements, a tensile stress emerges in the concrete element. Exceedance of the tensile capacity of the concrete element by the tensile stress results in cracks. These cracks affect the theoretical bearing capacity of floors minimally. As a result, this cause of cracking is in-practice usually ignored, as structural design codes allow a maximum crack width of 0.2 mm. Yet, combined with cracks due to additional causes, bending or loading as such, the maximum crack width is often exceeded (Nuiten & Rinsma, 2021).

Plastic shrinkage occurs in the plastic phase of freshly cast concrete. The main cause of this is by incorrect curing conditions of the concrete, in which the surface dries too fast (De Schutter, 2017). More specifically, it is caused by evaporation of free water at the surface of concrete. If this evaporation is continuous, and solid particles are restrained, it creates a capillary pressure between solid particles causing a negative pressure (Slowik et al., 2008). Between the particles a gap arises which allows air to enter the concrete paste. These air positions form weak spots in the concrete, and when paired with shrinkage cause cracking (Combrinck & Boshoff, 2013). Plastic shrinkage typically occurs in large concrete surfaces such as floor slabs. This is enhanced combined with high evaporation rates, dry climates, or hot temperatures (Combrinck & Boshoff, 2013).

Thermal shrinkage is for massive concrete structures, such as underground parking structures, an important aspect. In parking structures monolithic floors, walls, or connections between elements are often affected by thermal cracking (De Schutter, 2017). This is mostly due to hydration reaction of cementitious binder. This process leads to heat generation, mainly affecting large concrete elements. Cracking by thermal shrinkage can be related from two origins: internal- and external restraints (Lopes et al., 2013; De Schutter, 2017).

Internal restraint cracks are formed due to temperature gradients between the inner force and surface of the concrete element. The surface of the element is often cooler than the inner parts, or this is caused by too early removal of formwork. The outside of the element is restrained to shrink by the inside, inducing a tensile force. If this force exceeds the concrete tensile strength, cracks occur. The crack pattern of internal restrained cracks are usually random maps. The severity of these cracks are dependent on the Young's modulus, creep and relaxation. Whereas cracks due to external restraints are caused by bond force between two concrete elements. The main cause of this force is due to separate execution between two concrete elements. Relevant factors that impact the external process are the dimensions and contact area of the elements, as a large contact area could cause cracks due to both internal and external restraints. (Lopes et al., 2013; De Schutter, 2017).

Drying shrinkage is caused by volume reduction of cast concrete due to evaporation of water. This is a result of captured water from capillary pore or physically adsorbed on hydration products (De Schutter, 2017). Drying shrinkage is an important cause of cracking. In parking structures cracking due to drying shrinkage is often seen in compressive layers near supports of floors or between columns (SGS Intron, 2017).

Restrained rotation
Floor joints are not only susceptible to cracks due to shrinkage, but they are also subjected to rotations. Due to application of compressive layers on prefab slabs a monolithic behaviour is created. The compressive layer creates a hogging bending moment located at the support of floor slabs. Velthorst (2007) provided design guides for hollowcore slabs with integrated compressive layers. A clear weakness of this system is that cracks in the floor joints are almost unavoidable, due to combination of shrinkage, rotation, and creep. Nuiten & Rinsma (2021) confirmed that in parking structures cracks of floor joint are frequently observed, additionally due to insufficient strength of the compressive topping layer.

Expansion joints
Expansion joints offer a solution to restrained shrinkage and rotations by permitting these movements. Expansion joints are small discontinuities in elements to allow these movements. In order to prevent cracking, the discontinuity gap is filled, commonly by a flexible sealant. Failure of sealants are the underlying issue of leakages in parking garages (Donnelly et al., 2006; SGS Intron, 2017; ACI Committee 362, 2000). ACI Committee 362 (2000) stated that leakage in parking structures can be related to issues regarding sealants, most commonly at expansion joints. A common problem with these sealants is that the application surface deteriorates over time causing intrusion of water. Moreover, leakage occurs due to tearing of the sealant as a result of exceedance of its tensile capacity (Nuiten & Rinsma, 2021).

Typically, expansion joints consists of connections between sub- and superstructure, as shown in Subsection 2.2.3. Yet, by permitting horizontal movements and rotations additional designing is needed. Faults in design are frequently made in practice. Use of wrong- or no interlayer material increase horizontal forces between sub-and superstructure, causing support end failure (Nuiten & Rinsma, 2021).

Interaction of damage mechanisms
Damage mechanisms can also induce or initiate other damage mechanisms. Donnelly et al., (2006) stated that corrosion caused by chlorides is often initiated or accelerated through ingress of existing cracks. Moreover, corrosion of reinforcement may also cause cracks in concrete to large expansion of steel. Not only does the cracking allow for ingress of chlorides or other chemicals, but it also allows for future growth of shrinkage related cracks, such as drying- or thermal shrinkage (Holt & Leivo, 2004). Additionally, cracks often accompany transfer of water, and subsequently causing leakage (ACI Committee 362, 2000). An overview of the mentioned types of damage and their potential causes is provided in Table 2.1.

Table 2.1 Overview of types of damage with corresponding causes according to literature.

	Cause
Corrosion	Chloride ingress • Faulty design using wrong exposure class • Insufficient concrete cover • Ingress through existing cracks
Cracking	Restrained deformation • Plastic shrinkage • Thermal shrinkage • Drying shrinkage • Thermal movement Deterioration mechanisms • Freeze-thaw • ASR • Sulphate attack Applied load Faulty design in expansion joints Rotation of floor at supports Interface between floors due to deflection
Spalling	Spalling of beam elements by rotation of floor element due to a faulty design or execution Corrosion
Leakages	Inadequately sealing of expansion joints Thermal movements Cracks

2.3.3 Summary

The chlorine environments of parking structures enhances the deterioration mechanisms significantly. As a result, corrosion and corrosion induced damage is frequently occurring according to literature. Besides, the literature review showed that damage mechanisms initiates and enhances other damage mechanisms. For context, corrosion by chloride ion penetration may pose for expansion of rebar, resulting in cracks and leakage. Vice versa, crack induced corrosion is also commonly mentioned. Other commonly mentioned deterioration mechanism is freeze-thaw. Causes of freeze-thaw include scaling of the deck and spalling of concrete.

Moreover, common designs faults are found at expansion joints. Regularly discussed are faults in either material usage of supports, support end failure of structural elements, or inadequate sealing. Wrong- or no use of support materials cause vulnerabilities of cracks caused by thermal or drying shrinkage and by thermal movement. Leakages are often caused by inadequate sealing or little maintenance over the years.

Furthermore, design and construction faults are most commonly found in terms of plastic, thermal, and drying shrinkage induced cracks, the latter two being due to movement restraints. Besides, cracking of prefab elements due to rotation at supports and insufficient detailing of compressive topping layers add to these faults.

2.4 Research gap

The state-of-the-art provides an initial overview of possible types of damage and corresponding causes which occur in parking structures. The work of Nuiten & Rinsma (2021) summarized several damages occurring in Dutch parking structures, although they did not cover all types of damages found.

Therefore, the identified research gap is the lack of overview on types of damages in Dutch parking structures. This is remarkable, as literature also emphasized that the observed damage is frequently seen and caused by the same faults.

Whilst the state-of-the art provides insight into a large amount of damages, based on international and Dutch literature, these might not all be applicable for parking structures located in The Netherlands. Additionally, the literature found provided little information on correlation between factors such as element of occurrence, elapsed time after a damage occurred, or a distinction between underground- or aboveground parking structures.

3 Methodology

3.1 General

In order to obtain an overview of types of damage in parking structures, data is collected from Adviesbureau Hageman. The data collection is a key element to provide insight into types of damage and their respective causes which occur in parking structures. Section 3.2 describes the source from which the data is collected and an elaboration on the approach applied in the data collection. Limitations of the data collection are given in Section 3.3. An analysis and findings of the data are presented in Chapter 4.

3.2 Data collection strategy

The literature study provided an overview of types of damage which occur in parking structures, using both Dutch and international literature. Although, in order to answer the first research question an overview needs to be acquired for only Dutch parking structures. To obtain this overview, data is collected from reports on damage in parking structures of Adviesbureau Hageman, a consultancy firm with 65 years of experience in the forensic engineering industry.

The total archive of Adviesbureau Hageman contains almost 12,000 reports, varying from forensic analysis up to research. A selection was made of these reports to only contain forensic analysis on concrete parking structures. This selection was performed by filtering the titles of the reports on several terms. These terms encompass “park”, to collect the reports containing “parkeergarage” or “parking” in its title, and “garage”. Additionally, several reports on damage in parking structures were obtained through manual inspection of the report titles.

The archival reports are extensive documents, usually between 10-30 pages, regularly describing the characteristics of the building, such as year of construction, observations made during an inspection of the damage, the type of damage, cause of damage, location and element in which it occurred in, and occasionally recommendations on repairs. From these reports, several parameters are collected and used to form an overview of types of damage in Dutch parking structures. The data from the archival documents date from 1977 until May 2024, which include both public and private parking garages.

Several parameters were collected from the forensic reports to obtain the dataset. The data collection is performed by manually inspecting each report on the required data parameters. The parameters included in the data collection have been chosen in line with the sub-questions of the first research question. In order to obtain a thorough answer to the sub-questions the following parameters are collected:

- Type of damage
- Cause of damage
- Type of element the damage occurred in
- Year of inspection
- Year of construction
- Type of parking structure (above/underground)

The parameters 'type of damage' and 'cause of damage' are collected in order to provide an overview of the occurring damages in parking structures, answering sub-question 1-1. The 'type of element' and 'type of parking structure' help achieving an indication to the location of the parking damage, answering sub-questions 1-2. Lastly, the 'year of inspection' and 'year of construction' gather possible correlations between the cause or type of damage and the time period that they occurred in, answering sub-question 1-3. These parameters were collected in Microsoft Excel and analysed using the programming language Python. Storing the data according to the mentioned parameters ensures good post-processing possibilities. The data analysis is performed using the programming software Python. The main benefit of this software is the easy implementation of formulas and clear visual graphs. A flowchart of this process is presented in Figure 3.1.

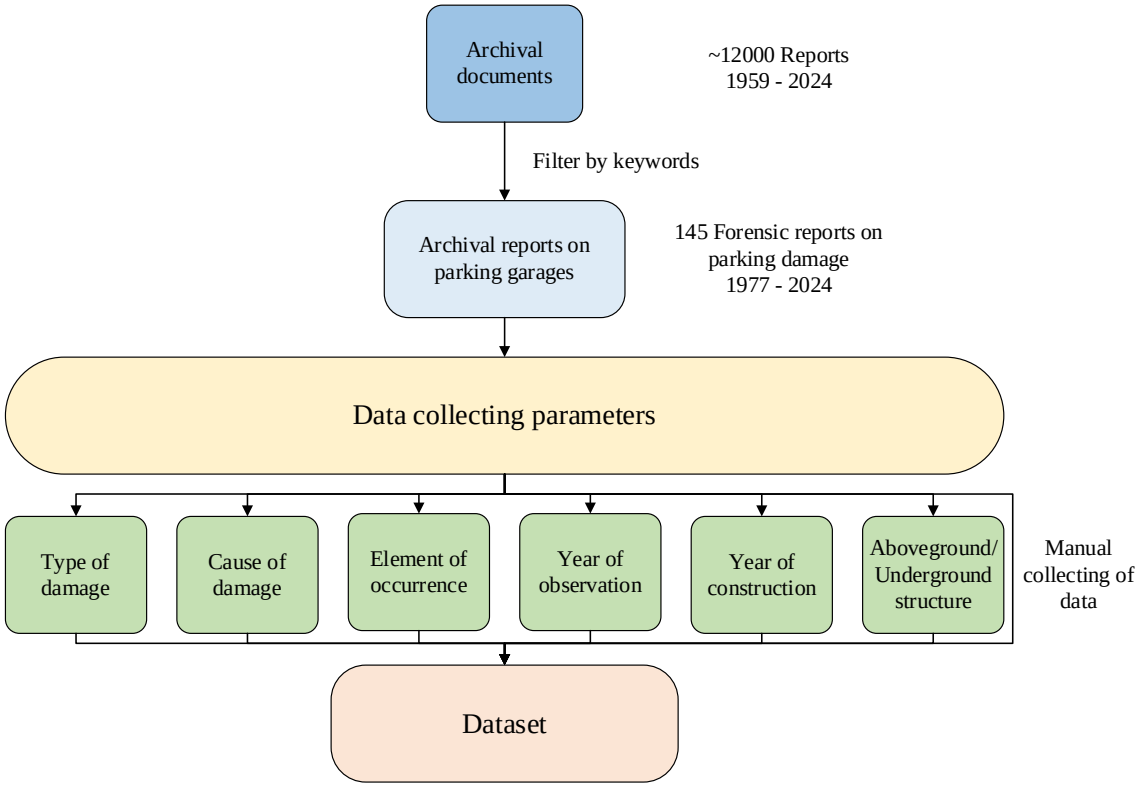

Figure 3.1 Flowchart of data collection.

Type of damage
The category ‘type of damage’ describes the visual damage or defect which was observed in the report. If multiple of the same types of damage, with identical cause and in the identical structural element, occur within a singular parking structure it is noted down once. If the same type of damage occurs, but in different elements or as result of different causes, it is collected as different damages.

Cause of damage
The ‘cause of damage’ is based on the findings and conclusions drawn in the archival document. Noted in the category are the certain or most probably causes which caused the damage. Uncertain or unspecified causes of damaged are noted down as ‘unknown’. If various factors initiated or contributed to the damage, both factors are noted down.

Type of element
The type of element describes the structural element in which the damage occurred. In the case that the damage is present in several structural elements, all affected elements are included. The type of element is determined either by visual inspection of archival images or technical drawings.

Year of inspection and construction
The year of inspection is provided by the archival documents. The construction year is not always specified within the report. If this data was not provided within the forensic report, the Basisregistratie Adressen en Gebouwen[1] (BAG) was consulted. This register maintains an online tool, BAG Viewer, in which information related to buildings are stored. Using this tool the year of construction was found for construction years which were not mentioned in a report.

Type of parking structure
The type of parking structure describes whether the structure is an above- or underground parking structure.

3.3 Limitations of the data

The collected data is limited in several aspects. The total dataset is a sample of all the parking garage damage in The Netherlands. Moreover, as qualitative data is collected the results might not represent all the damage of parking structures in The Netherlands. As such, the collected data remains a general indication of the damage in Dutch parking structures.

Secondly, since the data is provided by a private consultancy firm a certain bias is present. A bias in the form of limited expertise or scope within the company possibly skews the results. Additionally, in the timespan during which Adviesbureau Hageman performed their analyses, several changes could have been implemented within the company. Factors such as growth of the company or change in expertise could potentially affect the results from the data.

Thirdly, the archival files are filtered using the words “park” or “garage”. Reports not including these keywords in its title are not included. Thus, reports discussing forensic analysis on parking structures without either of these words in its report title are not included in the data analysis.

[1] Basisregister Adressen en Gebouwen is a public database, containing data on buildings and addresses in The Netherlands

4 Data analysis

4.1 General

The dataset totals 145 forensic reports, from which 234 damages were observed. The dataset is provided in Appendix A. Section 4.2 provides a global overview of the acquired data, elaborating on construction years, the types of damage found, and differences between above- and underground structures. Subsequently, an in-depth analysis of the types of damage is provided in Section 4.3 and their respective causes and elements of occurrence are presented in Section 4.4. Finally, Section 4.5 presents findings between time period and the observed damage.

4.2 General findings

An overview of the year of construction of the structures in the dataset are plotted in Figure 4.1. The histogram represents the year of construction of the parking structures, representing both public- and private parking structures. For context, a public parking garage is seen as a structure accessible to the general public, whereas private parking garages are not. The latter generally being located underneath residential buildings. The results indicate an increase in amount of constructed parking structures between the years 2000 and 2008. After 2008 fewer constructions of parking structures were observed.

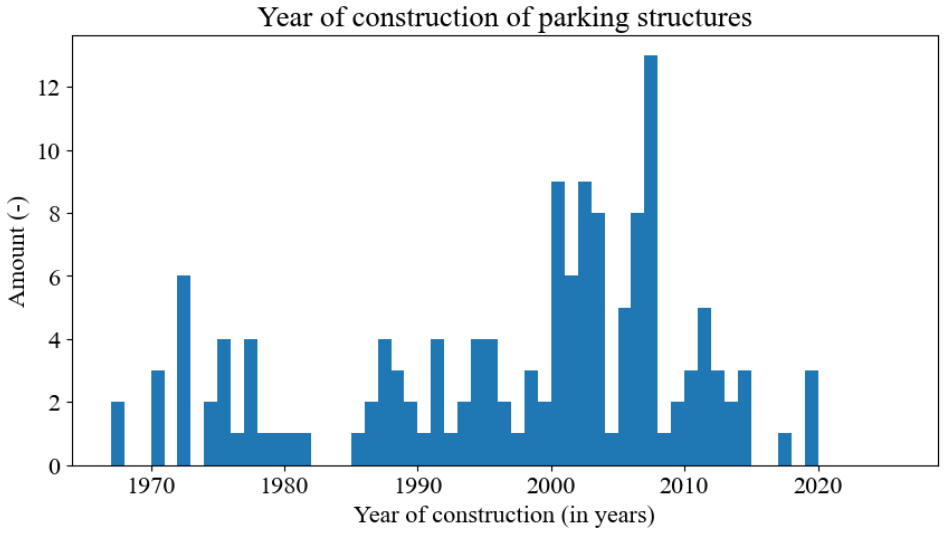

Figure 4.1 Histogram of year of construction of parking structures.

An indication of the elapsed time after which damage occurs is presented in Figure 4.2. These results are calculated by deducting the year of observation with the year of construction. As a result, a timeframe is obtained of the amount of years after which an observation is performed in a parking structure.

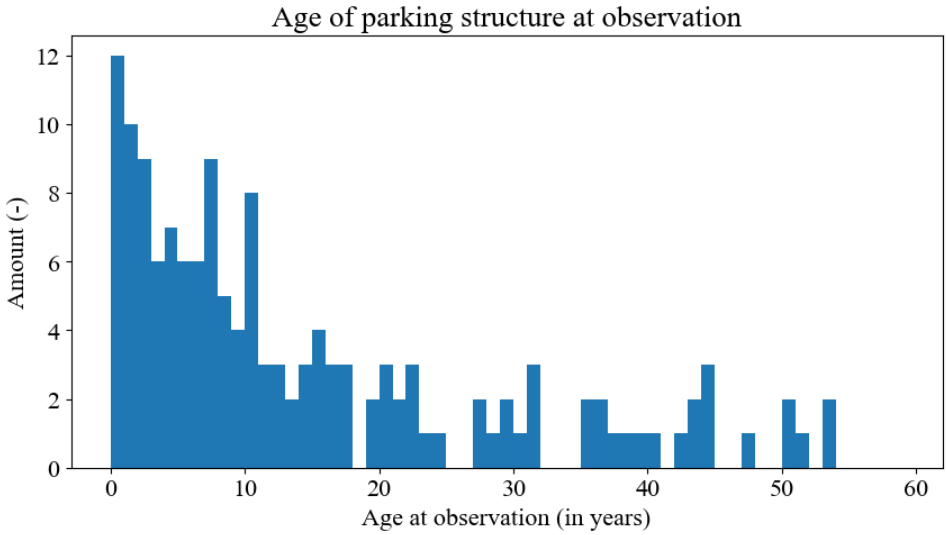

Figure 4.2 Histogram of the age of a parking structure at observation.

As a structure approaches the end of its service life it is more likely to encounter degradation mechanisms. Parking structures are generally designed for a service lifespan of 50 years. The data in Figure 4.2 suggests that most damages occur within 11 years after construction. Consequently, one could argue that a majority of the observed damage in structures is related due to faults in design or construction rather than due to degradation of a structure.

An equal amount of aboveground and underground structures were observed in the dataset, with 74 underground (51.0%) and 71 aboveground (48.9%) parking structures. Moreover, the types of damage occurring in aboveground and underground structures are presented in figures 4.3 and 4.4, respectively.

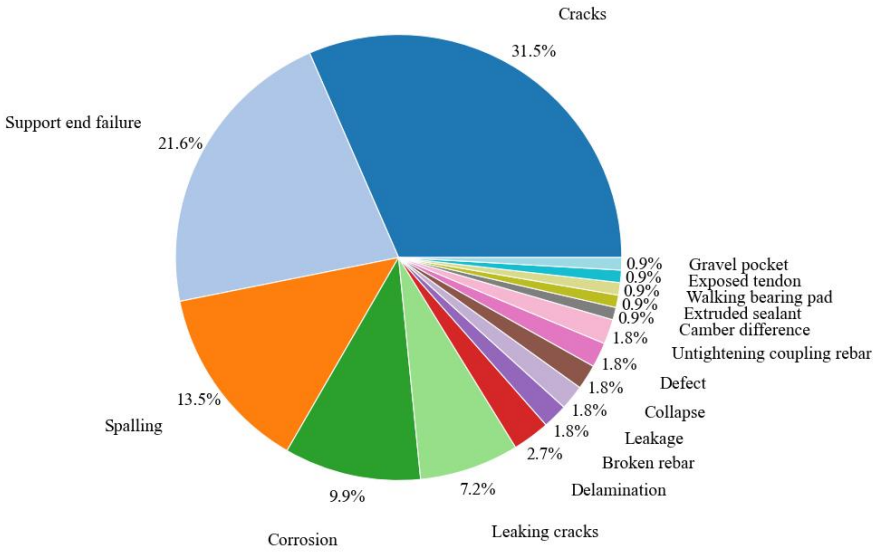

Figure 4.3 Damage occurring in aboveground parking structures.

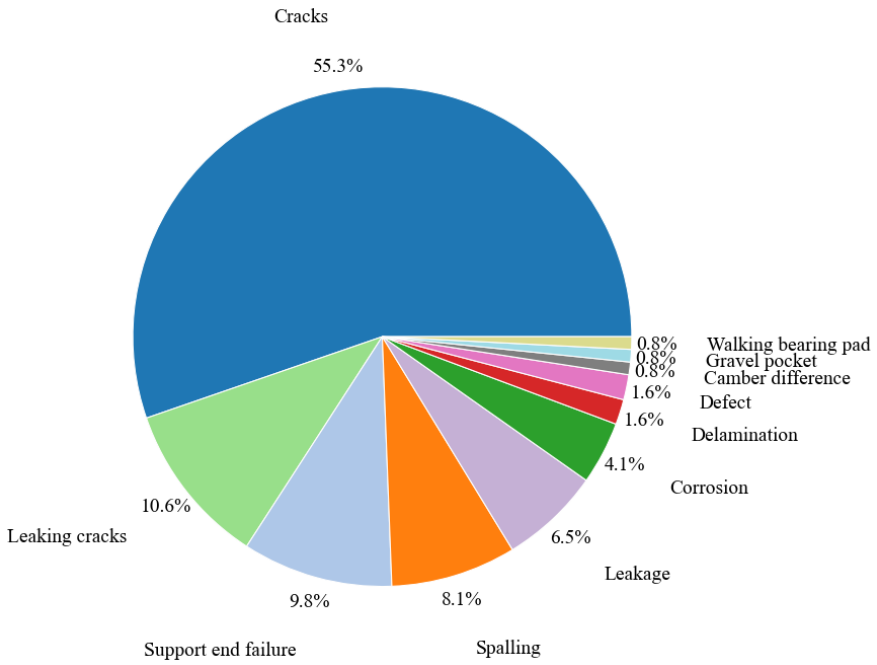

Figure 4.4 Damage occurring in underground parking structures.

A difference in occurring damage between above- and underground parking structures is observed. Cracks are the most common types of damage for both aboveground and underground parking structures. However, in aboveground structures this contribution is significantly lower (31.8%) than for underground structures (55.3%). This difference is also found in support end failure which occurs more for aboveground structures (21.8%) than for underground structures (9.8%). Moreover, a difference is seen in the occurrence of corrosion in aboveground structures (10.0%) than for underground structures (4.1%).

4.3 Types of damage

The aforementioned 234 types of damage encompass observed damages from the archival reports. A deconstruction of the observed damages into types of damage is given in Table 4.1.

Table 4.1 Overview of types of damage resulting from data collection.

Observed damage	Number of observations (-)	Percentage of total (%)
Cracks	103	44.0
Support end failure	35	15.4
Spalling	26	10.7
Leaking cracks	21	9.0
Corrosion	16	6.8
Leakage	10	4.3
Delamination	5	2.1
Defect	4	1.7
Collapse	2	0.9
Walking bearing pad	2	0.9
Untightening coupling rebar	2	0.9
Gravel pocket	2	0.9
Camber difference	2	0.9
Broken rebar	2	0.9
Exposed tendon	1	0.4
Extruded sealant	1	0.4

The results indicate that the large majority of the observed damages in parking structures are cracks, including both leaking and non-leaking cracks. Whether a crack was leaking or not was determined based on the observations in the archival reports. During the collection a distinction was made between leaking cracks and leakage in order to create a clear difference between leakage as a result of cracks and other factors.

Besides cracks (44%), support end failure (15.4%), spalling (10.7%), leaking cracks (9.0%), corrosion (6.8%) and leakage (4.3%) are frequently observed damages. Less common are delamination (2.1%) of compressive top layers or structural defects (1.7%). A defect is defined as an insufficiency of structural capacity within a design or structure.

Moreover, several less common observed damages contribute to the data, encompassing: collapse, walking bearing pad, untightening of coupling reinforcement of TT-slabs, gravel pockets, difference in camber, broken rebar, exposed tendons, and extruded sealants.

Causes for types of damage with 10 or less observations are found in Appendix B. The frequent, amount of observations larger than 10, are presented in the following sections.

4.4 Cause of damage

4.4.1 Cracks

The general data implied that cracks are the most common form of damage in parking structures. The causes of cracks as collected in the dataset are shown in Figure 4.5.

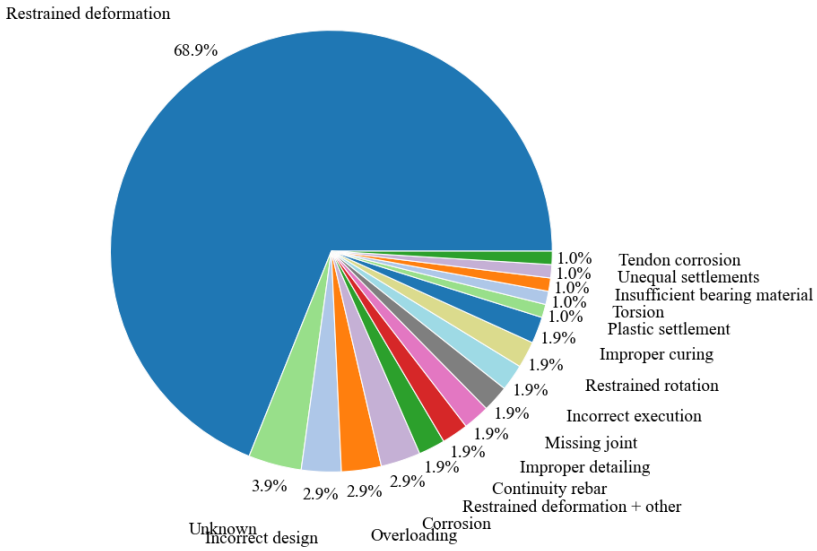

Figure 4.5 Causes of cracks in parking garages.

The results suggest that restrained deformations are the most prevalent cause of cracks. Restrained deformation is an overarching term for deformations either due to shrinkage, thermal influence, or applied load. From the observed data, more than 70% of the cracks in parking garages are caused by restrained deformation, if restrained rotations and a combination of restraints are included. The remaining causes are divided into smaller shares. The amount of degradation induced cracks consists of only 3.9% due to corrosion. In Figure 4.6 the distribution of cracks in elements and sub-elements of the category floors are presented.

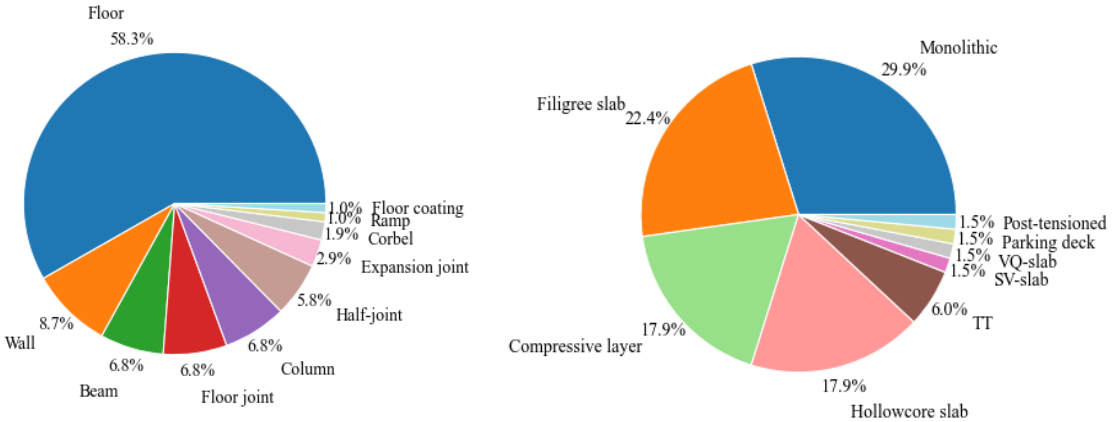

Figure 4.6 Distribution of cracks occurrence in element types (left) and sub-elements of floors (right).

Cracks were significantly more observed in floor elements than other elements. This is expected since floor elements are often designed with large continuous spans as well as many adhering elements, forming constraints. The most affected types of floor elements are in-situ cast floor elements, monolithic (29.9%), filigree slab (22.4%), and a compressive topping layer (17.9%). All of these elements are entirely- or partially casted in-situ. Therefore, it is suggested that a large contribution of restrained deformation is particularly caused by restrained shrinkage.

4.4.2 Support end failure

The causes of support end failure are displayed in Figure 4.7. The results suggest that the causes of support end failure are divided in equal size. The largest contribution of support end failure is due to the presence of continuity rebar (30.6%), followed by improper bearing material (16.7%) and the 'walking' of bearing pads (8.3%). Moreover, incorrect design of the connection (8.3%), with regard to support or rebar configuration, and restrained deformation (8.3%) or a combination of various factors (8.3%) contributed slightly.

The most affected elements are corbels (30.6%), half-joints (25%) and support beams (19.4%), as seen in Figure 4.7. Columns (13.9%) and walls (5.6%) are less frequently subjected to this damage mechanism.

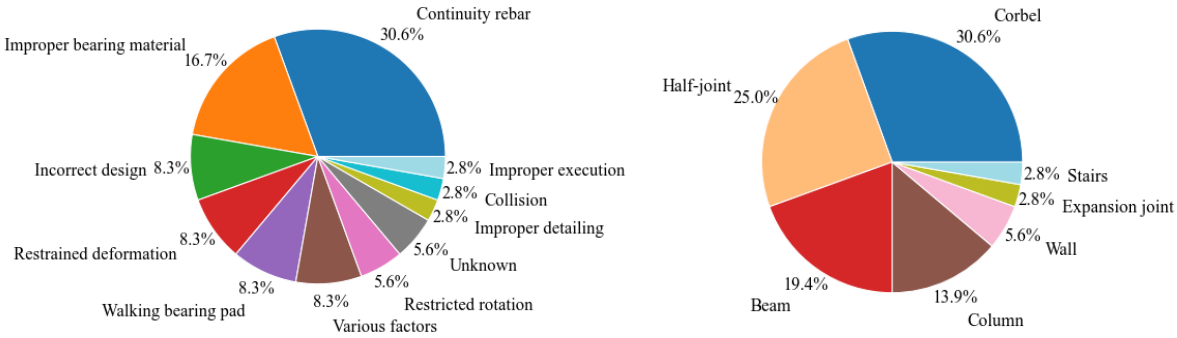

Figure 4.7 Causes of support end failure (left) and in elements subjected to support end failure (right).

Contrary to the causes in cracks, support end failure presents a wider range of possible contribution to the failure mechanism. Occasionally, multiple faults were made in the design, which was denoted as 'Various factors (8.3%)'. Based on the causes found in the data, it is indicated that the support end failure originates solely due to faults in design or execution.

4.4.3 Spalling

The causes of spalling in parking structures are enumerated in Figure 4.8. The findings imply that it is predominantly caused by fire of vehicles within a parking structure. Fire is an accidental load, thus not being categorized as either degradation or fault in design or execution. Besides fire, a small percentage of spalling is caused by corrosion and carbonation (12.0%), frozen water in shafts of hollowcore slab (4.0%), tendon corrosion (4.0%), and restrained deformation (4.0%).

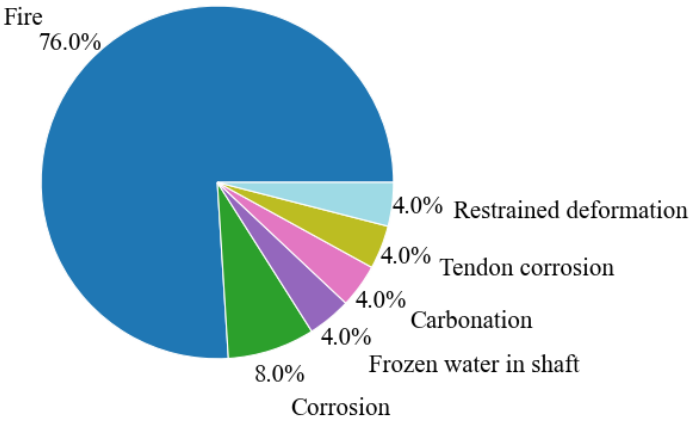

Figure 4.8 Causes of spalling (left) and in element of occurrence (right).

In Figure 4.9, the distribution of spalling affected elements and sub-elements from the category floors is presented. The findings argue that floor elements are the most frequent affected element by spalling, at 84% of the total amount of observations. From the types of floor elements, TT- and hollowcore slabs have been affected significantly more than monolithic or filigree slabs.

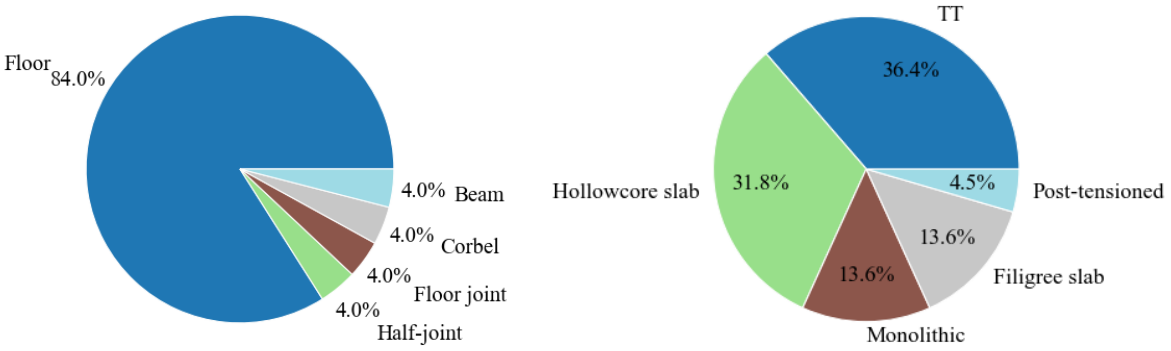

Figure 4.9 Elements (left) and floor types (right) subjected to spalling.

4.4.4 Leaking cracks

Leaking cracks are cracks in a parking structure which showed signs of water transfer during the observation. Characteristics for cracks that transfer water is the crack penetrating the entire cross-section of an element, thus allowing for water transfer. The causes of this type of damage are presented in Figure 4.10.

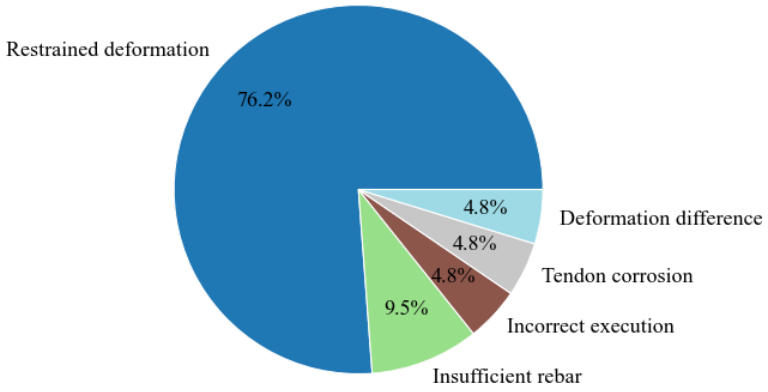

Figure 4.10 Causes of leaking cracks in parking garages.

The results of Figure 4.10 show close resemblance to the causes found for non-water transferring cracks. Restrained deformation is implied to be the predominant cause for leaking cracks (76.2%), closely matching the contribution for non-water transferring cracks (68.9%). In Figure 4.11 the distribution of elements and sub-elements in which leaking cracks occur are presented.

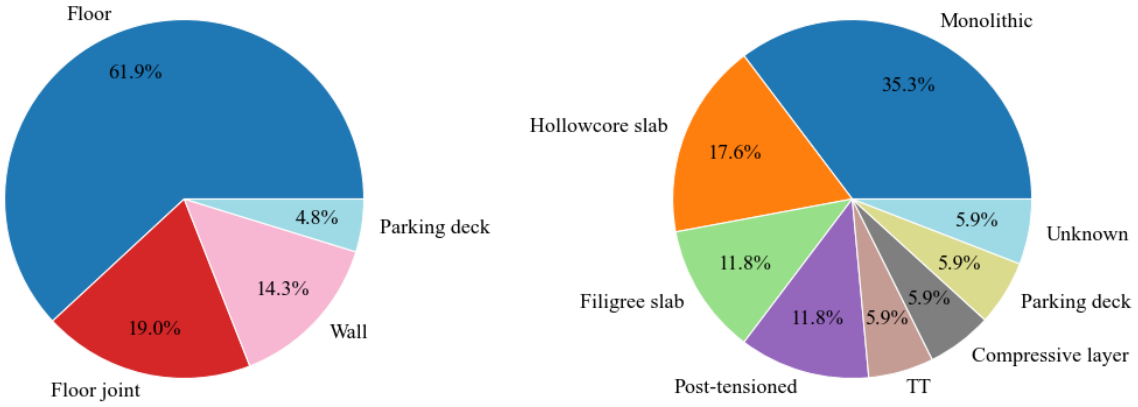

Figure 4.11 Types of elements (left) and floor types (right) subjected to leaking cracks.

The predominant element in which leaking cracks occur in are floors elements (61.9%) and floor joints (19.0%), similar to non-water transferring cracks. From which monolithic floors (35.3%), hollowcore slabs (17.6%), filigree slabs (11.8%), and post-tensioned floors (11.8%) are the most common, reinforcing the claim of large contribution of shrinkage in restrained deformations.

4.4.5 Corrosion

Chloride induced corrosion was seen as the most common type of degradation in concrete parking structures according to literature. The causes of corrosion induced damage and location of occurrence are presented in Figure 4.12.

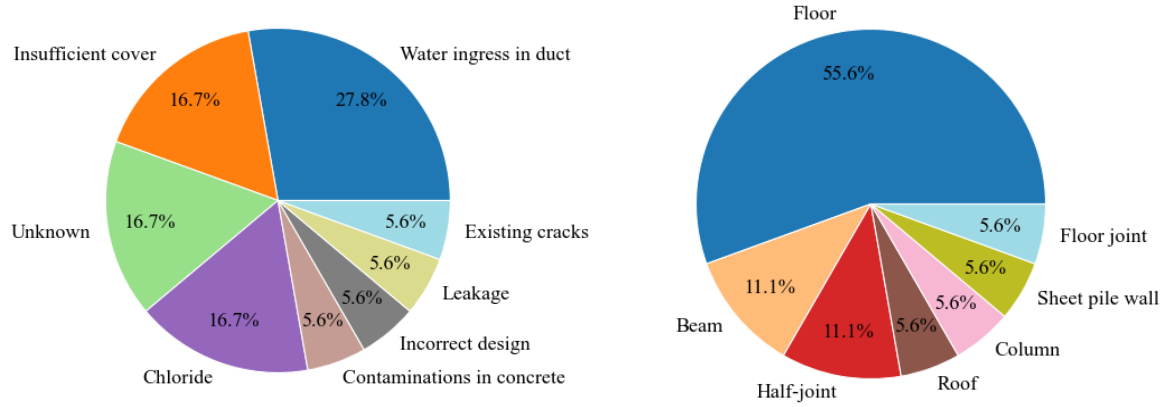

Figure 4.12 Causes of corrosion (left) and elements subjected to corrosion (right) in parking garages.

The findings suggest that the most common causes of corrosion are due to water ingress in prestress tendon ducts (27.8%), insufficient concrete cover (16.7%), and chlorides (16.7%). Yet 16.7% of the causes of corrosion were unknown. Moreover, a smaller contribution to the causes of corrosion are due to initiation through leakage or existing cracks. Corrosion appears mostly in floor elements (55.6%), followed by beams (11.1%), and reinforcement located at half-joint connections (11.1%), as seen in Figure 4.12.

4.4.6 Leakage

The causes of leakage in parking structures is displayed in Figure 4.13. The results indicate that the majority of the leakage is due to incorrect design, of both joint (30.0%) and joint material (10.0%). Moreover, damage of the joint sealant (10.0%) and failure of the sealant (10.0%) contribute to a large part of leakage.

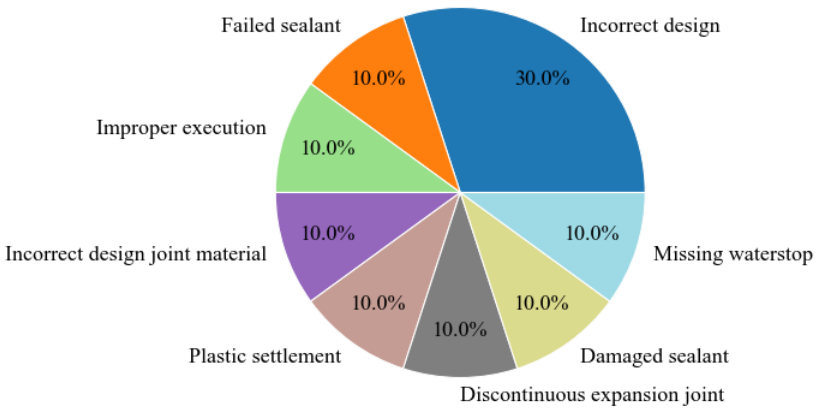

Figure 4.13 Causes of leakage in parking structures.

The observations of elements and sub-elements of walls affected by leakage are presented in Figure 4.14. The data indicates that leakage occurs most frequently in expansion joints (50.0%) or in wall elements (40.0%). Sheet pile wall elements are the most critical at half of the leakages, followed by diaphragm walls (25.0%), and in-situ casted walls (25.0%).

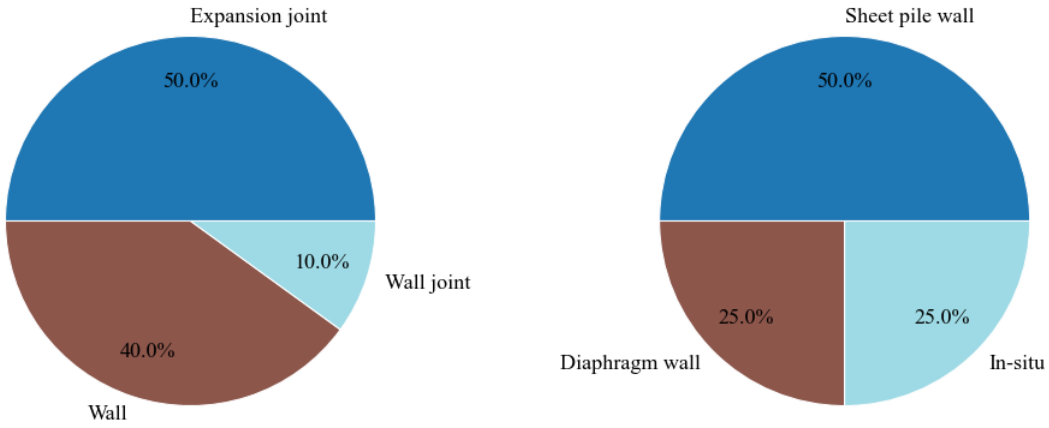

Figure 4.14 Elements (left) and types of wall elements (right) affected by leakage.

4.5 Influence of elapsed time

Types of damage are plotted in a histogram plot, displaying the age of a structure at observation versus the amount these observations. The age at observation is defined as the time between year of construction and observation. This is calculated by deducting the year of observation with the year of construction.

4.5.1 Cracks

The results of Section 4.3 suggested that the majority of the causes of cracks are due to restrained deformation, in particular due to shrinkage. Shrinkage is strongly time-dependent and generally occurs within several years after construction, depending on the type of shrinkage. In Figure 4.15 the age of parking structures at observation of cracks is plotted.

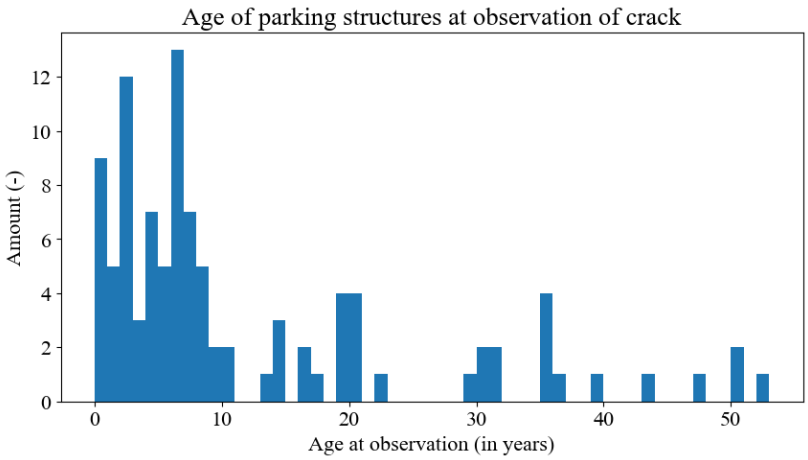

Figure 4.15 Histogram of age at observation for cracks.

The histogram in Figure 4.15 indicates that the majority of the cracks are observed within ten years after construction. Even though the observation might not have been performed soon after initiating of the damage, it suggest that majority of the damage is encountered early on the lifetime of the structure. The age at observation for cracks solely caused by restrained deformation are displayed in Figure 4.16.

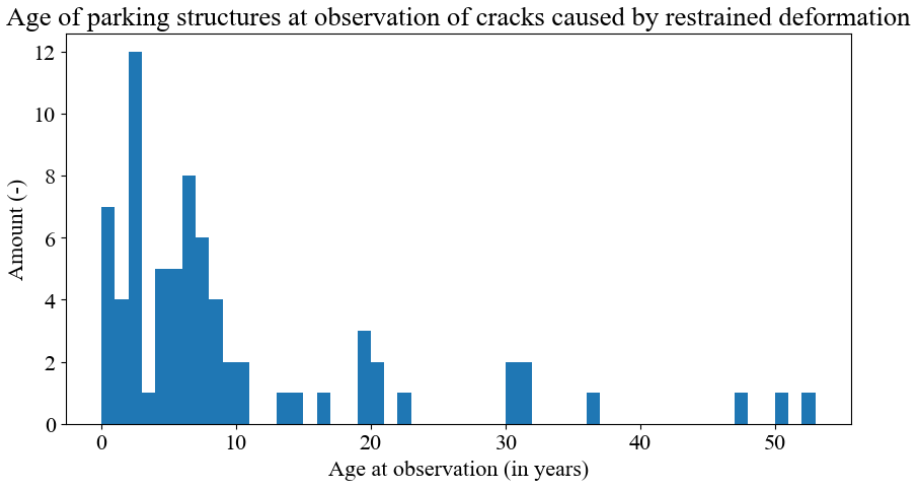

Figure 4.16 Histogram of age at observation for cracks caused by restrained deformation.

The findings imply that a majority of cracks in the within ten years of the parking structures lifetime. Although, even after further specifying the cause, observations of restrained deformation induced cracks are still found beyond the ten years. The causes of cracks other than restrained deformation after ten years are listed in Table 4.2.

Table 4.2 Causes of cracks at age of structure larger than 10 years.

Cause of cracks (> 10 years)	**Amount (-)**
Corrosion	3
Overloading	2
Missing joint	2
Improper curing	1
Improper detailing	1
Unknown	1
Unequal settlements	1
Incorrect execution	1
Incorrect design	1
Tendon corrosion	1
Continuity rebar	1

The most common causes of cracks, other than restrained deformation, ten years after construction are corrosion (3 occurrences), overloading (2 occurrences) and a missing joint (2 occurrences).

4.5.2 Support end failure

In Figure 4.17 the age of a parking structure at observation of the support end failure is presented. The results indicate that the support end failure was primarily observed within 15 years after construction of the structure, with the largest amount of observations at eight years after construction. Furthermore, observations of this type of damage were made up to 41 years after construction.

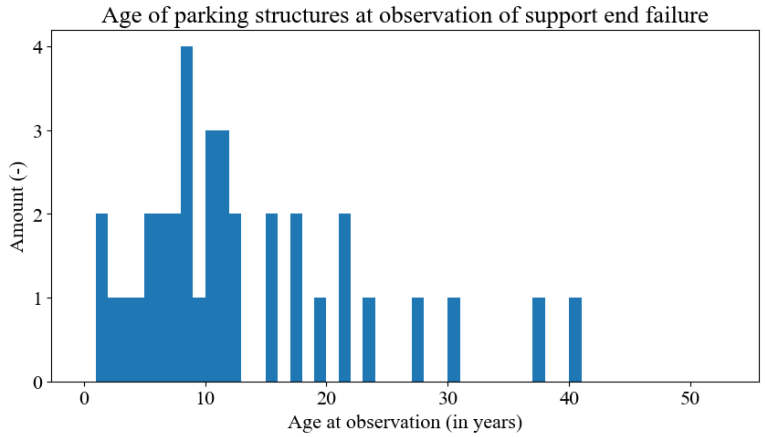

Figure 4.17 Histogram of age of parking structures at observation of support end failure.

4.5.3 Leaking cracks

The results of the data analysis of the age of parking structures at the observation of leaking cracks are shown in Figure 4.18. The majority of the observations of damage were within 11 years after construction, with a smaller amount of observations past 11 years. These results resemble the findings of non-leaking cracks.

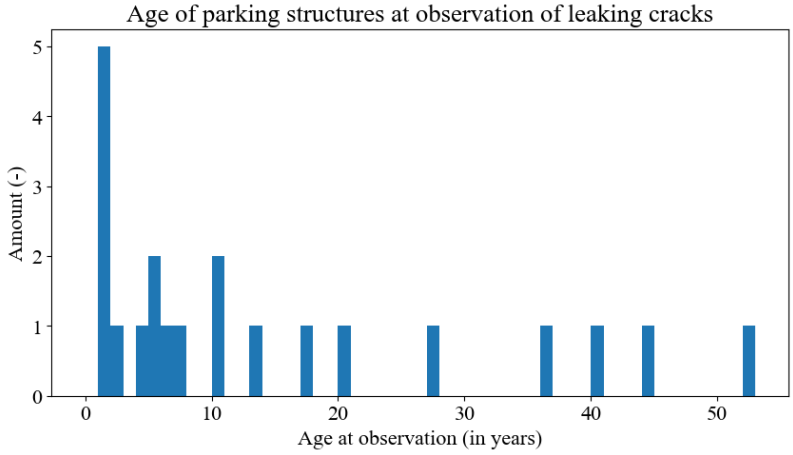

Figure 4.18 Histogram plot of age at observation for leaking cracks.

The total amount of observations of leaking cracks were significantly lower than for non-water transferring cracks, 21 compared to 103 respectively. Even though the time of observations are represented by a smaller amount, the results are moderately similar to the results of non-water transferring cracks.

4.5.4 Corrosion

Figure 4.19 presents the age of parking structures at observations of corrosion. The findings indicate that corrosion is found during several parts of the lifetime of a parking structure. The largest amount of observations were made between 39 and 45 years after construction of the parking structure.

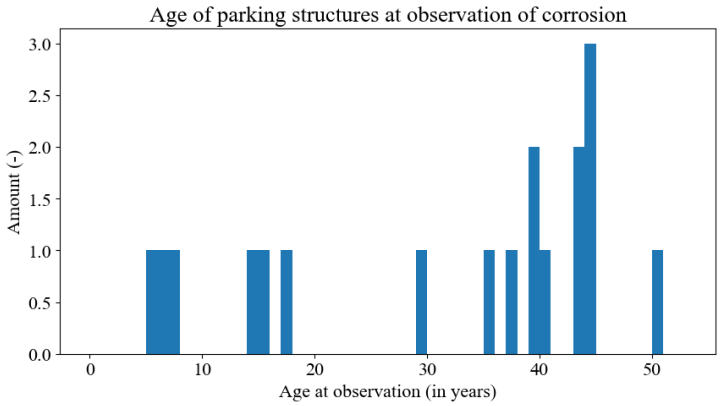

Figure 4.19 Histogram plot of age at observation for corrosion.

Detailed analysis of the data shows that for age at observation before 35 years the causes are different than for observations after 35 years. The early observations, being earlier than 35 years, encompass insufficient cover (2 observation), contaminants in concrete (1 observation), incorrect design (1 observation), leakage (1 observation), and unknowns (2 observations).

Late observations, being later than 35 years, include water ingress in tendon ducts (5 observations), chlorides (3 observations), insufficient cover (1 observation), and existing cracks (1 observation).

4.5.5 Leakage

The age at observation for leakage in parking structures is shown in Figure 4.20. The results indicate that leakage is observed in various stages of a parking structures' lifetime. Most leakages have been observed within 15 years after year of construction. However, due to the small sample size no direct conclusions can be drawn.

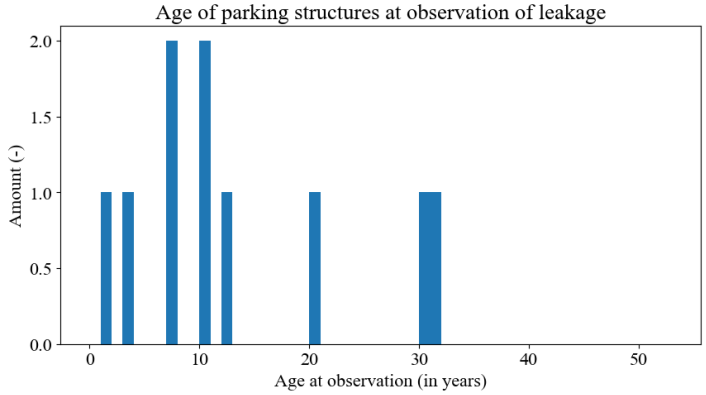

Figure 4.20 Histogram plot of time since observation for leakage.

5 Damage catalogue

5.1 General

Chapter 5 presents a damage overview of the types of damage following the data analysis and literature study. The types of damage were solely derived by the data analysis, whilst some mitigating measured were found in literature. This overview briefly describes the characteristics of the damage, the potential causes, and mitigation measures to prevent or reduce the damage. Section 5.2 describes the structure of the overview. Sections 5.3 - 5.6 describe characteristics, causes, and preventive measures of the types of damage based on the data.

5.2 Structure of overview

For clarity, the damage overview is divided into four structural elements, as each structural element has distinct types of damage. These elements are divided into sub-elements to describe specific types of damage or defects related to a sub-element. The sub-elements are based on the types of elements found during the data collection. The structure of the elements in the overview are presented in Table 5.1.

Table 5.1 Division categories of element and sub-elements.

Element	Sub-element
Floor	Hollowcore slab
	TT slab
	Filigree slab
	Post-tensioned floor
	Monolithic floor
Support	Corbel
	Half-joint
	Beam support
Wall	Diaphragm wall
	Sheet pile wall
	Cast in-situ wall
Expansion joint	-

For each sub-element a list of characteristic types of damage is formed. For certain types of damage, the damage is applicable for multiple elements, cracks in compressive layers as such, and is mentioned as a general type of damage. The total overview of the types of damage for each sub-element is given in Table 5.2.

Table 5.2 Overview of types of damage per each element or sub-element.

Element	Sub-element	Type of damage
Floor	-	Cracks in compressive layers of prefab floors
	-	Corrosion in compressive layers
	-	Leakage along floor joints
	Hollowcore slab	Cracking of slab
	Filigree slab	Incorrect detailing of floor joints
		Cracking of slab
	Post-tensioned floors	Corrosion of tendons
	Monolithic floors	Cracking of floor
Support	-	Support end failure
	-	'Walking' bearing pads
	Half-joints	Incorrect detailing of half-joint reinforcement
Walls	Cast in-situ walls	Leaking cracks
	Diaphragm wall	Leakage
	Sheet pile wall	Leakage
Expansion joints	-	Cracking of expansion joints
	-	Failure of joint sealant

5.3 Floor elements

5.3.1 General types of damage

Cracks in compressive layers of prefab floors

Characteristic cracks in compressive layers of prefab floors span along the floor joints, as shown in figures 5.1 and 5.2. Cracks are to be expected both at the support as well as along the interface between adjacent elements. The cracks along the interface joint for hollowcore slab floors systems are expected at regular intervals of 1.2 m or 2.4 m, which equate to once- or twice the width of a slab.

Figure 5.1: Cracks along the longitudinal interface of slab elements, 1.2m separation between each crack (Adviesbureau Hageman).

Figure 5.2: Cracks along the support of slab element (Adviesbureau Hageman).

Restrained deformation, shrinkage, thermal contraction, or rotation, is the main cause of the cracks (figures 5.3 and 5.4). In case the largest crack width is present at the surface, either bending or a combination of bending and restrained deformation is the cause. If the crack width is approximately equal over the entire cross-sectional height, the main cause is restrained deformation. Additionally, insufficient concrete cover or difference in camber or span of adjacent prefab elements are possible causes of cracks.

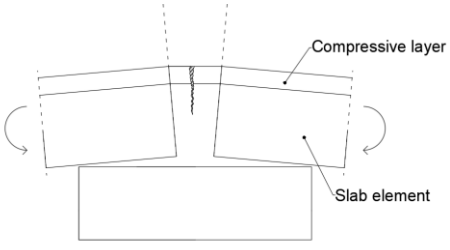

Figure 5.3 Cracks as result of restrained rotation.

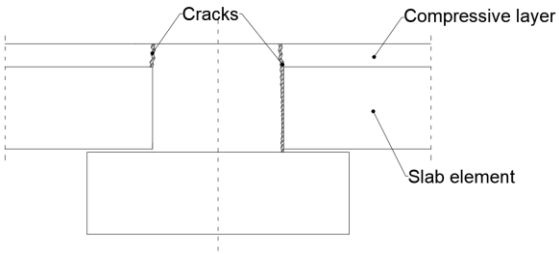

Figure 5.4 Cracks as result of restrained shrinkage.

These cracks are complicated to completely prevent. Besides, a crack width up to 0.2 mm is permitted. However, reduction of crack width can be achieved by implementation of a denser reinforcement mesh. By increasing the amount of reinforcement, the stresses within the reinforcement are lowered, and thus the crack width. Moreover, adjustments within the concrete mixture, reduction of water and w/c ratio, minimizes shrinkage of the mixture.

Corrosion in compressive layers

Characteristics of corrosion in compressive layers are cracks, locally spalled concrete, or stained corrosion marks on the floor element, as shown in figures 5.5 and 5.6. Corrosion marks can be expected located directly above the position of the reinforcement mesh or at locations of existing cracks. Furthermore, local reductions of rebar can be expected (Figure 5.8).

Figure 5.5 Cracks as result of corroded rebar (Adviesbureau Hageman).

Figure 5.6 Corrosion of reinforcement in compressive layer (Adviesbureau Hageman).

Corrosion is frequently caused by the chlorine environment in combination with insufficient cover or incorrect exposure class of concrete mixture (Figure 5.7). These design faults are frequent occurring causes. Additionally, ingress of water or chlorides through existing cracks contribute to the occurrence of corrosion.

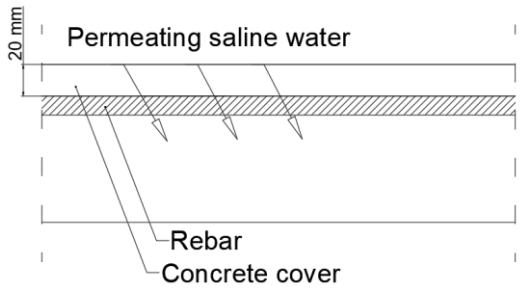

Figure 5.7 Permeation of saline water as result of insufficient concrete cover.

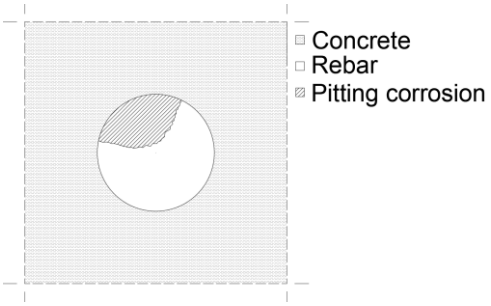

Figure 5.8 Cross-sectional reduction as a result of pitting corrosion.

To mitigate chloride ingress, integration of a larger height of concrete cover delays the chloride attack on rebar. Moreover, application of exposure class XD3 is prescribed for concrete mixtures in these environments. Furthermore, a water impermeable layer coating layer reduces the amount of ingress from water and chlorides into the concrete.

Leaking along floor joints

Characteristics for leakage along floor joints are portrayed by visible signs of present or previous occurring water transfer (figures 5.9 and 5.10). Leakage is commonly accompanied by cracks, especially at longitudinal floor joints of prefab floors, and occasionally accompanied by corrosion stains.

Figure 5.9 Leakage at longitudinal joint of hollowcore slab (Adviesbureau Hageman).

Figure 5.10 Leakage at support joint of hollowcore slab (Adviesbureau Hageman).

Common causes for leakage along floor joints are existing cracks, largely caused by restrained deformations, as shown in Figure 5.11. Furthermore, occurring causes of leakage are failure of damage of joint sealant, schematised in Figure 5.12.

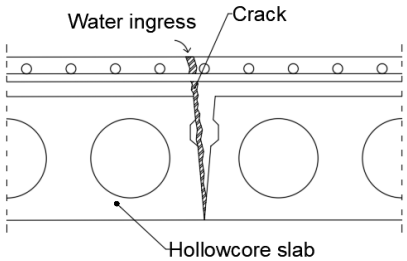

Figure 5.11: Leakage through cracks in longitudinal joint of hollowcore-slab

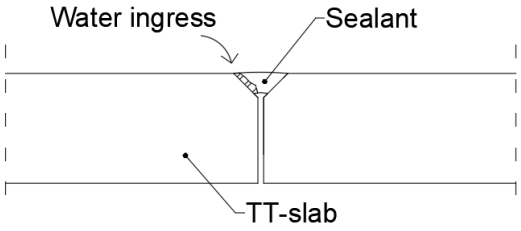

Figure 5.12: Leakage through failure of sealant material in TT-slabs

Reduction of leakage at floor joints are by prevention or minimization of cracks or by application and maintenance of the joint sealant. For mitigation measures see ‘Cracks in compressive layers of prefab floors’ and ‘Failure of sealant’.

5.3.2 Hollowcore slabs

Cracks in hollowcore slabs

Characteristics for cracks in hollowcore slabs are cracks spanning the entire height of the cross-section. These cracks can occur at any location in a hollowcore slab and are susceptible to leaking. These cracks generally occur in a parking structure at a change of floor layout, corners in floor layouts, or perpendicular to the continuous span. Examples of cracks in hollowcore slabs are shown in figures 5.13 and 5.14.

Figure 5.13 Cracks at the underside of hollowcore slab (Adviesbureau Hageman).

Figure 5.14 A multitude of cracks formed in a hollowcore-slab (Adviesbureau Hageman).

Cracks are frequently induced in hollowcore slabs due restrained deformations imposed by cohesion between compressive layer and the slab element or adhering slab elements (Figure 5.15). Additionally, differences in span lengths between adhering slabs (Figure 5.16), adherence of elements other than hollowcore-slabs, or change of cross-section mid span contribute to this cause. Furthermore, a potential cause of cracks are due to freezing of entrapped water in a slab shaft.

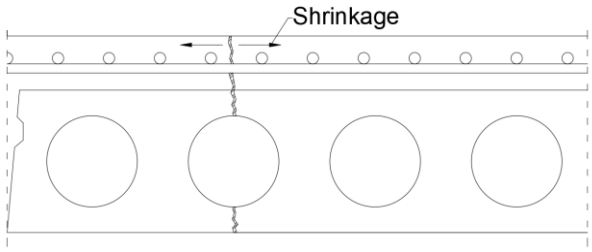

Figure 5.15 Shrinkage from top layer inducing cracks in the hollowcore-slab.

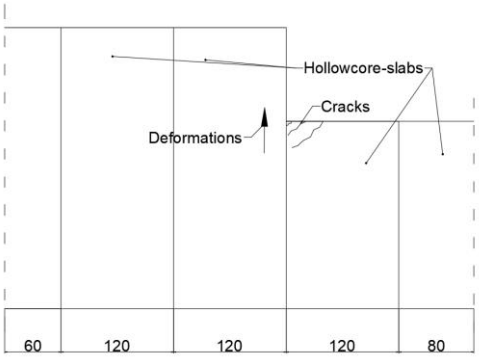

Figure 5.16 Top view of floorplan: cracking at change in layout of floor plan.

For mitigation of cracks in compressive layers due to restrained deformation see “Cracks in compressive layers of floors”. Furthermore, use of partial-width hollowcore slabs avoid changes of cross-sections mid span. Moreover, integration of expansion joints within the design reduces the total span length. These are preferably located at changes in layout of the floor plan.

5.3.3 Filigree slabs

Incorrect detailing of floor joints

A defect, or incorrect design, of floor joints of filigree slabs was the cause of a collapse in a parking structure (Figure 5.17). Due to ignorance of correct reinforcement detailing of filigree joints, a brittle failure mechanisms occurred (Figure 5.18).

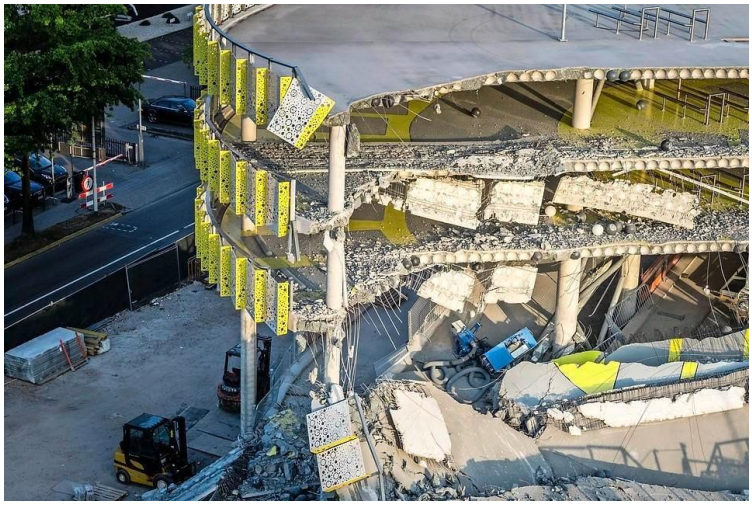

Figure 5.17: Collapse of parking garage using filigree floors (Engelaar, n.d.)

The causes of the collapse was incorrect detailing of the longitudinal joint of the filigree slab. Additionally, due to a smooth surface of the prefab element due to self-compacting concrete a poor cohesion between prefab slab and in-situ concrete was created.

Figure 5.18: Brittle failure mechanism of bubble deck slab joint (Rijksoverheid, 2022)

Design should be carried out conform revised norms and standards, which avoids this failure mechanism.

Cracks in filigree slabs

Characteristics crack in filigree slabs are known for two types of cracks. Cracks are commonly located at the bottom prefab slab mid span, or perpendicular to the span direction. These cracks appear shortly after casting the in-situ compressive layer of the concrete. Moreover, cracks often occur through the entire height of the cross-section, at midspan of the largest adjacent span direction. Examples of cracks in filigree slabs are shown in figures 5.19 and 5.20.

Figure 5.19 Cracks running through adjacent filigree slab elements as result of restrained deformations (Adviesbureau Hageman).

Figure 5.20 Cracking at underside of filigree slab (Adviesbureau Hageman).

Insufficient propping of elements during casting of the compressive layer during execution cause cracks at the underside of the prefab filigree element (Figure 5.21). Restrained deformation is a frequent cause of cracks spanning the entire height due to the combination of prefab element and in-situ cast compressive layer (Figure 5.22). This is generally caused as result of large uninterrupted spans of adjacent elements.

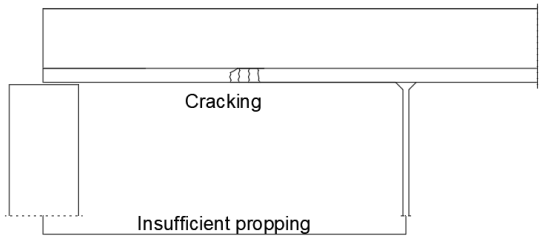

Figure 5.21 Cracking due to insufficient propping during execution.

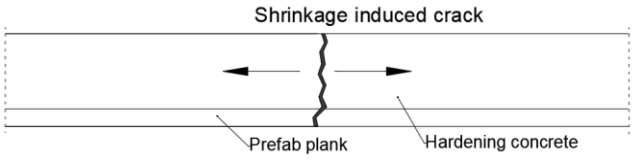

Figure 5.22 Cracking of both prefab plank and in-situ cast concrete.

Installation of propping elements according to standards prevent unnecessary cracks during execution. The restrained deformation initiated cracks are difficult to avoid. Besides, a crack width up to 0.2 mm is permitted for parking structures. Reduction of crack width is achieved by implementation of a denser reinforcement mesh. By increasing the amount of reinforcement, the stresses within the reinforcement are lowered, and thus the crack width. Moreover, integration of expansion joints reduce large concurring spans.

5.3.4 Post-tensioned floors

Corrosion of post-tensioned floor tendons

Corrosion of post-tensioned floor tendons can be characterized by leakage of tendon lubricant, exposed tendons at the pavement surface, and formation of cracks, as shown in figures 5.23 and 5.24. This damage only occurs for older post-tensioned floor systems built before 1985.

Figure 5.23 Spalling as result of failure of prestress tendon (Adviesbureau Hageman).

Figure 5.24 Visible exposed tendon lubricant (Adviesbureau Hageman).

Causes of tendon corrosion re-occurs due to ingress of water in the tendon duct. Contributing factors of water ingress are permeation of water through the parking deck, ingress of water through tendon anchors, or ingress of water during construction of the floor. Subsequently, tendons of early post-tensioned floor systems were poorly protected by lubrication.

Modern post-tensioned floors do not suffer from this damage phenomenon as these use a different duct system than before. Whereas before the tendon ducts existed from multiple segments, making them prone to water ingress, current tendons consist of a singular duct, mitigating this problem. Reparation of damaged tendons is achieved by installation of new tendons within the floor, which after installation are tensioned accordingly.

5.3.5 Monolithic floors

Cracks in monolithic floors

Characteristic cracks within monolithic floor slabs occur frequently at halfway the span length, spanning perpendicular to the span direction. Moreover, common positions of cracks are along the connection between wall elements or at corners of wall elements, as presented in figures 5.25 and 5.26. These cracks generally span the complete height of the cross-section, making them prone to leakage and corrosion induced damage.

Figure 5.25 Cracks in monolithic floor, restraint by adhering walls (Adviesbureau Hageman).

Figure 5.26 Cracks along connection between sheet pile wall (Adviesbureau Hageman).

Cracks are, alike previously mentioned crack initiations, predominantly caused by restrained deformations. Contributing factors encompass large uninterrupted spans of monolithic floor, adhering elements, or incorrect reinforcement detailing (figures 5.27 and 5.28).

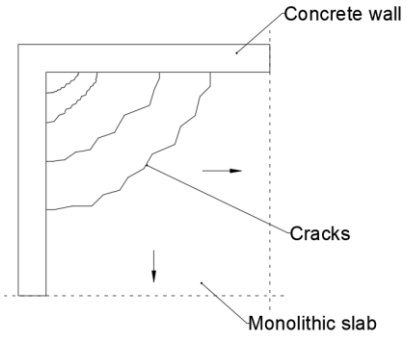

Figure 5.27 Shrinkage induced cracking as result of restraints by wall elements.

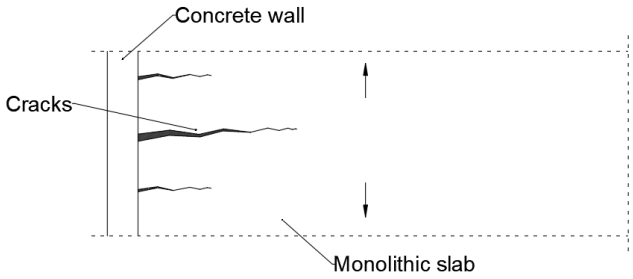

Figure 5.28 Shrinkage induced cracking at boundary between monolithic floor and wall.

Complete avoidance of these cracks is near impossible. Besides, a crack width up to 0.2 mm is permitted according to norms and standards. Reduction of crack width is achieved by implementation of a denser reinforcement mesh. By increasing the amount of reinforcement, the stresses within the reinforcement are lowered, and thus the crack width. Moreover, adjustments within the concrete mixture, reduction of water and w/c ratio minimizes shrinkage. Additionally, reduction of span length by integration of expansion joints, mitigates stresses within concrete. However, for water retaining monolithic floors the latter mitigation measure is not feasible.

5.4 Support elements

5.4.1 General types of damage

Support end failure

Support end failure is a failure mechanism in which concrete edges or corners are locally cracked or spalled. This phenomenon is found at supporting elements. In parking structures, half-joints, corbels, columns, and support beams are frequently affected. The support end failure mechanism at a support beam and half-joints are shown in figures 5.29 and 5.30, respectively.

Figure 5.29 Local support end failure of concrete support beam (Adviesbureau Hageman).

Figure 5.30 Local support end failure of half-joints (Adviesbureau Hageman).

Support end failure is affected by various factors, encompassing factors are improper placement of bearing material, insufficient rotational freedom between the connecting elements, stiff connections due to grouting of continuity rebar, or due to imposed horizontal loading as result of restrained movement, as schematised in figures 5.31 and 5.32.

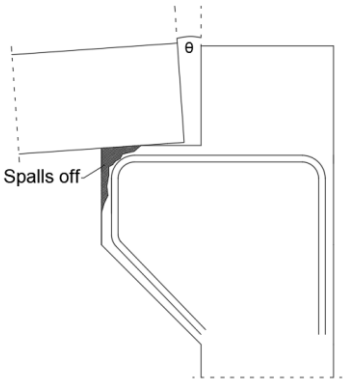

Figure 5.31 Support end failure due to restriction of rotation within the connecting elements.

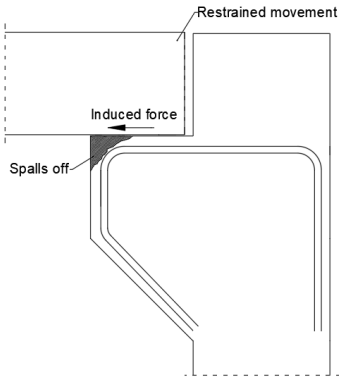

Figure 5.32 Support end failure due to horizontal forces exceeding capacity.

Support end failure is largely avoided by correct placement and material of bearing material. By permitting horizontal movement and rotations the failure mechanism is generally avoided. Restrained deformation due to continuity reinforcement is prevented installing a flexible sealant around the voids of the reinforcement, in order to permit horizontal movements.

Walking bearing pads

'Walking' bearing pads are characteristically expressed by extruding bearing material from its connection, as presented in figures 5.33 and 5.34. This type of damage occurs at corbels, support beams, or half-joints. The mechanism can occur for various types of bearing materials, elastomeric or steel pads as such.

Figure 5.33 Extruding elastomeric bearing pads at support of slabs (Adviesbureau Hageman).

Figure 5.34 Gradual walking of elastomeric bearing pads (Adviesbureau Hageman).

Causes of walking bearing pads comprise of insufficient fixation, or incorrect placement of bearing pads or uneven loading conditions of the bearing material. Additionally, cyclic loading such as expansion and contraction gradually affect the location of the bearing material, schematised in Figure 5.35.

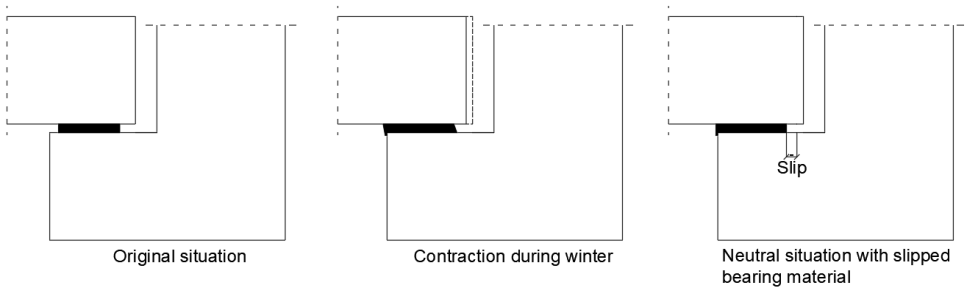

Figure 5.35 Gradual 'walking' of bearing pads as a result of cyclic loading.

By correct design and placement of the bearing element following norms EN1337 and EN1992-1-1 this failure mechanism is generally avoided.

5.4.2 Half-joints

Incorrect detailing of half-joint reinforcement

Incorrect detailing of half-joint reinforcement is categorised as a defect. Characteristic signs of damage due to improper detailing are cracks in the re-entrant corner of the half-joint. The incorrect reinforcement detailing is schematised in Figure 5.36.

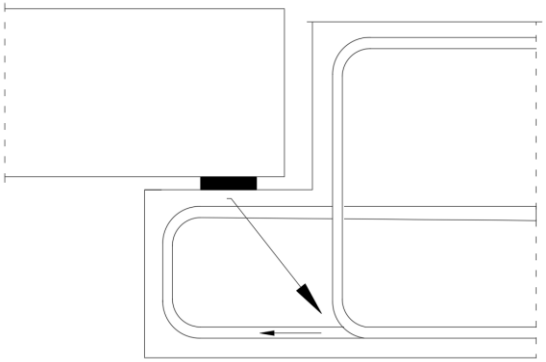

Figure 5.36 Incorrect design due to inability to achieve equilibrium of forces.

The underlying issue of this defect is the incorrect detailing of reinforcement within half-joints. Due to an underestimation of the shear slenderness of the half-joints were designed with insufficient shear reinforcement.

Prevention of this defect is by application of additional stirrups at the re-entrant corner of half-joint design. Another possible solutions is by bending the anchorage of longitudinal reinforcement towards the half-joint to make equilibrium with the compressive strut, as shown in figures 5.37 and 5.38.

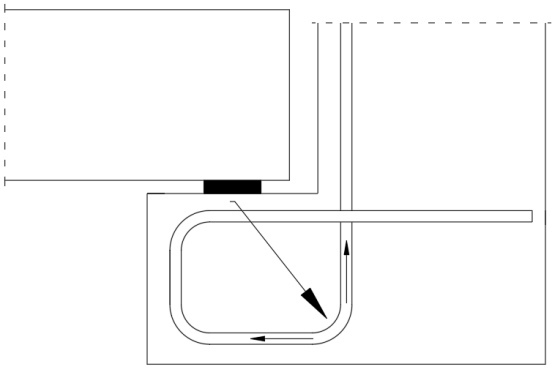

Figure 5.37 Equilibrium of connection by bending the longitudinal reinforcement towards the connection half-joint.

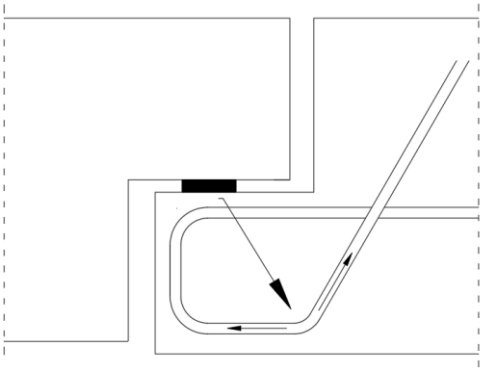

Figure 5.38 Equilibrium of connection provided by use of longitudinal reinforcement.

5.5 Wall elements

5.5.1 Cast in-situ walls

Leaking cracks

Leaking cracks in cast in-situ walls are notably found at the connection between wall and floor elements. These cracks are vertically oriented, increasing in crack width towards the adhering element, as shown in figures 5.39 and 5.40.

Figure 5.39 Cracks in cast-in situ wall, accommodated by leakage (Adviesbureau Hageman).

Figure 5.40 Cracking in concrete cast in-situ wall, increasing in crack width towards the floor element (Adviesbureau Hageman).

Restrained deformations is the predominant cause of cracks in cast in-situ walls. Restraints caused by adherence between wall and floor element restrain deformations of the wall element and subsequently initiate formation of cracks, as schematised in Figure 5.41. Moreover, discontinuities between expansion joints of floor and wall elements are a re-occurring cause.

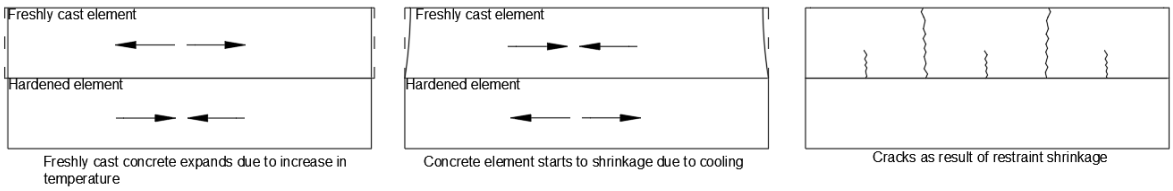

Figure 5.41 Schematization of cracks in in-situ wall elements as result of restrained deformation of adjacent floor.

Minimization of cracks is achieved by implementation of a dense reinforcement mesh, lowering the stresses in reinforcement and subsequently lowering the crack width. Additionally, changing the composition of concrete mixture contributes to a reduction of the severity of shrinkage.

5.5.2 Diaphragm walls

Leakage in diaphragm walls

Characteristic locations of leakage in diaphragm walls comprise of wall joints between segments or from protruding bars. The latter being characterized by water transfer through the protruding reinforcement, presented in figures 5.42 and 5.43.

Figure 5.42 Leakage right above concrete beam element (Adviesbureau Hageman).

Figure 5.43 Leakage at protruding bars in diaphragm wall (Adviesbureau Hageman).

Joints between diaphragm wall elements are susceptible locations to leakage due to an interface between two elements or due to bentonite inclusion. Moreover, due to plastic settlement and bleeding of the concrete during the execution, creating voids surrounding the reinforcement. Protruding reinforcement provides a path for water transfer from these voids (Figure 5.44).

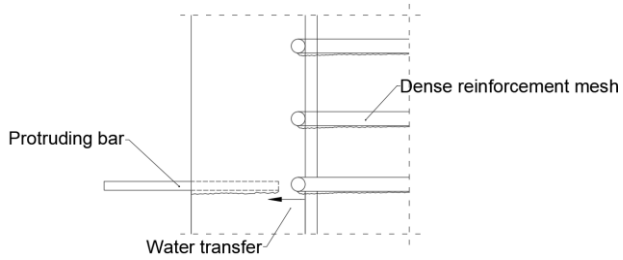

Figure 5.44 Permeating of water through sedimentation ducts under reinforcement.

Mitigation encompasses installation of water stops between joints of diaphragm walls in order to reduce leakage through joints. Although, according to NEN-EN 1538 diaphragm walls cannot be expected to be completely watertight, and damp or wet patches are allowed to occur. Therefore, forms of water transfer are to be expected and permitted.

5.5.3 Sheet pile walls

Leakage

Characteristics of leakage in sheet pile walls are frequently situated at connections between adhering elements, floors or beams as such. Visible indications of leakage are expected to occur at these locations. Moreover, joints of sheet pile elements are susceptible to leakage. Examples of leakage at sheet pile wall elements are given in figures 5.45 and 5.46.

Figure 5.45 Leakage at sheet pile wall located at floor joint (Adviesbureau Hageman).

Figure 5.46 Leakage at connection between sheet pile wall and concrete floor (Adviesbureau Hageman).

Leakage of support connections are commonly caused from deformations between the adhering elements. Besides, leakage at joints of sheet pile wall elements can be caused by failure of the interlocking connection or due to rotations of the sheet pile wall elements.

Similarly to diaphragm walls, small amounts of water ingress is to be expected. However, mitigation measures can be taken to minimize water transfer, such as welding of sheet pile slots or installation of a sheet pile slot sealant could reduce water transfer.

5.6 Expansion joints

5.6.1 General types of damage

Cracking of expansion joints

Characteristic cracks in expansion joints are commonly found alongside the direction of the expansion joint, as shown in figures 5.47 and 5.48. Moreover, cracks occur frequently in elements bridging both sides of the expansion joint.

Figure 5.47 Cracking beside expansion joint (Adviesbureau Hageman).

Figure 5.48 Cracking next to expansion joint due to incorrect installation (Adviesbureau Hageman).

Common causes in expansion joints encompass discontinuity of the expansion joints (Figure 5.49). Moreover, misaligned of expansion joints between connected elements are a potential cause of cracks between the expansion joint, schematised in Figure 5.50.

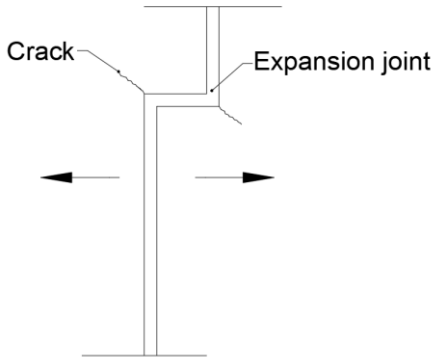

Figure 5.49 Cracking in expansion joint due to irregularity within the joint.

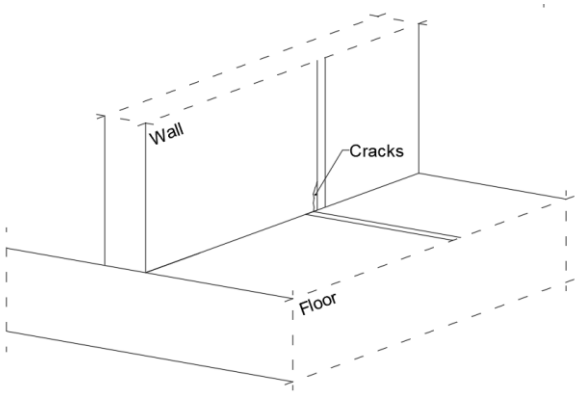

Figure 5.50 Non-aligned of expansion joints inducing cracks between the joints.

The damage mentioned is generally mitigated by correct design, in which expansion joints are aligned, without any discontinuities within the joint.

Failure of sealant

Damage to joint sealants can be comprised by a multitude of factors, encompassing extruding of the sealant, loss of cohesion, or loss of adhesion of the sealant. Extruding sealant can be recognized by compressed and exposed joint from the expansion joint. Cohesion loss of sealant can be recognized by either cracking or tearing of the sealant. This damage occurs in the middle of the sealant, spanning parallel to the joint. Adhesion loss of sealant is known to disconnect the sealant from the adhering joint material, leaving larger gaps between sealant and joint, depicted in figures 5.51 and 5.52. Damaged sealants are often accompanied by leakage of the joint.

Figure 5.51 Failure of adhesion and leakage of joint (Adviesbureau Hageman).

Figure 5.52 Adhesion failure of joint sealant (Adviesbureau Hageman).

Common causes of failure of expansion joint sealant encompass incorrect installation, exceedance of the tensile capacity of a sealant, insufficient space for expansion, or degradation of the sealant over time.

Prevention of sealant failure is largely achieved by installing and designing the sealant according to suppliers' specifications.

6 Discussion

First, several previously mentioned limitations of the data analysis are briefly reiterated before further discussions of the results. After, the general results of the data analysis are discussed, followed by discussion on the types of damage, their causes, and the time related findings.

The data analysis was performed on a limited sample size. Whilst the sample size of 145 reports presented various types of damage, for the types of damages with little observations the results of the data analysis were difficult to interpret. Due to little observations for such damage, observations had larger impact on the data. Besides, the limited amount of data affects the generalizability of the results.

Subsequently, the data is provided by a private consultancy engineering firm, which could provide certain bias within the data. Lastly, the archival documents were mostly filtered by the two keywords “park” or “garage”, making it presumable that not all archival files on parking structures are analysed.

General data

The construction years of the parking garages were either retrieved from the archival files or by using the BAG-register. In Figure 4.1 these dates were plotted in a histogram which suggested that a majority of the parking garages were built from the year 2000 up to 2009. As no distinction was made between private or public parking structures it is unknown whether this increase is predominantly found in either one. Although, the increase indicates a desire for more parking amenities. Possibly, this could be related due to it being more common to build a parking structure underneath residential buildings.

Subsequently, a histogram plot was presented in figure 4.2 showing the age at observation of damage. The plot indicates that a significant amount of damage is observed within the first 10 years after completion of the structure. This does not represent the time after which damage occurs in the structure, as this depends on more factors. Ignorance of the damage by the owner of the structure is presumably the most common factor which could delay the time between occurrence and observation. Therefore, the data in the histogram is potentially skewed to the right. Even though the data might be skewed, it can be concluded that a majority of the observed damage is found within the first 10 years after completion. As concrete degradation generally occurs at the end of service life, it implies that the majority of the observed damage is either due to faults in design or execution.

The conclusion of above is supported by the results provided in the histogram plot of year of construction. As the majority of the Dutch parking garages are most probably built from the year 2000 and onwards, an increase in deterioration induced damage is expected to arise from the year 2030 and onwards.

Types of damage
The data on types of damage suggest that almost half of the observed types of damage are cracks. Following frequently reoccurring types of damage are support end failure, spalling, leaking cracks, corrosion, and leakage.

Interestingly, similarities between types of damage were found in previous findings by de Jong (1992). Even though these findings are made for all concrete structures, similarities are found. Restrained shrinkage was mentioned by de Jong (1992) as most common cause, alike the results found by the data analysis. Although some types of damage differ in frequency of occurrence, damages such as corrosion, support end failure, and delamination are alike in findings.

The overview by de Jong (1992) was based on experience from Adviesbureau Hageman in the approximate timeframe 1960-1990. The data from this research was used from the timeframe 1977-2024. Whilst there is a small overlap in timeframes, the data between 1992-2024 was not. It is interesting to see that as similar damages were observed in 30 years later, it indicates that the same faults are being made, despite the knowledge gained over the years.

Cause of damage
The results of the causes of damage indicated that the majority of the damage is induced either by faults in design or execution. Restrained deformations play a role in not only crack formation, but also support end failure. Remarkably, no freeze-thaw initiated damage is present in the dataset. This suggests that the occurrence of freeze-thaw induced cracks, as found in the overview obtained by literature, generally occurs in international parking structures rather than in Dutch structures. Moreover, these conclusions were found for more degradation induced damages, such as ASR or sulphate attack. Whilst both types of damage were mentioned in literature, no observation were investigated in the dataset.

An interesting result was found for fire induced spalling of concrete elements. The majority of the spalling occurred at floors, which coheres with the fact that burning vehicles are placed either directly on top or below them. However, the sub-elements of the floors show that spalling occurred more often for both TT- and hollowcore-slabs. Hollowcore- and TT-slabs are commonly prefabricated with higher strength concretes. A characteristic of higher strength concrete is that the permeability is lower compared to normal strength concretes. Expansion of air within voids generates higher internal stresses, consequently causing explosive spalling (Phan, 1996).

Influence of elapsed time
For crack formation it was found that a large amount of cracks were observed within the first 5 years and the majority of the cracks within eight years (Figure 4.15). For the support end failure the majority of the damage was observed within the first 12 years. A possible explanation for the failure occurring slightly later in a structures lifetime is as a result of the initiation of the failure mechanism being prolonged. The failure mechanism is influenced by a variety of parameters, as suggested in Subsection 4.3.2. Amongst which walking of bearing pads, an initiation of damage which does not occur immediately but over numerous cycles, further elaborated in Subsection 5.4.1.

Although, these findings supports the previous observation that a majority of the damage is caused by faults in execution or design, rather than due to degradation. The remaining types of damage were analysed in similar fashion. However, due to the scarcer amount of observations, the data became difficult to interpret.

Moreover, observations of corrosion in a parking structure were generally found after 35 years. A further detailed analysis showed that a majority of the damage after 35 years was caused by water ingress in tendon ducts or chlorides in concrete. Causes of corrosion within 35 years after construction was found to encompass insufficient cover, contaminants in concrete, incorrect design, or leakage. Although the analysis for corrosion is based on limited observations, 16 in total, it suggests a difference in causes in respect of the elapsed time. Furthermore, in the general overview of the construction years the conclusion was made that a majority of the parking structures is built after the year 2000 up to 2010. For concrete reinforcement with a cover of 50 mm or larger the initiation of chloride induced corrosion may take up to 10 years or longer (Cusson, 2009). Since most parking structures have been constructed in the past 20 years, this could potentially explain a small amount of observations on chloride induced corrosion in parking structures.

7 Conclusion

Although parking structures are a vital part of the infrastructure in The Netherlands, damage frequently occurs, which lead to the following research question: *"How can frequently occurring damage in concrete parking structures in The Netherlands be related to its causes?"*. Through a data analysis, based 145 forensic reports of Adviesbureau Hageman on damage in parking structures, this study provided insightful findings.

The results of the data analysis imply that both faults in design and execution are the predominant causes of damage in parking structures rather than deterioration, based on the observed types of damage and time interval between year of construction and year of observation. The findings suggest that the three most observed types of damage encompass cracks, at 44% of the observations, the support end failure (15.4%), and spalling (10.7%). Overall, the damages in parking structures were frequently observed in expansion joints, floor-, wall-, and support elements. Additionally, the findings indicate that the frequency of observed types of damage differs between under- and aboveground parking structures. For underground structures, cracks accounted for the most observed type of damage at almost 66%, whereas for aboveground structures various damages were of equal size.

However, the data analysis was performed on a dataset with a limited sample size and retrieved from a private engineering firm, therefore impacting the generalizability of the results. Nevertheless, the results provide a satisfactory insight of damage in parking structures.

From the findings of the data analysis a damage catalogue is developed, describing the characteristics, causes, and mitigating measures of the observed types of damages. It emphasizes important design and execution aspects for engineers and offers a tool for the identification of damages within parking structures.

In conclusion, this research relates causes of frequently occurring damage in parking structures through a data analysis on the element of occurrence, elapsed time, and types of damage, showing that damage predominantly originated from faults made in design or execution. The findings provide insight into the occurring damages, important design aspects, and mitigation measures for future structures.

Part II

A study of the support end failure behaviour in concrete corbels

8 Introduction

8.1 Background

Repeatedly, faults in both design and execution are being made in Dutch parking structures. Results of the data analysis, prior in this research, on types of damage in Dutch parking indicated that the support end failure is the second most frequently observed damage, specifically in concrete corbels. Although this failure mechanism does not always result in loss of structural capacity, it is essential for the durability of the structure, especially as the chlorine environment poses enhanced corrosion rates of exposed rebar.

Previous studies concluded that support end failure can be prevented by appropriate design of the support element (Hermanson & Cowan, 1974). A sufficiently large distance between the bearing pad and the outer edge of the support is often seen as preventive measure of the support end failure (Kriz & Raths, 1965; Hermanson & Cowan, 1974). Additionally, the reinforcement configuration of the corbel is suggested as important design parameter (Mattock 1976; Hermanson & Cowan, 1974).

Interestingly, the contradiction between frequently observed cases of support end failure in-practice and easy preventive measures, indicate a possible lack of understanding on the behaviour of this failure mechanism, or insufficient attention during construction.

8.2 Objective

The aim of Part II of this research is to obtain a better understanding of the support end failure behaviour. By carrying out an exploratory research using various numerical calculations it is intended to gain an insight in this behaviour. Numerical analyses are utilized to efficiently study the effect of design parameters and generate results. Moreover, an effort is made to approximate the numerical results with an analytical model.

8.3 Research question

Various design parameters have been mentioned by prior research to affect the support end failure. Consequently, the primary research question of Part II to be answered in this study is:

“ To what extent can the behaviour of the support end failure be assessed by a parametric study using a finite element model?”

In order to obtain an answer to this question two sub-questions were formed:

2.1 Which parameters influence the damage mechanism?
2.2 How do the parameters influence the behaviour of the damage mechanism?

8.4 Outline

In Chapter 9, a brief analysis is provided on the failure mechanisms of corbel elements, including past studies on the support end failure.. In Chapter 10, experimental and numerical results of Neupane et al. (2017) are used to validate a finite element model made in the finite element software ATENA (Červenka et al., 2021).

Subsequently, a corbel is designed in accordance to Eurocode 2 in Chapter 11. The corbel is numerically modelled and loaded until failure to provide insight into the behaviour of the corbel and act as a reference point for the parametric study.

After, a parametric study is conducted in which effect of change of the support conditions and loading conditions on the corbel are studied (Chapter 12). The results of the parametric study are analysed in detail, whereafter analytical models are tested against these results, in Chapter 13. Finally, a discussion and conclusion of the findings of Part II is given in Chapter 14 and 15.

A flowchart of both Part I and II of this research is provided in Figure 8.1.

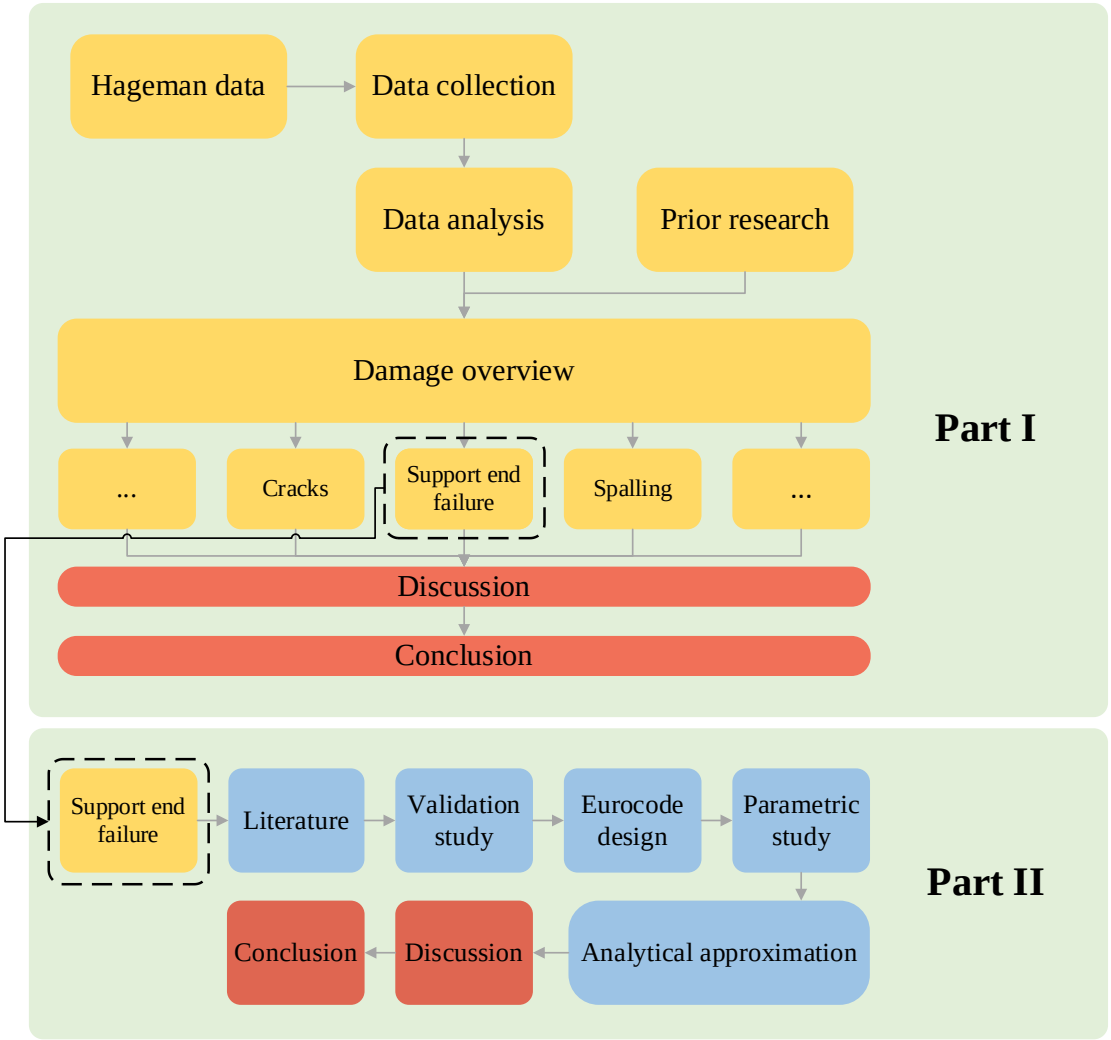

Figure 8.1 Flowchart of Part I and II of this research.

9 Literature study

9.1 General

A brief literature study is performed on the failure mechanisms of corbels and, more specifically, on prior research of the support end failure mechanism. In Section 9.2 the failure mechanisms of the corbels are enumerated, followed by an overview of research on the support end failure mechanism (Section 9.3).

9.2 Failure mechanisms of corbels

Corbels have been extensively studied over numerous years. Kriz and Raths (1965) were probably amongst the first to categorize possible failure mechanism of corbels into two categories: primary and secondary failure. Schematisations of the failure mechanisms observed in the experiments are displayed in Figure 9.1.

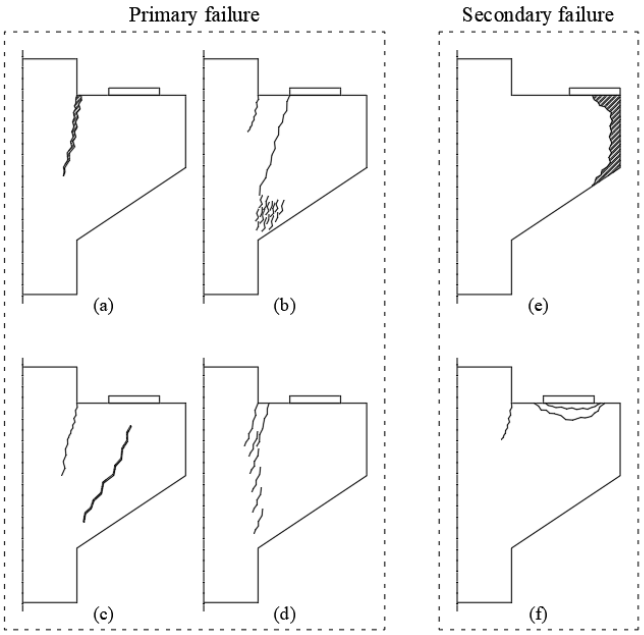

Figure 9.1 Schematisations of primary and secondary failures of corbels based on experimental tests of Kriz and Raths (1965).

As shown in Figure 9.1, the behaviour of the individual primary failures was described by Kriz and Raths (1965) as:

a) Flexural tensile failure of the main reinforcement;
b) Flexural compression failure due to crushing of concrete;
c) Diagonal splitting failure of the compressive strut;
d) Shear failure at the interface between corbel and column.

The secondary failures were described as:

e) Corbel end failure
f) Exceedance of concrete strength underneath the bearing pad.

In the data analysis the support end failure was predominantly found to occur in corbel elements. However, elements such as columns, walls, or half-joints could also be affected by this failure mechanism. Therefore, the corbel end failure, as mentioned above, is being referred to, within this research, as the support end failure.

9.3 Support end failure

Kriz and Raths (1965) were probably amongst the first to describe the support end failure. They remarked that the failure mechanism did not occur as long as the depth under the bearing pad exceeded half the entire height of the corbel, as schematised in Figure 9.2.

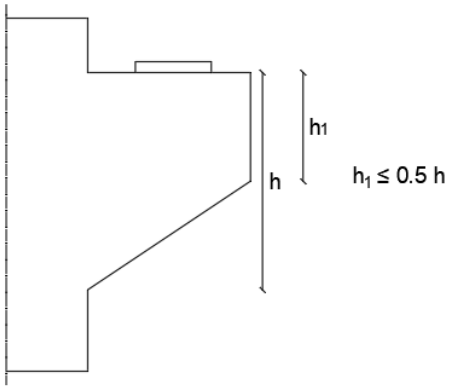

Figure 9.2 Conditions to mitigate support end failure according to Kriz and Raths (1965).

Moreover, several studies concluded that the failure mechanism is generally avoided by correct and appropriate design (Hermanson & Cowan, 1974; Forster & Powell, 1994). The appropriate design was mainly related to positioning of the support. Both Kriz and Raths (1965) and Hermanson and Cowan (1974) agreed on a minimum distance between the support and edge of the corbel of 50 mm. In addition, the bearing pad should be positioned within the vertical bends of the main reinforcement (Hermanson & Cowan, 1974). Somerville (1973) suggested a distance depending on the type of anchorage method, contrary to a set value of 50 mm.

More recent research has been conducted by Neupane et al. (2017), which studied strengthening possibilities on incorrectly detailed existing in corbels, using a carbon fibre-reinforced polymer. A series of corbels was tested, one of which studied the remaining capacity of a corbel after the support end failure mechanism had occurred. The failure load of this series was compared to the identical corbel setup without occurrence of the failure mechanism, which showed a loss in capacity of approximately 5%.

Based on the literature study it is apparent that the support end failure is seen as a secondary failure mechanism of corbels. Whilst several studies addresses the support end failure mechanism, this usually comprises of design measures of corbels in order to mitigate the failure mechanism. Additionally, these studies did not elaborate on the behaviour of the mechanism, such as initiation or development of the failure crack.

10 Model validation study

10.1 General

Neupane et al. (2017) investigated strengthening methods of poorly detailed reinforced concrete (RC) corbels using carbon fibre-reinforced polymer. In this study a RC corbel was tested until failure by applying a vertical displacement on the bearing pad elements. One of the specimens of the series of experiments, named PE-C, was used to investigate the support end failure mechanism. In this specimen a steel bearing pad was placed on the edge of the corbel in order to achieve the desired support end failure mechanism. Additionally, the study modelled replicated the experiment using a 3D finite element model.

A two-dimensional model is made in the finite element software ATENA and compared to the results from Neupane et al. (2017) (Červenka et al., 2021). Section 10.2 describes the experimental and numerical data of Neupane et al. (2017), encompassing the setup and results. Elaboration on the material models of the finite element model of this research is provided in Section 10.3, followed by the boundary conditions and meshing of the model (Section 10.4). Lastly, the numerical results are presented and compared to the experimental- and numerical data of Neupane et al. (2017) in Section 10.5.

10.2 Experimental data

10.2.1 Corbel dimensions and rebar configurations

The dimensions of the corbel setup and rebar configuration are shown in Figure 10.1, comprising of two corbels situated on either side of a concrete column. The column reinforcement consists of four longitudinal bars of ϕ16 mm and six stirrups of ϕ10 mm. The reinforcement of the corbel elements contain two longitudinal reinforcement bars of ϕ13 mm and two stirrups, of ϕ10 mm in diameter, surrounding the entire reinforcement configuration.

The corbel elements span 250 mm with a height of 350 mm, of which the lower 150 mm tapers off. The total height of the column is 650 mm with a width of 200 mm. Two steel bearing plates are situated on the edges of the corbels. The steel plates are 60 mm wide and 20 mm high, spanning the entire depth of the corbel. The depth of the corbel 170 mm and is uniform over the entire cross-section.

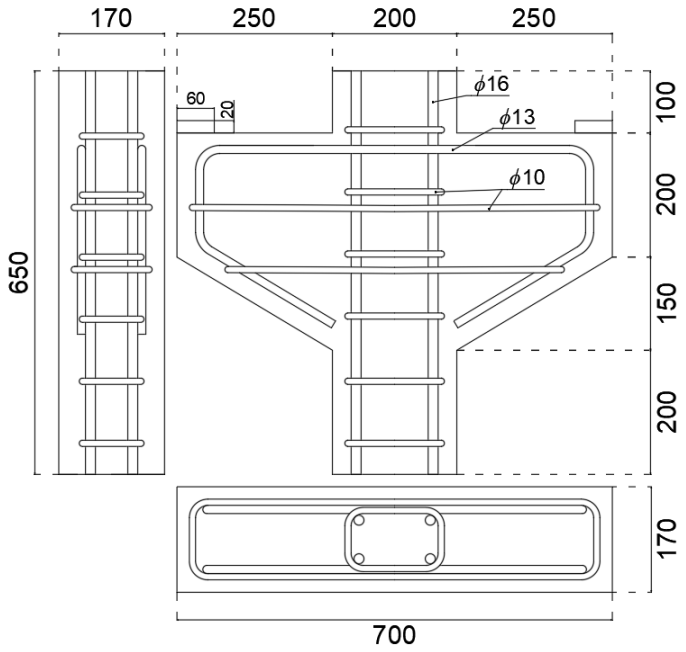

Figure 10.1 Dimensions of concrete corbel and rebar configuration in mm.

10.2.2 Experimental setup

In the experiment, the corbel element was loaded as a uniform load at the bottom of the column and simply supported in the middle of the bearing pads. Various parameters of the corbel element were monitored: displacement, applied load, and strain of the main reinforcement. The displacement at the top of the plate was monitored using LVDT's (Linear Variable Differential Transformer). The exerted load on the column was measured with a load cell. The strain of the main reinforcement was measured by strain gauges attached to the main reinforcement. The loading- and monitoring setup are shown schematically in Figure 10.2.

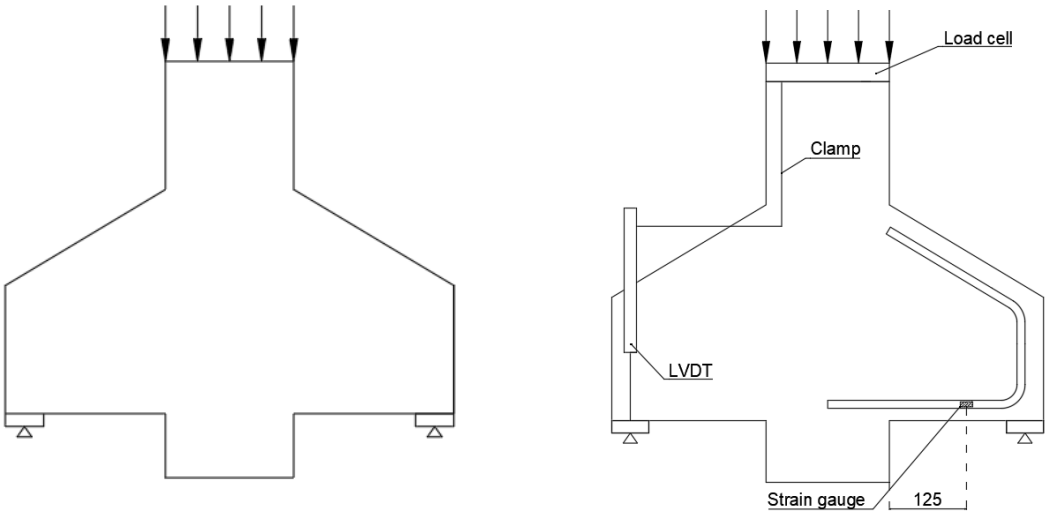

Figure 10.2 Setup of experiment: Loading conditions (left) and monitoring (right).

10.2.3 Experimental results

Failure mechanism

Experiment PE-C portrayed two distinct cracks before the support end failure occurred. The first crack initiated at the re-entrant corner of the column, whereafter a crack formed diagonally between the support and the column. Subsequent to the occurrence of both cracks, the support end failure occurred, as shown in Figure 10.3.

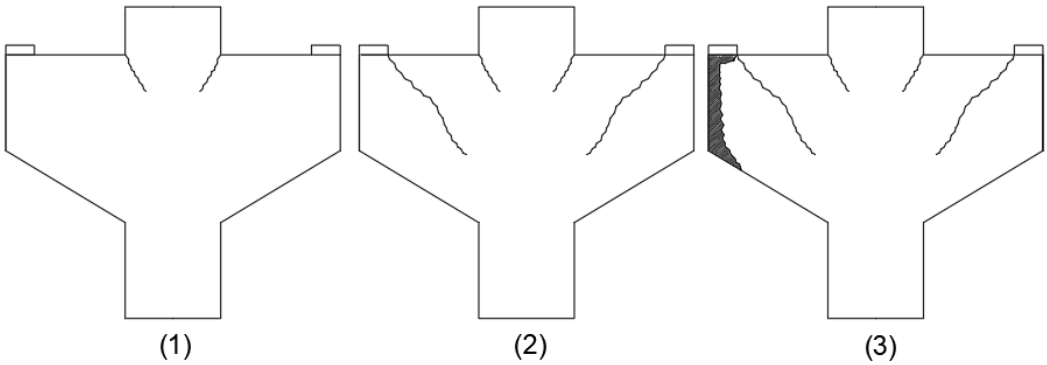

Figure 10.3 Schematic display of initiation of cracks, in order 1-3.

Load-displacement

In Figure 10.4, the experimental- and numerical results by Neupane et al. (2017) are presented. Specimen PE-C failed at a measured load of 458.4 kN at a displacement of 1.25 mm. The results by the numerical model differ slightly from the experimental data, the largest difference being present below 0.5 mm. The initial stiffness in the load-displacement curve obtained by the numerical model is larger than the initial stiffness of the experiment. Neupane et al. (2017) mentioned that this discrepancy is caused by crushing of gypsum between the steel bearing plates and the concrete corbel. To compensate for slip in the of the experiment, one could deduct the displacement of the experimental data by 0.3 mm (Figure 10.5).

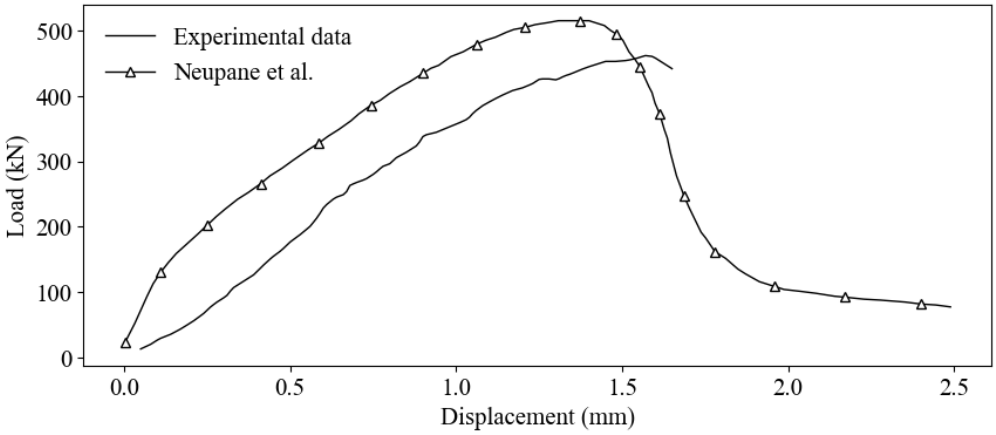

Figure 10.4 Load-displacement curve of experimental data and numerical model by Neupane et al. (2017).

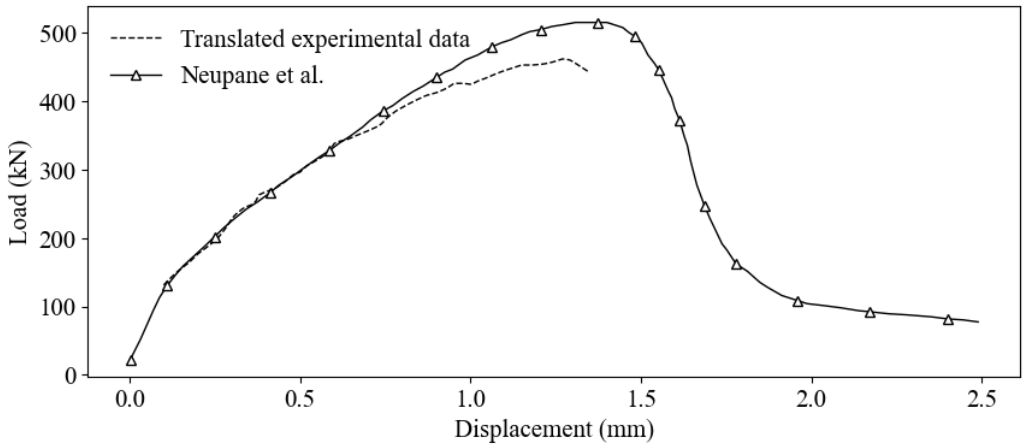

Figure 10.5 Load-displacement curve of translated experimental data and numerical model by Neupane et al. (2017).

The shift of the experimental data shows that the load-displacement curve of the numerical data matches the experimental data up to an estimated displacement of 0.6 mm. Furthermore, both failure load and displacement of the model are slightly larger compared to the experiment, at a failure load of 515.4 kN at an estimated displacement of 1.45 mm. Whilst the numerical results differ to some extent, it shows that the support end failure can be accurately modelled with a 3D finite element model.

Strain in reinforcement

The experimental results of the strain in main reinforcement are shown in Figure 10.6. The measured strain in the reinforcement was plotted against the load exerted at the foot of the column. Additionally, Neupane et al. (2017) mentioned that the main reinforcement did not yield in case of support end failure, which is verified by the strain of the reinforcement at the characteristic yield strength.

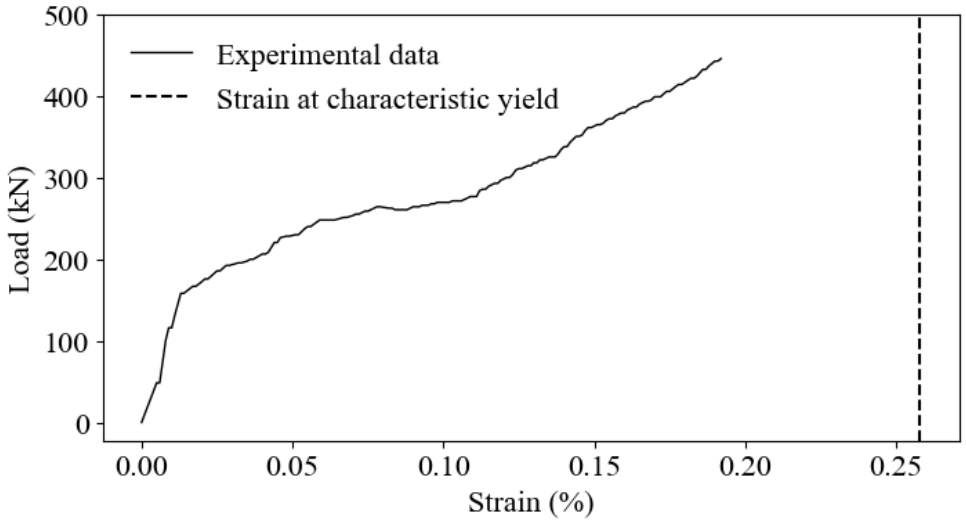

Figure 10.6 Strain of main reinforcement versus loading of corbel element.

10.3 Material models

The previously discussed numerical results by Neupane et al. (2017) showed that the experimental results could be replicated by a 3D finite element model. A numerical model is made using the finite element software ATENA, in which the experiments are replicated (Červenka et al., 2021). The results from the mentioned experiment are used for validation of the numerical model. The material properties, corbel dimensions, and rebar configurations mentioned in this experiment are replicated in the numerical model. First, the material properties and constitutive material models are elaborated, followed by the constitutive models applied in the finite element calculation.

10.3.1 Mechanical properties

Concrete corbel

The material properties of concrete used in the numerical model are based on the material properties from experimental results of Neupane et al. (2017). The 28-day mean cylinder compressive and tensile strength of the used concrete mixture were 45.52 MPa and 2.66 MPa respectively. Several material properties, not mentioned in the research, encompass the modulus of elasticity, fracture energy, and various compressive strains. These have been estimated in accordance with report RTD:1016-1:2022 (RTD) and fib Model Code 2010 (Hendriks & Roosen, 2022; FIB, 2013). The RTD is a guideline for nonlinear finite element analysis of concrete structures provided by the Dutch government. The Poisson ratio and density of the concrete is set at 0.2 and 2500 kg/m^3, respectively. The formulas and mechanical properties of the concrete are enumerated in tables 10.1 and 10.2.

Table 10.1 Formulas to calculate material properties according to RTD.

Mechanical property	Formula
Mean modulus of elasticity (E_{cm})	$22000 * (0.1 * f_{cm})^{0.3}$
Modulus of elasticity at 28 days (E_{ci})	$21.5 * 10^3 * (f_{cm} / 10)^{1/3}$
Fracture energy (G_{Fk})	$0.7 * 0.073 * f_{cm}^{0.18}$
Strain at max. comp. stress (ε_{c1})	$0.7 * f_{cm}^{0.31}$
Elastic compressive strain (ε_e)	f_{cm} / E_{ci}
Plastic strain (ε_{cp})	$\varepsilon_{c1} - \varepsilon_e$

Table 10.2 Material properties of concrete corbel element.

Mechanical properties	Value	Unit
Mean cylinder compressive strength (f_{cm})	45.52	MPa
Mean tensile strength (f_t)	2.66	MPa
Mean modulus of elasticity (E_{cm})	34664	MPa
Modulus of elasticity at 28 days (E_{ci})	35631	MPa
Fracture energy (G_{Fk})	0.104	Nmm/mm^2
Strain at max. comp. stress (ε_{c1})	0.00228	-
Elastic compressive strain (ε_e)	0.00128	-
Plastic strain (ε_{cp})	0.001	-
Poisson ratio (ν)	0.2	-
Density (ρ)	2500	kg/m^3

Steel bearing pads

The steel plates used as bearing pads in the experiments were referred to by Neupane et al. (2017) as mild steel. As the material properties were not specified, assumptions were made for the material properties of the steel, enumerated in Table 10.3.

Table 10.3 Assumed material properties of steel plates.

Mechanical properties	Value	Unit
Young's Modulus (E_s)	200,000	MPa
Poisson's ratio	0.3	-
Yield strength (f_y)	550	MPa
Density (ρ)	7850	kg/m^3
Hardening modulus	10,000	MPa

Steel reinforcement

The Young's Modulus and yield strength of the reinforcement were provided by the study. It is assumed that the mentioned yield strength is the characteristic yield strength, due to insufficient clarification. The mechanical properties of the steel reinforcement are shown in Table 10.4.

Table 10.4 Material properties of steel reinforcement.

Mechanical properties	Value	Unit
ϕ10 (Stirrup)		
Yield strength (f_{yk})	390	MPa
Young's Modulus (E_s)	190,000	MPa
Density (ρ)	7850	kg/m^3
ϕ13 (Main reinforcement)		
Yield strength (f_{yk})	490	MPa
Young's Modulus (E_s)	190,000	MPa
Density (ρ)	7850	kg/m^3
ϕ16 (Vertical reinforcement)		
Yield strength (f_{yk})	490	MPa
Young's Modulus (E_s)	190,000	MPa
Density (ρ)	7850	kg/m^3

10.3.2 FE model and constitutive model

The finite element software ATENA is used for the numerical modelling of the corbel. The modelling is performed in ATENA Science GiD. The calculation and analysis are performed in ATENA Studio. A 2D numerical model was used, rather than a 3D, to approximate the behaviour of the concrete corbel. Reason being the reduced computational time and the expectation that the support end failure acts similar in a 2D plane.

The concrete behaviour was modelled using the Cementitious2 material model in ATENA. Cementitious2 describes the concrete behaviour as a fracture-plastic model, simulating fracturing in tension and the plastic behaviour in compression. The elements were idealised as 2-dimensional plane stress elements, assuming a thin element.

An important assumption within this study is the simplification of the corbel element in a two dimensional space. Arguably the most important assumption made by modelling in 2D is the uniform width of the model, in particular for the bearing pad. In practice, the bearing pad should be placed with a prescribed edge distance along all edges of the support. However, this cannot be modelled in 2D. This difference is notably found in the horizontal stress distribution between the bearing pad and the corbel, as schematised in Figure 10.7.

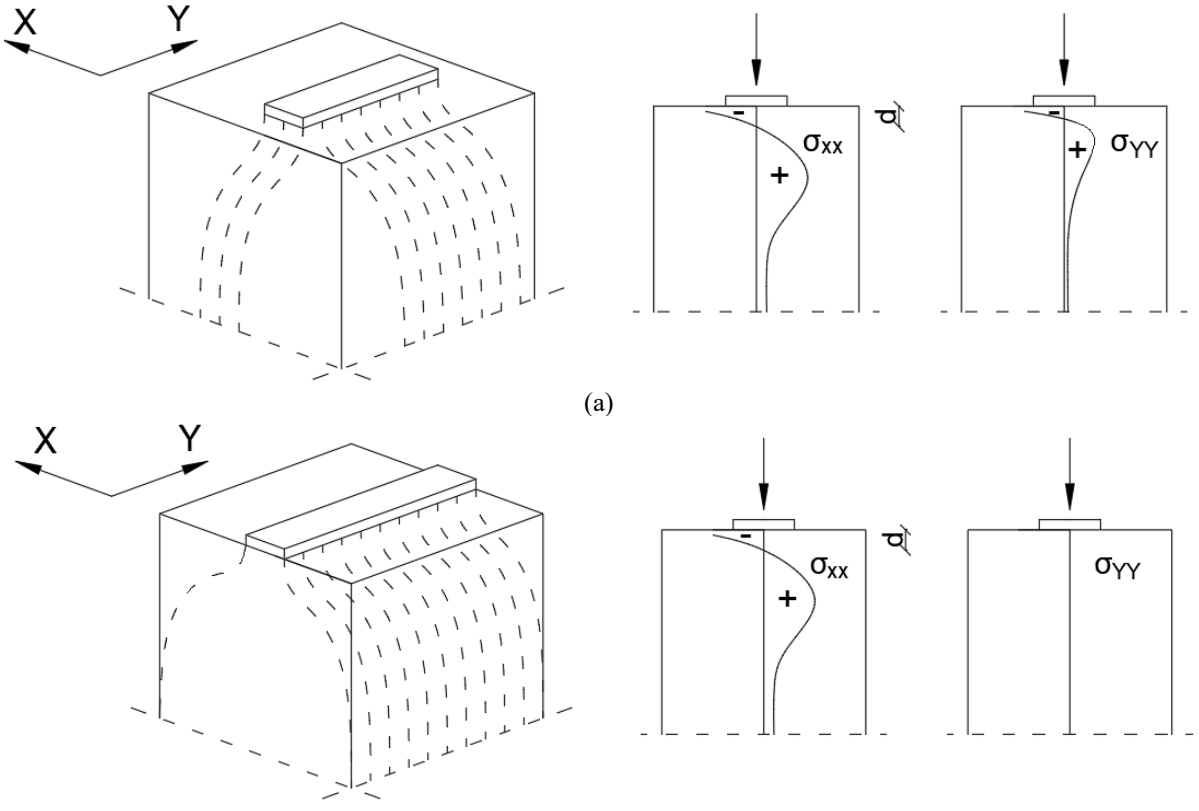

Figure 10.7 Horizontal stress distribution for bearing pad with edge distance (a) and along the entire width (b) (Leonhardt, 1977).

The 2D finite element model assumes equal width of the bearing pad, therefore it calculates the horizontal stresses below the bearing pad as model (b) of Figure 10.7. Although, for an appropriately designed corbel the horizontal stresses would distribute in both directions, as per model (a) of Figure 10.7. Since the support on the corbel in the experimental study by Neupane et al. (2017) covers the entire width of the corbel, this assumption holds true.

Constitutive model: Concrete

Geometrical nonlinearity

The displacements of the experimental results are an order of magnitude of millimetres, thus the displacements and rotations of applied load on the corbel are deemed insignificant Additionally, the experiment subjected the corbel to pure vertical loading. Therefore, the geometrical nonlinearity is set to linear.

Compressive behaviour

The material behaviour of concrete in compression is based on the Menétrey-Willam failure surface. The compressive concrete model assumes hardening of concrete until the plastic strain is reached. After reaching the plastic strain the concrete starts crushing, following a linear softening law based on the plastic strain and crush band, as seen in Figure 10.8. The stress at onset of crushing (f'_{co}) has been estimated according to the graph shown in figure 10.8, assuming that this stress is equal to twice the tensile strength.

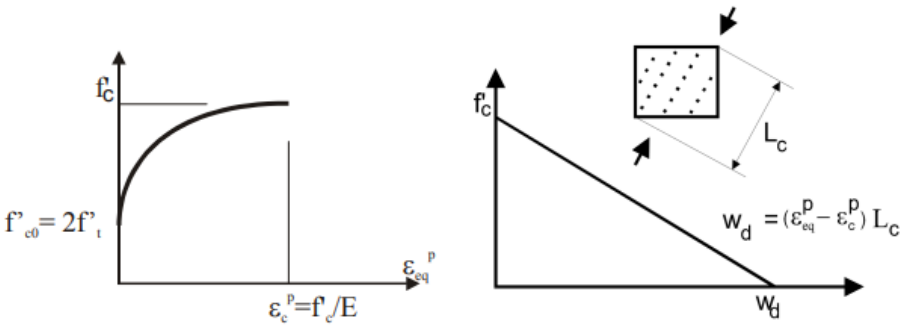

Figure 10.8 Compressive hardening (left) and softening behaviour (right) modelling (Červenka et al., 2021).

The crack band length (L_c) parameter is important as it scales the strains obtained from the finite element calculation into plastic displacement w_d. The plastic displacement is assumed as the default setting by ATENA at 0.5 mm, based on experimental results by Van Mier (1986).

After lateral cracking of concrete the compressive strength of concrete is reduced. According to Hendriks and Roosen (2022) the concrete compressive strength (σ_c) should be reduced by at least 60%. In the ATENA model this reduction is calculated according to the Modified Field Theory using a reduction factor (r_c). This factor is calculated according to formulas (1) and (2).

$$\sigma_c = r_c * f_c' \quad (1)$$

$$r_c = \frac{1}{0.8 + 170 * \varepsilon_1}, r_c^{lim} \leq r_c \leq 1.0 \quad (2)$$

Lastly, the eccentricity of the Menétrey-Willam surface is set at 0.52, according to default setting provided by ATENA.

Tensile behaviour

The tensile behaviour is modelled as linear elastic before cracking and by exponential softening after cracking. Preliminary analysis were performed with both fixed- and rotating crack models. In the model using a fully rotating crack model, initial cracking at the re-entrant corner occurred, followed by cracking along the compressive strut. Yet, the support end failure was not captured as main failure mechanism, only slight cracking at the corner is observed (Figure 10.9). The preliminary analysis with a fixed crack model presented a detailed representation of the support end failure, as can be seen in Figure 10.10.

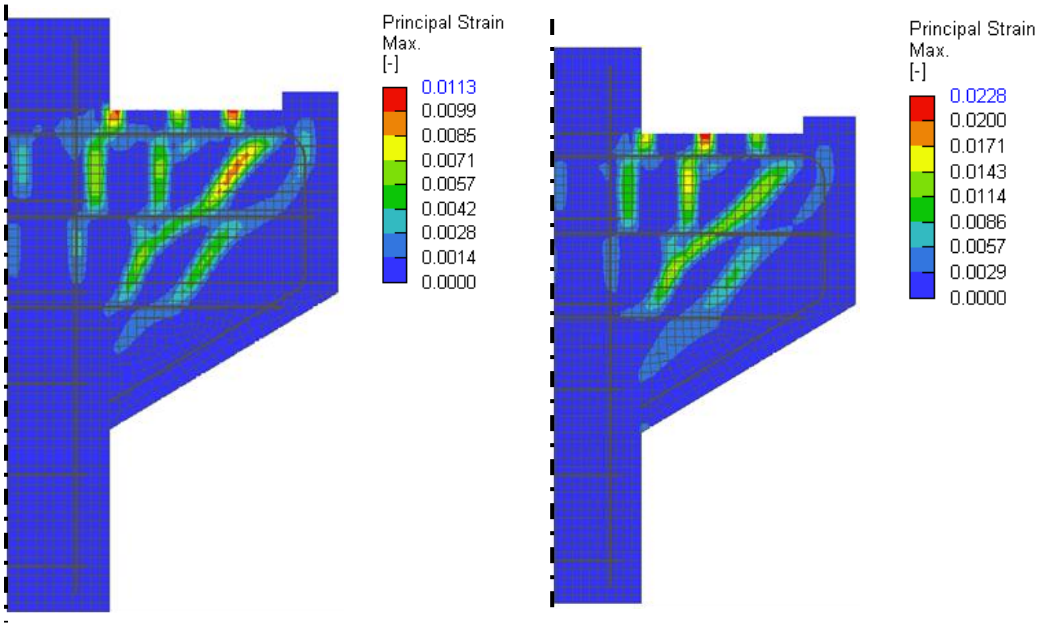

Figure 10.9 Principal strain at load of 425 kN, load step 100, and 527 kN, load step 170, using a rotated crack model.

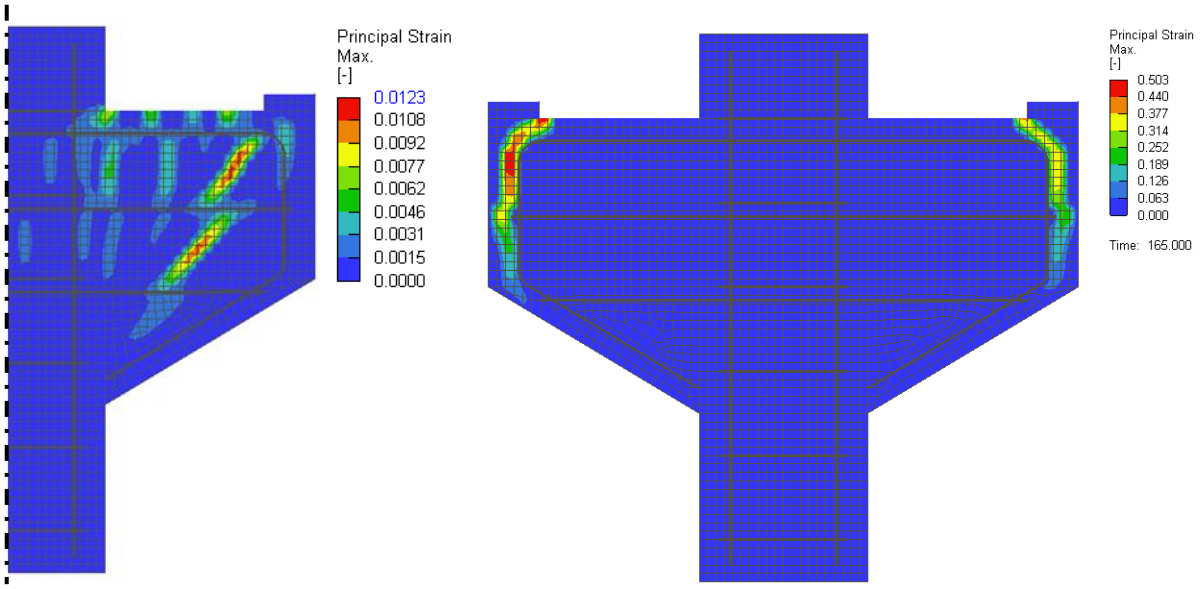

Figure 10.10 Principal strain at load of 425 kN, load step 100, and 33 kN, load step 168, using a fixed crack model.

As the support end failure behaviour was accurately captured in the model using a fixed crack model, this was adapted into further models.

The tensile softening behaviour of the concrete is described by Hordijk's (1991) exponential softening formula, as seen in Figure 10.11. The tensile capacity (f_t) and the fracture energy (G_f) were provided in Subsection 10.3.1.

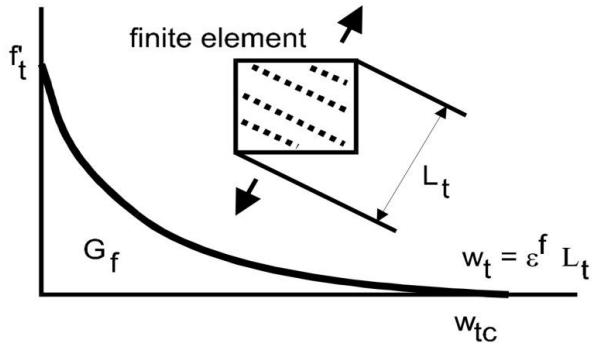

Figure 10.11 Schematisation of Hordijk's exponential softening formula (Červenka et al., 2021).

Moreover, a minimum crack spacing was introduced. The crack spacing is calculated incorrectly when using a mesh size smaller than the aggregate size without a lower bound for the crack spacing. As cracks in concrete would generally form along aggregates, a minimum crack spacing distance is set at 20 mm, based on the aggregate size used in the experiment.

Shear behaviour

The fixed crack model calculates the direction of the crack perpendicular to the principal stress direction. During loading the direction of the principal stresses can change. The fixed crack model does not change its crack orientation according to the direction of the principal stresses, thus inducing a shear stress in the element. A reduction of the shear stiffness is necessary in order to prevent overestimation of the shear stiffness.

The shear stiffness is calculated by multiplying the normal stiffness in the cracked state (K_n^{cr}) by a shear factor (r_g). The normal stiffness in the cracked state is calculated by dividing the tensile stress in the softening curve by its crack width, as portrayed in Figure 10.12. The shear factor is assumed to be 20 (-), the default setting of ATENA based on empirical results.

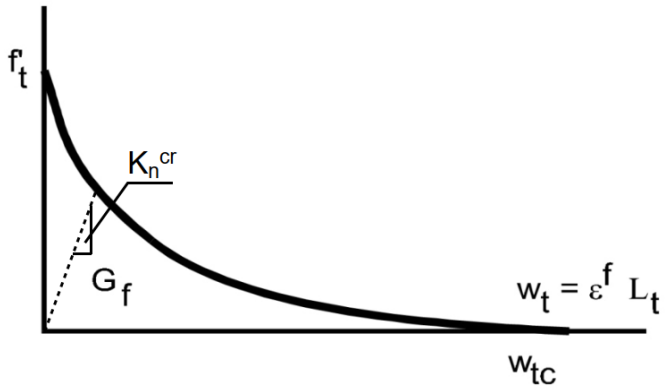

Figure 10.12 Stiffness tangent of normal stiffness in cracked state.

Constitutive model: Bearing pad

The steel bearing plates are modelled and idealized as plane-stress elements. The material behaviour of the steel bearing plates is modelled as a bilinear element, meaning that after the yield has been reached of the steel the stress increases due to hardening.

Constitutive model: Reinforcement

The concrete reinforcement is modelled as discrete rebar using embedded reinforcement. This modelling assumes uniaxial stress in the reinforcement. The material behaviour of the rebar is modelled as bilinear. Assumed is that the reinforcement has a maximum tensile strength of 514.5 MPa at a strain of 2.5 (%). Neupane et al. (2017) mentioned that the support end failure occurred before the longitudinal concrete rebar yielded. Ergo, the uncertainty of strain hardening is deemed unsignificant. The reinforcement is modelled with a perfect bond between the concrete and the reinforcement.

10.4 Boundary conditions and meshing

10.4.1 Loading- and boundary conditions

In the experimental setup the corbel was loaded at the bottom of the column and supported at the steel bearing pads. In the numerical model the loads are applied in the middle of the steel bearing pads and the structure is supported at the base of the column, both are shown in Figure 10.13. In the numerical model the column foot is simply supported in both X and Y-axis. The steel bearing pads are assumed to be fixed to the concrete corbel element.

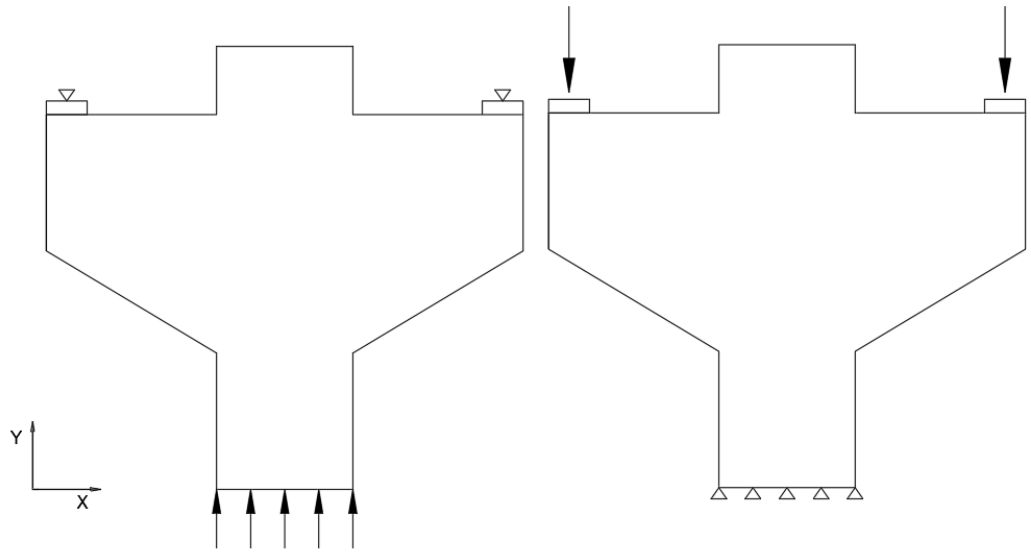

Figure 10.13 Schematisation of loads and supports in the experimental test setup (left) and the numerical model (right).

The loading of both, experiment and numerical model, are displacement controlled. In the experiment the load is applied with a displacement of 0.0084 mm/s at the column foot. In the numerical model two displacements, of 0.084 mm per load step, are applied in the middle of both bearing pads.

10.4.2 Meshing

Three mesh sizes have been compared on their load-displacement curve, depiction of cracks, and load-strain curve, as all are known from the experiment. The three mesh sizes are 10x10, 15x15, and 20x20 mm^2. A comparison of the results between the experimental results can be found in Subsection 10.5.2. Quadrilateral elements are used to mesh the steel plates and concrete elements. The meshing and overview of the 2D model is provided in Figure 10.14.

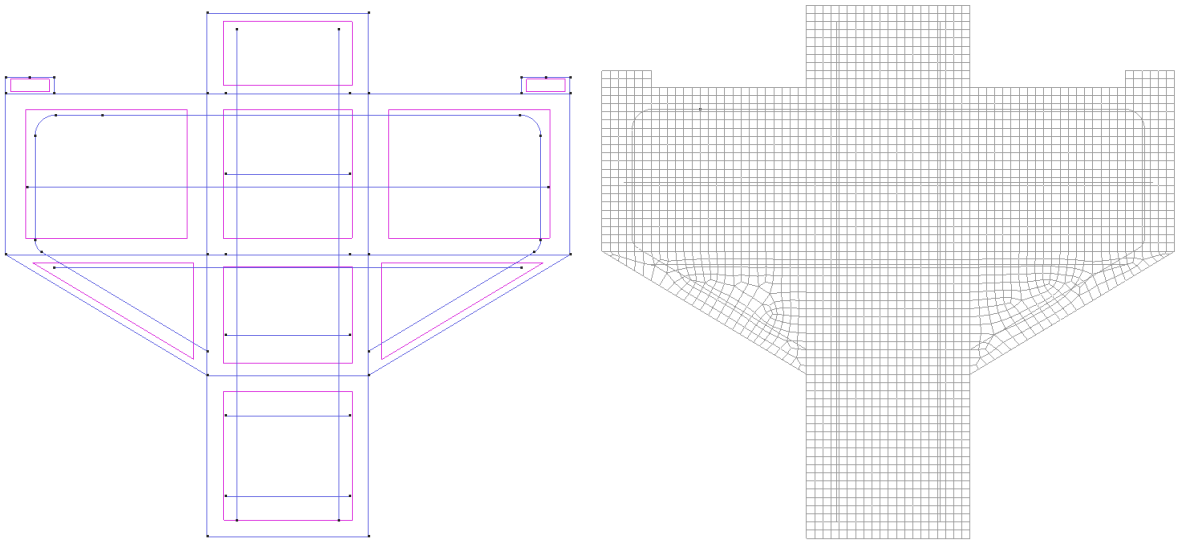

Figure 10.14 Overview of the model and 10x10 mesh of the finite element model.

Solution procedure

The failure mechanism of the experiment shows brittle behaviour of the corbel when the support end failure occurs, as the crack develops along the main reinforcement of the corbel. Both displacement and force-controlled models can be applied for this model, as the analysis is both mainly performed until failure. Although, the post failure behaviour could be indicatively used. Therefore, a displacement-controlled analysis is used.

Solution method

A Full Newton-Raphson (FNR) solution and Line Search (LS) solution procedure are used in the analysis. The FNR updates the stiffness tangent in every iteration, contrary to the modified Newton-Raphson which only updates the stiffness tangent every step size. The FNR is chosen over a modified Newton-Raphson (MNR), or arc-length, as it calculates the stiffness the most accurately. The Arc-length method would be the suggested method if the after failure behaviour would be modelled or snap-back behaviour is expected. However, for this research the moment at which the support end failure occurs is analysed, rather than the post-fracture behaviour. The LS method is adapted to either increase or decrease the speed of the analysis.

Convergence criteria

Force-based, displacement-based, and energy-based convergence criteria are initially applied in the model. The convergence criteria for the FNR method and LS method are found in tables 10.5 and 10.6, respectively.

Table 10.5 Convergence criteria for FNR method.

Convergence criteria FNR	Value (-)
Displacement limit	0.01
Force limit	0.01
Energy limit	0.001

Table 10.6 Limits and parameters for LS method.

Line search parameter	Value (-)
Energy limit	0.8
Iteration limit	3
Maximum η	0.1
Minimum η	1

Monitoring

The monitoring equipment used during the experiment is shown in Figure 10.15. These conditions are resembled in the experimental data by monitors 1, 2, and 3. In the numerical model monitor 1 records the stress in the reinforcement instead of the strain, recorded by a strain gauge in the experiment. The monitored stress is divided by the mean Young's Modulus of the reinforcement to obtain the strain. This can be assumed as the failure mechanism occurred before yielding of the main reinforcement (Neupane et al., 2017). Monitor 2 measures the displacement underneath the bearing pad, and monitor 3 measures the total reaction force at the base of the column.

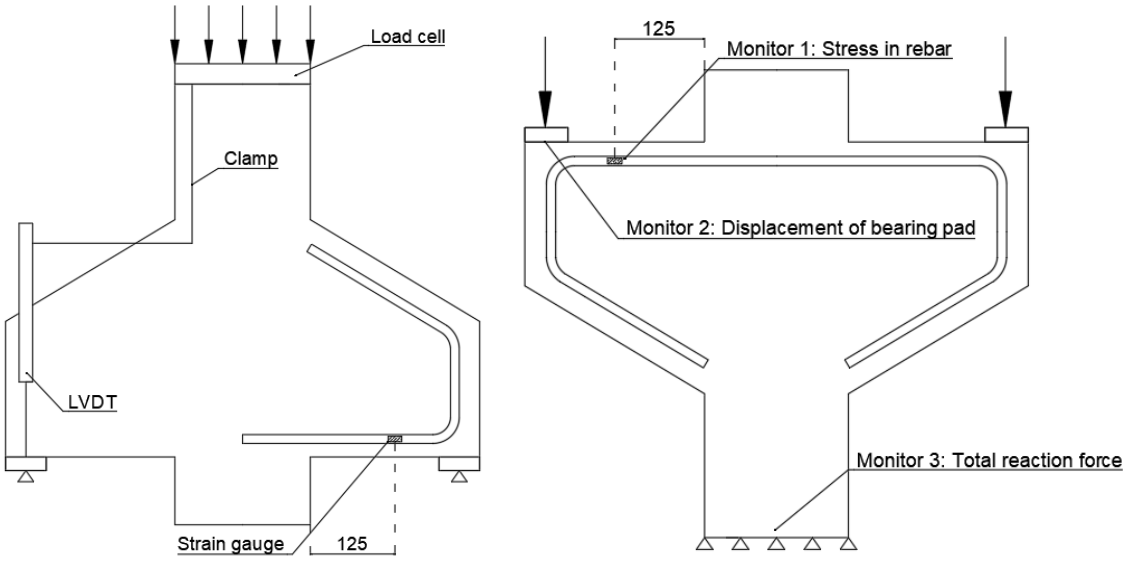

Figure 10.15 Experimental monitoring setup (left) and monitoring setup numerical model (right).

10.5 Numerical results

10.5.1 General

The results of the numerical analyses are presented and compared to the experimental data. The results of the numerical model are compared to the load-displacement curves, development of principal strains, and the load-strain curve of the experimental data. This comparison is made for the mesh sizes 10x10 mm^2, 15x15 mm^2 , and 20x20 mm^2.

10.5.2 Validation

Load-displacement

The load-displacement curves for the three mesh sizes, experimental data, and numerical model by Neupane et al. (2017) are displayed in Figure 10.16. The results of the numerical model show a difference in initial stiffness, up to approximately 0.3 mm. As previously mentioned, this was caused in the experiment due to crushing of gypsum. The experimental data in which the displacement is reduced by 0.3 mm, to correct for slip at the beginning, is plotted in Figure 10.17.

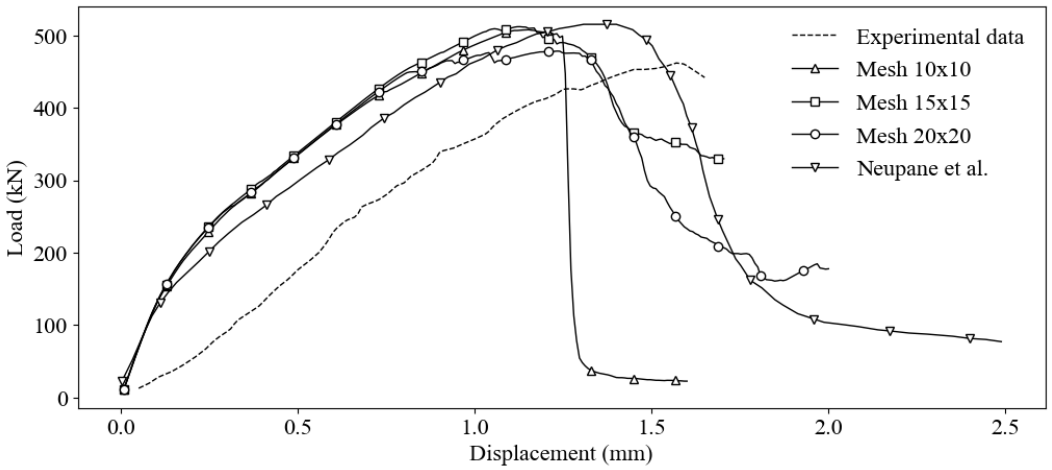

Figure 10.16 Comparison between numerical and experimental results.

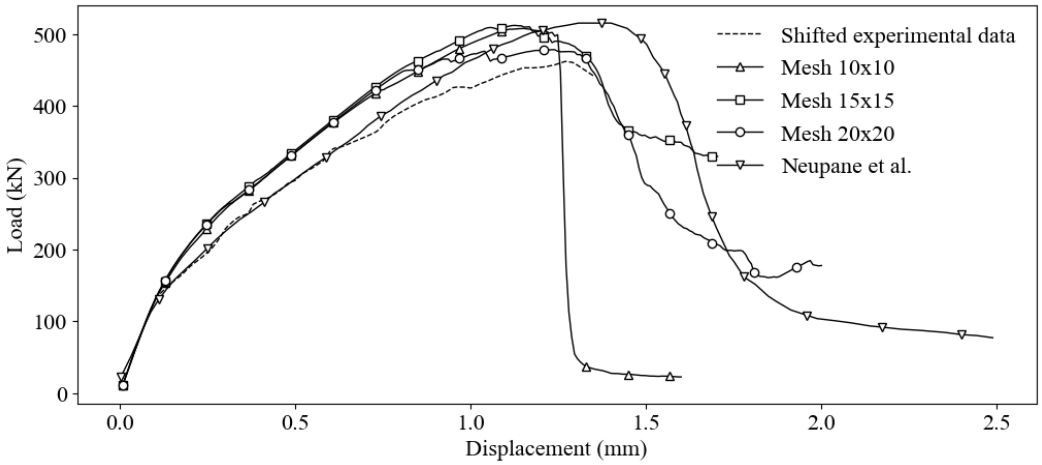

Figure 10.17 Comparison of load-displacement curves between numerical and shifted experimental data.

In the experiment the support end failure occurred at a vertical load of 458.4 kN. The numerical results of the maximum load and displacement at maximum load are presented in Table 10.7.

Table 10.7 Results of maximum load, load at failure, and displacement at failure from both numerical and experimental model.

Mesh size	Maximum load	Displacement at maximum load
10x10	507.9 kN	1.15 mm
15x15	512.0 kN	1.13 mm
20x20	478.4 kN	1.23 mm
Experimental data	458.4 kN	1.26 mm

The results of the numerical model fit the experimental data well. The stiffness of the load displacement curve of the various mesh sizes approximates the stiffness of the load displacement curve of the experimental results. Mesh size 10x10 mm^2 differs notably from mesh sizes 15x15 mm^2 and 20x20 mm^2 by its steep decrease in load after failure. The large decrease in load for mesh size 10x10 mm^2 suggest the occurrence of a brittle failure mechanism, contrary to the moderate decreases from mesh sizes 15x15 mm^2 and 20x20 mm^2.

Failure mechanism

The failure mechanism of the three meshes were compared to each other, by comparing the principal strain. Based on the experimental data the failure mechanism is known, portrayed in Figure 10.18. The first crack originated in the re-entrant corner of corbel, followed by a second crack spanning diagonally from the bearing pad up towards the concrete column. After propagation of both cracks the support end failure occurred.

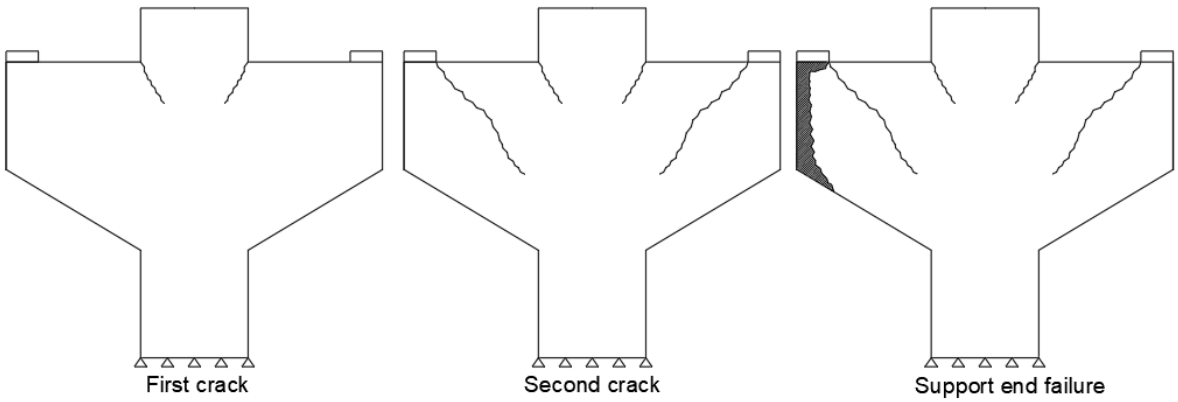

Figure 10.18 Crack formation in the experiment before support end failure mechanism initiates.

The maximum principal strain at various applied loads for mesh size 10x10 mm^2 is presented in Figure 10.19. At an applied load of 268 kN ((a) in Figure 10.19), the largest strain is observed at the re-entrant corner. Upon increasing the load to 437 kN ((b) in Figure 10.19), the largest strain was observed in the same direction and location as the second crack, as observed in the experiment. Consequently, the support end failure occurred at 508 kN and was completely developed at step (c) in figure 10.19.

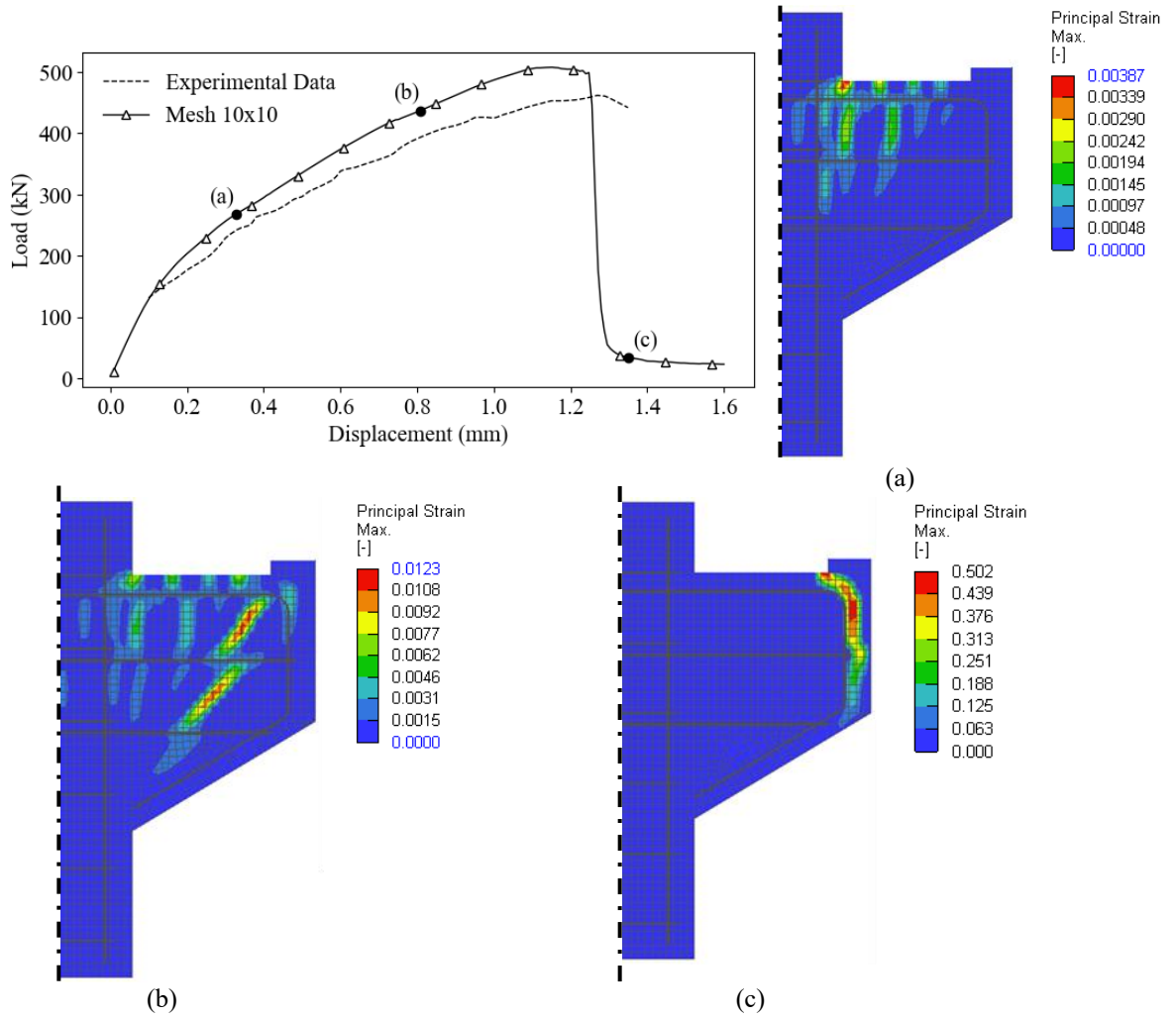

Figure 10.19 Maximum principle strain plot at loads 268 kN (a), 437 kN (b), and 32 kN (c) for mesh size 10x10 mm^2.

The maximum principal strain for mesh sizes 15x15 mm^2 and 20x20 mm^2 are presented in figures 10.20 and 10.21, respectively. For mesh size 15x15 mm^2, the first and second crack are represented at an applied load of respectively 272 kN and 453 kN ((b) and (c) in Figure 10.20). Although, as the load was increased only potential support end failure strains were observed. Eventually the corbel failed along the diagonal crack. Mesh size 20x20mm^2 showed similar behaviour, in which largest principal strain was initially observed at the re-entrant corner at an applied load of 268 kN ((a) in Figure 10.21), followed by the second crack at 448 kN ((b) in Figure 10.21). As the load was increased, an increase in principal strains along the main reinforcement were observed. However, before the support end failure developed any further, failure occurred at the diagonal crack.

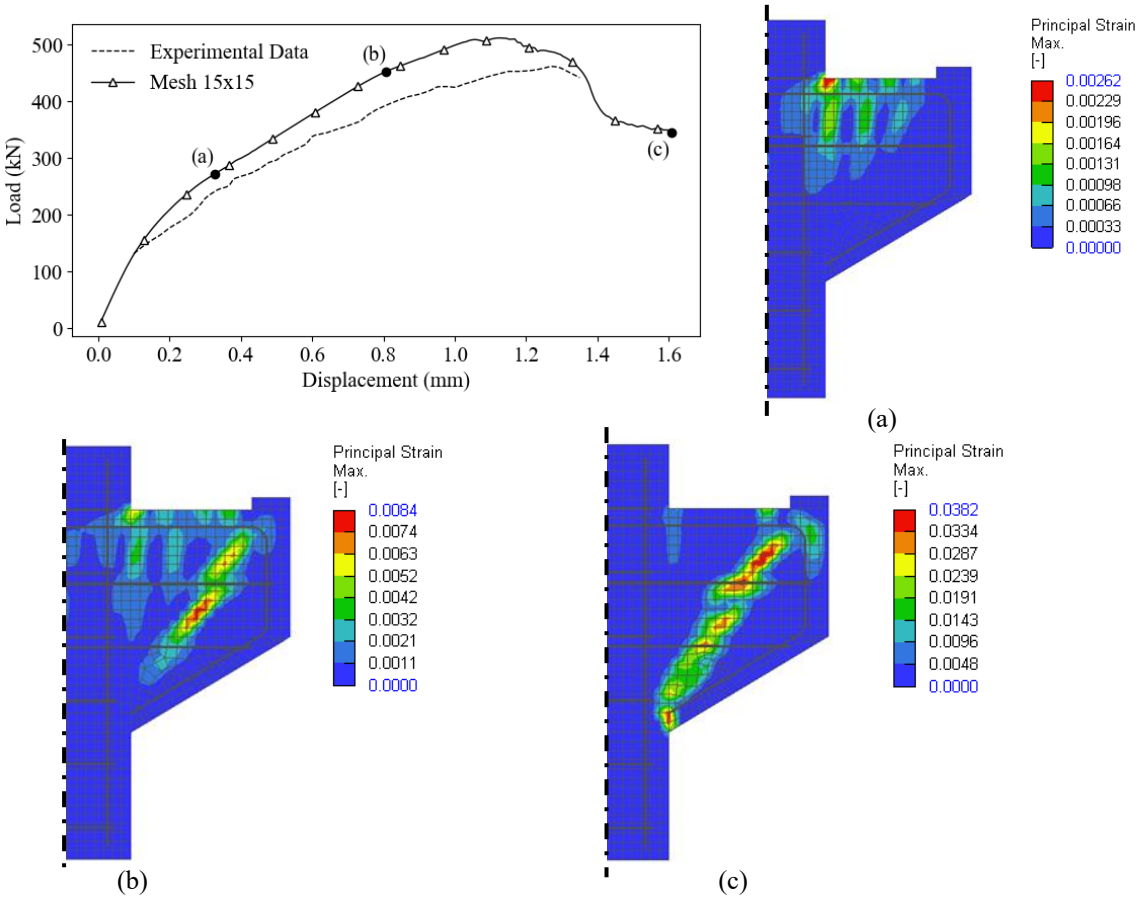

Figure 10.20 Maximum principle strain plot at loads 272 kN (a), 453 kN (b), and 345 kN (c) for mesh size 15x15 mm².

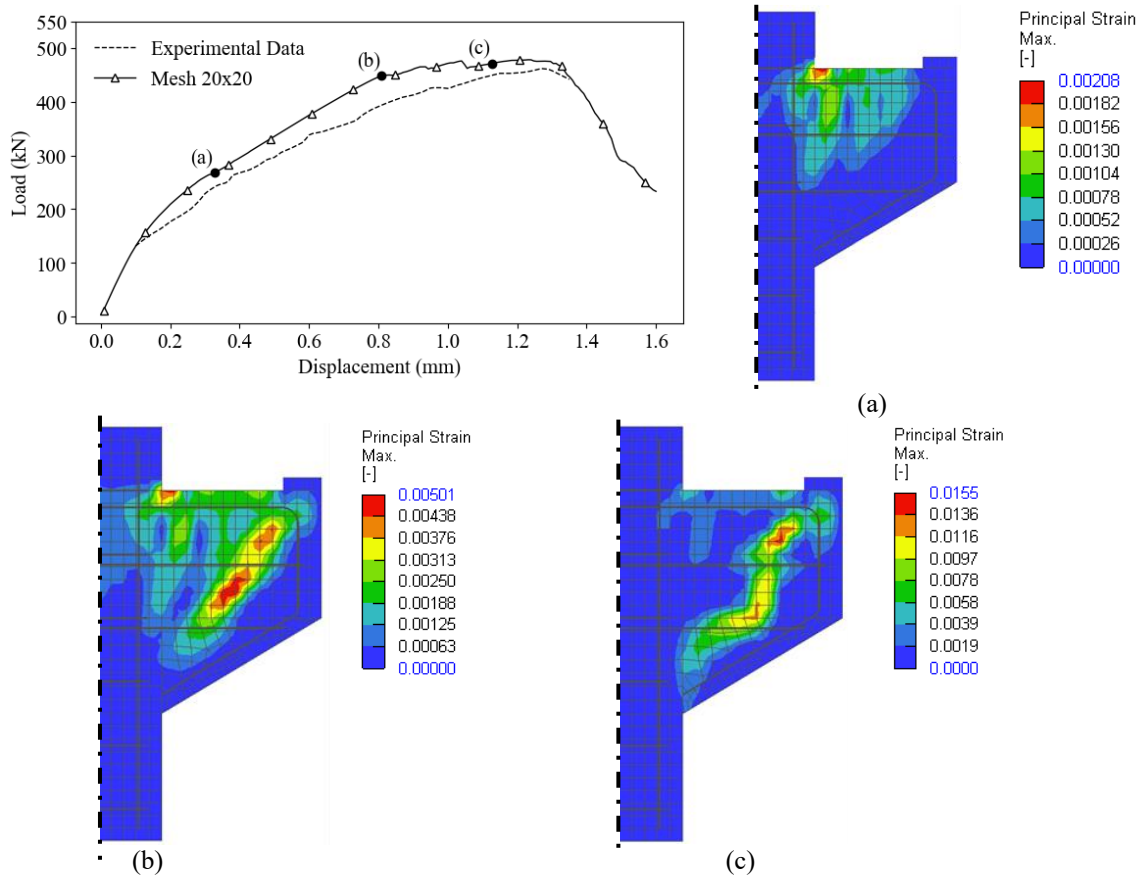

Figure 10.21 Maximum principle strain plot at loads 268 kN (a), 448 kN (b), and 472 kN (c) for mesh size 20x20 mm².

The numerical results showed that the three mesh sizes accurately represented the crack at the re-entrant corner and the second crack, compared to the experimental results. Moreover, Mesh size 10x10 mm^2 failed by support end failure, contrary to mesh sizes 15x15 mm^2 and 20x20 mm^2 in which failure occurred along the second crack. The inaccuracy of not representing the correct failure mechanism is probably due to the applied large mesh size. Since the support end failure was only accurately represented for mesh size 10x10 mm^2, it is concluded that this is the preferred mesh size for depiction of the failure mechanism.

Reinforcement strain

The load-strain curve provides the last comparison method. A comparison of the results of the numerical model and experimental results are displayed in Figure 10.22. The results of the numerical models showed rather close resemblance to results of the experimental data.

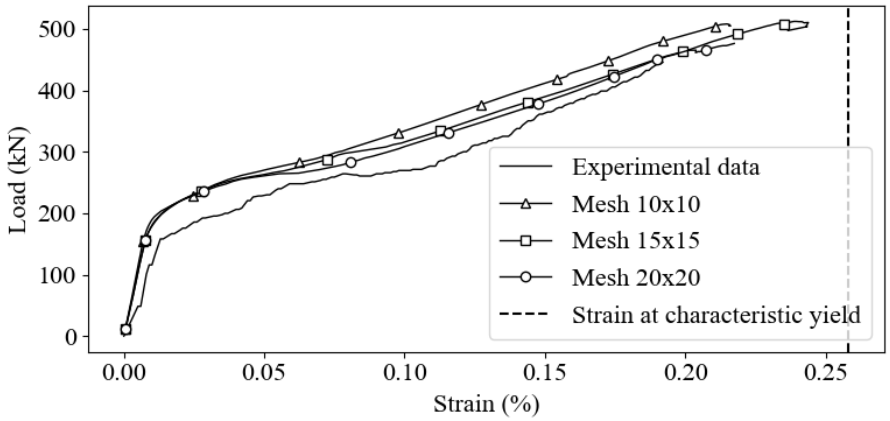

Figure 10.22 Comparison between numerical results and experimental data of load-strain curves for main reinforcement.

The initial development of the curves is identical for all mesh sizes. The development beyond a strain of 0.25 % between the mesh sizes is nearly identical. Mesh sizes 15x15 and 20x20 reach a slightly larger strain, as found by the slightly larger displacement in the load-displacement curves, although this difference is insignificant. Moreover, the slope of the numerical and experimental curves show similar results.

10.5.3 Concluding remarks

A summarisation of the findings of the validation study is given below:

- The 2D numerical model showed close approximation of the experimental results of Neupane et al. (2017). For this validation the load-displacement diagram, failure mechanism, and tensile strain of the main reinforcement were used.
- Taking into account that in the test there was an initial deformation of gypsum, the numerical results of both load-displacement and load-strain fit well to the experimental results.
- The support end failure mechanism could only be captured with a fixed crack model.
- A mesh sensitivity analysis indicated that only a mesh size of 10x10 mm^2 could accurately depict the support end failure behaviour. Therefore, it is recommended that further analysis use similar size.

11 Corbel behaviour under Eurocode design

11.1 General

Prior research concluded that support end failure is prevented by appropriate corbel design and execution, as previously stated (Hermanson and Cowan, 1974; Forster and Powell, 1994). However, the impact of changes, for example due to incorrect execution, on such design are unknown. In a preliminary analysis, horizontal loading was applied to the corbel configuration of the model validation study. Due to the poor design of the corbel, it failed prematurely by a primary failure mechanism. Therefore, it was concluded that the design of the corbel was not suitable for the parametric study. As result, a model was designed according to Eurocode 2.

The corbel is designed in accordance with Eurocode 2 and modelled in ATENA, elaborated in respectively Sections 11.2 and 11.3. In the numerical analysis the corbel was loaded until failure and analysed at various loads to provide insight into the behaviour under normal conditions, and to act as a reference point to the parametric study. The results of the analysis are presented in Section 11.4. Subsequently, a selection of parameters were changed to study its impact on the behaviour of the corbel (Chapter 12).

11.2 Design configuration

11.2.1 Corbel configuration

A corbel was designed in accordance with the current standard, NEN-EN 1992-1-1 (2011), EC2 in short (Nederlands Normalisatie Instituut, 2011). For the design, concrete strength class C40/50 and B500B for the reinforcement were taken into account. The calculations which led the current design are found in appendix D. An overview of the dimensions of the design conform EC2 are visualised in Figure 11.1.

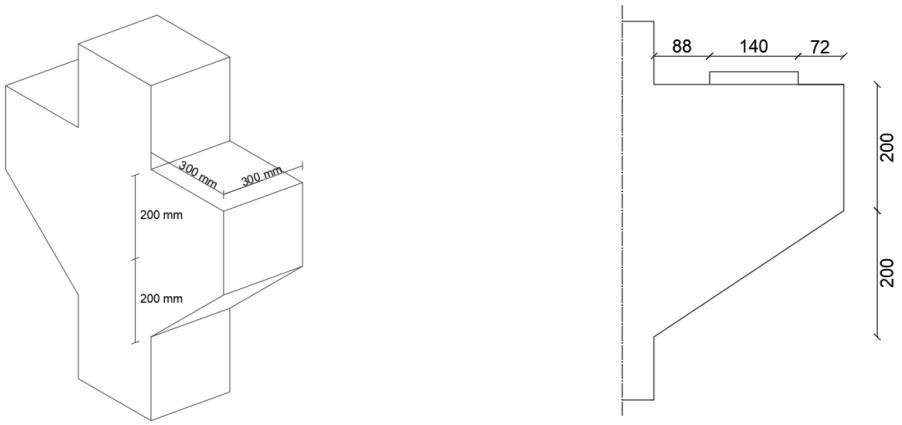

Figure 11.1 Dimensions of the corbel, dimensions in mm.

11.2.2 Reinforcement configuration

An important aspect regarding support end failure is the reinforcement detailing of the corner or edge section of the corbel. Bending the tensile reinforcement in the vertical plane is arguably more prone to support end failure than in the out-of-plane direction (Figure 11.2). Therefore, vertically bent main reinforcement is used as anchorage method in the corbel design.

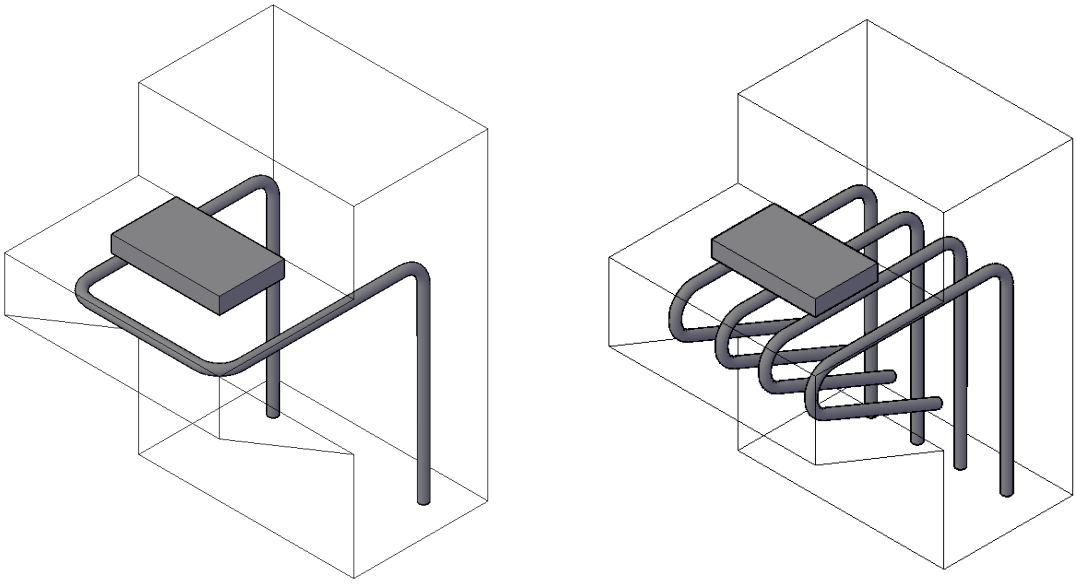

(a) (b)

Figure 11.2 Possible reinforcement configuration of out-of-plane anchorage (a) and in-plane anchorage (b) of tensile reinforcement in a corbel.

The reinforcement configuration of corbel elements can be designed using either the strut-and-tie model (STM) or a deep-beam model (DBM). In both models, the internal forces of the corbel are schematised by compressive and tensile members, as shown in Figure 11.3. Formulas to calculate the locations of these nodes for both models are prescribed in EC2. With the locations of the nodes, the required main reinforcement is calculated by using bending moment equilibrium at Node 2, resulting in the required surface area of the main reinforcement.

Essentially, the difference between both models is the location of Node 2. For the designed corbel, the vertical distances between the main reinforcement and Node 2 for STM and DBM are respectively 325 mm and 250 mm (Figure 11.3). Consequently, a larger required sectional area of main reinforcement is calculated with the DBM.

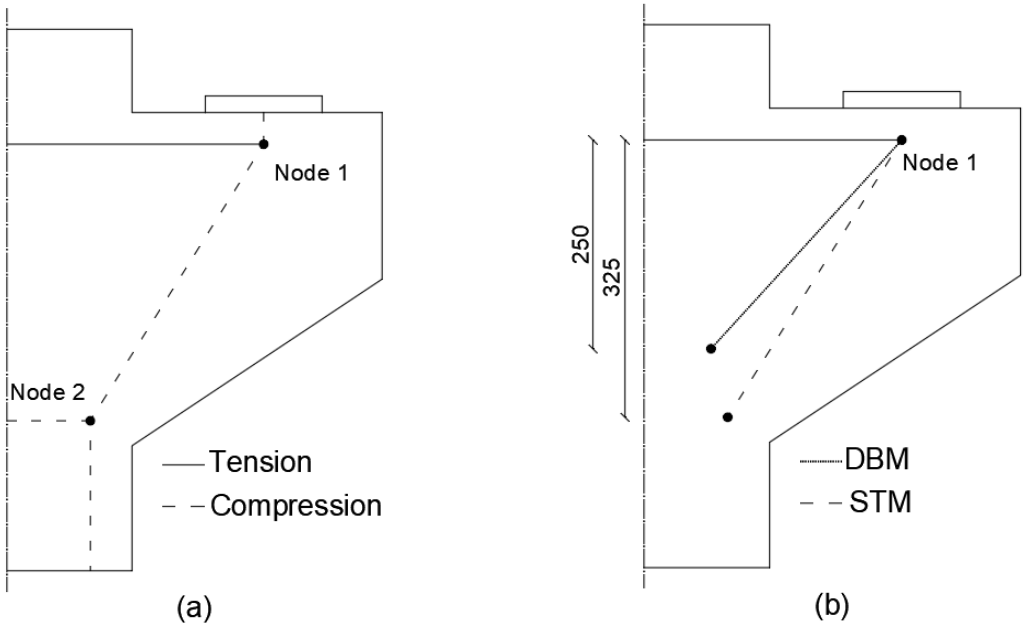

Figure 11.3 Schematisation of internal forces in a corbel (a) and position of nodes 2 for DBM and STM (b) (see also appendix D).

The reinforcement configuration of the corbel was designed with the STM, further elaborated in appendix D. An overview displaying the dimensions and reinforcement configuration of the corbel are presented in Figure 11.4.

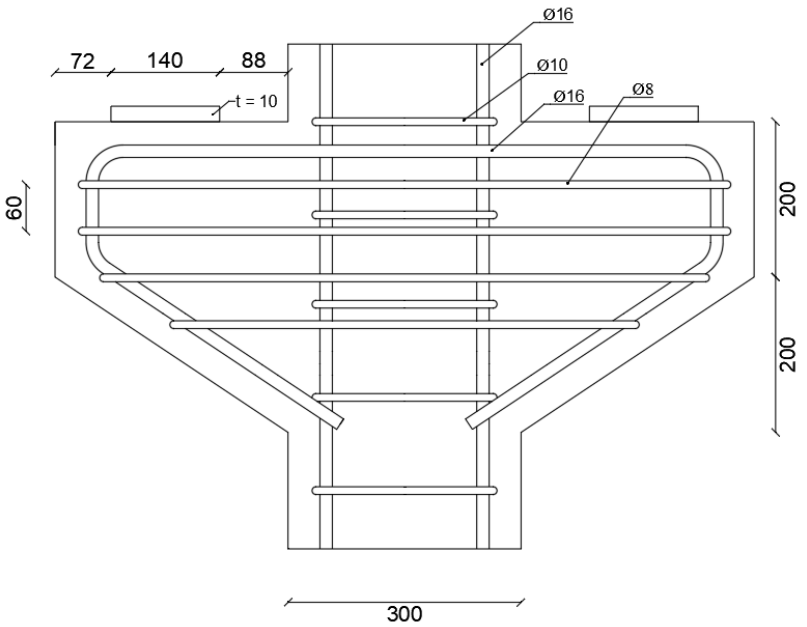

Figure 11.4 Overview of corbel design, dimensions in mm.

11.3 Numerical model

11.3.1 Material properties

The corbel was designed with concrete strength class C40/50 and reinforcement strength class B500B. The material properties of an elastomer are chosen as bearing pad, as it is expected that it distributes the load uniformly. In the analysis, the mean strength parameters of the material are used to predict the physical behaviour of the corbel. Mechanical properties of concrete, reinforcement steel, and the elastomer can be found in tables 11.1, 11.2, and 11.3, respectively.

Table 11.1 Mechanical properties of concrete strength class C40/50.

Mechanical properties	**Value**	**Unit**
Mean modulus of elasticity (E_{cm})	35000	MPa
Tensile strength (f_t)	3.5	MPa
Compressive strength (f_{cm})	48	MPa
Fracture energy (G_{Fk})	0.0875	Nmm/mm^2
Plastic strain (ε_{cp})	0.0009	-
Poisson ratio (ν)	0.2	-
Density (ρ)	2500	kg/m^3

Table 11.2 Mechanical properties of the reinforcement.

Mechanical properties	**Value**	**Unit**
Young's Modulus (E_s)	200,000	MPa
Poisson's ratio	0.3	-
Yield strength (f_{yd})	550	MPa
Density (ρ)	7850	kg/m^3
Fracture strain ε_2	0.025	-
Ultimate strength (f_u)	578	MPa

Table 11.3 Mechanical properties of elastomer bearing pad.

Mechanical properties	**Value**	**Unit**
Young's Modulus (E_s)	10	MPa
Poisson's ratio	0.499	-

11.3.2 Constitutive models

The constitutive models for concrete and reinforcement are the same as the constitutive models used in the validation study (Chapter 10). The steel bearing was replaced by an elastomeric bearing pad in order to represent the situation in reality and probably to distribute the load more uniformly. The constitutive model for the elastomer was simplified as linear elastic, with the material properties provided in Table 11.3.

11.3.3 Meshing

A mesh size of 10x10 mm^2 is used for the concrete element, based on the results of the model validation study. However, compared to the mesh in the validation study in Chapter 10, several adaptations were made to the mesh of the model, as explained below.

First of all, an unstructured mesh of 10 mm was used for the lower half of the corbels. Even though the dimensions of both lower half's are identical, an asymmetric mesh is obtained after mesh generation (Figure 11.5).

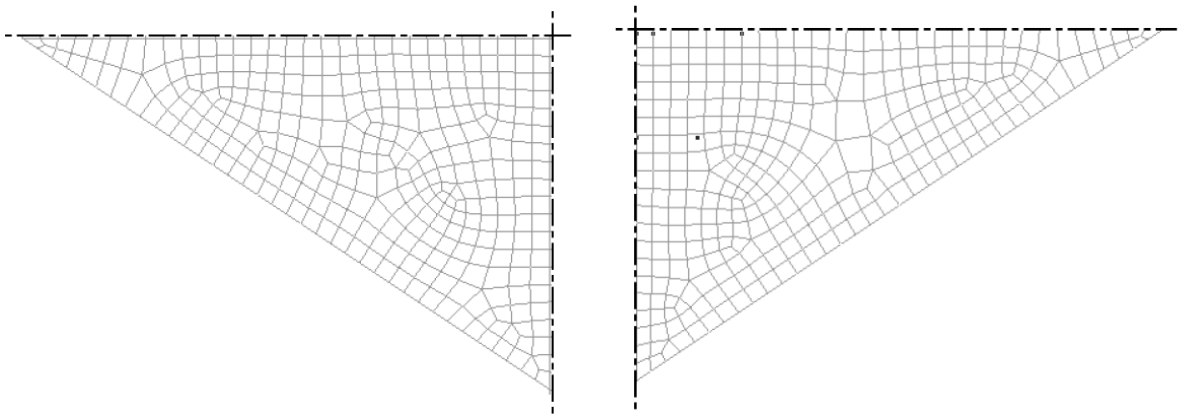

Figure 11.5 Meshing of corbel: left lower half (a) and right lower half (b).

Furthermore, the thickness of the bearing material was reduced to 10 mm, as opposed to 20 mm before. If a mesh size of 10 mm were to be used for the adapted bearing element, the behaviour of the elastomer would not be visible due to the limited amount of nodes and integration points. Additionally, the edge distance between the bearing pad and the edge is 72 mm. For this distance, the nodes of the bearing element and corbel do not align with each other. In order to provide a more accurate interaction between bearing pad and concrete, and to model the behaviour more accurately, a mesh size of 5 mm was used for the bearing element. Additionally, a master-slave connection (as it is mentioned in ATENA) between the concrete (master) and bearing pad (slave) was used in order to connect the nodes from both elements to each other, by fixing the nodes to each other in X- and Y- direction.

11.3.4 Loading- and boundary conditions

The corbel is loaded by a uniform line displacement, contrary to the concentrated displacement modelled in the validation study. The uniform line displacement is modelled as an equally large vertical displacements on each node of the bearing pad, shown in Figure 11.6. At each load step a displacement of 0.0075 mm was added to every node.

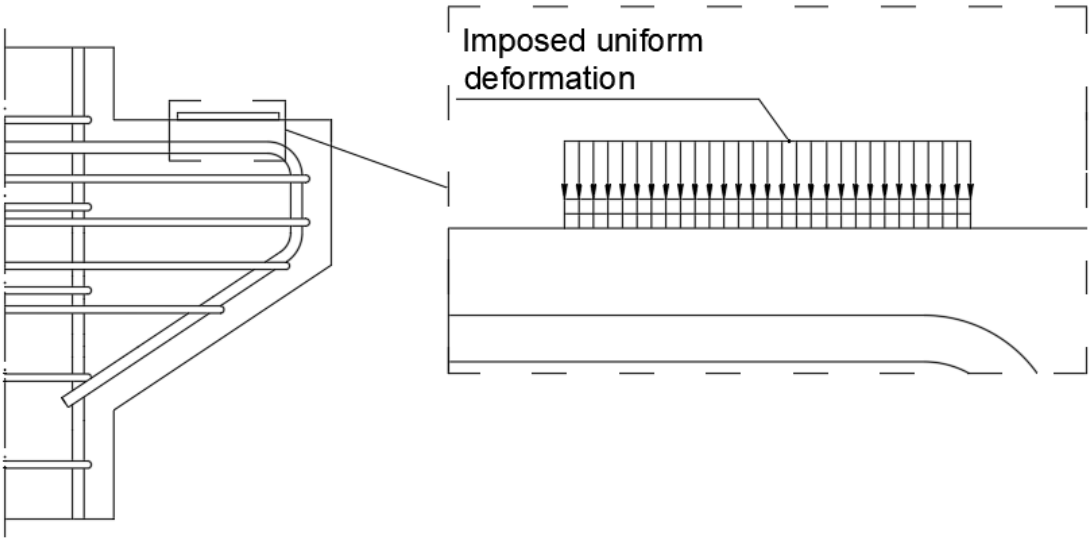

Figure 11.6 Loading conditions on the bearing pad.

The support conditions of the model are presented in Figure 11.17. The column is simply supported along the foot of the column in vertical direction. Additionally, it is horizontally restrained by a support at both the top and the bottom of the column.

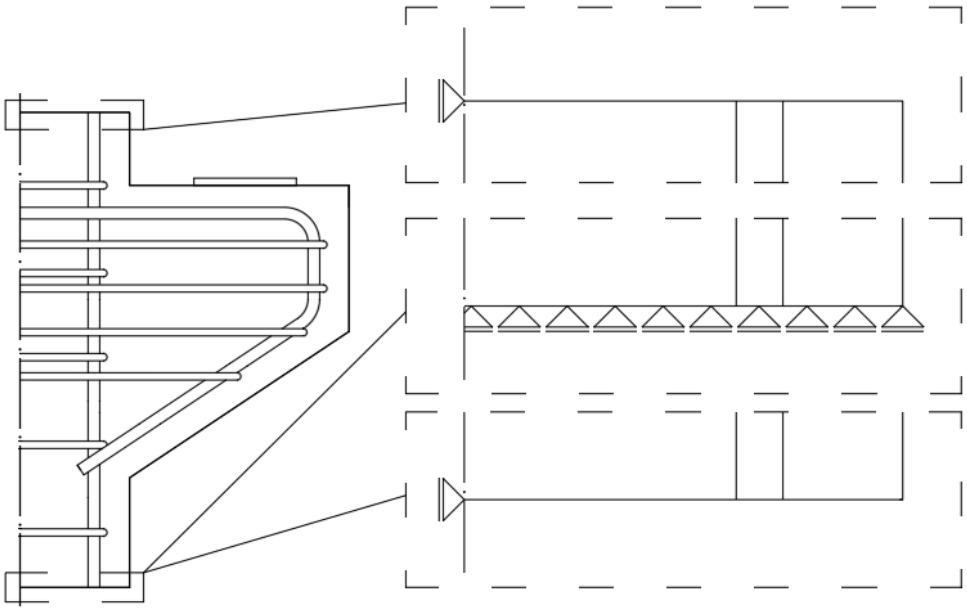

Figure 11.7 Support conditions of the column in vertical and horizontal direction.

11.3.5 Monitoring

In ATENA, several monitor points were used to observe the development of the reinforcement stresses in the tensile reinforcement and the stirrups at various vertical loads. The location of the monitors were iteratively determined by running an initial analysis of the corbel in order to distinguish the locations of the cracks. Based on the locations of the cracks, monitor sets were placed accordingly, whereafter the analysis was reconducted. Three cracks were distinguished during the analysis, resulting in three monitor sets, as shown in Figure 11.8. With the monitor points it is intended to analyse the stresses in the reinforcement crossing the cracks.

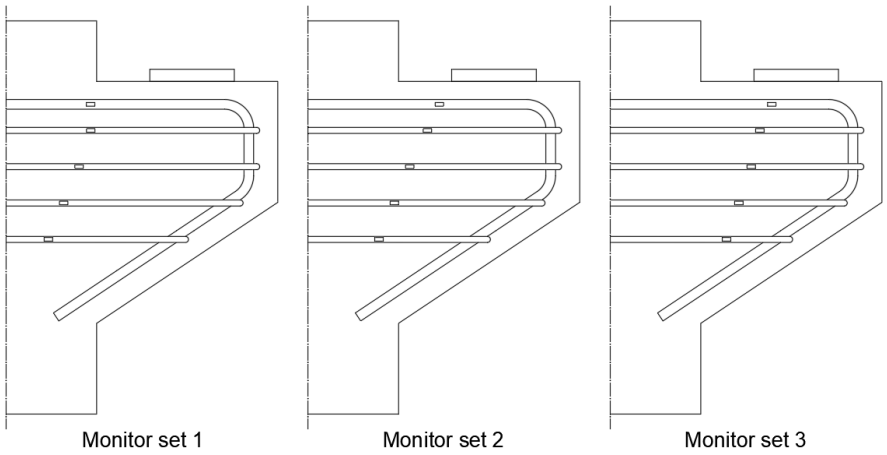

Figure 11.8 Locations of monitor sets in the numerical model.

Additionally, monitor points were placed below the middle of the bearing pad to monitor both vertical and horizontal displacements. Moreover, the vertical applied force was monitored by summation of the individual applied displacements on top of the bearing pad.

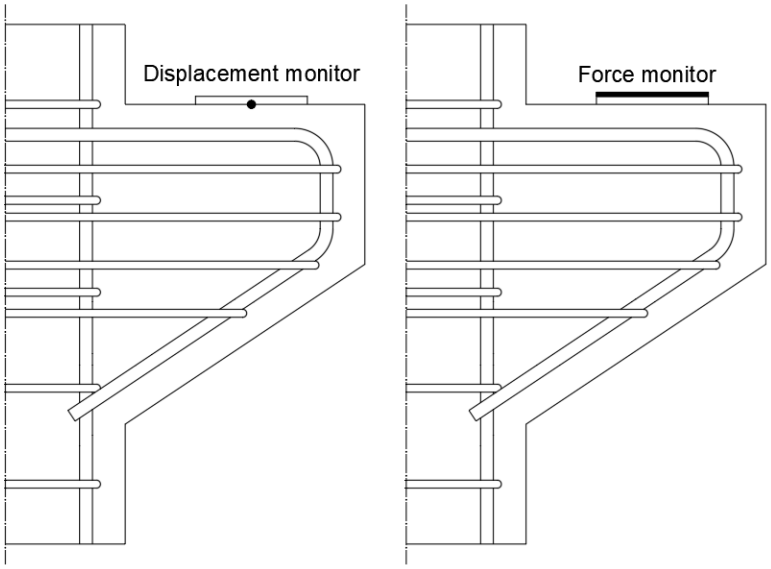

Figure 11.9 Displacement and force monitors.

11.4 Numerical results

The corbel was loaded until failure and its behaviour was analysed at several load steps. The corbel was designed for a vertical load of 400 kN. It failed at a maximum vertical load of 837 kN and 826 kN at the left and right bearing pad, respectively. The difference between the design load and capacity results from use of mean material properties in the numerical model, whilst the design load was calculated taking material reduction factors into account. The load-displacement (L-D) diagram for both bearing pads is presented in Figure 11.10.

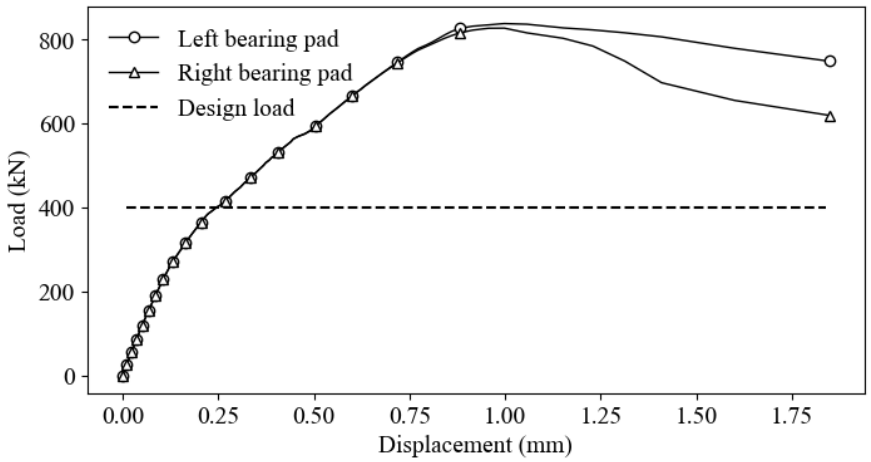

Figure 11.10 Load-displacement curve of the corbels, designed according to EC2.

A difference between the load on the left- and right support was observed in the L-D diagram both before- and after the maximum load. The difference starts at a vertical displacement of approximately 0.8 mm, which equates to a vertical load of 730 kN. At displacements larger than 1 mm a greater reduction load is measured on the right corbel compared to the left corbel. It indicates that the corbels behave in an asymmetric manner. A small asymmetric behaviour was also observed in the crack model in Figure 11.11, which displays the cracks with a calculated crack width larger than or equal to 0.05 mm. The asymmetry in the crack model is mainly found in the lower sections of the corbels, in which the left corbel shows three cracks compared to two cracks in the right corbel.

For numerical reasons, a crack does not have to occur exactly at the same instant. As soon as a crack arises on one side, the loading condition for the opposite side is directly different from the loading conditions at the side where the crack came first.

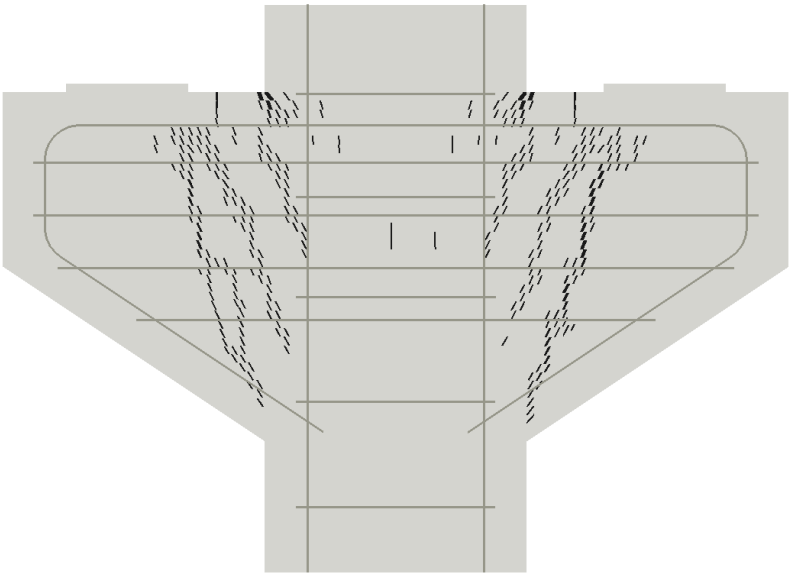

Figure 11.11 Crack model, with a minimum crack width of 0.05 mm, at a vertical load of 815 kN.

Three individual cracks were observed in the crack propagation during the numerical analysis. The crack propagation at various applied loads and the distinction between cracks are shown in Figure 11.12. In the following paragraphs the cracks are being referred to as crack 1, crack 2, and crack 3, and are described as follows:

1. Crack below the re-entrant corner;
2. Crack along the compressive strut of the corbel;
3. Second crack along the compressive strut.

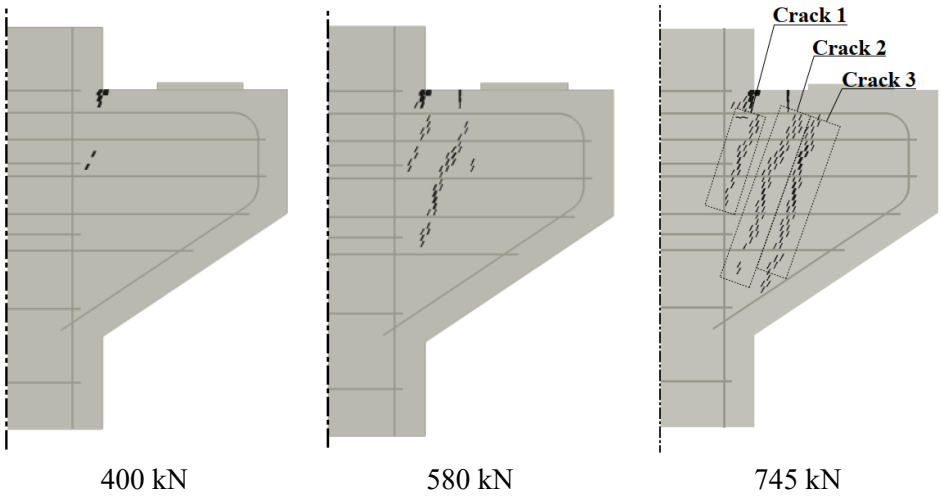

Figure 11.12 Development of cracks, with a minimum crack width of 0.05 mm, for various loads.

Crack 1 starts in the re-entrant corner between the corbel and the column element. Up to the design load of 400 kN hardly any cracks have formed in the corbel elements. Upon exceeding the design load, crack 1 increased in length followed by initiation of crack 2. At a vertical load of approximately 580 kN the initiation of crack 3 began. After further increasing the vertical load, the crack width enlarged until the corbel failed. In the following paragraphs, the crack development of the numerical analysis is elaborated in further detail.

Re-entrant corner

Initial cracking occurred at the re-entrant corner followed by propagation of crack 1, as shown in Figure 11.13. At a vertical load of 271 kN a maximum observed crack width was 0.04 mm, measured at the surface of the corbel. The crack propagated vertically, extending past the main reinforcement and stirrup 1. The crack width gradually decreases over the height of the crack, from top to bottom.

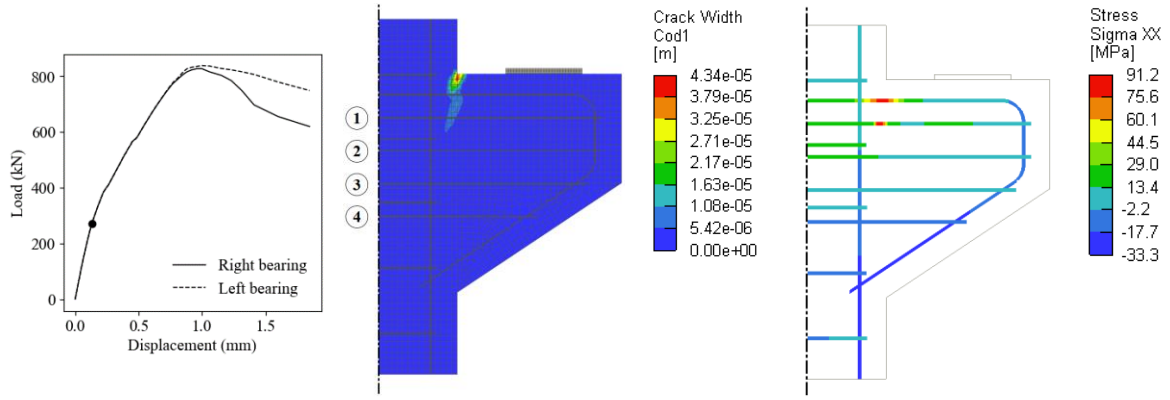

(a) (b) (c)

Figure 11.13 Load-displacement curve (a), crack width plot (b), and reinforcement stresses (c) at an applied vertical load of 271 kN.

The characteristics of the crack, meaning the decreasing crack width over its height, suggest that the crack is caused by bending. Moreover, for a bending initiated crack the highest stresses are expected to occur in the reinforcement closest to the surface. However, slightly larger strains are measured in stirrup 1 rather than in the main reinforcement (Figure 11.14). Furthermore, upon a more detailed inspection of the principal strains in the concrete corbel, it becomes apparent that the principal strain between the main reinforcement and stirrup 1 is larger than at either main reinforcement or stirrup 1. Therefore, it indicates that the crack at an applied load of 271 kN is not solely caused by bending. Even more so, one could argue that the crack can be divided into two parts: above and below the main reinforcement. Presumably, the crack above the main reinforcement is solely caused by bending, whilst the crack below the main reinforcement is not.

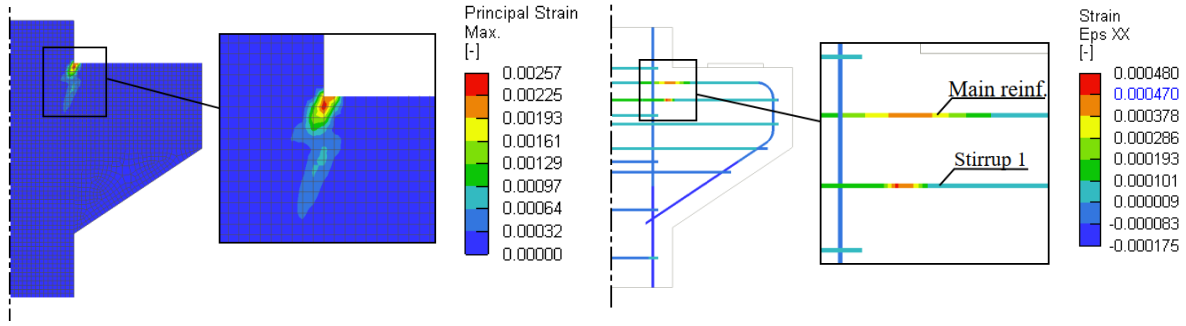

(a) (b)

Figure 11.14 Principal strains of concrete (a) and horizontal strains in reinforcement (b) at an applied vertical load of 271 kN.

In Figure 11.15, the development of the tensile stresses in the reinforcement measured by monitor set 1 is displayed. According to monitor set 1, the highest tensile stresses occur at the applied vertical load of 271 kN in the tensile reinforcement, followed closely by stirrup 1. This contradicts the previous plot of the horizontal strains in the reinforcement, which showed larger strains in stirrup 1. This can be explained by the positioning of the monitor points. The monitor points were manually placed along the cracks, based on an initial run of the numerical analysis, which may deviate slightly from the maximum stress at that crack. Therefore, a slight difference is found between the monitored reinforcement stress and the reinforcement strains.

Taking this into account, up to a load of 125 kN the stresses in the reinforcement gradually increase. Between a load of 125 kN and 225 kN a larger linear increase is observed in the main reinforcement. After a load of 225 kN, the reinforcement stresses in stirrup 1 increase at a higher rate than the main reinforcement.

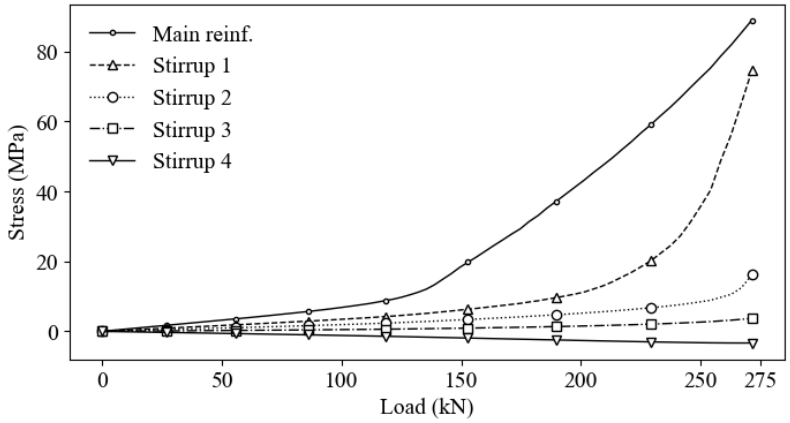

Figure 11.15 Development of reinforcement stresses in crack 1 up to an applied load of 271 kN.

For a purely bending initiated crack the increases in stress would develop at a similar rate, as the crack width for a bending initiated crack is linear over the height of the crack, as shown in Figure 11.16. This can be seen in the reinforcement development up to an applied load of 125 kN. Shortly after, the bending initiated crack intersects the main reinforcement, explained by the increase in stress of the main reinforcement. As the stress increases in stirrup 1 at a higher rate, it suggests a different cause. Thus, the crack is not solely initiated by bending, as previously suggested. Nevertheless, the largest tensile forces remain in the main reinforcement as the sectional area of the reinforcement is larger than the of the stirrups, as shown in Figure 11.16.

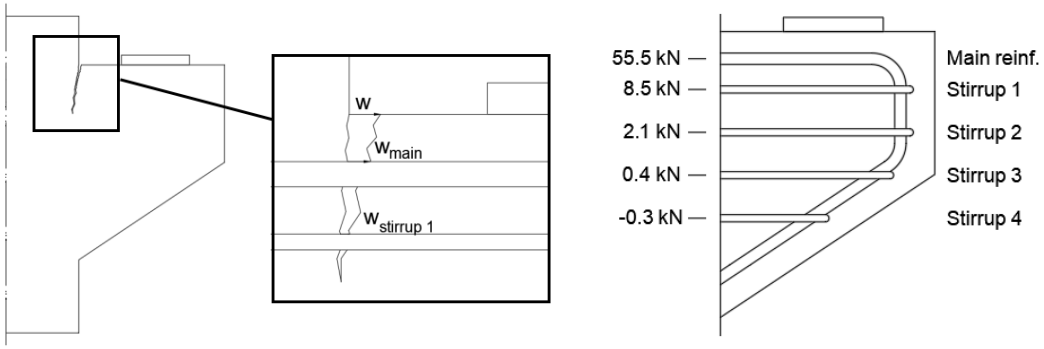

Figure 11.16 Schematisation of crack pattern for a bending initiated crack and the internal forces of the reinforcement for an applied vertical load of 271 kN.

Design load & crack 1

Once the design load of 400 kN was reached, crack 1 had increased in both length and crack width (Figure 11.17). A maximum crack width of 0.11 mm is observed at the re-entrant corner. Therefore, the corbel design meets the crack width limit prescribed by EC2 of 0.2 mm for chlorine environments. As mentioned, crack 1 increased in length intersecting both stirrup 1 and 2, resulting in further rise of the reinforcement stresses. The stresses in the reinforcement reached a maximum of 276 MPa, and thus remained below the yield stress.

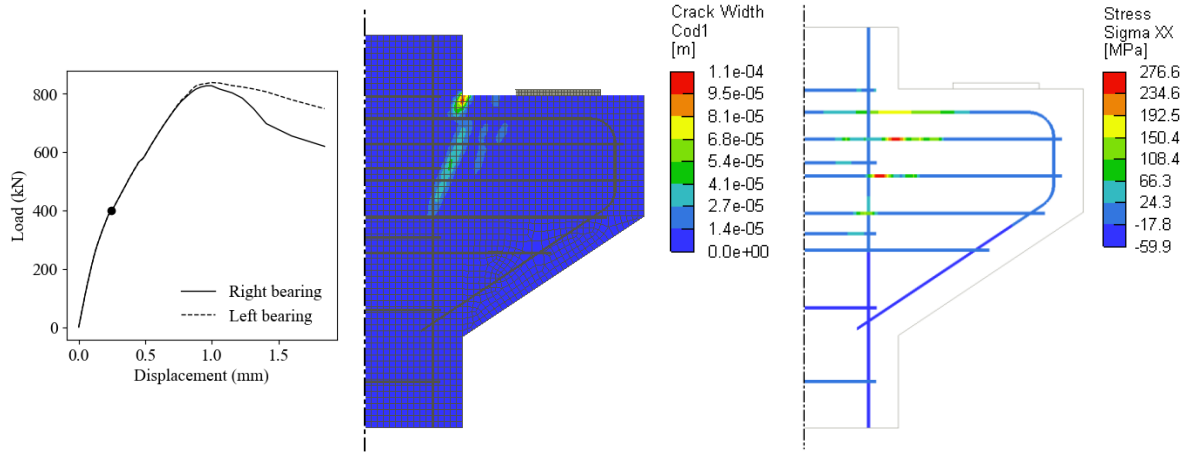

Figure 11.17 Load-displacement diagram (a), crack width plot (b), and reinforcement stresses (c) at design load of 400 kN.

Cracks along compressive strut

Upon increasing the vertical load on the corbel, crack 2 formed and propagated up to a vertical load of 575 kN, whereafter crack 3 developed until failure of the right corbel. The crack propagation of both cracks is displayed in Figure 11.18. At an applied vertical load of 575 kN crack 2 is completely developed. It starts between the main reinforcement and stirrup 1 and extends past stirrup 3. The maximum crack width of crack 2 at this applied load is 0.08 mm. After further increasing the load, crack 3 propagates in parallel direction to crack 2. At an applied vertical load of 745 kN the crack starts below the main reinforcement and extends past stirrup 4, as does crack 2.

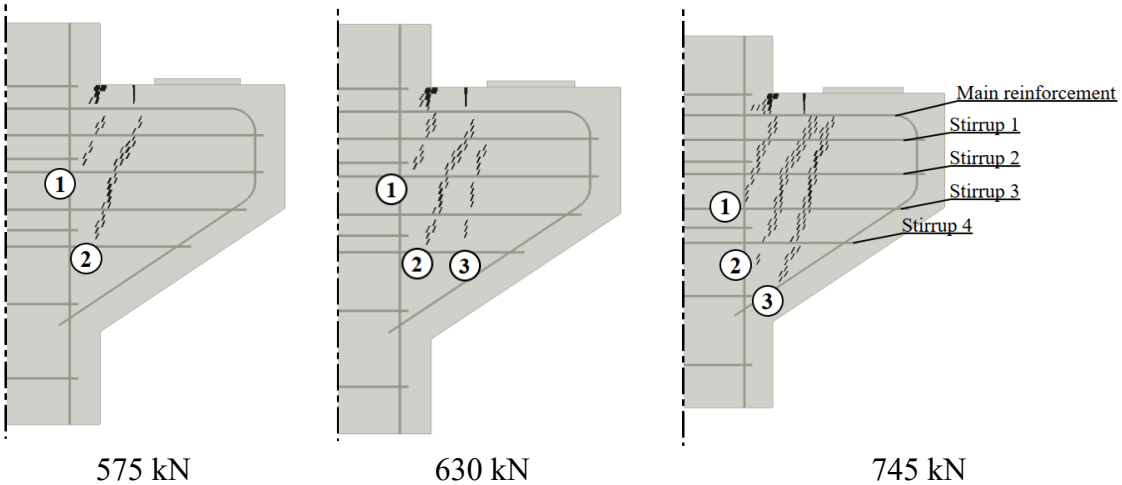

Figure 11.18 Crack propagation, of cracks larger than 0.05 mm. in the corbels at an applied vertical load of 575 kN, 630 kN, and 745 kN.

The load displacement diagrams for both vertical displacement and horizontal displacement are given in Figure 11.19. Up to the design load of 400 kN limited horizontal displacement is measured. Beyond the design load an increase in horizontal displacement is measured, explained by increase of the amount of cracks and crack widths.

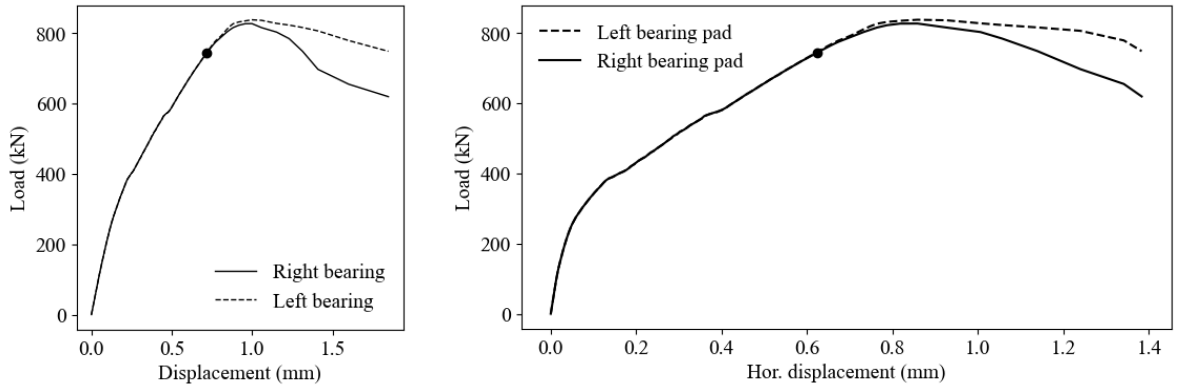

(a) (b)

Figure 11.19 Load - vertical displacement (a) and load - horizontal displacement (b) curves,.

Cracks 2 and 3 are probably initiated due to a sort of splitting failure of the compressive strut. The compressive strut is an inclined region which transfers compressive stresses from the applied load of the bearing pad to the column, schematised in Figure 11.20. The compressive axial stresses induce tensile stresses in transverse direction. Whenever the tensile capacity of concrete is exceeded, cracks occur.

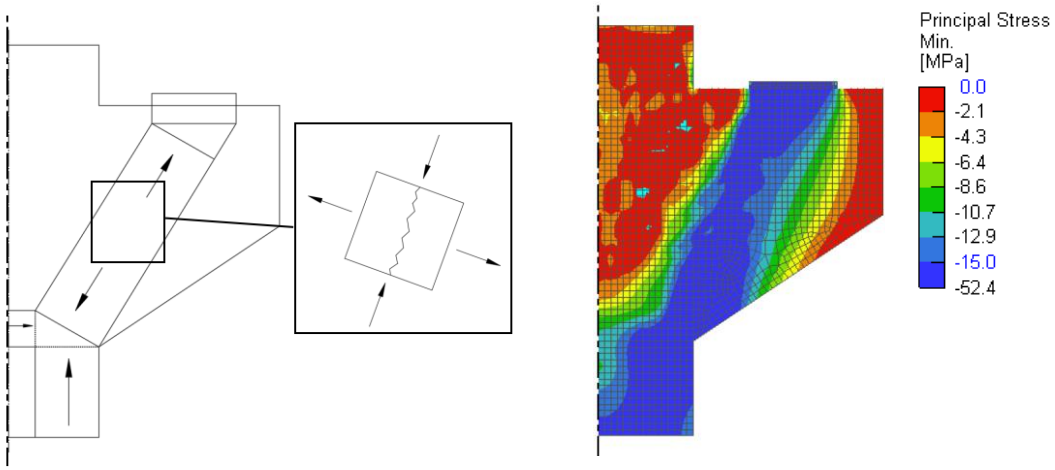

(a) (b)

Figure 11.20 Schematisation of cracking in compressive strut (a) and minimal principal stresses from the numerical model for vertical load of 745 kN (b).

In Figure 11.21, the crack model and corresponding reinforcement stresses are displayed for a vertical load of 745 kN. A small difference in crack propagation between the lower half of either corbels can be seen. The maximum crack width has increased to 0.35 mm, positioned at the re-entrant corner. Moreover, crack 3 became the consecutive largest crack with a width of 0.13 mm, situated between stirrups 1 and 3. Consequently, this led to the yielding of stirrup 2.

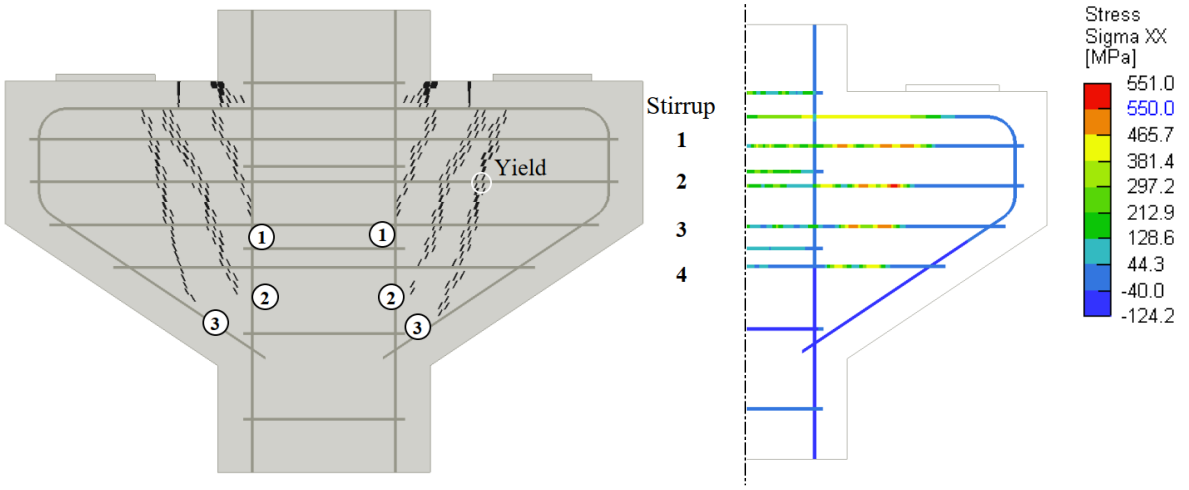

Figure 11.21 Crack model and reinforcement stresses at a vertical load of 745 kN.

Furthermore, the crack propagation is also reflected by plotting the reinforcement stresses of all cracks for an individual reinforcement element, as shown in figures 11.22 and 11.23. Both figures reflect a reduction in stresses once a new crack propagates in the corbel. In Figure 11.22 this phenomenon occurs at an applied load of 390 kN and 570 kN, in which the reinforcement stresses of stirrup 1 in crack 1 and 2 reduced. As the corbel reached its capacity, the stresses in the reinforcement at crack 3 is yielding.

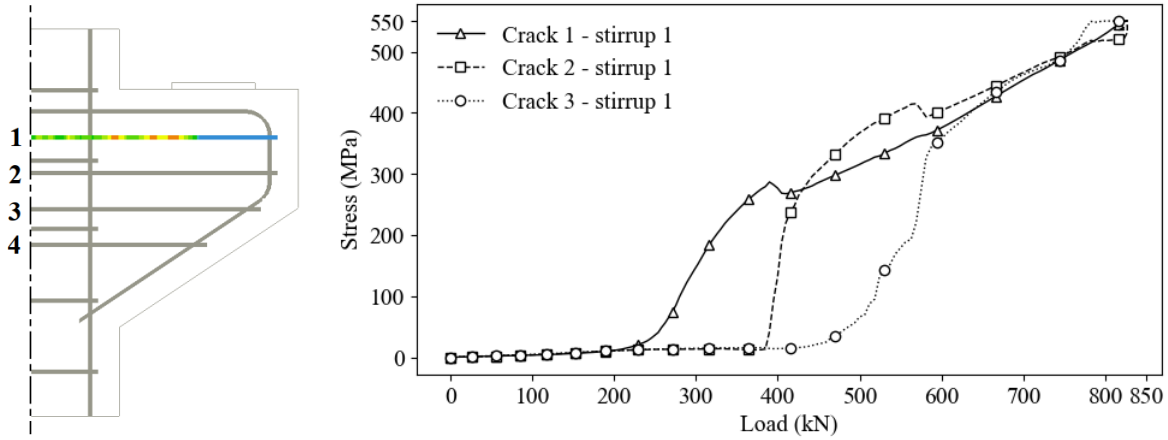

Figure 11.22 Development of stresses in stirrup 1 up to failure.

Similar behaviour is observed in the development of the stresses in stirrup 3, with some differences. A clear difference is shown in the development of the stresses in crack 1 after crack initiation of crack 2. Whilst the stresses in stirrup 1 gradually increased, the stresses in stirrup 3 remained almost constant with increased load. Furthermore, yielding is at crack 3 occurs at an applied load of approximately 750 kN.

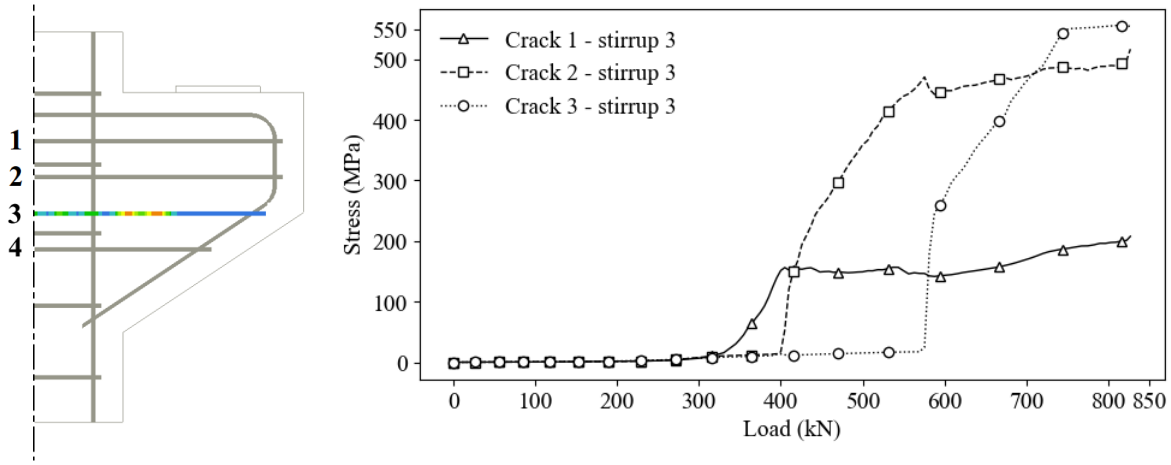

Figure 11.23 Development of stresses in stirrup 3 up to failure.

Finally, failure of the right corbel occurred at a vertical load of 826 kN. A detailed development of the failure is shown by three consecutive load steps in figures 11.24 and 11.25. Initially, the crack width in the top half of crack 3 increases, followed by an even larger increase in crack width at the bottom half of the corbel.

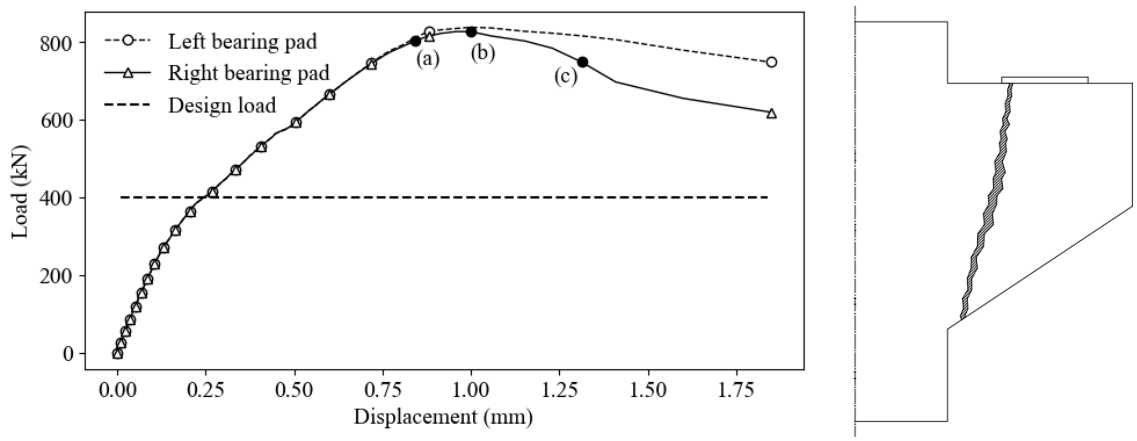

Figure 11.24 Load-displacement denotation of loads at 800 kN (a), 825 kN (b), and 748 kN (c), and depiction of failure crack.

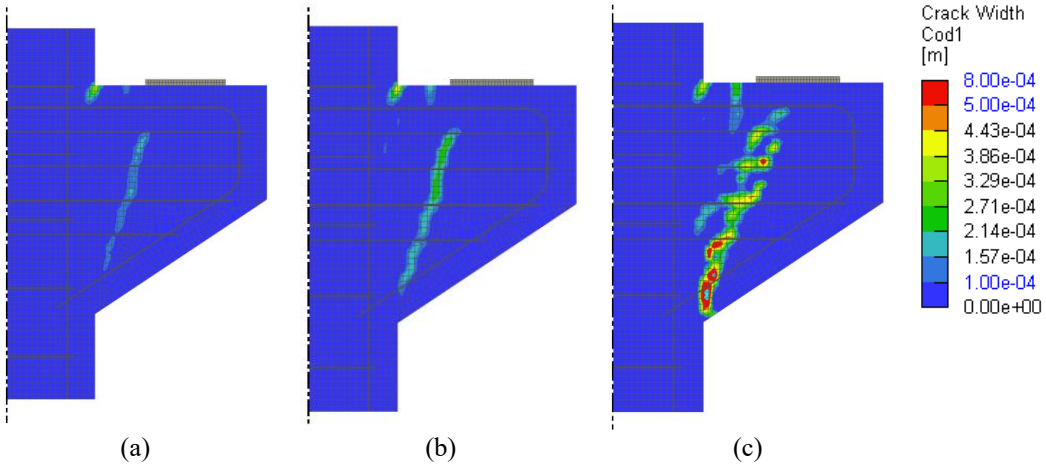

Figure 11.25 Consecutive crack width plot from a vertical load of 800 kN (a), 825 kN (b), and 748 kN (c).

Several assumptions made in the design of the corbel are examined. In the design of the corbel the strut-and-tie model (STM) was used over deep beam model (DBM). In these models, the compressive strut is generally schematised as a linear zone. In reality, however, the width of the compressive strut varies over its height, as shown in Figure 11.26.

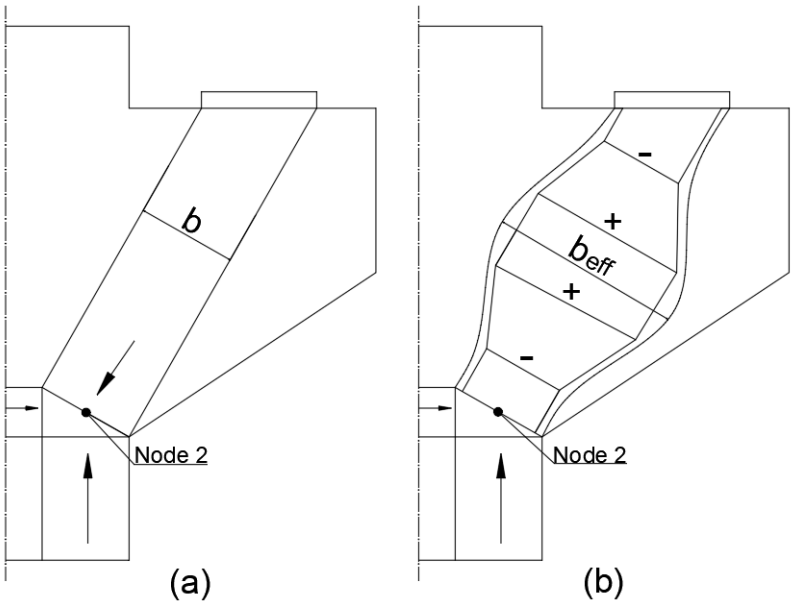

Figure 11.26 Schematisation of linear (a) and varying width (b) of compressive strut.

The increase in effective width of the compressive strut results in smaller compressive stresses. The difference between the STM and the DBM is essentially a larger internal lever arm. For the STM an internal lever arm of 0.9 times the effective height was used, versus 0.7 times for the DBM, which effectively led to less tensile reinforcement needed. In Figure 11.27, the locations of the internal lever arms and inclination of the compressive strut were schematized for both STM and DBM, overlaying a plot of the principal compressive stresses at design load.

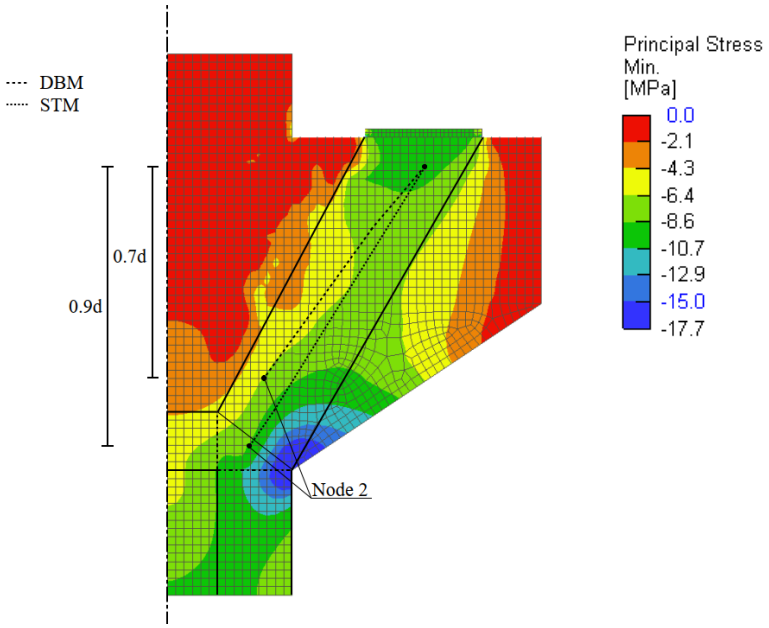

Figure 11.27 Locations of the nodes for STM and DBM over an underlying principal stress plot at design load of 400 kN.

In Figure 11.27, the compressive strut of the corbel is predominantly visible by the stresses smaller than -2.1 MPa. At both ends of the compressive strut the stresses are slightly higher than midway due to a different effective width of the compressive zone. The stresses in the corbel underneath the bearing pad found within a range of -8.6 MPa and 10.7 MPa, as shown in Figure 11.27.

The location of Node 2, for either STM or DBM, can be verified by the distribution of stresses. At Node 2 equilibrium of stresses is made by three compressive members: compressive strut, horizontal, and vertical component (Figure 11.28).

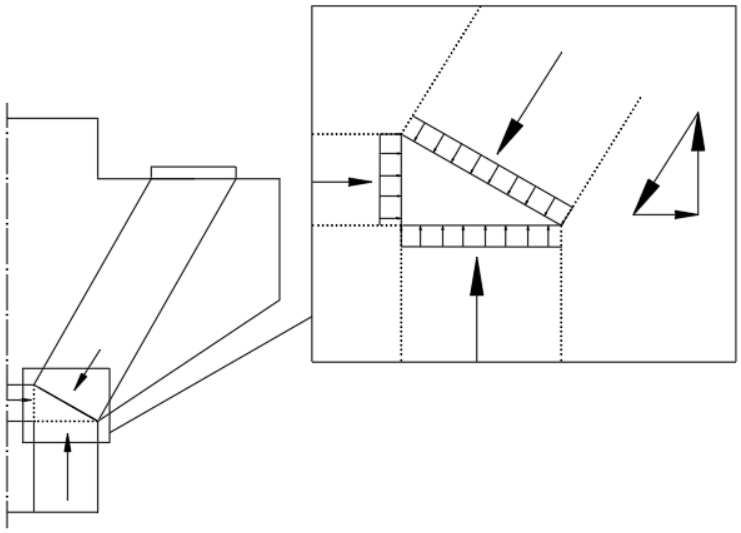

Figure 11.28 Schematisation of CCC Node 2.

By distinguishing the horizontal and vertical compressive components in the principal stress plot, the position of Node 2 according to the numerical model can be located. In figures 11.29 and 11.30, the vertical and horizontal stresses are plotted, which clarify these regions. The height of the horizontal compressive strut was estimated at 70 mm, based the majority of the horizontal stresses in Figure 11.29. The width of the vertical compressive strut was approximated at 150 mm, based on the results of Figure 11.30.

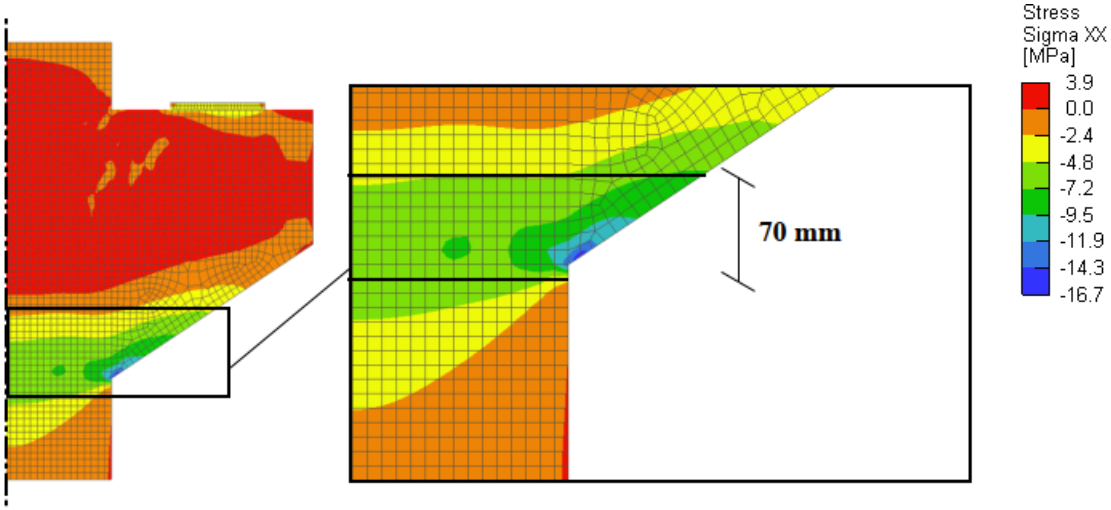

Figure 11.29 Horizontal stresses in the corbel at an applied load of 400 kN.

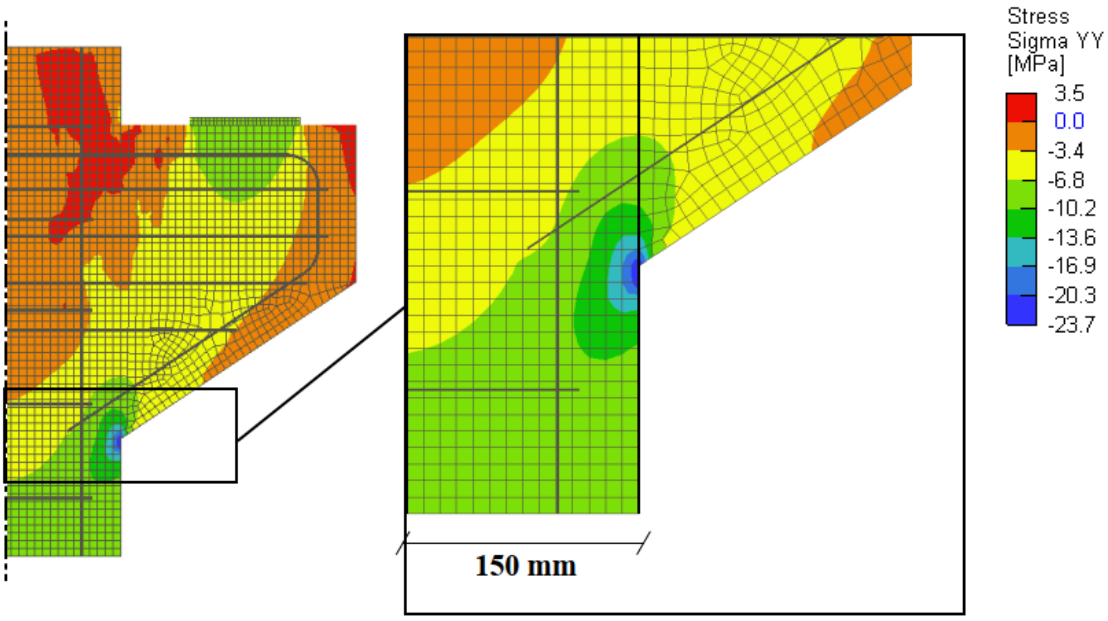

Figure 11.30 Vertical stresses in the corbel at an applied load of 400 kN.

The height of the horizontal compression member and width of the vertical compression member at Node 2 was calculated at 62 mm and 100 mm, respectively. These results differ only marginally from the results as obtained by the numerical model. Therefore it is concluded that the design according to the strut-and-tie model is sufficient.

Subsequently, the assumption of a uniform vertical stress distribution by using a elastomeric bearing pad is verified. The vertical stresses in the bottom of bearing pad are presented in Figure 11.31. The vertical stress at the bottom of the bearing is largely within the range of -9.3 MPa and -9.7 MPa. By dividing the design load of 400 kN by the surface area of the bearing pad (300x140 mm^2), a vertical stress of -9.5 MPa is obtained. The stress in the lower corners of the bearing pad is slightly higher than the uniform distribution. This can be explained by the deformation of the bearing pad, which is slightly more deformed at the corners of the bearing pad, due to soft nature of an elastomer. In effect, this causes the larger stresses at the corners of the elements.

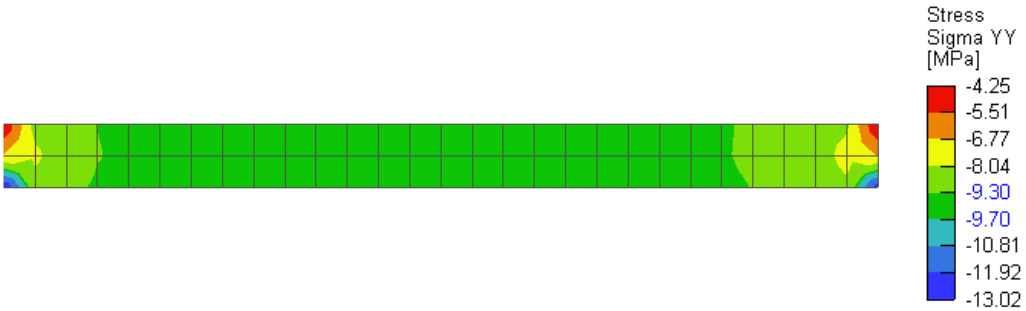

Figure 11.31 Vertical stresses in bearing pad at an applied vertical load of 400 kN.

12 Numerical study of support end failure

12.1 General

In order to study the behaviour of the support end failure into further detail, a number of parameters of the corbel and support configuration as used in Chapter 11 were changed. This exploratory study is performed with the intention to achieve a better understanding on the behaviour of the support end failure. Moreover, it could possibly distinguish the individual contribution of the design parameters, answering sub-question 2.2. Two numerical studies are performed to study these changes. In Section 12.2 the first numerical study was performed, in which the bearing pad was placed on the edge. In the second numerical study the bearing pad was placed on the edge and additionally loaded in horizontal direction (Section 12.3).

12.2 Influence of position and dimensions of bearing pad

12.2.1 Corbel configuration

To study the influence of the bearing pad positioning, the bearing pad was moved to the edge of the corbel. This resulted in the corbel configuration as shown in Figure 12.1, referred to as specimen A. No further adaptations were made to other design parameters, boundary conditions, material properties, or the numerical model. Further elaboration on these topics is provided in Chapter 11.

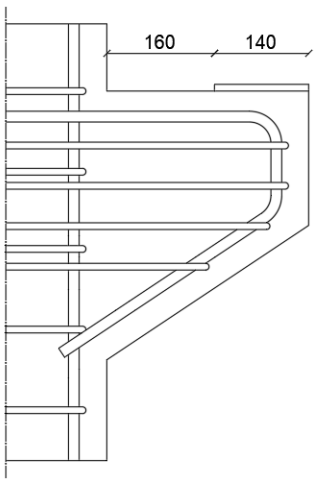

Figure 12.1 Schematised configuration of specimen A, dimensions in mm.

By placing the bearing pad on the edge of the element the bending moment, acting on the corbel, is enlarged. Consequently, at a smaller applied load a larger bending moment is induced. Therefore, one can expect crack propagation at a smaller applied load. Moreover, due to the larger bending moment it might induce vertical cracks along the surface of the corbel.

12.2.2 Numerical results - specimen A

The corbel was loaded until failure and its behaviour was analysed at several load steps. In Figure 12.2, the L-D diagram and crack model at an applied load of 623 kN are displayed. The corbel failed at an applied load of 616 kN and 623 kN at the left and right bearing pad, respectively. Even though it exceeded the design load of 400 kN, failure occurred before reaching the capacity of the original design of 826 kN.

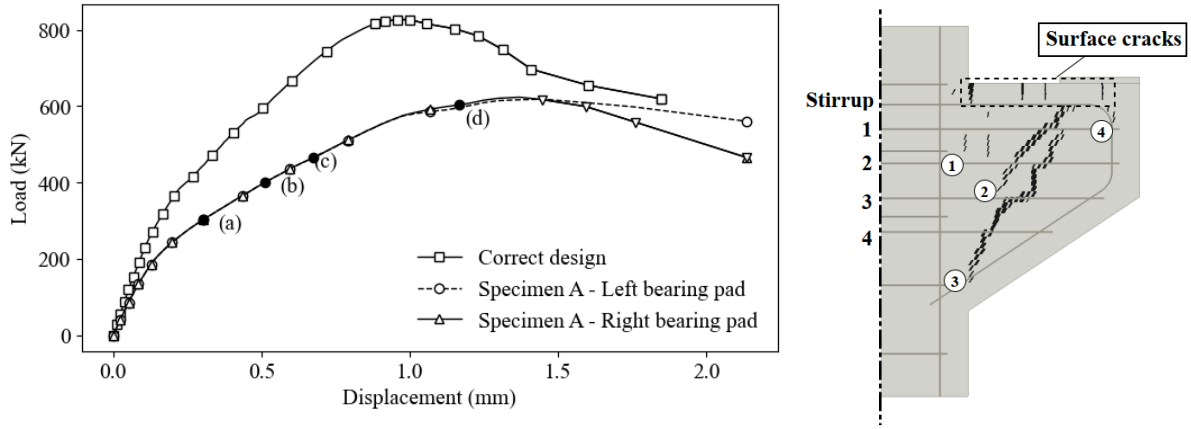

Figure 12.2 Load-displacement diagram and crack model at an applied load of 623 kN, minimum crack with of 0.01 mm.

The crack development at various load steps is presented in Figure 12.3. Initial cracks occurred in the re-entrant corner at an applied load of 180 kN, whereafter it vertically extended to stirrup 2. After increasing the load to 300 kN ((a) in Figure 12.3), a vertical crack propagated at the surface of the corbel denoted as surface cracks. At a slightly higher load, crack 2 initiated at an applied load of 360 kN.

At the design load of 400 kN ((b) in Figure 12.3), cracks 1 and 2 were present in the corbel. The maximum crack width at design load was 0.14 mm, measured at the re-entrant corner. Therefore, it remained below the crack width limit of 0.2 mm for chlorine environments as prescribed by EC2. Nevertheless, specimen A performed worse compared to the original situation, in which crack 2 had not yet propagated and crack 1 had a significantly smaller crack width of 0.01 mm.

Up to an applied load of 457 kN ((c) in Figure 12.3), cracks 1 and 2 increased in both crack width and length. Shortly after, at 464 kN, crack 3 occurred between stirrups 1 and 2. It extended up to the main reinforcement and below the stirrup 4 until 603 kN ((d) in Figure 12.3).

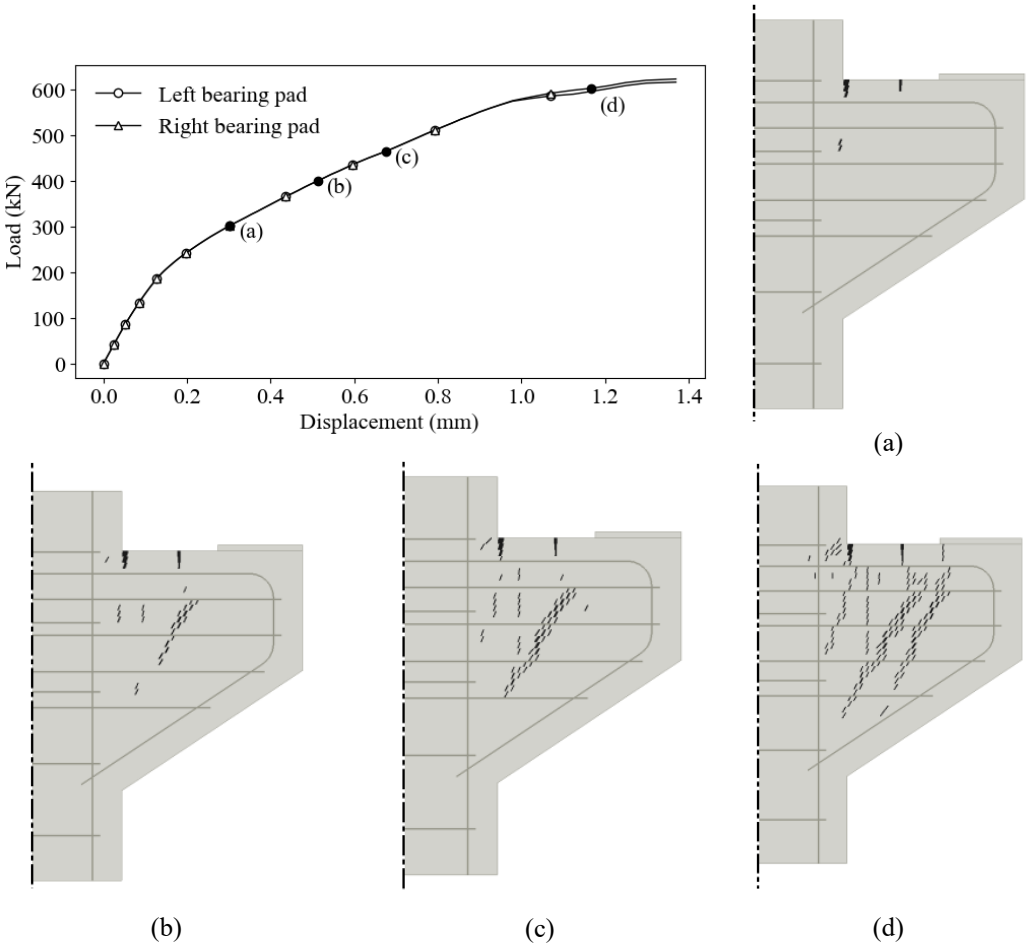

Figure 12.3 Load-displacement denotation and development of cracks, with a minimum crack width of 0.05 mm, at 300 kN (a), 400 kN (b), 457 kN (c), and 603 kN (d).

Difference in capacity between the original design and specimen A can be related from the change in dimensions. The increased lever arm between bearing pad and column is the most important change. The bending moment at the interface between column and corbel is increased. As far as design in concrete the corbel schematisation changed from a short cantilever to a long cantilever, as per EC2 annex J.3. The difference between short and long cantilever is the requirement for additional vertical stirrups. Nevertheless, the capacity of the corbel still exceeds its design load, due to the use of mean material strength.

The crack propagation of the specimen A shows similarities to the original design. Crack 1 occurs at the re-entrant corner, followed by cracks 2 and 3 along the compressive strut. Although, changing the location of the bearing pad lead to several differences. First of all, several vertical cracks formed at the surface of the corbel, extending to the main reinforcement. These cracks are presumably initiated by the increase of the bending moment, as a result of a larger lever arm. Moreover, the inclination of cracks 2 and 3 is more diagonal than in the original design. As the bearing pad was placed further from the column, the compressive stresses results in higher horizontal force for the same vertical load. This can only be accomplished if the inclination of the compressive strut becomes shallower. As cracks 2 and 3 are caused by some sort of splitting, due to tensile stresses perpendicular to the compressive stresses, the inclination of the cracks alter.

The tensile stresses in the reinforcement are provided for the same load steps as the crack development, in Figure 12.4. The grey areas signify stresses lower than 0 MPa and the marked areas as yielding.

As stated before, the crack propagation increased in specimen A comparatively to the original design. Consequently, larger tensile stresses are observed in the reinforcement. No significant changes in behaviour of the reinforcement are observed in the stresses of the reinforcement up to an applied load of 457 kN ((b) in Figure 12.4), besides its enlargement. However, at an applied load of 603 kN ((d) in Figure 12.4), several differences are found. First of all, the reinforcement has yielded in the stirrups, whereas the stresses in the bend of the main reinforcement have increased along its length, whereas this section was loaded in compression before.

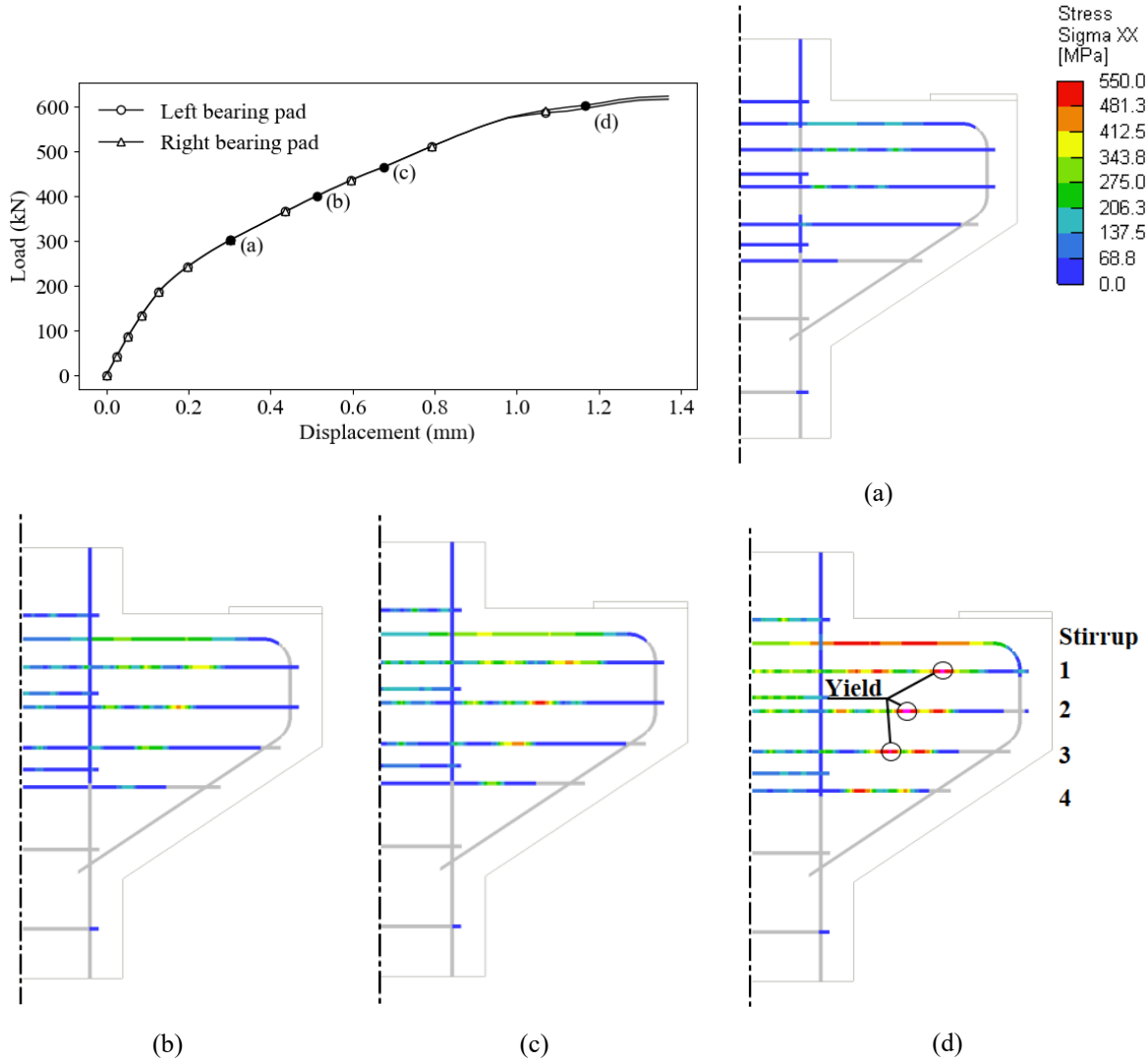

Figure 12.4 Reinforcement stresses at 300 kN (a), 400 kN (b), 457 kN (c), and 603 kN (d).

When the applied load reached 608 kN ((d) in Figure 12.4), initiation of the support end failure is observed in both corbel elements. The first cracks formed at the height of the main reinforcement, in vertical direction below the centre of the bearing pad. As the load reached respectively 623 kN and 616 kN at the right and left bearing pad, the crack extended to the surface of the corbel in vertical direction and along the bend of the main reinforcement in downwards direction (Figure 12.5). The crack width of the support end failure measured at 0.1 mm.

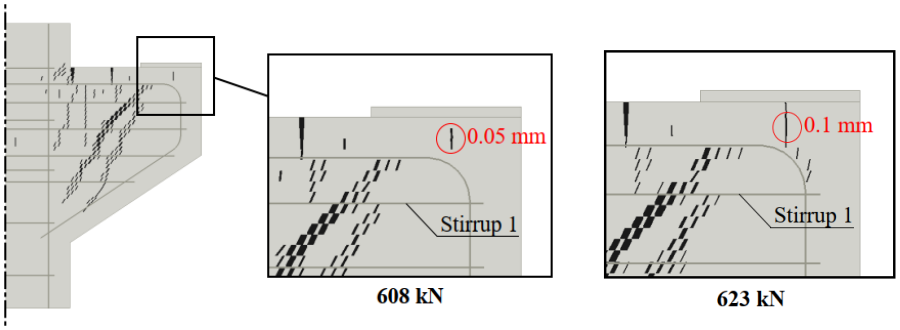

Figure 12.5 Development of the support end failure cracks at 608 kN (left) and 623 kN (right).

Though, at 623 kN the maximum capacity of the corbel was reached, cracks 2 and 3 increased in crack width, which lead to primary failure by splitting of the compressive strut (Figure 12.6). Slight increases were noticed in the crack propagation of the support end failure. The cracks extended past stirrup 1 up to stirrup 2. Although, the corbel failed before the support end failure could develop any further. Therefore, it was concluded that under the investigated situation the support end failure mechanism does not occur. In order to provide more insight, adjustments were made to the design.

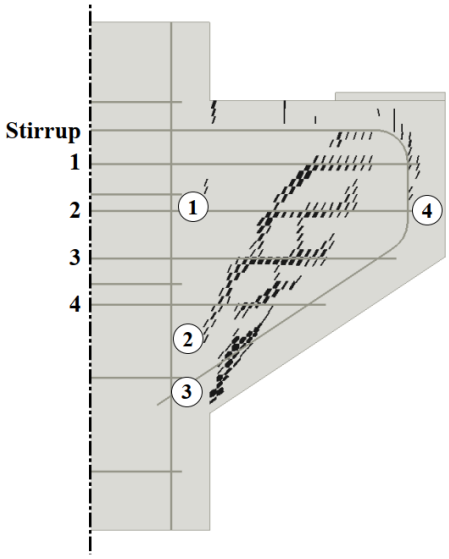

Figure 12.6 Crack model, with a minimum crack with of 0.01, of the corbel at 597 kN after failure of the corbel.

12.2.3 Adjusted corbel configuration

In the adjusted corbel configuration the length of the bearing pad length was reduced to 70 mm, shown in Figure 12.7. Since the load is introduced in the unreinforced zone (cover) the support end failure is expected to occur. The corbel configuration with the shortened bearing pad is referred to as specimen B.

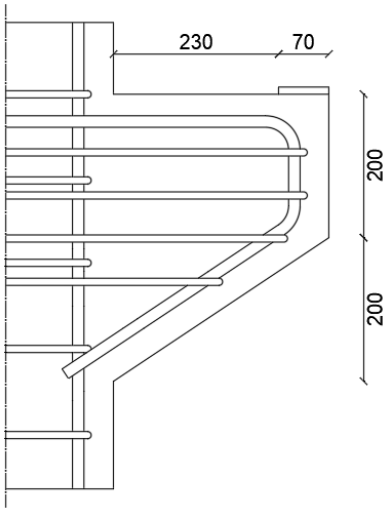

Figure 12.7 Schematised configuration of specimen B, dimensions in mm.

12.2.4 Numerical results - specimen B

The L-D diagram of the design conform EC and specimens A and B are presented in Figure 12.8. The bearing capacity of the specimen B was measured at 372 kN, considerably lower than the capacity of the original design of 826 kN and specimen A of 623 kN.

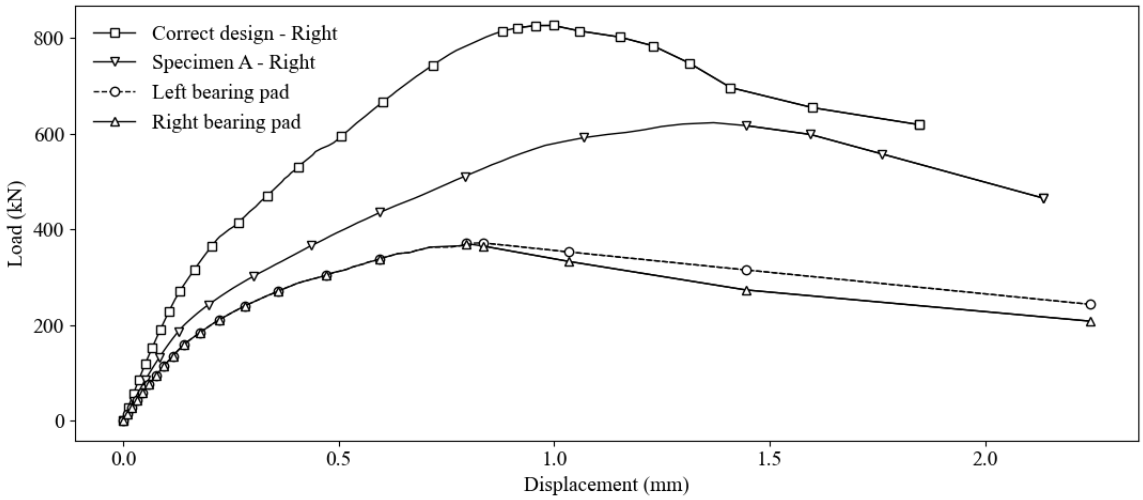

Figure 12.8 Load-displacement diagram of specimen B.

In Figure 12.9, the crack development in the corbel is presented for various vertical loads. At an applied load of 288 kN ((a) in Figure 12.9), vertical cracks occur along the re-entrant corner and at the surface of the corbel. Upon increasing the load to 303 kN ((b) in Figure 12.9), propagation of an inclined crack along the compressive strut is observed, denoted as crack 2. Moreover, a vertical crack initiates besides the bearing pad. After further increase to 338 kN ((c) in Figure 12.9), a second crack forms along the compressive strut, labelled as crack 3.

Cracks indicating the support end failure, with a crack width of 0.01 mm, occurred at an applied load of approximately 307 kN. The initiation of the support end failure arguably starts at an applied load of 351 kN. This is further elaborated in the following paragraphs. The support end failure cracks developed until 365 kN ((d) in Figure 12.9), at which failure of specimen B occurred.

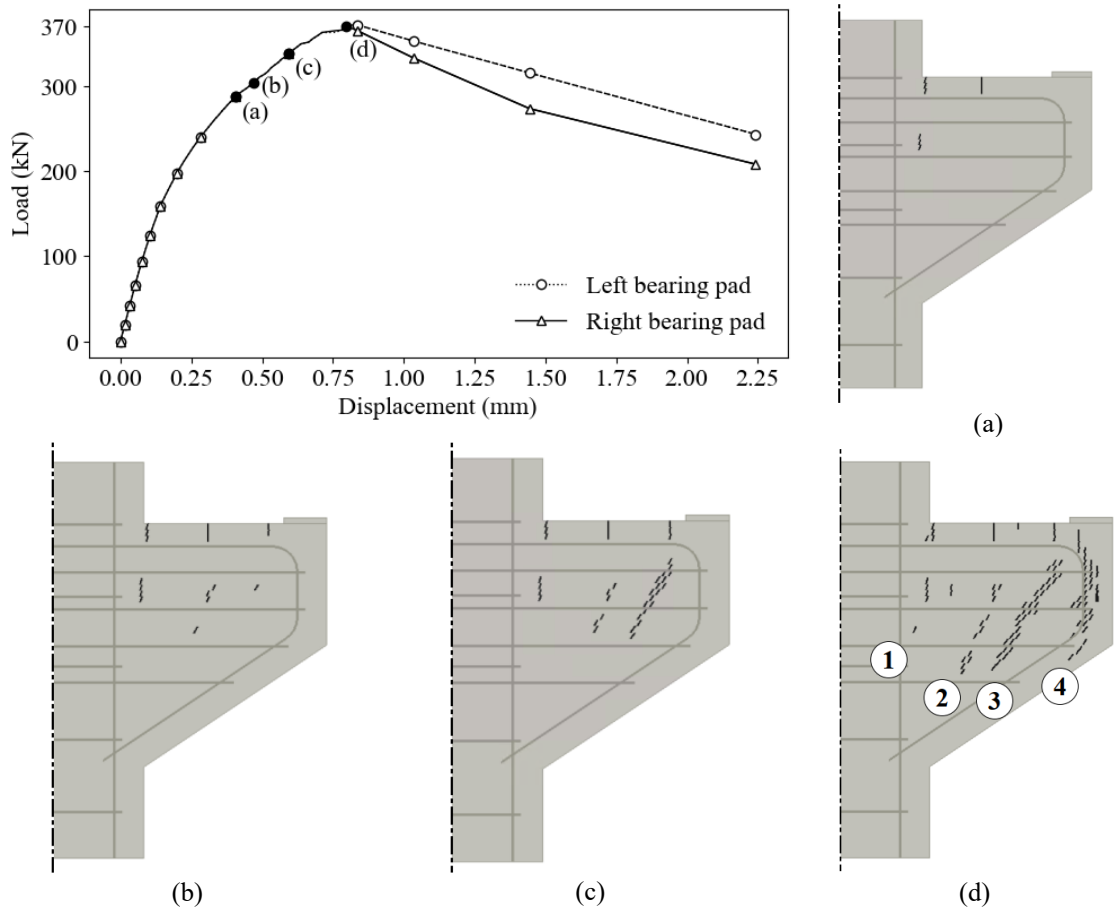

Figure 12.9 Development of cracks, with a minimum crack width of 0.05 mm, at a vertical applied load of 288 kN (a), 303 kN (b), 338 kN (c), and 365 kN (d).

The observed crack development for specimen B is relatively similar as for the specimen A. The main differences are found in the load range in which cracks 2 and 3 occurred and a complete representation of the support end failure. For specimen B, cracks 2 and 3 developed between an applied load of 303 – 362 kN, whereas these developed in a larger range for specimen A (360 – 616 kN). This is presumably caused by the increase lever arm. As a result, cracks 2 and 3 initiated a lower applied load. The development of the tensile stresses in the reinforcement, up to an applied load of 370 kN, are presented in Figure 12.10.

Similar as before, the grey areas indicate stresses lower than 0 MPa and the yield in the reinforcement is marked. The stresses in the reinforcement did not exceed yield strength before failure of the corbel. Up to an applied load of 300 kN the stresses in the reinforcement behaved as observed in specimen A. As the applied load reached 313 kN, tensile stresses increased along the upper bend in the main reinforcement. The stresses continued to increase along the main reinforcement in downward direction as the applied load increased. Right before failure occurred, the tensile stresses extended to the lower bend in the main reinforcement, as seen in corbel (d) of Figure 12.10.

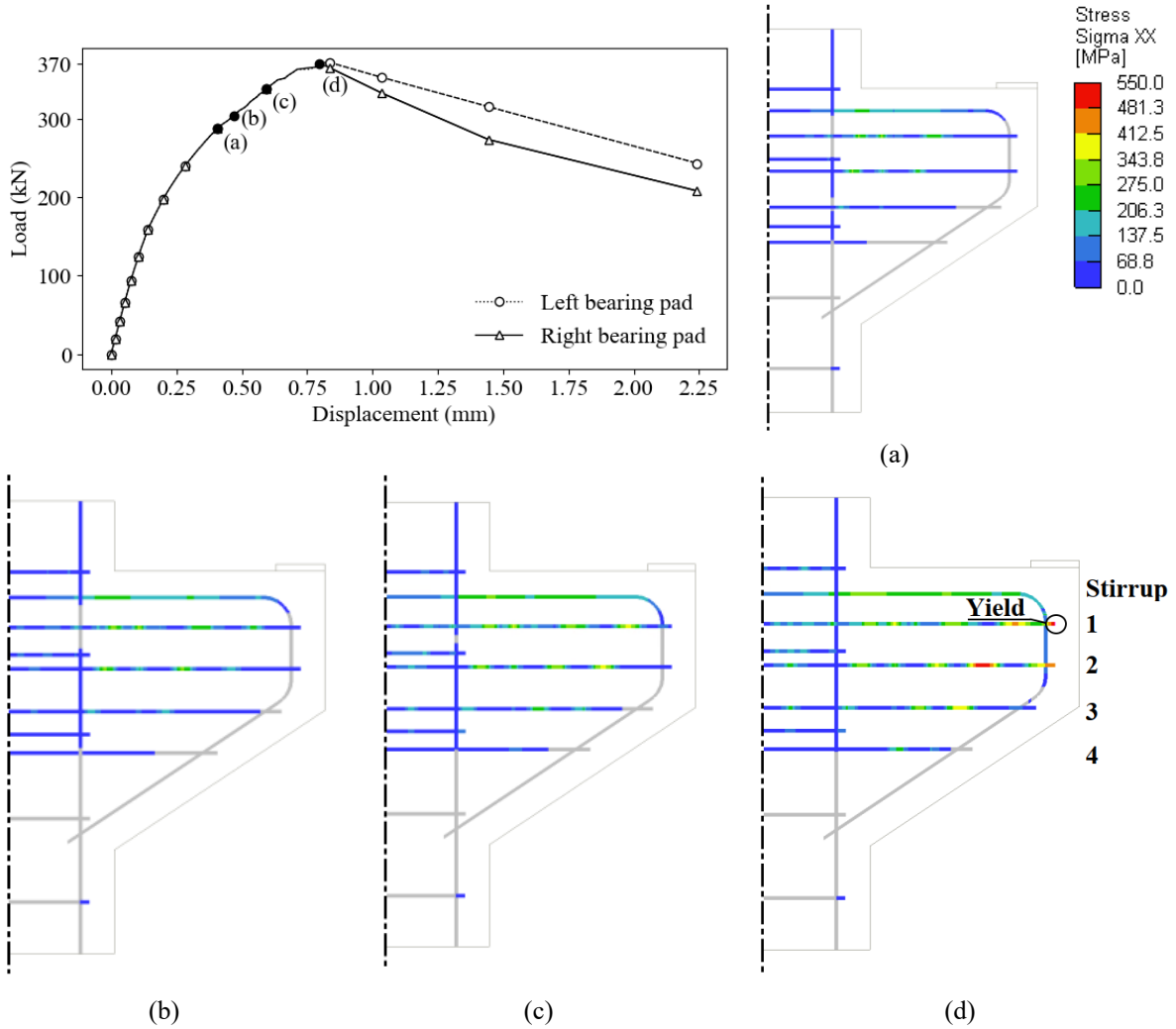

Figure 12.10 Stresses in the reinforcement at a vertical applied load of 288 kN (a), 303 kN (b), 338 kN (c), and 365 kN (d).

Support end failure

An indicative overview of the development of principal tensile strains of the support end failure mechanism is provided in Figure 12.11. The behaviour of the support end failure mechanism is categorised into four stages:

a) Initial cracks
b) Initiation
c) Failure
d) Post-failure development

In the following paragraphs, the behaviour of the support end failure is elaborated at each stage. The initial cracks occur at an applied load of 307 kN ((a) in Figure 12.11) , followed by initiation at 351 kN ((b) in Figure 12.11). The measured limit of the corbel is reached at 371 kN ((c) in Figure 12.11), whereafter a fully developed support end failure is observed at 166 kN ((d) in Figure 12.11).

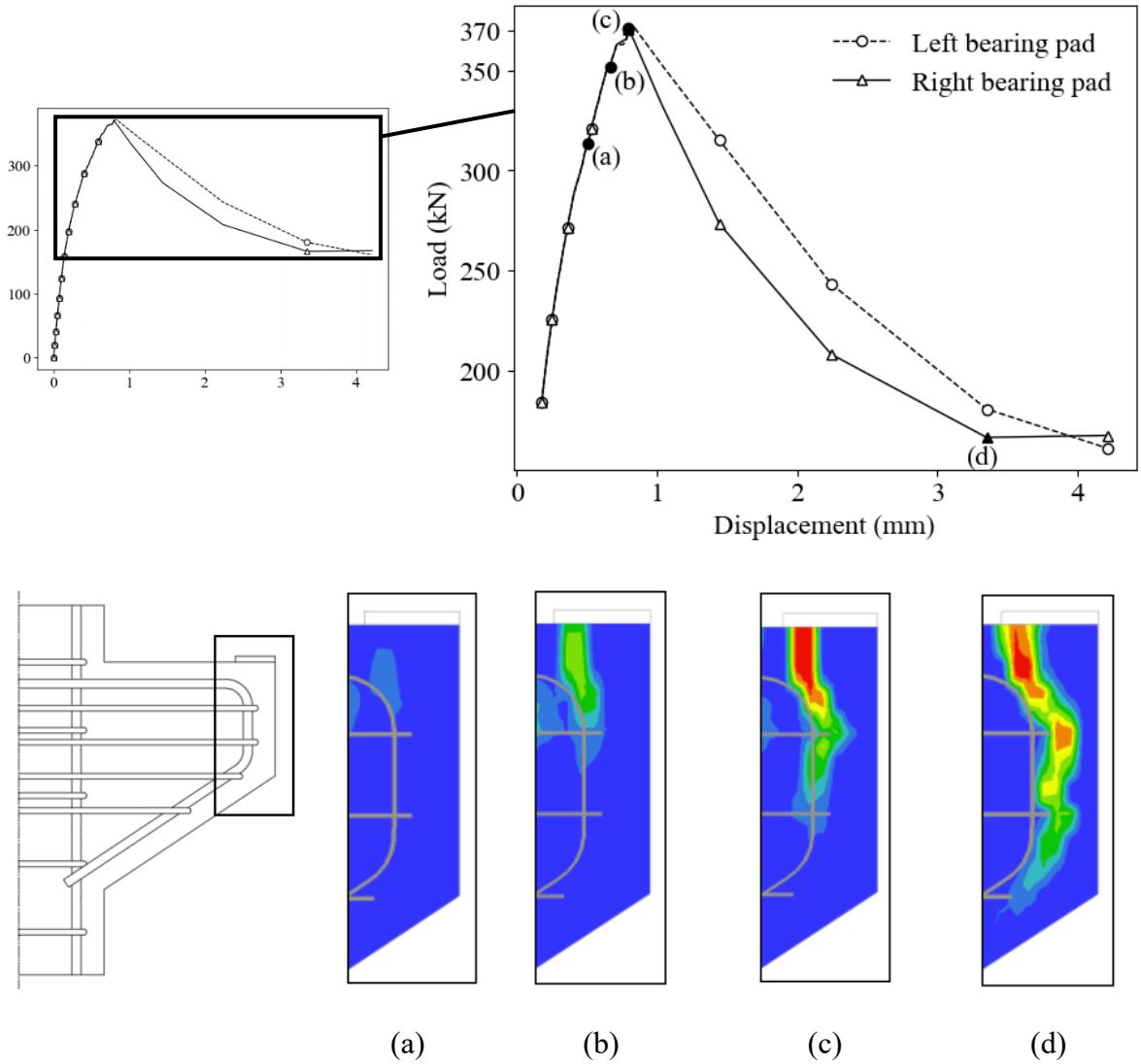

Figure 12.11 Development of support end failure indicatively shown by principal tensile strains, at 307 kN (a), 351 kN (b), 371 kN (c), and 166 kN (d).

(a) Initial cracks

The first crack, with a crack width equal or larger than 0.01 mm, of the support end failure in the corbel was observed at an applied vertical load of 307 kN. The initial crack is located at the height of the main reinforcement. After increase of the applied load, the crack extended vertically in upward direction and along the main reinforcement in downward direction (Figure 12.12). At the consecutive two load steps after 307 kN, respectively 314 kN and 339 kN, the tensile stresses gradually increased downwards in the bend of the main reinforcement (Figure 12.13). These stresses arise as result of the development of the support end failure cracks.

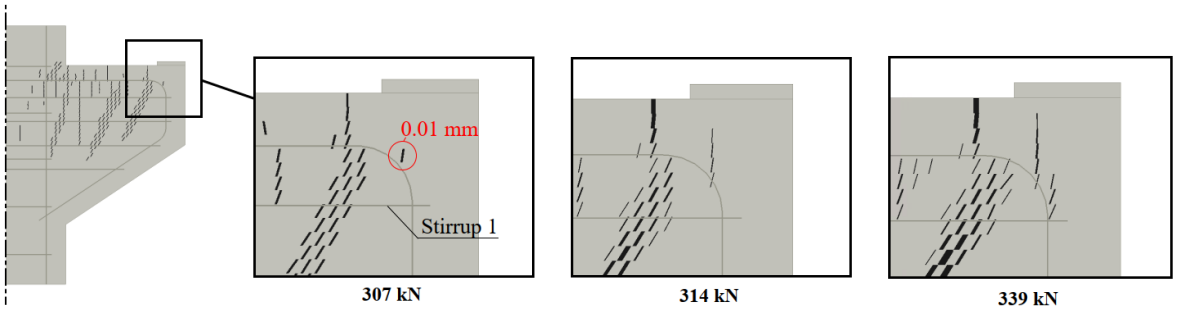

Figure 12.12 Initiation and development of support end failure at various applied vertical loads, displayed by a crack model with minimum crack width of 0.01 mm.

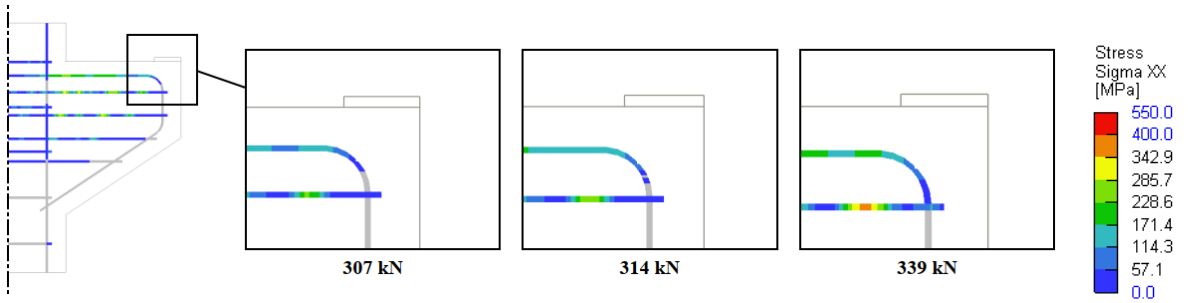

Figure 12.13 Development of tensile stresses in the bended section of the main reinforcement at various load steps.

One could question as to why the initial cracks occur at the height of the main reinforcement. This can be explained by the principal stress distribution between bearing pad and concrete element. The principal stress trajectories and horizontal stress distribution are drawn in Figure 12.14 for a uniformly loaded concrete element with a stiff bearing pad.

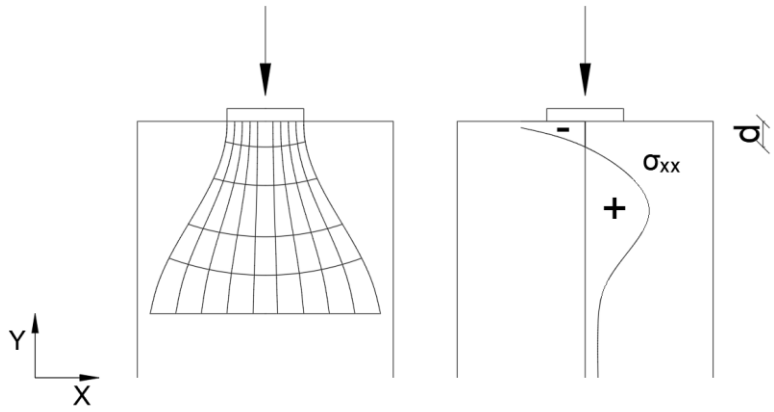

Figure 12.14 Principal stress trajectory and horizontal stress distribution of a uniformly loaded concrete element (Leonhardt, 1977).

The vertical compressive stresses gradually disperse from the bearing pad over the larger concrete element. Perpendicular to the vertical stress trajectories span horizontal stresses, denoted as σ_{xx}. At the initial depth below the bearing pad the horizontal stresses are in compression due to confinement of concrete. Beyond depth “d”, the tangential stresses change from compression to tension. Eventually, a maximum tensile stress is reached at a certain depth.

The situation for the corbel is slightly different as the bearing pad is placed on the edge of the element. Since the bearing pad is placed on a free edge, the stresses cannot disperse in both directions. Nevertheless, the results of the numerical model can provide further insight into the behaviour (Figure 12.15). In Figure 12.15, tensors of the principal tension stresses are shown at an applied load of 274 kN. The tensors in pink represent a tensile stress larger than the mean tensile capacity of the concrete, which resulted in cracking in the consecutive load step.

Contrary to the previously mentioned theory, tensile stresses are observed below the right half of the bearing pad, at the upper surface of the corbel. The stresses closest to the free edge show higher tensile stresses. At a larger depth, the principal tension stresses diminish to 0 MPa. Reason for the tensile stresses directly at the surface are due to the lack of confinement from surrounding concrete. This also explains the increase in tensile stresses closer to the free edge, as there is less concrete resisting these stresses.

Moreover, the horizontal stresses measured below the left half of the bearing pad are in compression. These are not displayed in the graph as the tensors are filtered to solely tension. The compressive stresses continue up to 10 mm below the left half of the bearing. After reaching this depth the horizontal stresses gradually increase in tension until the location of crack initiation, as shown in Figure 12.12. Downwards from this tensor the tensile stresses gradually decrease again, which shows that the behaviour underneath the left half of the bearing pad matches the mentioned theory. Therefore, it explains as to why the support end failure crack initiated at the height of the main reinforcement.

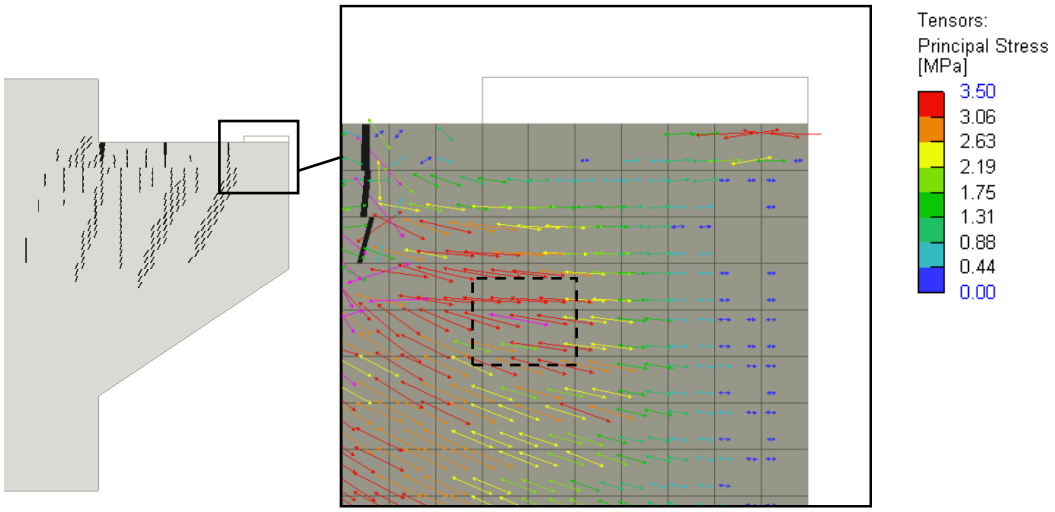

Figure 12.15 Tensors of principal tension stresses of integration points at an applied load of 274 kN.

(b) Initiation

The crack propagation as shown in Figure 12.12 provides a good indication of the initiation of the support end failure cracks, the crack width is very minimal. A noticeable increase occurs at a vertical load of 351 kN, at which the principal tensile strains abruptly increase from 2.6% to 5.7% (Figure 12.16). Similar results are observed in the crack width, which doubled from 0.02 mm to 0.05 mm.

At 349 kN, the maximum principal strain was measured directly besides the main reinforcement, which gradually decreased across the neighbouring area. Upon increasing the load to 351 kN, the principal strain spanned from the surface of the corbel until stirrup 1.

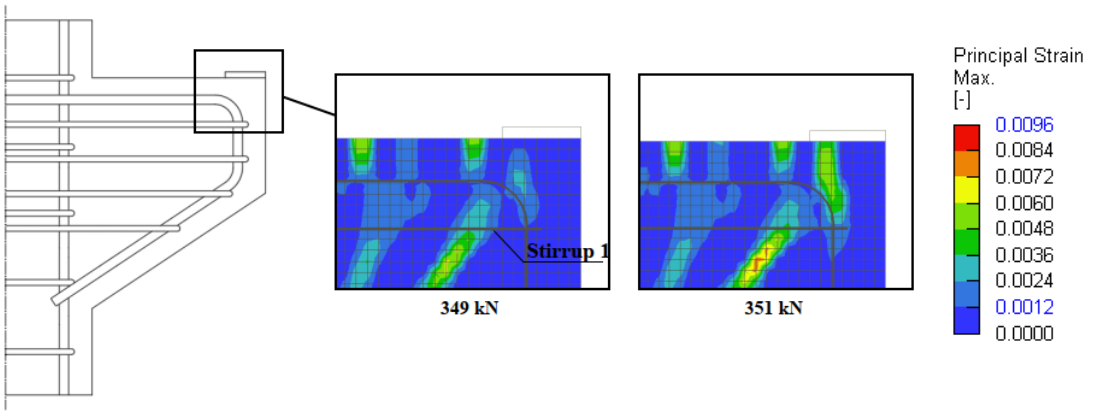

Figure 12.16 Abrupt increase in principal tensile strains between applied load of 349 kN and 351 kN.

It is worth considering whether the direction of the crack is logical. The crack spans in vertical direction from the top surface of the corbel up to the main reinforcement. A crack occurs in concrete if the principal tension stresses are exceeded. The corresponding angle of the crack is always perpendicular to the inclination of the principal tension stresses, or parallel to the direction of the principal compression stresses. Thus, by investigating the principal compression stresses in the corbel, the crack direction can be verified.

The principal compression stresses in the corbel at an applied load of 274 kN are displayed in Figure 12.17. The direction of the principal compression stresses below the bearing pad is almost in exact vertical direction, thus explaining the vertical crack initiation.

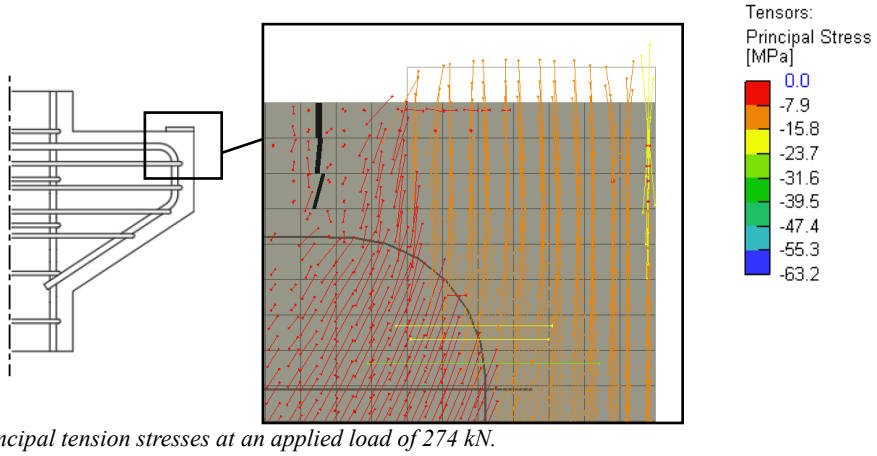

Figure 12.17 Principal tension stresses at an applied load of 274 kN.

(c) Failure

Upon reaching the capacity of specimen B at 371 kN, the support end failure extended to stirrup 2. The principal strain development showed the characteristic support end failure behaviour, by cracks along the outline of the stirrups and main reinforcement (Figure 12.18).

The largest principal strain developed at the surface of the corbel and decreased over its depth. Between the surface of the corbel and the main reinforcement, the principal strains span in vertical direction. As they reach the main reinforcement, it changes into an inclined direction in order to move along stirrup 1. As the strains pass stirrup 1, it moves back along the surface of the main reinforcement.

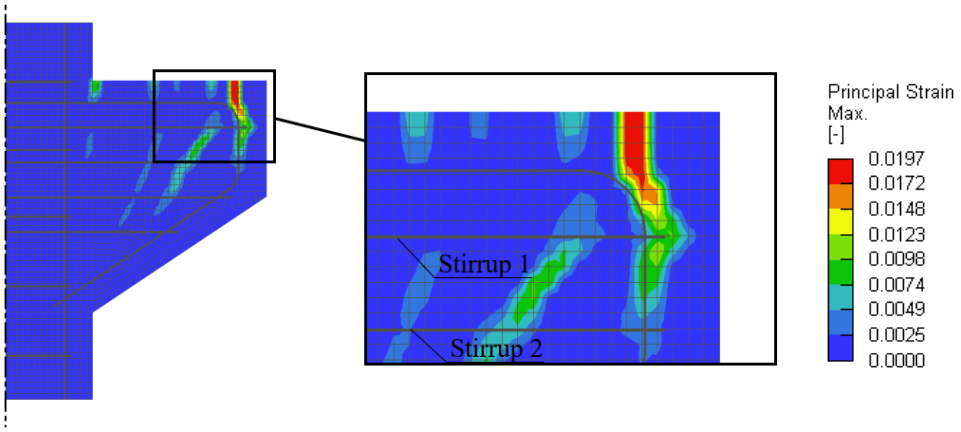

Figure 12.18 Principal strain at an applied vertical load of 371 kN.

Previously it was observed that the initial support end failure cracks caused an increase in tension in the bend of the main reinforcement. In Figure 12.19, the tensile reinforcement stresses are presented at an applied load of 371 kN. The maximum stresses measured in the reinforcement are just below yield, with the maximum stresses occurring in stirrup 3. Furthermore, tensile stresses increased along the vertical section of the main reinforcement, extending past stirrup 2. Besides, the stresses in the areas of the stirrups nearing the support end failure cracks, increased significantly.

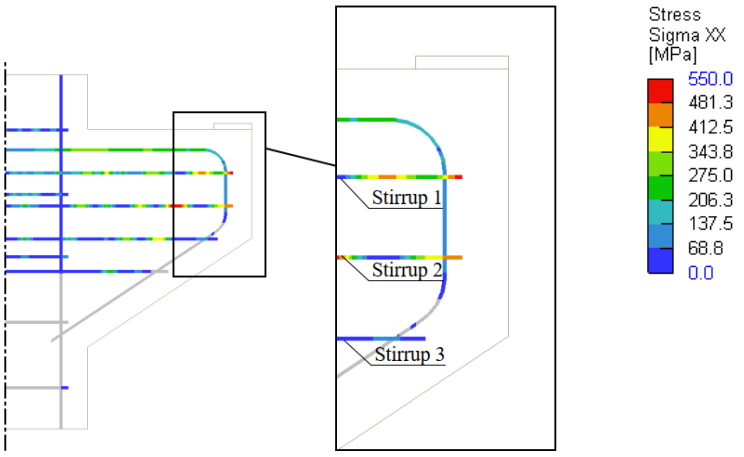

Figure 12.19 Reinforcement stresses at an applied load of 371 kN.

The propagation of the support end failure cracks resulted in the vertical section of the main reinforcement to function as tensile reinforcement, whilst this was first inactive. As the crack developed further downwards, a larger portion of the main reinforcement is transformed to tensile reinforcement, which may lead to an insufficient anchorage length. One might expect that instead of the vertical failure plane an inclined failure plane may occur, as presented in Figure 12.20.

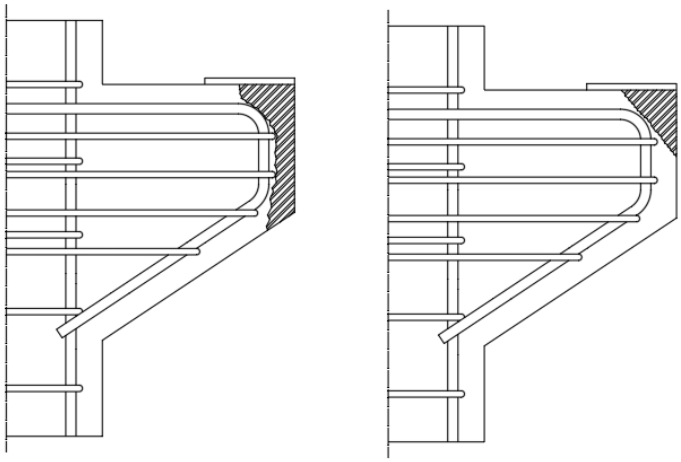

(a) (b)

Figure 12.20 Potential failure planes of support end failure.

By further examining the principal stresses more insight into the crack propagation is provided. The principal compression stresses at the applied loads of 328 kN, 351 kN, and 371 kN are presented in Figure 12.21. The tensors at the initial crack stage, 328 kN, are uniformly distributed below the bearing pad, followed by progression into the inclined compressive strut. At the initiation stage, the vertical crack is more pronounced, as it increased in both length and width. The tensors on both sides of the crack remain uniformly distributed in downwards direction. Although, the stresses of the tensors beside the crack increase, which is even more apparent at the limit point stage, 371 kN.

Barely any stresses can be transferred through an existing crack. As the crack increases in vertical direction, the path of the principal strain tensors at the right side of the crack become disrupted. As reaction, the tensors continue in downward direction in order to transfer the stresses to the compressive strut. By doing so, the crack develops further in vertical direction. This process repeats itself during the entire support end failure mechanism until the bottom of the corbel is reached.

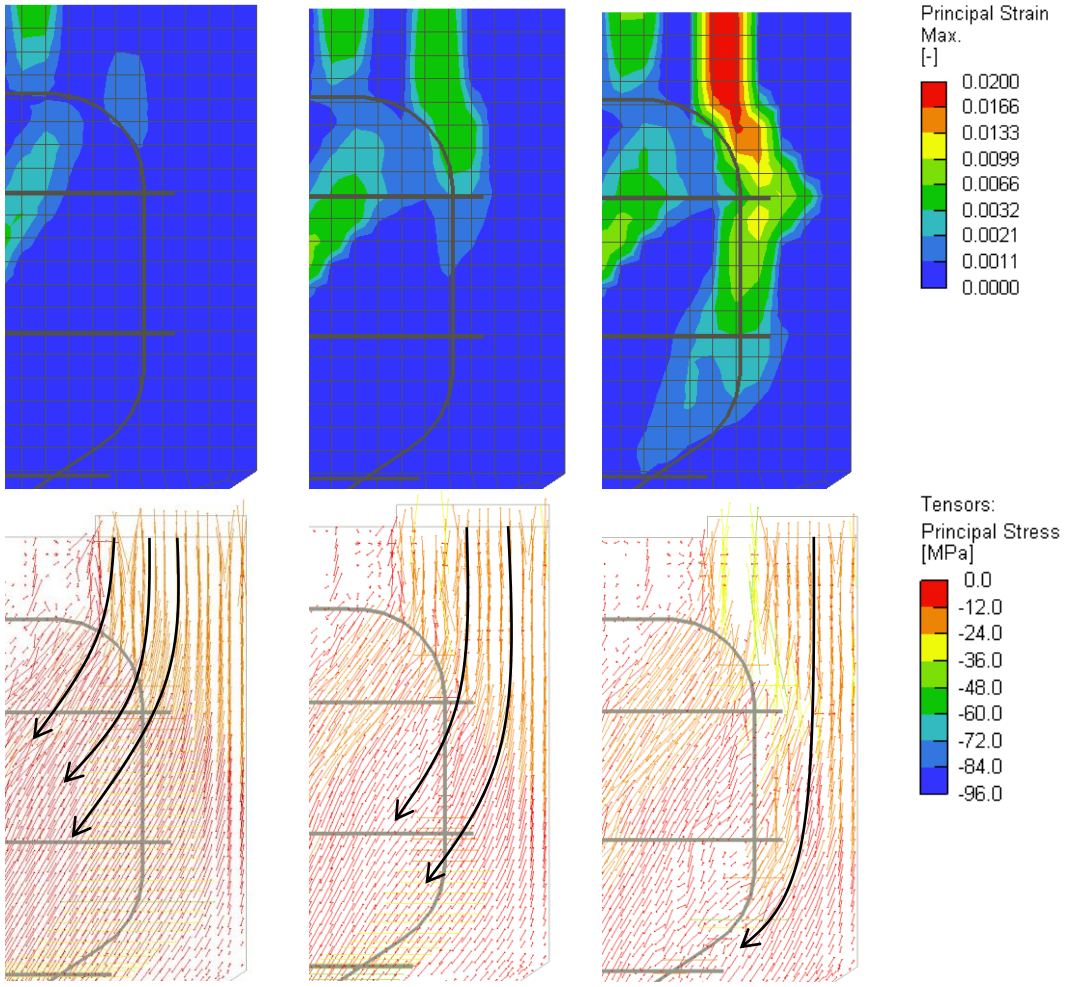

(a) (b) (c)

Figure 12.21 Evolution of principal strains and principal compression tensors at (a) initial cracks, (b) initiation, and (c) limit point.

(d) Post-failure development

After surpassing the limit point, large displacements are measured in the consecutive load steps. The displacement increased from 0.8 mm at limit point, to 4.2 mm at an applied load of respectively 161 kN and 167 kN for the left and right bearing pad (Figure 12.22). Moreover, after the limit point a difference in load was measured between the left- and right bearing pad.

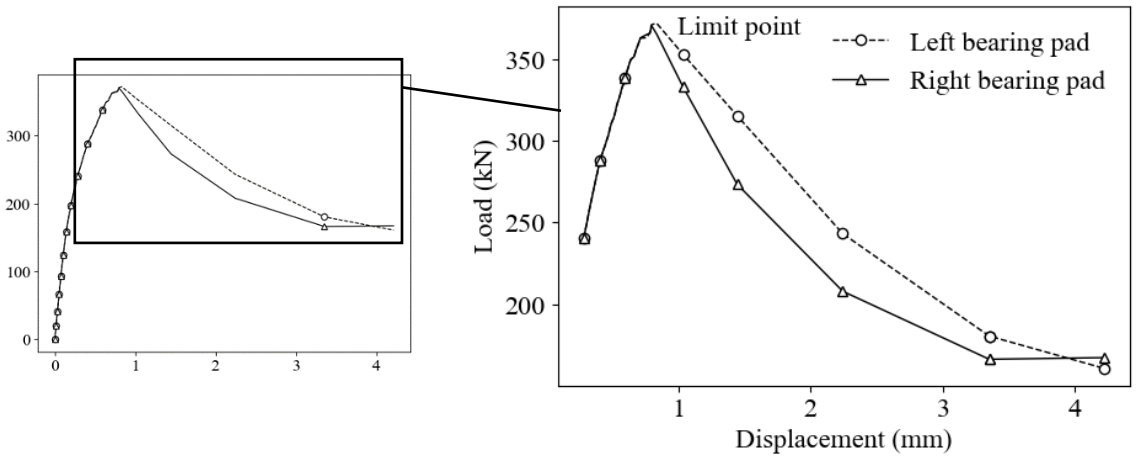

Figure 12.22 Load-displacement diagram of the consecutive steps after the limit point.

The large steps in displacement after the limit point suggest that the model became more unstable. A potential cause for instability of the model is brittle failure of the corbel. At the measured load of 166 kN, the support end failure developed over the entire height of the corbel, as shown in Figure 12.23. The characteristics of the support end failure are well represented by its shape.

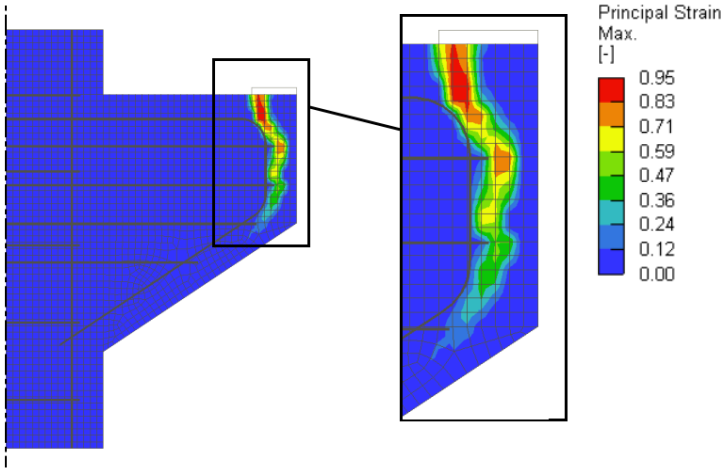

Figure 12.23 Principal strain at an applied vertical load of 166 kN, post limit point.

Attention should be paid to the order of magnitude of the measured principal strains. The highest principal strain in the corbel was measured at almost 100%. Brittle failure of the corbel is the reason for both the unstable behaviour after the limit point and the order of magnitude of the principal strains. As the crack continued over almost the entire height of the corbel, it can no longer withstand any forces. In practice, such continuous crack would cause the concrete section to separate of the corbel element. However, in the finite element simulation both sides remain attached to each other through elements. In an attempt to transfer the stresses through the greatly reduced cross-sectional area, it causes these large strains. Although the order of magnitude is inaccurate, the trajectory of the principal tension strains still provide insight into the failure plane.

12.2.5 Concluding remarks

The important findings of the numerical experiment which studied the influence of the bearing pad position are enumerated below.

- By placing the bearing pad on the edge of the corbel, the capacity of the corbel reduced, explained by an enlarged exerted bending moment and altered stress introduction. Consequently, the crack propagation altered slightly, although the failure mechanism remained the same and the capacity exceeded the design load.
- As the bearing pad was shortened to 70 mm and placed on the edge of the corbel, a similar crack propagation was observed, albeit at lower applied loads. As the load reached 371 kN the support end failure occurred, before reaching the design load.
- Based on the principal strain plots and principal stress trajectories, the support end failure mechanism was categorized into four stages: initial cracks, initiation, failure, post-failure development, respectively at 307 kN, 351 kN, 371 kN, and 166 kN.
- For the support end failure induced by solely a vertical load, initial cracks propagated at the height of the main reinforcement, which developed in vertical direction. The crack initiation was measured by an exceedance of tensile capacity along the bend section of the main reinforcement.
- In the post-failure development, the crack had propagated over the entire height of the corbel in vertical direction.

12.3 Influence of horizontal loading

12.3.1 Corbel configuration

A second experiment was conducted in which the influence of a horizontal load on the support end failure was studied. In practice, these generally occur due to imposed deformations. In this experiment, the bearing pad was positioned at the edge of the corbel. A concrete block (240x80 mm), reinforced by three bars of 16 mm, was added on top of the bearing pad in order to resemble the interaction between supported element, bearing pad, and corbel. The material properties were assumed to be equal to those of the corbel, strength class C40/50. The configurations of the corbel with the additional concrete block are presented in Figure 12.24, referred to as specimen C.

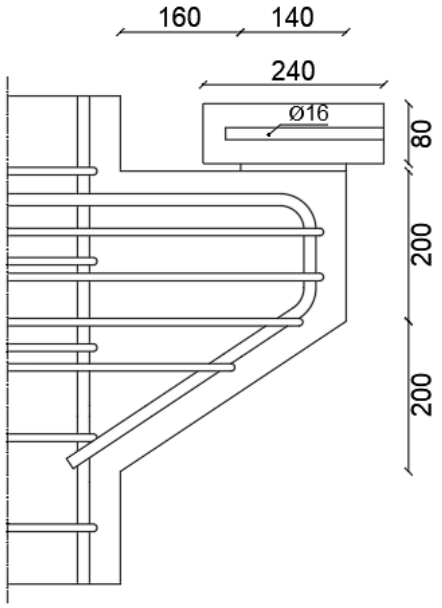

Figure 12.24 Corbel configuration of specimen C, dimensions in mm.

12.3.2 Loading- and boundary conditions

Loading conditions

The loading of the corbel element consisted of both a vertical and horizontal load. The corbel was vertically loaded up to the design load of 400 kN, after which a horizontal load was applied up to 0.2 times the vertical load. This factor is derived from the frictional coefficient of an elastomer according to art. 8.1.4 of NEN 6720, which equates to a horizontal force of 80 kN (Nederlands Normalisatie Instituut, 2007).

The vertical force was applied on the top of the added concrete block as a uniformly distributed load. Since the model is two dimensional, this was modelled as a line load. Furthermore, the horizontal force was applied as uniform load on the outer edge of the added concrete block. A schematisation of these conditions is provided in Figure 12.25. Monitors were placed in the same positions as the applied loading.

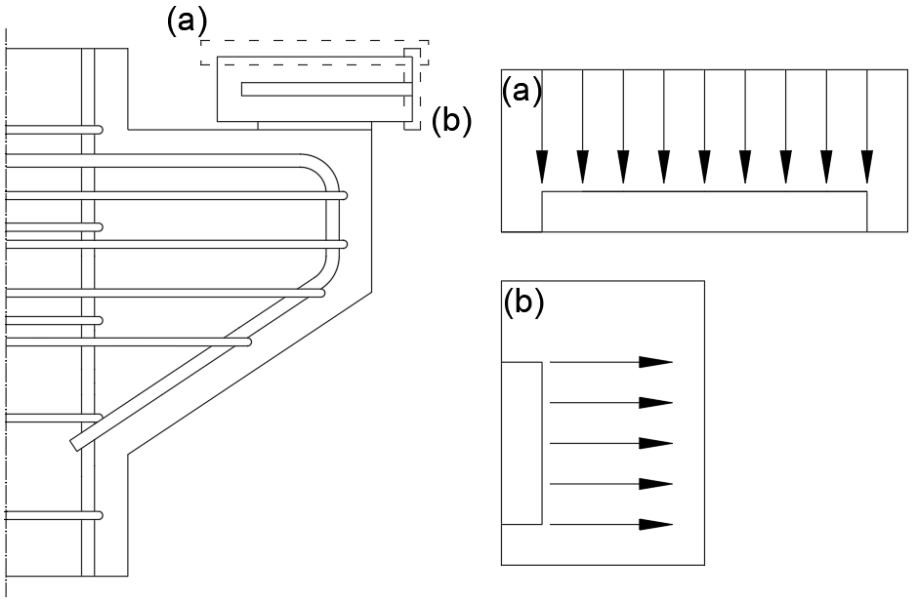

Figure 12.25 Schematisation of applied loads of specimen C.

The previous analyses were displacement controlled. The numerical analysis of specimen C the loading is already determined before the analysis. It would be difficult to exactly match the prescribed load with a displacement controlled analysis. Therefore, the load application was changed to force controlled. The downside of a force controlled analysis is that the load displacement behaviour after reaching the limit point cannot be found. This is not a problem because this exploratory study was mainly aimed to study the behaviour up until failure, and thus can be applied for these circumstances. The loads were applied in two consecutive instances. This load was held as constant as the horizontal load gradually increased on the corbel.

Boundary conditions

The boundary conditions of the corbel configuration remained mostly similar to the previous numerical models. The support conditions of the corbel remained identical, further elaboration found in Section 11.3. The concrete block element was attached to the bearing pad with a master-slave connection, in which the assumption is made that the nodes of the concrete block are fixed to the nodes of the bearing pad, in both horizontal and vertical direction.

Meshing

The meshing of the corbel remained identical to previous analysis, a detailed elaboration is provided in Subsection 11.3.3. Moreover, the concrete block was meshed using a mesh size of 10 mm.

12.3.3 Numerical results – specimen C

It was known from the numerical results of specimen A that the corbel, with a 140 mm long bearing pad placed on the edge, could resist a vertical load of 400 kN. Since the loading of specimen C did not vary up to the vertical load of 400 kN, the specimens behaved identical. An in-depth elaboration on the behaviour of the corbel up to a vertical load of 400 kN is given in Subsection 12.2.2. In the following paragraphs, only the numerical results for the combined horizontal and vertical loading are discussed.

In Figure 12.26, the L-D diagram of both the horizontal and vertical load curves are presented. The intended loading was achieved as the vertical load increased until the design load was reached, after which it was kept constant. After the design load was reached, the horizontal stresses were gradually increased.

The modelled horizontal load of 80 kN was not reached as the corbel failed at a lower horizontal load. At a respective combined vertical and horizontal load of 400 kN and 64.4 kN, the support end failure mechanism caused failure of the corbel. After failure of the corbel, a reduction of displacement was observed in the L-D diagram of approximately 0.1 mm.

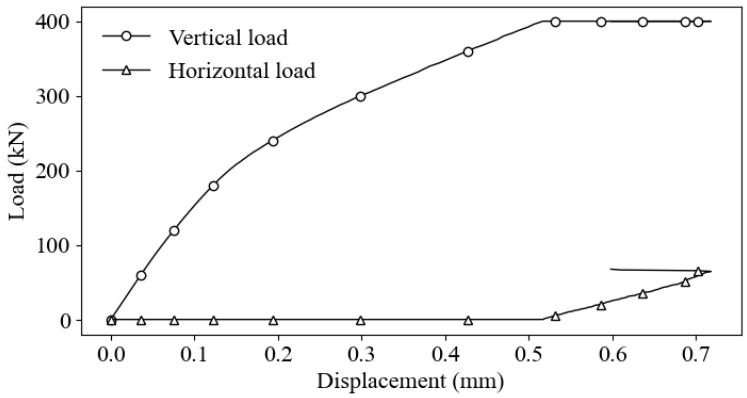

Figure 12.26 Load-displacement diagram of specimen C.

Before further elaboration of the support end failure, the behaviour of the corbel before failure under horizontal loading is briefly discussed at three load steps leading up to failure (Figure 12.27).

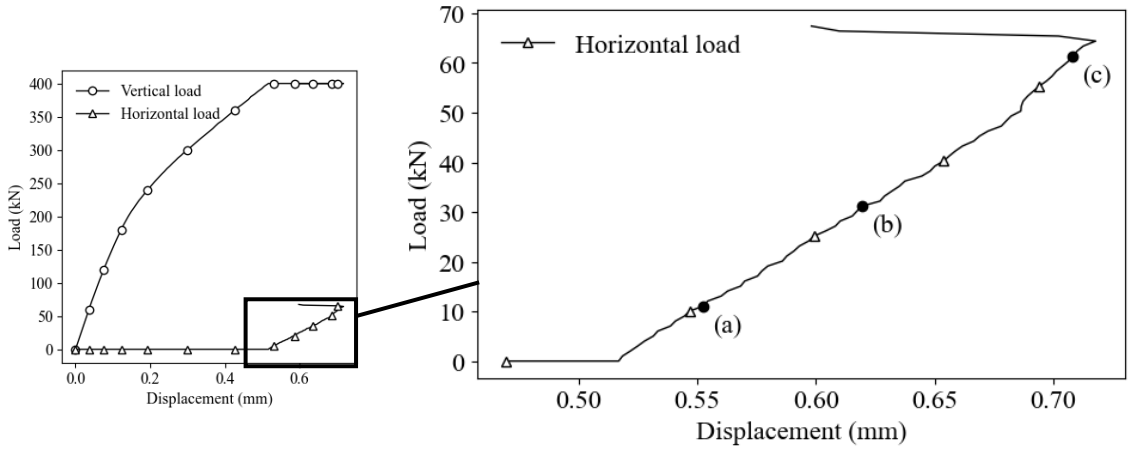

Figure 12.27 Denotation of discussed load steps before support end failure.

As the horizontal load reached 10 kN, at load (a) in Figure 12.28, crack 2 propagated between stirrups 1 and 2. Furthermore, the concrete loading block has three vertical cracks at the upper surface. Presumably, these cracks are initiated by splitting stresses as result of the applied vertical load.

After increasing the horizontal load to 30 kN, crack 3 and a vertical crack besides the bearing pad initiated. Cracks 2 and 3 developed in both length and crack width in the consecutive load steps. Interestingly, the trajectory and inclination of crack 3 is nearly identical as observed in specimen A, even though the loading conditions differ.

At load (c) in Figure 12.28, crack 2 spanned between the main reinforcement up to stirrup 4. Crack three propagated from the main reinforcement up to stirrup 3. The maximum crack width for cracks 2 and 3 was 0.11 mm and 0.07 mm, respectively. Moreover, a vertical cracking is observed below the middle of the bearing pad, spanning between the surface of the corbel up to the main reinforcement.

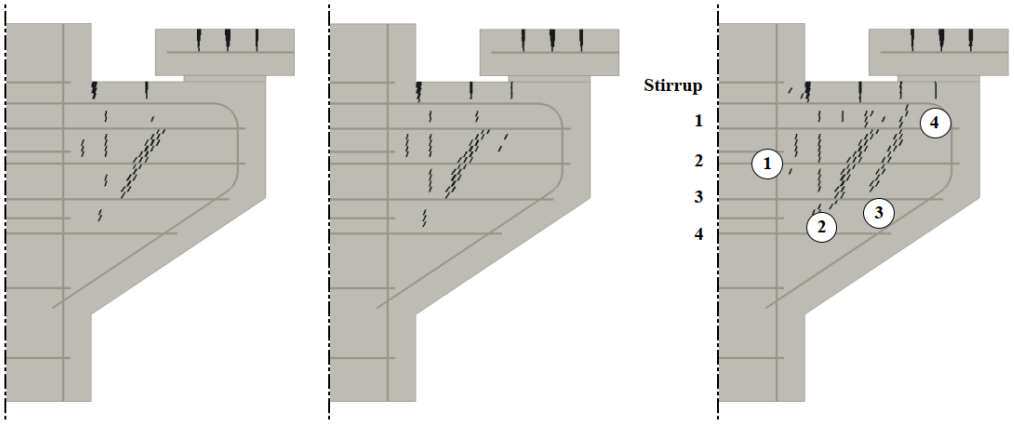

Figure 12.28 Crack model showing crack with a minimum width of 0.05 at a horizontal load of 10 kN, 30 kN, and 60 kN.

The tensile stresses in the reinforcement at load steps (a), (b), and (c) are presented in Figure 12.29. Besides the increases in tensile stresses of the stirrups and main reinforcement as a result of crack propagation, increases of tensile stresses along the bend section of the main reinforcement were measured at load step (c). Based on the numerical results of specimen B, this could potentially indicate initiation of the support end failure.

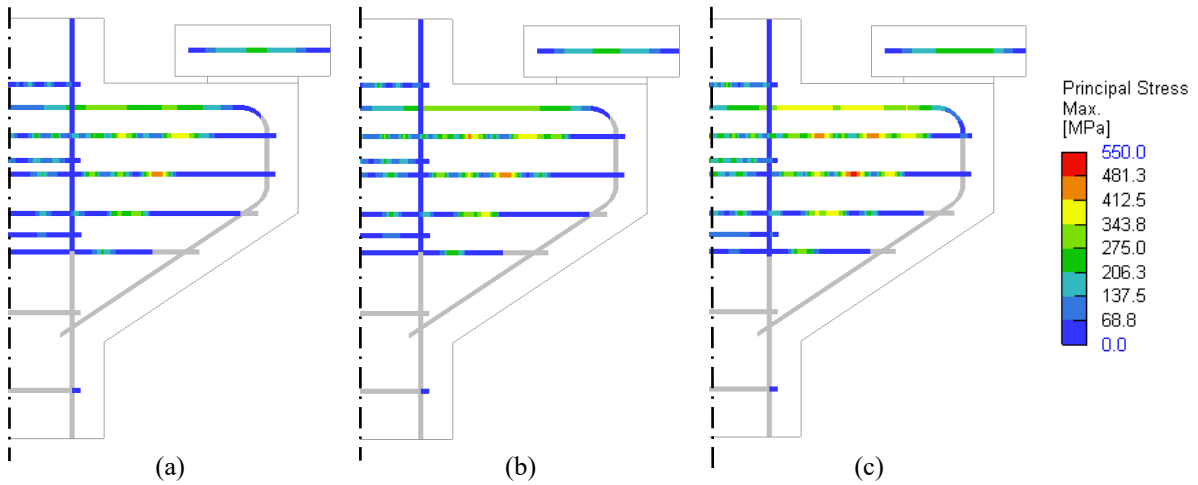

Figure 12.29 Development of reinforcement stresses at a horizontal load of 10 kN, 30 kN, and 60 kN.

Support end failure
The behaviour of the support end failure was categorized into four stages, encompassing:

a) Initial cracks
b) Initiation
c) Failure
d) Post-failure development

The four stages of the support end failure are indicatively shown based on principal strain plots, as shown in Figure 12.30. Initial support end failure cracks occurred in the corbel as the horizontal load reached 52.5 kN ((a) in Figure 12.30). Briefly after, this crack extended into what is described as initiation of the support end failure, at 64.4 kN ((b) in Figure 12.30). The corbel had failed as a horizontal load of 65.4 kN ((c) in Figure 12.30) was applied. Furthermore, the support end failure had completely developed at 67.4 kN ((d) in Figure 12.30).

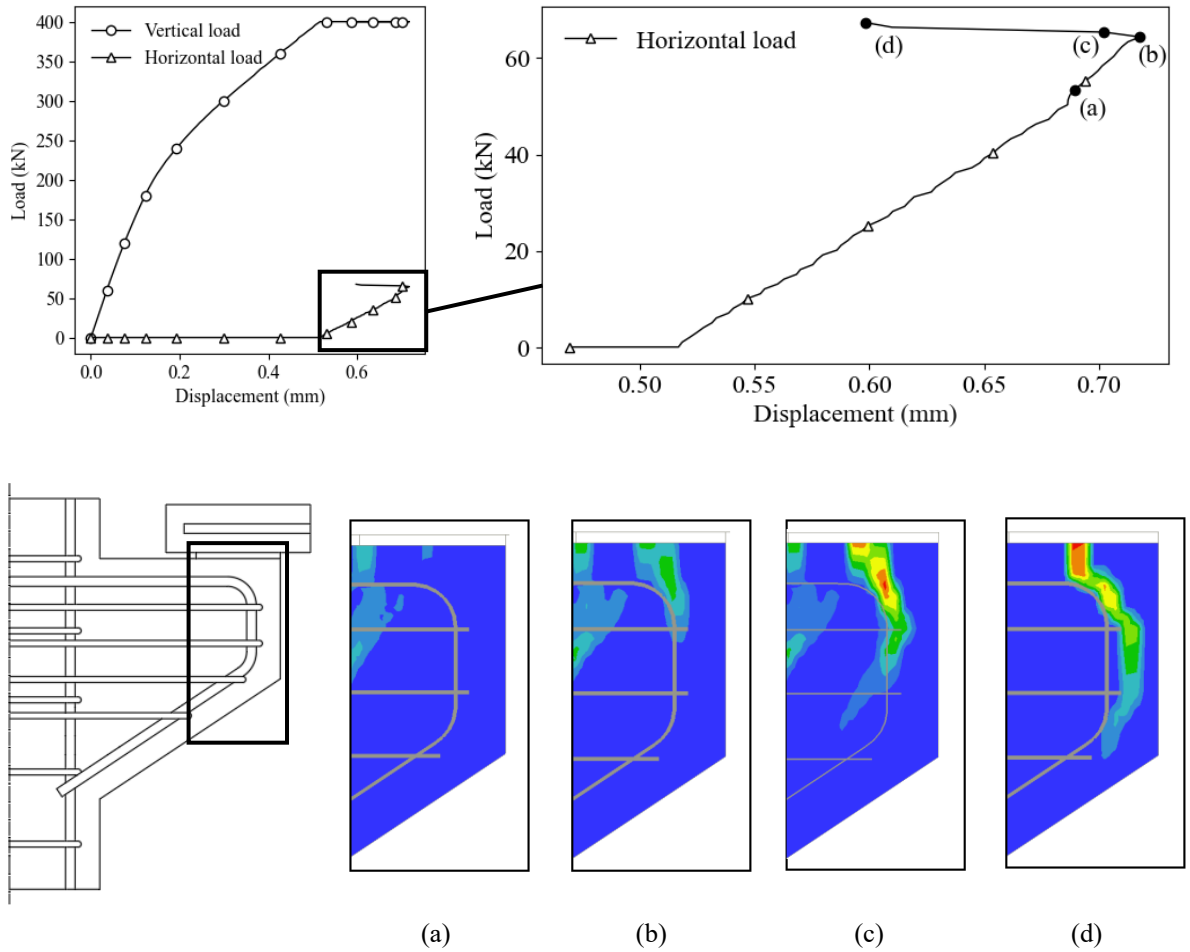

Figure 12.30 Development of support end failure indicatively shown by principal tensile strains, at an applied horizontal load of 52.5 kN (a), 64.4 kN (b), 65.4 kN (c), and 67.4 kN (d).

An interesting finding is that after reaching a horizontal load of 64.4 kN the vertical displacement decreased, even though the horizontal load increased. Although, the support end failure increased in development in consecutive load steps. Therefore, it would be expected that the displacement of the corbel would increase at both load steps (c) and (d).

The decrease in displacement can be explained by an upwards lift of the displacement monitor. To reiterate, the displacement monitor was placed in the middle at interface between bearing pad and corbel. In Figure 12.31, the deformed model, amplified by factor 10, under a horizontal load of 66.4 kN is presented. Two support end failure cracks developed in the elements next to the monitoring point. These cracks were at a slight inclination and were kept at this inclination as a fixed crack model was adapted. As the cracks increased in crack width, the nodes on the disjointed concrete edge lifted slightly, and thus caused the reduction in displacement.

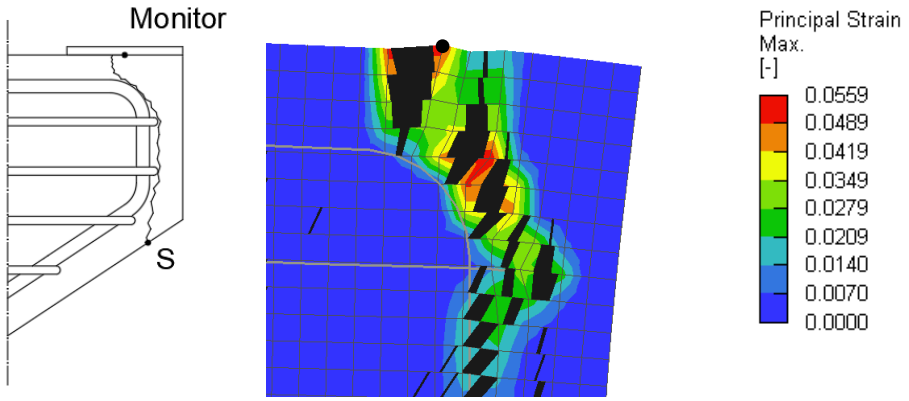

Figure 12.31 Schematisation of displacement monitor with respect to failure and the displaced model, amplified by factor 10, at 66.4 kN horizontal load.

This behaviour can be avoided by placing the monitoring point at a slight distance from the cracks. In Figure 12.32, the L-D diagram is plotted in which displacement are measured at the corner of the corbel. As expected, the vertical displacement increased as the horizontal load increased. Moreover, the displacement can be seen increasing even after failure of the corbel initiated. This is caused by the force-controlled analysis, which increases the load at each load step.

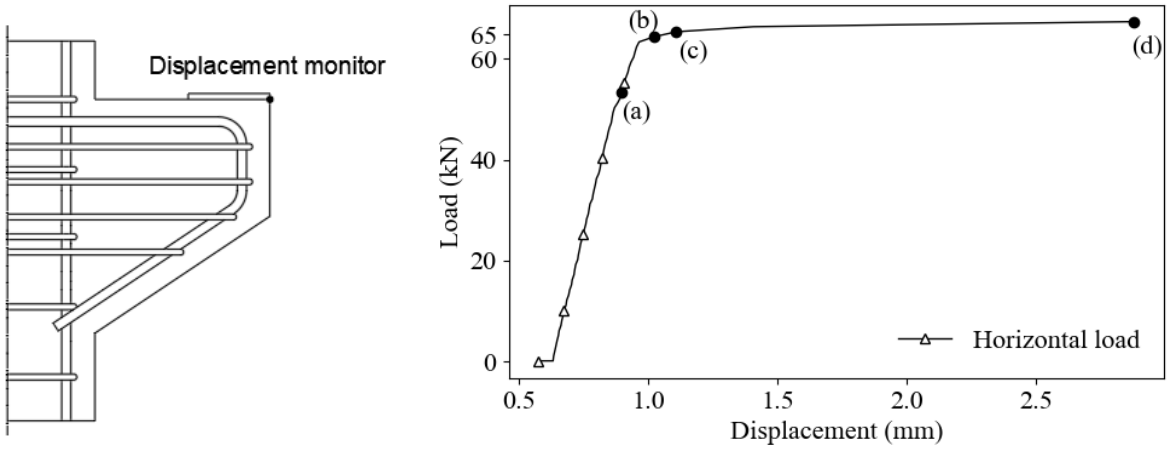

Figure 12.32 Load-displacement diagram, displacement measured at the corner of the corbel.

(a) Initial cracks

Initial support end failure cracks were observed in the corbel as the horizontal load reached 51.3 kN (Figure 12.33). The cracks span in vertical direction from the surface of the corbel up to the main reinforcement. Although, it is not evident in which element the crack initiates based on the crack model. Moreover, the cracks at the surface of the corbel are slightly inclined. At the consecutive load step, 52.3 kN, cracks propagated along the bend of the main reinforcement.

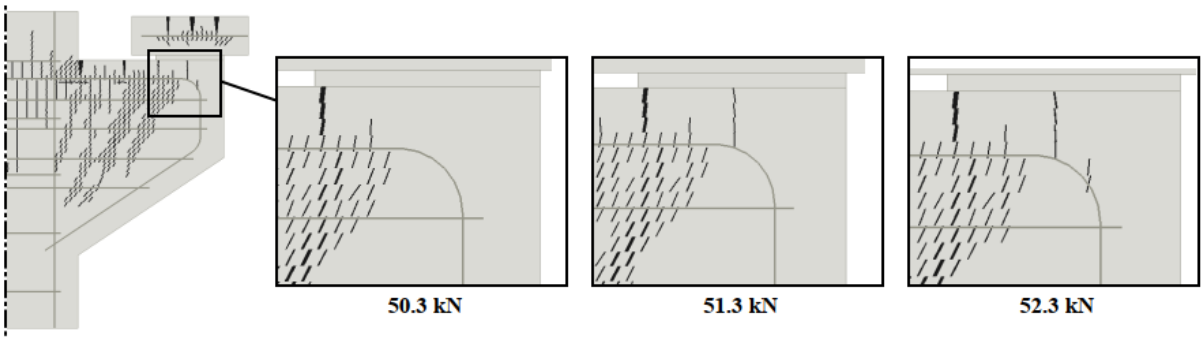

Figure 12.33 Crack model of the corbel at three consecutive horizontal loads of 50.3 kN, 51.3 kN, and 52.3 kN, with a minimum crack width of 0.01 mm.

In the numerical analysis of specimen B, it was suggested that initial support end failure cracking could be indicated by increases of tensile stresses along the bend section of the main reinforcement. In Figure 12.34, tensile stresses in the reinforcement are presented for the same three consecutive load steps.

At a horizontal load of 50.3 kN and 51.3 kN, the tensile stresses in the bend section of the main reinforcement are nearly identical. As the crack extended along the bend section, at 52.3 kN, tensile stresses increased along this section. Although, the support end failure had already initiated in the previous load step. Presumably, this is affected by the initiation of the support end failure, which started at the height of the main reinforcement for a specimen B, yet developed from the surface of the corbel for specimen C. Nevertheless, the increase in tensile stresses arose reasonably close to initiation.

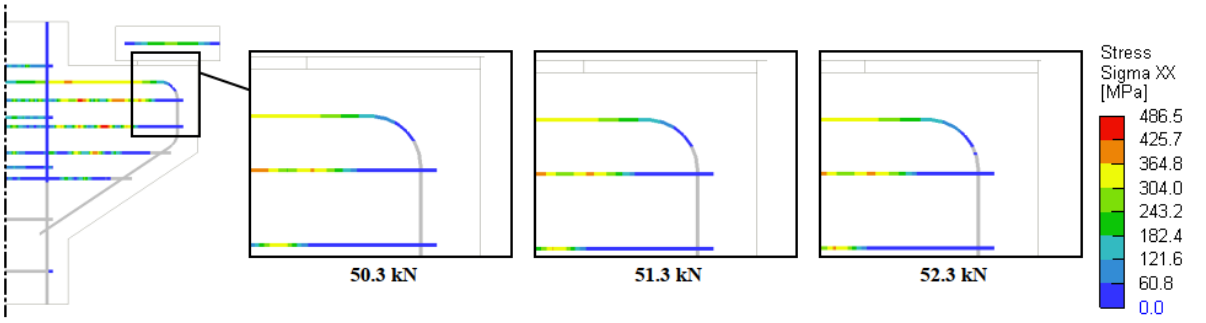

Figure 12.34 Tensile stresses in the reinforcement at three consecutive load steps 50.3 kN, 51.3 kN, and 52.3 kN.

The cause of the slight inclination of the cracks, as mentioned above, can be explained by principal stress trajectories. In Figure 12.35, principal stress trajectories are shown at a horizontal load of 10 kN and at initiation of the support end failure cracks at 51.3 kN.

For a combined vertical and horizontal load of respectively 400 kN and 10 kN, the tensors representing the principal compressive stresses are completely vertical below the bearing pad. As the horizontal load is increased, the tensors change in the same direction of the horizontal load. The inclination gradually decreases over height and towards the edge of the corbel.

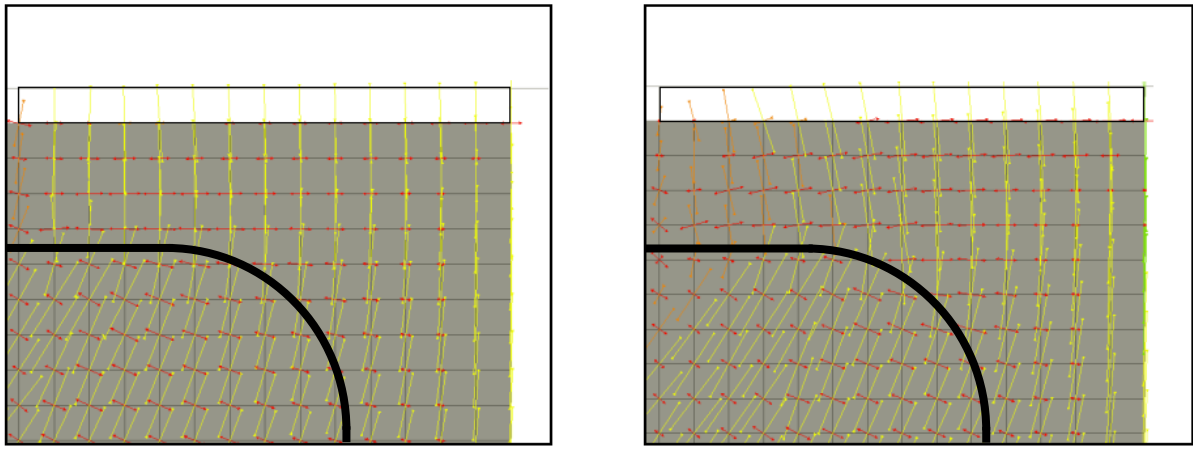

Figure 12.35 Principal stress trajectories at a horizontal load of 10 kN and 51.3 kN.

The crack model in Figure 12.33 could not provide sufficient information on the crack initiation of the failure. A detailed insight into the crack initiation is provided with a visualisation of the principal stress tensors at a horizontal load of 50.3 kN (Figure 12.36).

The principal stress tensors which are coloured in light blue, exceed the tensile strength of concrete. Three inclined tensors exceeding the tensile strength are observed in the load step before crack initiation. This does not prove at which exact location the crack initiates, however it does suggest that the crack does not initiate at the surface of the corbel.

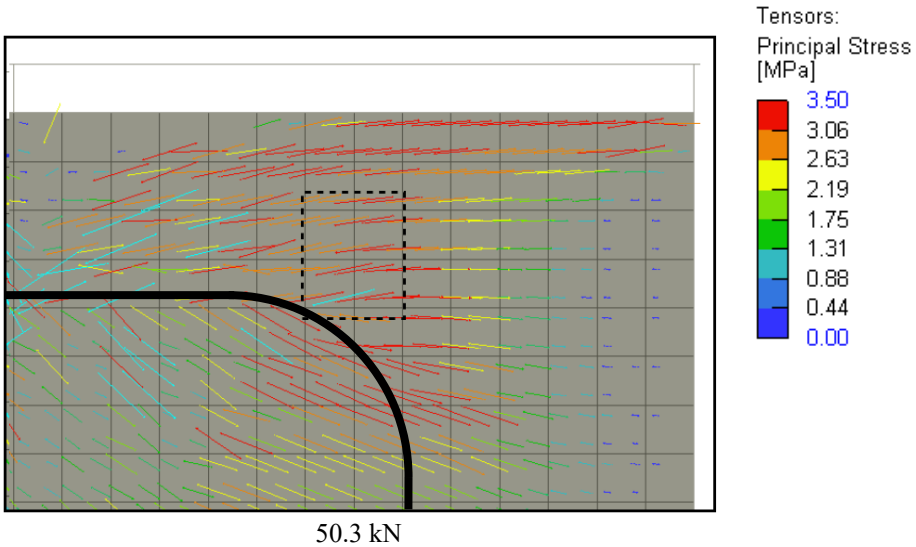

Figure 12.36 Tensor model of the principal tensile stresses at a horizontal load of 50.3 kN.

(b) Initiation

Although initial crack were observed at a horizontal load of 51.3 kN, the width of 0.01 mm was not significant to denominate it as initiation. The initiation of the support end failure mechanism was observed at 64.4 kN horizontal load, as the principal strains abruptly increased in both length and order of magnitude (Figure 12.37).

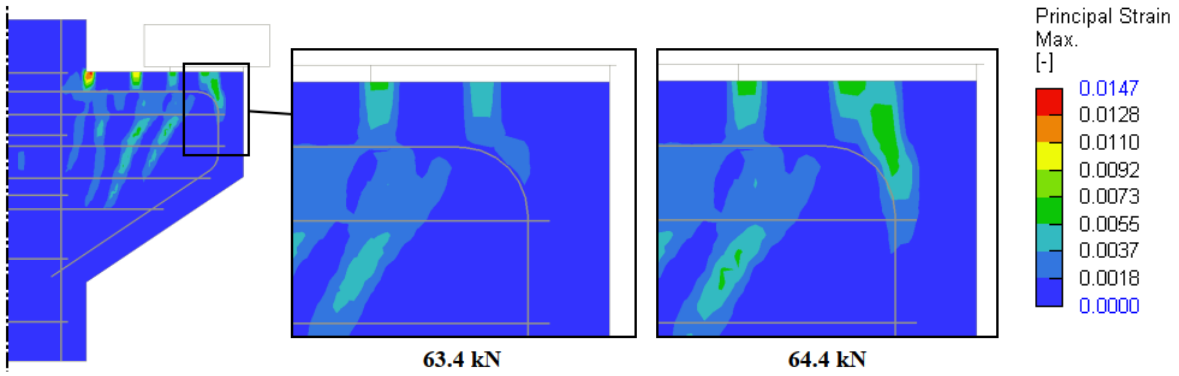

Figure 12.37 Principal strain for horizontal loads of 63.4 kN and 64.4kN.

Furthermore, the initiation is well displayed by principal stress tensors (Figure 12.38). The tensors depict the initiation of the vertical crack accurately by the disruption of the stress trajectories, as a horizontal load of 64.4 kN was reached. Moreover, in the prior load step, several tensors exceeding the tensile limit were observed at various heights of the corbel cover. It seems that the crack initiated at the surface of the corbel, as a tensor exceeding the tensile strength is placed on the same vertical plane as the crack. Although, this cannot be established as there are several tensors of similar order of magnitude present around the vertical plane of the crack.

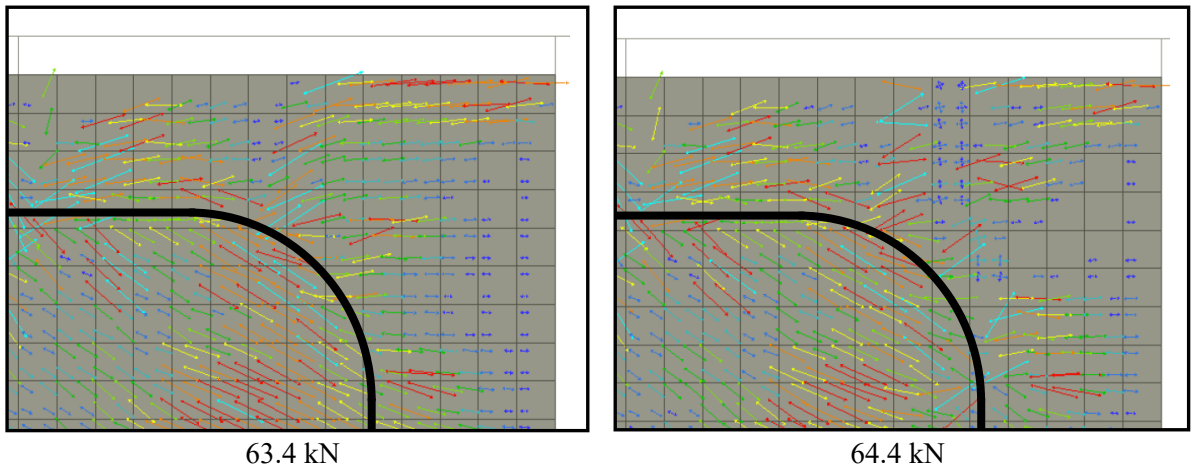

Figure 12.38 Tensor model of the principal stresses at 63.4 kN and 64.4 kN horizontal load.

(c) Failure

In the consecutive load step after initiation, at a horizontal load of 65.4 kN, it was concluded that the corbel had failed by support end failure, based on principal strains. The principal strains in the corbel provide an accurate presentation of the failure mechanism (Figure 12.39). The trajectory of the principal strains spans from the surface of the corbel up to stirrup 1, at an inclination of approximately 60°.

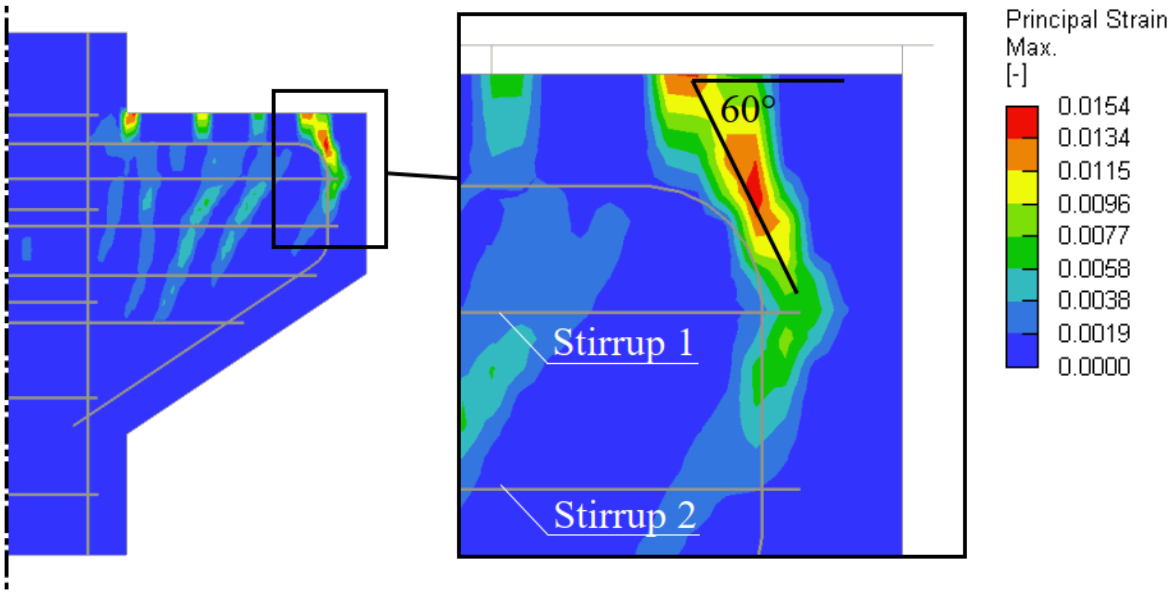

Figure 12.39 Principal strains in the corbel at a 65.4 kN horizontal load.

The tensile stresses in the reinforcement as result of the failure cracks are shown in Figure 12.40. The maximum tensile stress has exceeded the yield stress in the reinforcement at the outer edges of stirrup 1. Moreover, the vertical section of the main reinforcement, between its two bends, has increased in stresses along the entire height. Interestingly, the tensile stresses in this section of the main reinforcement are noticeably similar, in both distribution and order of magnitude, as the section at failure of specimen B.

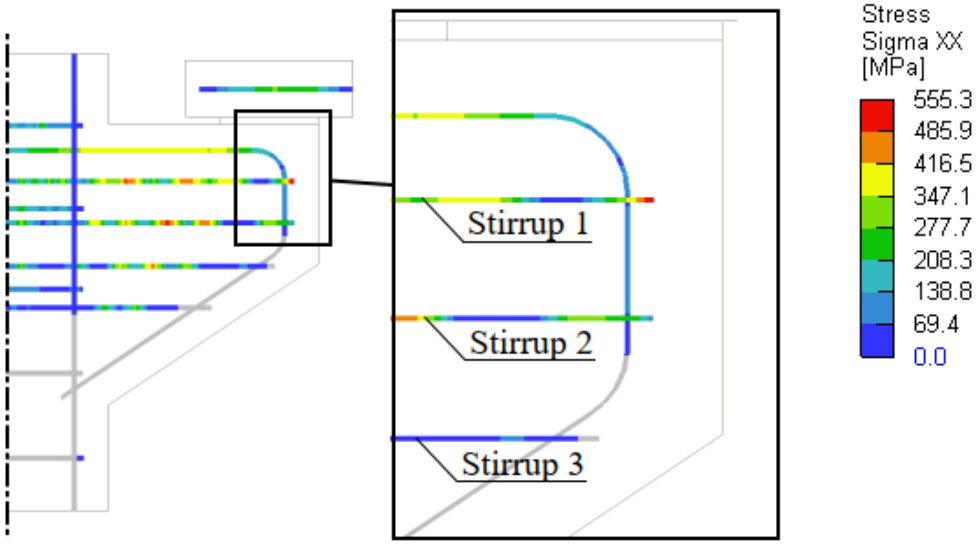

Figure 12.40 Tensile stresses in the reinforcement at 65.4 kN horizontal load.

One could question whether the crack propagation in downward direction is understandable, as one might expect that the applied horizontal load could induce a shear failure plane, as shown in Figure 12.20. In Figure 12.41, principal strains and principal stress tensors at (a) initial cracks, (b) initiation, and (c) failure are displayed. The failure plane is similar to specimen B, in which the crack continued over the entire height of the corbel.

At the initial cracks, the trajectories of the principal compressive stress tensors are predominantly vertical. At initiation of the failure, a crack formed dividing the stress tensors below the bearing pad. At this load step, the stress tensors at the surface of the corbel are slightly inclined. Although, the inclination of the stress tensors decreased at a larger depth in the corbel. At a depth of stirrup 1, the inclined tensors had become vertical. A similar situation occurred as in specimen B, in which the initial principal stress trajectory of the tensors is obstructed by the crack. As result, these travel in further downwards direction around the reinforcement. Consequently, the crack increases along the reinforcement over the height of the corbel.

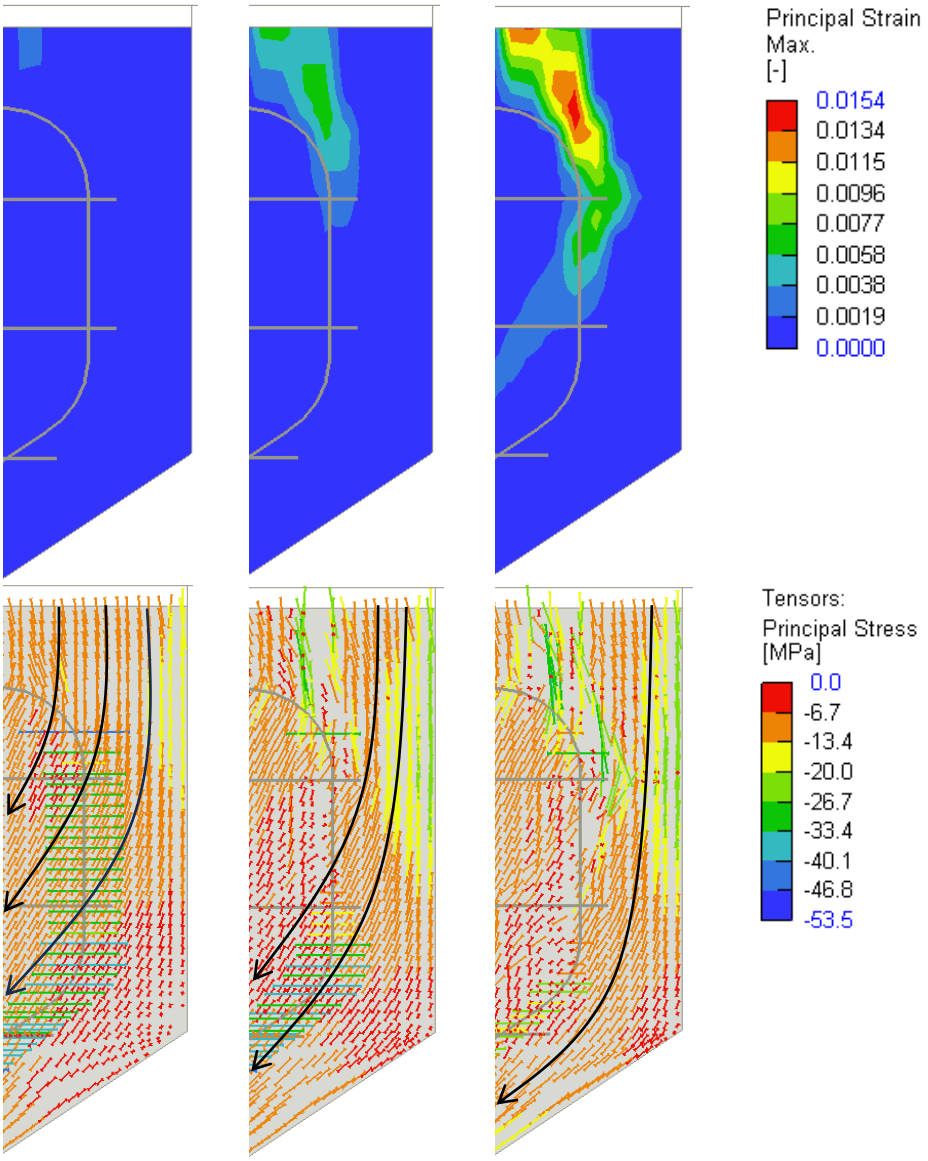

(a) – 52.3 kN (b) – 64.4 kN (c) – 65.4 kN

Figure 12.41 Principal strains and principals stresses at (a) initial cracks, (b) initiation, and (c) failure.

(d) Post-failure development

As the horizontal load increased, the support end failure grew in both length and width, extending past stirrup 3 with a maximum crack width of 3.6 mm. Once again, the characteristic crack propagation of the support end failure is depicted well by the principal strains, as shown in Figure 12.42. Although, the crack development differs compared to failure as the principal strains in the section between the corbel surface and the main reinforcement span in vertical direction.

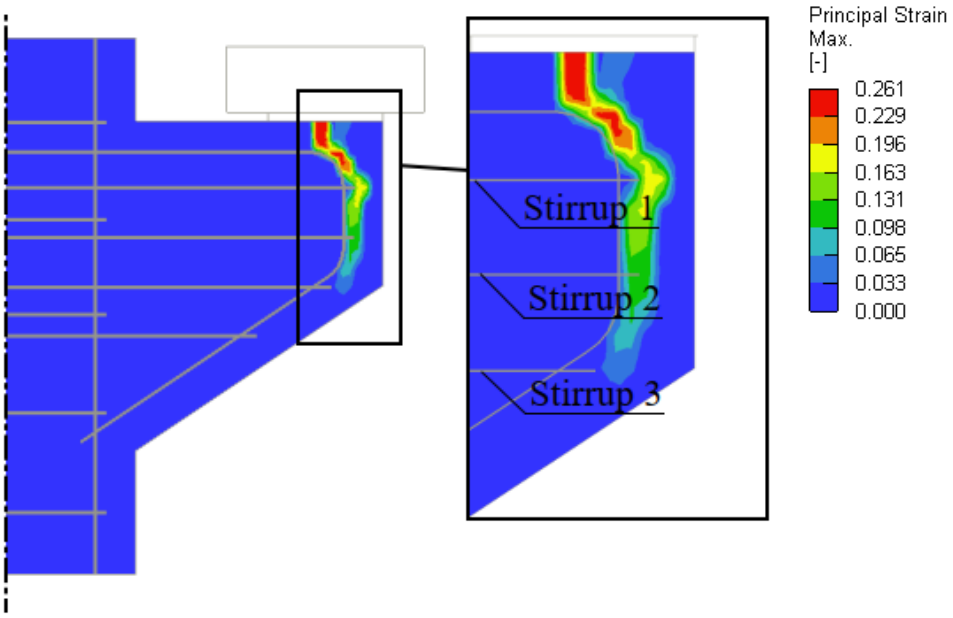

Figure 12.42 Principal strain model at horizontal load of 67.4 kN.

Even though the loading conditions for specimens B and C differed, the failure mechanism shows close resemblance to one another. It became apparent by the principal strain plots that the disjointed concrete sections of both specimens rotate around the bottom of the corbel, schematised in Figure 12.43.

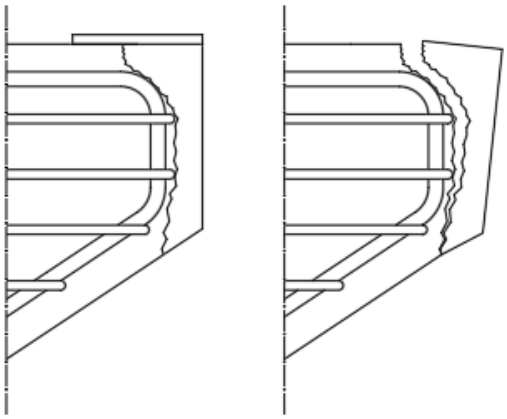

Figure 12.43 Schematisation of rotation of disjointed concrete section.

In Figure 12.44, the tensile stresses in the reinforcement are presented. The crack propagation along the main reinforcement affected the tensile stresses within, as the tensile stresses extended up to stirrup 2. Interestingly, the tensile stresses in the vertical section of the main reinforcement had decreased compared to the state at failure. Even more so, several concrete sections had debonded from the from the main reinforcement.

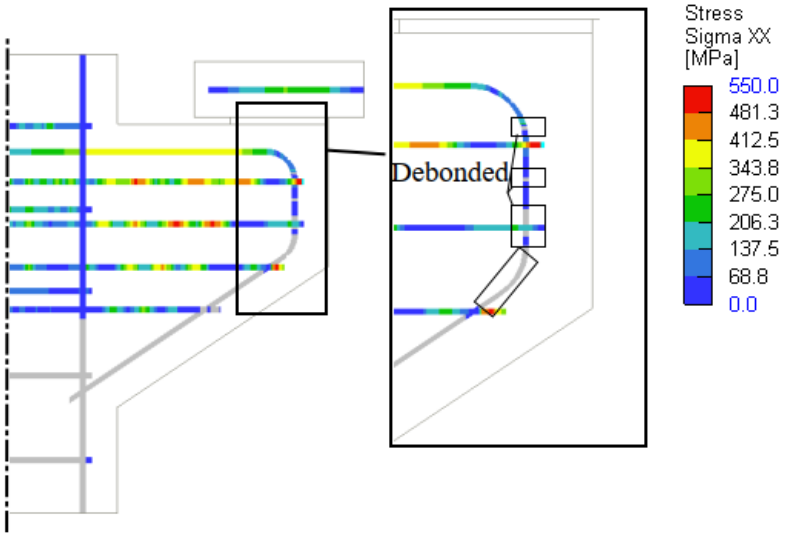

Figure 12.44 Tensile stresses in reinforcement at a horizontal load of 67.4 kN.

12.3.4 Concluding remarks

A brief summarisation of the important findings of the numerical study on the application of horizontal load is presented below.

- By placing the bearing pad of the original design on the edge of the corbel and loading it by a vertical load of 400 kN and horizontal load of 66.4 kN, the corbel failed by support end failure.
- The support end failure was distinguished into four phases: initial cracks, initiation, failure, post-failure development, respectively at 52.6 kN, 64.4 kN, 65.4 kN, and 67.4 kN.
- The initiation of the support end failure occurred between the upper surface of the corbel and main reinforcement. After increase of the horizontal load, the crack propagated at an inclined angle of approximately 60°.
- As the crack propagated along the main reinforcement, increases in tensile stresses along the vertical section of main reinforcement were observed.
- In the post-failure development, the support end failure crack had increased along the entire height of the corbel.

13 Analytical model

13.1 General

The numerical analyses proved that the support end failure could accurately be replicated. In the following chapter, an attempt is made to replicate the results in an analytical method. First, some background information of corbel behaviour design is provided in Section 13.2. Subsequently, the proposed model is elaborated in Section 13.3. Lastly, the proposed analytical model was tested on the numerical results in Section 13.4.

13.2 Damage mechanism

13.2.1 Corbel behaviour

Reinforced concrete elements are designed in regions in which the distribution of strain is either linear or nonlinear. The regions are so-called Bernoulli-regions (B-region) and Discontinuous-regions (D-region), in which B-regions represent regions with a linear strain distribution and D-regions represent a region with a nonlinear strain distribution. Concrete elements such as half-joints, pile caps, and corbels are categorized as D-region (Figure 13.1).

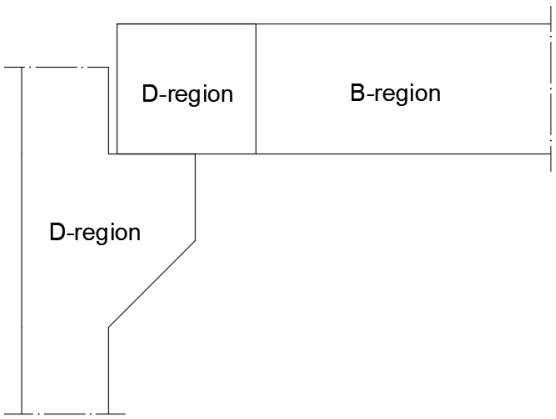

Figure 13.1 Schematisation of B- and D-regions of a corbel-beam connection.

B-regions are calculated according to Bernoulli's beam theory by assuming plane sections remaining plane. Yet, due to the nonlinear strain distribution in D-regions this same approach should not be used. For these regions the so-called strut-and-tie model (STM) can be used.

13.2.1 Strut-and-tie model

A strut-and-tie model, as stated in its name, consist of compressive struts and tensile ties which represent the flow of forces within a D-region. These members form a truss-like structure in which each node is in force equilibrium. Various different strut-and-tie models were designed for reinforced concrete corbels, as seen in Figure 13.2 (Collins & Mitchell, 1991; Yun et al., 1994; Yun & Chae, 2019).

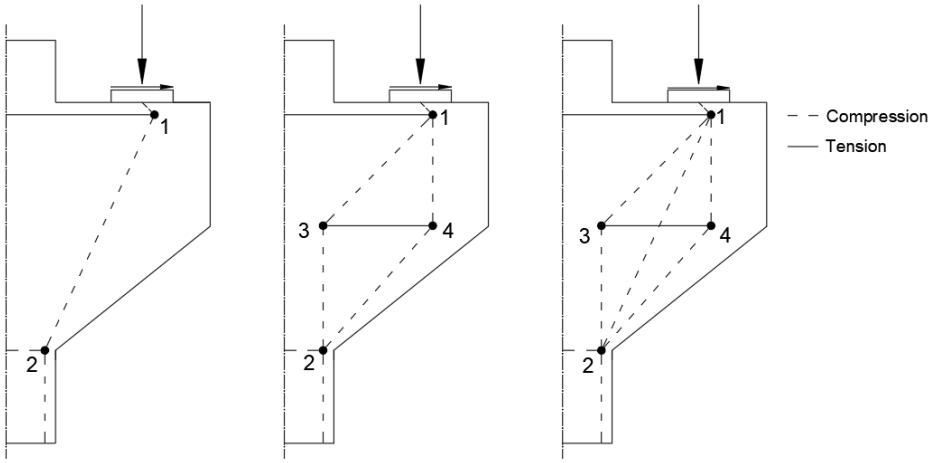

Figure 13.2 Strut-and-tie models for reinforced concrete corbels (Collins & Mitchell, 1991; Yun et al., 1994; Yun & Chae, 2019).

Even though the models may look slightly different, they are all based on a simple mechanics concept, consisting of a diagonal compressive region and a horizontal tensile tie to make force equilibrium. Generally, this concept is implemented in practice by utilizing the compressive concrete strength for the compressive strut and reinforcement to provide the tensile tie. Nodes with force configurations like the aforementioned are categorized as compressive-compressive-tension nodes, CCT in short. The stress distribution and force equilibrium of node 1 is schematized in Figure 13.3.

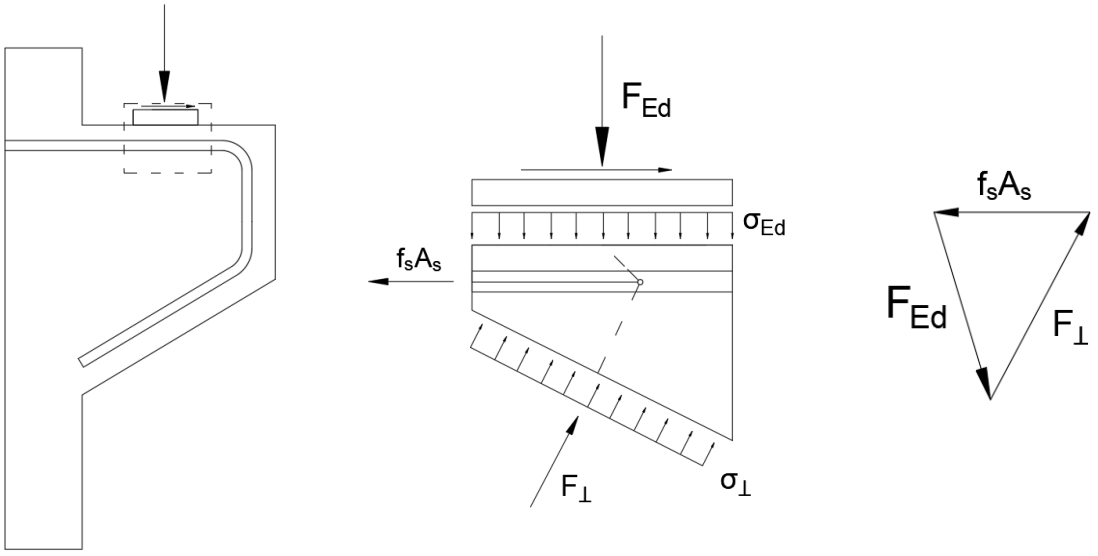

Figure 13.3 Schematization of stress distribution in CCT node 1.

A situation might take place in which the bearing pad is placed towards the outer edge of the corbel, for example due to improper execution. If such situation occurs, two potential problems arise: the support end failure and insufficient anchorage length of the main reinforcement.

13.2.2 Anchorage length

Stresses underneath a bearing pad disperse over the height of the corbel, as shown in Figure 13.4. This dispersion occurs under a certain angle which is unknown, denoted as "α" in Figure 13.4. Generally, a maximum dispersion angle of 45° is maintained (Nederlands Normalisatie Instituut, 2011). The connection suffices if the stresses remain within the main reinforcement, denoted as "Limit" in Figure 13.4. This limit is set at the inner side of the vertical section of main reinforcement, for main reinforcement using in-plane bend reinforcement as anchorage method.

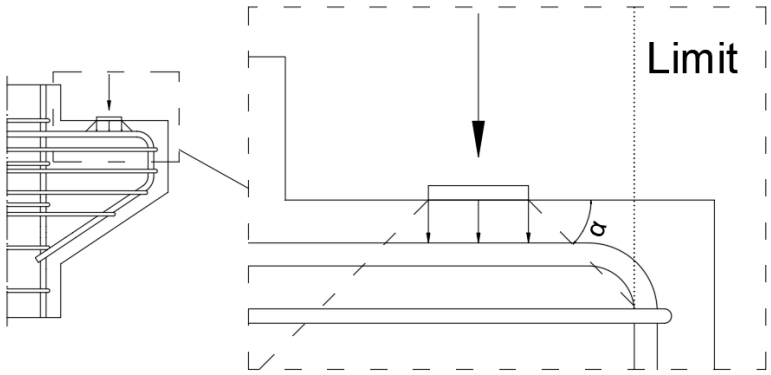

Figure 13.4 Schematisation of stress distribution underneath bearing pad.

If stresses disperse beyond this limit, the unreinforced concrete cover has to withstand this stress. In case these stresses exceed the tensile strength of the concrete, it cracks. The area underneath the bearing pad which disperse these stresses on the unreinforced concrete depend on various factors, such as bending mandrel of main reinforcement, bearing pad distance from the edge, and dispersion angle. A schematisation is presented in Figure 13.5, in which three distances between the bearing pad and the edge of the corbel emphasize the difference between amount of dispersed stresses.

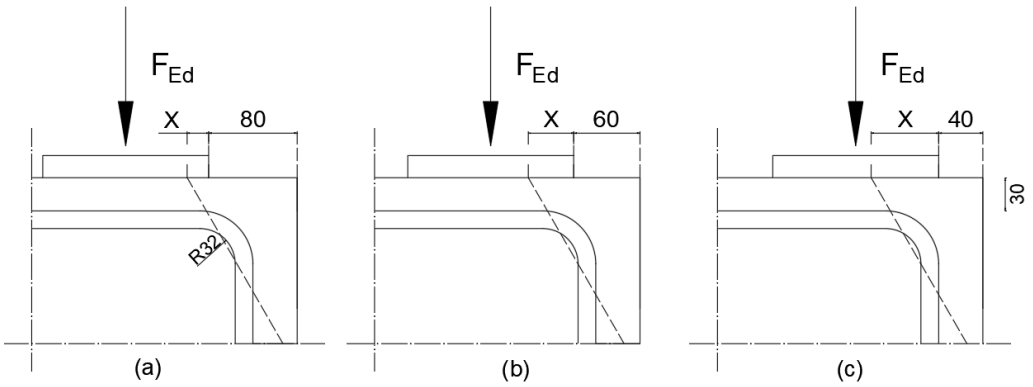

Figure 13.5 Dispersed stresses at a dispersion angle of 60° at various bearing pad distances to the edge.

This effect might contribute to the initiation of the support end failure mechanism. One could state that the support end failure occurs if the main reinforcement provides insufficient anchorage for the bearing stresses. Although, this could not be said in reverse order.

In Figure 13.6, the dispersion stresses are schematised for the design according to EC2, with a dispersion angle of 45°. In the given situation, a distance of 60 mm of the bearing pad is able to disperse its stresses onto the unreinforced concrete section. Whilst this does not suggest that the entire force under this area is dispersed onto the concrete cover, it does disperse stresses to some extent.

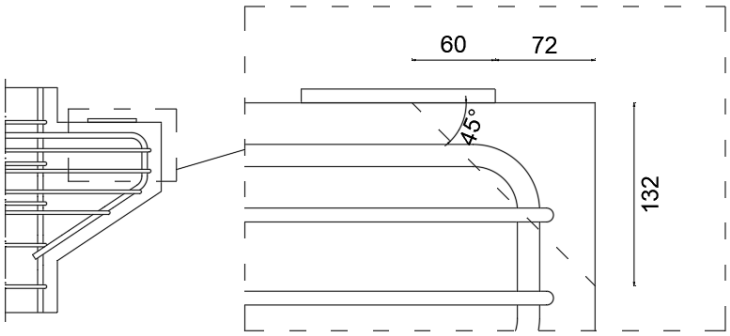

Figure 13.6 Dispersion stresses at an angle of 45° for the design according to Eurocode, dimensions in mm.

13.2.3 Support end failure

One could argue that the problem as stated above is the cause of the initiation of the support end failure. In the elaborated mechanism there are several external factors affecting the magnitude of the dispersed stresses, encompassing: the positioning of the bearing pad, detailing of reinforcement, or material of the bearing element.

In the experimental results of Neupane et al. (2017) and the numerical results of the parametric study, it was found that the support end failure developed over the entire height of the corbel. Whilst this behaviour is observed in practice, it has also been observed that the support end failure plane propagated diagonally from the support to the edge of the column, creating a situation as shown in Figure 13.7. In the analytical model it is assumed that the support end failure plane acts according to the latter crack orientation.

With this initial assumption, the forces acting along the interface of the corner section and on the surface can be schematised, as presented in Figure 13.7.

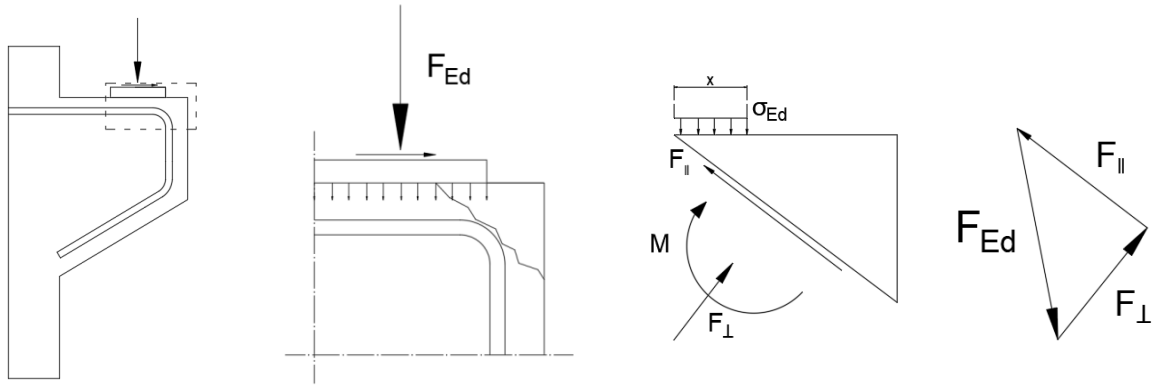

Figure 13.7 Schematisation of mechanical behaviour of support end failure.

First, several assumption of the analytical model are addressed. The support failure crack divides the bearing pad into two parts: a part connected to the corbel and a part disjointed from the corbel. The first assumption is that the horizontal and vertical loads are uniformly applied on the corbel. Secondly, it is assumed that the vertical and horizontal loads attached to the disjointed concrete section, only exert stresses on this section. Thirdly, it is assumed that the failure plane is completely straight. On the failure interface of the disjointed concrete section, three components are unknown: forces parallel and perpendicular to the interface and a bending moment.

The analytical method calculates the shear stress as result of the exerted load, and compares it to the formula to calculate the resistance of a shear interface as per EC2 section 6.2.5. If the shear strength is exceeded by the stresses parallel to the failure plane, the support end failure could potentially occur. The shear strength of an interface depends on the roughness of the interface, compressive stress perpendicular to the interface, and the tensile strength of the concrete, as in the formula below.

$$v_{Rdi} = c * f_t + \mu * \sigma_n$$

f_t	-	*mean tensile strength*
c	-	*dependent on roughness of the interface surface*
μ	-	*dependent on roughness of the interface surface*
σ_n	-	*stress perpendicular to the interface*

Whilst, section 6.2.5 of EC2 calculates the interface strength with the design tensile strength (f_{ctd}), the mean tensile strength is adopted in the analytical model in order to estimate the actual strength. The unknown forces and bending moment can be solved by force and bending moment equilibrium. A fifth assumption is that the axial stress is identical over the entire out-of-plane direction. With these assumptions stress σ_n can be solved. If the calculated shear strength is exceeded by the occurring shear stress, it is concluded that the support end failure has occurred. Essentially, it calculates if the support end failure occurs at given loading conditions (a multiplication of σ_{Ed}, x, and the width).

Analytical calculation - specimen B

In specimen B the failure occurred at a vertical load of 372 kN, which equates to a uniform applied stress under the bearing pad (300x70 mm^2) of 17.7 MPa. The failure plane of specimen B can be schematised as displayed in Figure 13.8. The failure plane is schematically drawn, starting at the initiation at the surface up to stirrup 1. Based on the trajectory the width (w) of the corner section, height (h) of the corner section, and length of the interface (l_{int}) are decided.

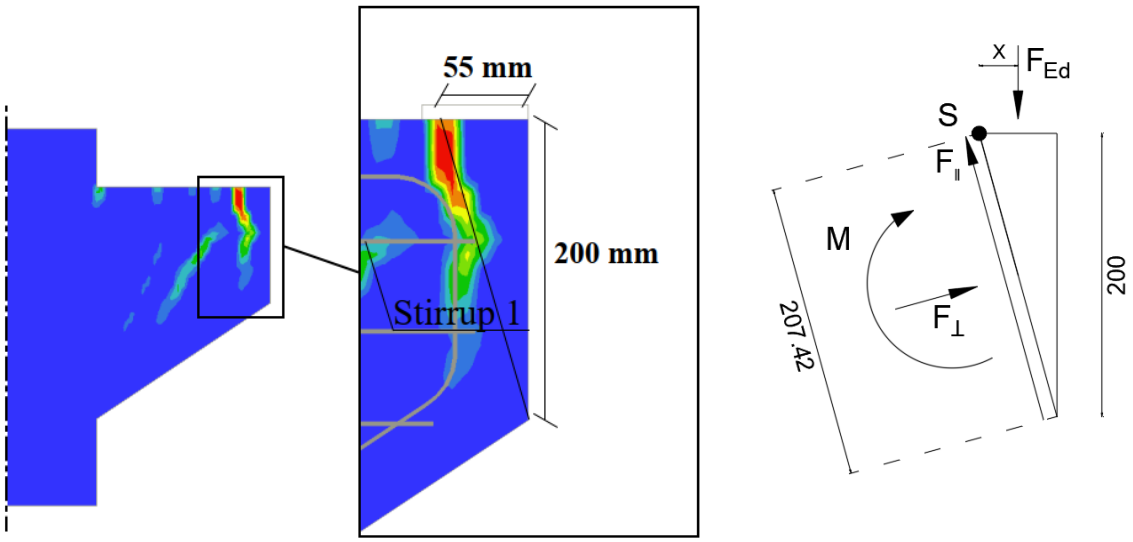

Figure 13.8 Schematisation of analytical calculation of the support end failure, dimensions in mm.

The interface stresses can be calculated by using force equilibrium and bending moment equilibrium at point "S" the following results are obtained:

$$(1)\ F_{\perp} = \frac{w}{l_{int}} * F_{Ed} = \frac{55}{207.45} * 17.7 * 55 = 258\ N/mm$$

$$(2)\ F_{II} = \frac{h}{l_{int}} * F_{Ed} = \frac{200}{207.45} * 17.7 * 55 = 938\ N/mm$$

$$(3)\ M = F_{\perp} * \frac{l_{int}}{2} - F_{Ed} * \frac{w}{2} = 938 * \frac{207.42}{2} - 17.7 * \frac{55^2}{2} = -10\ Nmm/mm$$

With the forces and the bending moments known, the stress distribution is calculated. Since the bending moment is of insignificant size, this has a negligible effect on the stress distribution. Dividing the force by the length of the interface results in the stresses.

$$(1)\ \sigma_{\perp} = \frac{F_{\perp}}{l_{int}} = \frac{258}{207.45} = 1.24\ N/mm^2$$

$$(2)\ \sigma_{II} = \frac{F_{II}}{l_{int}} = \frac{938}{207.45} = 4.5\ N/mm^2$$

With the axial stresses known, the resulting shear capacity for a concrete interface becomes:

$$v_{Rdi} = c * f_{ctd} + \mu * \sigma_n = 0.4 * \frac{2.5}{1.5} + 0.7 * 1.24 = 1.53\ MPa$$

Although, one could argue that the mean tensile strength of concrete should be used in order to approximate the mean strength, the calculation as followed.

$$v_{Rdi} = c * f_t + \mu * \sigma_n = 0.4 * 3.5 + 0.7 * 1.24 = 2.27\ MPa$$

The occurring shear strength, σ_{II}, exceeds the shear capacity by factor 2 (4.5 / 2.27). Therefore, the analytical model estimates that the support end failure should have occurred, albeit with a large difference compared to the numerical result.

Analytical calculation – specimen C

Specimen C failed as the vertical load remained 400 kN and the horizontal load reached 66.4 kN, resulting in uniform vertical and horizontal stresses of respectively 9.5 MPa and 1.58 MPa under the bearing plate (300x140 mm). In Figure 13.9, a schematisation of the analytical situation is displayed. In a similar manner, the trajectory of the crack is simplified by drawing a line between the crack at the surface and at the height of stirrup 1, as the crack proceeds in vertical direction from stirrup 1.

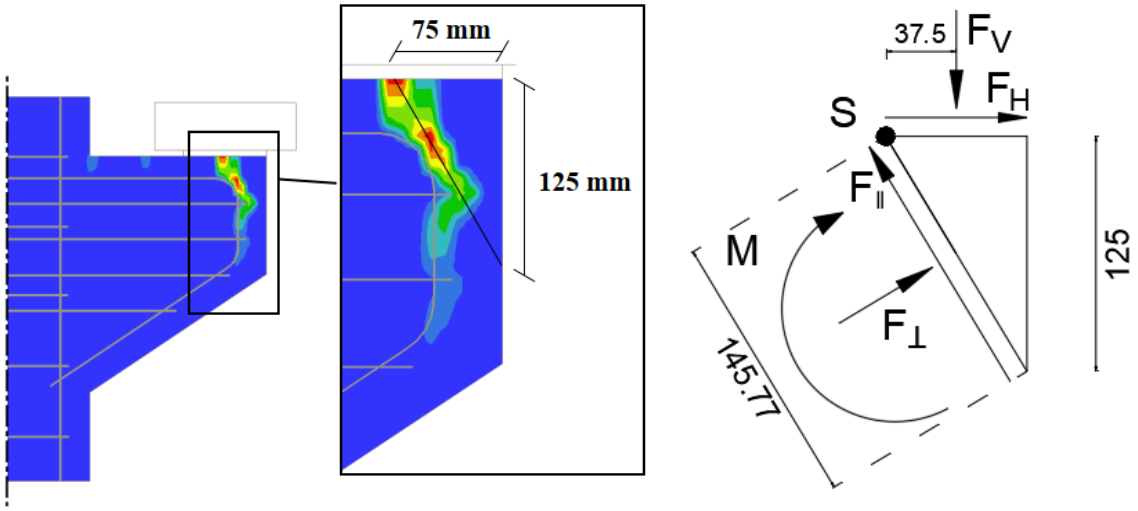

Figure 13.9 Schematised of analytical calculation of specimen C, dimensions in mm.

In a similar manner, the forces perpendicular and parallel to the interface are calculated.

$$(1)\ F_\perp = \frac{w}{l_{int}} * F_V - \frac{h}{l_{int}} F_H$$

$$= \frac{75}{145.77} * (9.5 * 75) - \frac{125}{145.77} * (1.58 * 75) = 265\ N/mm$$

$$(2)\ F_{II} = \frac{h}{l_{int}} * F_V + \frac{w}{l_{int}} F_H$$

$$= \frac{125}{145.77} * (9.5 * 75) + \frac{75}{145.77} * (1.58 * 75) = 672\ N/mm$$

$$(3)\ M = F_\perp * \frac{l_{int}}{2} - F_{Ed} * \frac{w}{2}$$

$$= 672 * \frac{145.77}{2} - 9.5 * \frac{75^2}{2} = 22259\ Nmm/mm$$

As the bending moment is of significant order of magnitude, the stress distribution along the interface is affected. Assuming the bending moment linearly distributes over the height of the interface, the following stress distribution is acquired (Figure 13.10).

$$\sigma_M = \frac{M}{W} = \frac{22259}{\frac{1}{6} * 145.77^2} = 6.29\ MPa$$

$$\sigma_{max} = \sigma_\perp \pm \frac{M}{W} = 1.81 \pm 6.29 = \ 8.1\ MPa\ (comp.)\ \&\ 4.47\ MPa\ (tens.)$$

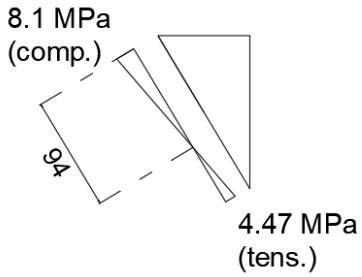

Figure 13.10 Stress distribution along the interface.

The stresses parallel to the interface are calculated accordingly.

$$\sigma_{II} = \frac{F_{II}}{l_{int}} = \frac{672}{145.77} = 4.61\ N/mm^2$$

The stresses parallel to the interface are only active along the interface which is in compression ($l_{int,comp}$). Therefore, the stresses are scaled to this length.

$$\sigma_{II} = \frac{l_{int}}{l_{int,comp}} * \sigma_{II} = \frac{145.77}{94} * 4.61 = \ 7.15\ N/mm^2$$

The axial stresses resulted in the following shear strengths.

$$v_{Rdi} = \ c * f_{ctd} + \mu * \sigma_n = 0.4 * \frac{2.5}{1.5} + 0.7 * 1.81 = 1.93\ MPa$$
$$v_{Rdi} = \ c * f_t + \mu * \sigma_n = 0.4 * 3.5 + 0.7 * 1.81 = 2.67\ MPa$$

As the shear stress of 7.15 MPa exceeds the mean capacity of 2.67 MPa, by a factor 2.67 (7.15/2.67). Similar to specimen B, the analytical model estimates that the support end failure should have occurred, with a similar margin as in specimen B.

13.2.4 Concluding remarks

A summarisation of the findings of the analytical approach are summed below.

- An analytical method, based on the shear resistance of an interface, was investigated on its applicability for a given situation, if the support end would occur.
- The analytical approach was tested on the numerical results of specimens B and C. In both instances the calculated shear stress exceeded the shear strength by factor 2 and 2.7 for specimen B and C, respectively. Whilst the analytical model suggest that the support end failure should have occurred, the approximation is inaccurate.

14 Discussion

The results of the model validation study and the numerical study of the support end failure, by means of several experiments, provided insight into the behaviour of the support end failure and showed that the behaviour could be numerically analysed. First, the finite element analyses are discussed. Subsequently, the causes as studied in Part II and the causes as observed in Part I are compared and discussed. Thirdly, the support end failure plane is discussed, comparing the findings from Part II to Part I. Lastly, the analytical model is discussed.

Numerical analysis
Neupane et al. (2017) experimentally investigated the support end failure mechanism and concluded that it could be accurately replicated by a 3D finite element model. The results of the 2D finite element model of this research show that it is able to replicate the experimental results to a certain extent. The most influential change in a 2D model is the assumption that all the elements are of the same thickness. In the experimental test by Neupane et al. (2017) a support was used over the entire width of the corbel, which the 2D model could mimic.

The design according to EC2 would in-practice maintain a distance from the support to all edges of the corbel. In the 2D model the support was modelled over the entire width of the corbel, which differs from a correct model. This results in differences between bearing stresses and the distribution of horizontal stresses perpendicular to the direction of load application. In Figure 10.7 the differences in horizontal stresses for the model in-practice and the 2D model are shown. Whilst the 2D model does not include the stresses in out-of-plane direction of the model, it remains to accurately capture the in-plane stresses and stress-distribution.

In addition, for the analysis of the support end failure behaviour, it is essential to study the largest tensile stress components in the corbel. Additionally, the numerical results indicated that the horizontal stress distribution below the inner half of the bearing pad followed the stress distribution as described in Figure 10.7. Lastly, the out-of-plane direction is not significant for the support end failure of the discussed corbel configurations, as the length of the bearing pad is larger than the width and the stresses can only be transferred in the direction of the column. Therefore, the assumption holds for this given corbel configuration.

Causes of support end failure
In the observed data, the support end failure never lead to collapse of a structure. Even more so, the corbels functioned even after damage. In the numerical experiments, however, the support end failure could only be accurately numerically studied if it lead to failure of the load application. Though, this does not imply that failure of the loading application, due to support end failure, indicates that the corbel has no residual capacity left. It can only be stated that for the given loading conditions the support end failure occurs. This was verified in the experimental study by Neupane et al. (2017), which showed that a corbel damaged by support

end failure, had a residual capacity of 95.5% its original capacity. Therefore, the author states that this numerical approach is valid, but conclusions should be drawn with care.

Based on the results of the data analysis, it was known that the support end failure is generally caused by continuity reinforcement combined with imposed horizontal loads, due to restrained deformation, or due to insufficient rotational freedom of the supported element. In the numerical studies, the support end failure was induced by placement of the support on the edge or by applying horizontal loading. Therefore, it is open to question whether the causes of the support end failure were studied like it occurs in practice.

One could argue that placement of a small bearing pad, such as in the model validation study and specimen B, on the edge of the corbel resembles, to some extent, the restrained rotation of a supported element. In both situations, the load is applied on the corbel by a insufficiently large support area. According to the experiment of Neupane et al. (2017) and the numerical results of specimen B, for a surface area of respectively 60x170 mm^2 and 70x300 mm^2 the support end failure occurred at an applied vertical load per corbel of 227 kN and 372 kN. In the author's opinion, these bearing capacities are unexpectedly large, as for specimen B the design load of 400 kN was almost reached. Although, these results are substantiated by the fact that this was experimentally proven by Neupane et al. (2017). This raises the question as to why the support end failure would occur in practice, if this unreinforced concrete edge has such a significant capacity. This uncertainty was enlarged by the results of specimen A, in which the bearing pad (140x300 mm^2) was placed on the edge of the corbel, yet the support end failure did not occur at a vertical load of 623 kN. The author suspects that in practice, the stresses underneath the bearing pad near the free edge of the corbel are higher due to deflection of the supported element. This was not taken into account in the numerical analysis. Although, one should pay attention to the influence of the stiffness of the bearing pad, as the author suspects that this effect is more beneficial for bearing materials with a higher stiffness.

Specimen C studied the influence of the horizontal loading, which in practice could be imposed by deformations of the supported element. Based on the data analysis, it was expected that horizontal loading would contribute to the support end failure, which was verified by specimen C. Although, the loading conditions at which the support end failure occurred, a vertical load of 400 kN and horizontal load of 67 kN, exceed the design load. Moreover, the study was performed for an unfavourable corbel configuration, in which the bearing pad was placed on the edge of the corbel. Therefore, in the author's opinion the individual contribution of the horizontal loading on the support end failure mechanism is unknown. Nevertheless, it is evident that it contributes to the development of the failure mechanism.

Furthermore, whilst specimen C studied the effect of horizontal loading on a corbel, it did not study the impact horizontal loading could have in the presence of continuity reinforcement. It is expected that for a smaller horizontal load the support end failure would occur.

Failure plane

In the experiment of Neupane et al. (2017) and the numerical experiments, the support end failure propagated along the entire height of the corbel. For a vertical load this could be explained based on the stress trajectories in the corbel. In the data analysis, it was also found that the failure plane of the support end failure could also develop as a shear plane. The author expected that specimen C, in which a horizontal load was applied on the corbel, would have portrayed the latter crack propagation. The crack did arise at an inclination between the surface

of the corbel and the main reinforcement. However, it further developed along the entire height of the corbel. This could have been influenced by the magnitude of vertical loading, which caused the crack to propagate in vertical direction. It is expected that the failure plane is affected by the height of the supporting element and the ratio between horizontal and vertical loading.

Analytical method

Whilst the results of the analytical model showed that the support end failure should have occurred for the given specimens, the model did not accurately approximate the numerical results. One of the main reasons is probably due to the assumption of crack plane. The approach is limited to the diagonal support end failure planes, although the failure planes of the numerical results were over the entire height of the corbel. Furthermore, the assumptions of the uniform stress distribution, for both vertical- and horizontal stresses, of the loading could have caused an overestimation of the applied shear stress. Whilst, this assumption is correct for an elastomer bearing pad, one should take this into account for different stress distributions. It is unknown whether this model provides more accurate results for a diagonal support end failure plane, as this would require more research.

15 Conclusion

As the support end failure remains one of the most frequently reoccurring types of damage in parking structures in The Netherlands, it is valuable to achieve a better understanding of its behaviour. Consequently, the research question of Part II was formed: *"To what extent can the behaviour of the support end failure be assessed by a parametric study using a finite element model?"*. By various finite element calculations of the support end failure, more insight was gained into its behaviour.

Experimental results were used as validation method for a 2D finite element model, which showed that the model could sufficiently replicate the experimental results and accurately describe the development of the failure crack. During preliminary analysis of the model it was found that only a fixed crack model could capture the failure mechanism. Additionally, a mesh sensitivity study concluded that mesh sizes larger than 10x10 mm^2 could not accurately portray the failure mechanism.

Several numerical studies were conducted on different corbel configurations to study the impact of parameters on the support end failure mechanism, including the behaviour of a corbel designed in accordance with Eurocode 2. The results showed that for a vertical load, the support end failure crack initiates below the surface of the corbel, while for a horizontal load, the crack initiates at the surface. Furthermore, the characteristic vertical crack propagation along the height of the corbel propagates in vertical direction due to disruption of the principal stress trajectory by cracks. It was established that for a uniform load combined with a support on the edge of a corbel, the support end failure mechanism does not have to occur. Furthermore, as the support width was reduced by half, under identical loading conditions, the support end failure occurred. These results were substantiated by the experimental results of Neupane et al. (2017). Additionally, it was found that by increasing a horizontal load, in combination with the support on the edge of the corbel, the support end failure could also be initiated. Despite these observations, in both instances a significant load had to be applied before the failure mechanism was initiated.

Moreover, an analytical approach was investigated with the aim to approximate if the support end failure could occur for known corbel dimensions and loading conditions. The results of the analytical model suggested that the exerted forces exceeded its capacity by a factor 2 – 2.5. Therefore, it was concluded that the analytical model does not accurately estimate the numerical results, for a support end failure crack spanning the entire height of the corbel.

In conclusion, part II of this research showed that a 2D finite element model can be used to accurately analyse the support end failure behaviour. With numerical experiments it was found that horizontal loading, position and size of the bearing pad contribute to the support end failure mechanism. Although, a significant load had to be reached before the failure mechanism occurred. Therefore, further research is required to determine the underlying causes of the frequent occurrence of this failure mechanism in practice.

16 Recommendations

Even though this research studied the behaviour of the support end failure mechanism, further research is required to obtain the underlying reason for the frequent observations of the support end failure in practice. Several recommendations are given on potential research on the support end failure behaviour.

Continuity reinforcement
The data analysis suggested that grouting of continuity reinforcement between support and supported element is a prevalent cause of support end failure. As the continuity reinforcement is integrated in the corbel, the author suspects that it affects the failure plane of the support end failure greatly. Additionally, it is expected that with a smaller horizontal loading the support end failure is initiated.

Stress distribution
The bearing pad in the exploratory study was assumed to be a soft elastomer, which deforms significantly under loading. The stiffness of the bearing material affects both the vertical stress distribution onto the concrete and rotational capacity of the supported element. It is expected that for stiffer bearing materials rotation of supported element would have a greater effect on the support end failure than soft bearing materials.

Parametric study on design configuration
Although the conducted numerical studies provided insight into the influence of the placement of and length bearing pad and the horizontal loading, more configurations related to faults made in practice could be studied. A fault which was frequently observed was an exorbitant amount of concrete cover. It is expected that the support end failure initiates at a smaller applied load for a configuration with a larger concrete cover. Additionally, since the failure mechanism is entirely reliant on the concrete section, additional studies could establish relations between failure load and corbel dimensions.

References

ACI Committee 362. (2000). 362.2R-00: Guide for Structural Maintenance of Parking Structures. In *American Concrete Institute*. Retrieved February 7, 2024, from https://www.concrete.org/publications/internationalconcreteabstractsportal/m/details/id/10245

Ahmad, S. (2003). Reinforcement corrosion in concrete structures, its monitoring and service life prediction—a review. *Cement and Concrete Composites*, *25*(4–5), 459–471. https://doi.org/10.1016/s0958-9465(02)00086-0

ASCE. (2005). *2005 Report Card for America's Infrastructure*. https://doi.org/10.1061/9780784478851

Bos, E., Van Savooyen, E., Blankendaal, M., & Delleman, P. (2020). *Parkeren in het ruimtelijk domein*.

Braam, R. (2010). Rekenvoorbeelden bij Eurocode 2 (13): Consoles. *Cement*, 58–64.

Broomfield, J. P. (2003). *Corrosion of Steel in Concrete: Understanding, Investigation and Repair, second edition*. https://doi.org/10.1201/9781482265491

Červenka, V., Jendele, L., & Červenka, J. (2021). *ATENA Program Documentation Part 1 T heory*. Retrieved June 24, 2024, from https://www.cervenka.cz/assets/files/atena-pdf/ATENA_Theory.pdf

Choi, Y. H., Kim, J., & Lee, K. (2006). Corrosion behavior of steel bar embedded in fly ash concrete. *Corrosion Science*, *48*(7), 1733–1745. https://doi.org/10.1016/j.corsci.2005.05.019

Collins, M. P., & Mitchell, D. (1991). *Prestressed concrete structures*. http://ci.nii.ac.jp/ncid/BA1148279X

Combrinck, R., & Boshoff, W. P. (2013). Typical plastic shrinkage cracking behaviour of concrete. *Magazine of Concrete Research*, *65*(8), 486–493. https://doi.org/10.1680/macr.12.00139

Concept Ingenieurs. (n.d.). *Parkeergarages*. conceptingenieurs.nl. Retrieved February 6, 2024, from https://conceptingenieurs.nl/diensten/inspectie-en-diagnose/parkeergarages

Cusson, D. (2009). Durability of repaired concrete structures. In *Failure, distress, and repair of concrete structures* (pp. 296–321). Woodhead Publishing Series in Civil and Structural Engineering. https://doi.org/10.1533/9781845697037.2.296

Darmawan, M. S. (2010). Pitting corrosion model for reinforced concrete structures in a chloride environment. *Magazine of Concrete Research, 62*(2), 91–101. https://doi.org/10.1680/macr.2008.62.2.91

De Boer, S. J., & Van Haastert, J. (n.d.). *PARKEERGARAGES*. Retrieved February 6, 2024, from https://handboek-prefab-beton.betonhuis.nl/Documenten/PBTO-hoofdstuk-11.pdf

De Jong, P. (1992). Bouwschade ter lering (I). *Cement, 2*, 26–28. https://www.cementonline.nl/artikelen/bouwschade-ter-lering-i

De Schutter, G. (2017). *Damage to concrete structures*. https://doi.org/10.1201/b12914

De Vree, J. (n.d.). *Breedplaatvloer, bekistingsplaatvloer*. joostdevree.nl. Retrieved February 12, 2024, from https://www.joostdevree.nl/shtmls/breedplaatvloer.shtml

Donnelly, J. P., Pulver, B. E., & Popovic, P. L. (2006). Condition assessment of parking structures. *Structures Congress 2006*. https://doi.org/10.1061/40889(201)105

Eichburg, D., Feero, B. A., & Nicastro, D. (2015, January 7). *Bearing pad durability in precast concrete garages*. Retrieved July 15, 2024, from https://www.constructionspecifier.com/bearing-pad-durability-in-precast-concrete-garages/

Engelaar, R. (n.d.). *De parkeergarage in aanbouw bij Eindhoven Airport stortte in 2017 in.* https://www.leidschdagblad.nl/cnt/dmf20220201_19445806?utm_source=google&utm_medium=organic

FIB. (2013). *fib Model Code for Concrete Structures 2010*. https://doi.org/10.1002/9783433604090

Forster, S. J., & Powell, R. E. (1994). Experimental investigation on rectangular corbels cast in high strength concrete. *UNICIV Report, R-338*. https://trid.trb.org/view/1150481

Fu, C., De-Ming, F., Ye, H., Huang, L., & Wang, J. (2021). Bond degradation of non-uniformly corroded steel rebars in concrete. *Engineering Structures*, *226*, 111392. https://doi.org/10.1016/j.engstruct.2020.111392

Hansson, C., Poursaee, A., & Jaffer, S. (2012). Corrosion of Reinforcing Bars in Concrete. *The Masterbuilder*, 106–124. http://ceramrtr.ceramika.agh.edu.pl/~szyszkin/eis/Corrosion%20Of%20Reinforcing%20Bars%20In%20Concrete.pdf

Hendriks, M. a. N., & Roosen, M. A. (2022). *Guidelines for Nonlinear Finite Element Analysis of Concrete Structures* (Report RTD:1016-1: 2022). Rijkswaterstaat Centre for Infrastructure.

Hermanson, B. R., & Cowan, J. (1974). Modified Shear-Friction theory for bracket design. *Journal of the American Concrete Institute*, *71*(2), 55–60. https://doi.org/10.14359/11169

Holt, E., & Leivo, M. (2004). Cracking risks associated with early age shrinkage. *Cement and Concrete Composites*, *26*(5), 521–530. https://doi.org/10.1016/s0958-9465(03)00068-4

Hordijk, D. (1991). Local approach to fatigue of concrete. *Doctor Dissertation*, ISBN 90-9004519-8.

Iqbal, M. (2007). Thermal movements in parking structures. *Aci Structural Journal*, *104*(5), 542–548. https://doi.org/10.14359/18856

Jabed, A., Tusher, M. M. H., Shuvo, Md. S. I., & Imam, A. (2023). Corrosion of Steel Rebar in Concrete: A Review. *Corrosion Science and Technology*, *22*(4), 273–286. https://doi.org/10.14773/cst.2023.22.4.273

Jang, S. Y., Kim, B. S., & Oh, B. H. (2011). Effect of crack width on chloride diffusion coefficients of concrete by steady-state migration tests. *Cement and Concrete Research*, *41*(1), 9–19. https://doi.org/10.1016/j.cemconres.2010.08.018

Keßler, S., Thiel, C., Große, C. U., & Gehlen, C. (2016). Effect of freeze–thaw damage on chloride ingress into concrete. *Materials and Structures*, *50*(2). https://doi.org/10.1617/s11527-016-0984-4

Kleinman, C. S. (2006, July 1). *Nokken met die tanden (1)*. Cement. Retrieved February 19, 2024, from https://www.cementonline.nl/artikel/nokken-met-die-tanden-1

Kovler, K., & Chernov, V. Y. (2009). Types of damage in concrete structures. In *Elsevier eBooks* (pp. 32–56). https://doi.org/10.1533/9781845697037.1.32

Kriz, L. B., & Raths, C. H. (1965). Connections in Precast Concrete Structures—Strength of Corbels. *PCI Journal*, *10*(1), 16–61. https://doi.org/10.15554/pcij.02011965.16.61

Lai, J., Cai, J., Chen, Q., He, A., & Wei, M. (2020). Influence of crack width on chloride penetration in concrete subjected to alternating Wetting–Drying cycles. *Materials*, *13*(17), 3801. https://doi.org/10.3390/ma13173801

Leonhardt, F. (1977). *Vorlesungen über Massivbau* (3rd ed., Vol. 3). Springer.

Liitvan, G. G., & Bickley, J. A. (1987). *Durability of Parking Structures: Analysis of Field Survey* (Vol. 100). https://doi.org/10.14359/3325

Lopes, A. N. M., Fonseca Silva, E., Dal Molin, D. C. C., & Toledo Filho, R. D. (2013). Shrinkage-reducing-admixture: effect on durability of high-strength concrete. *ACI Materials Journal*, *110*(4), 365–374.

Malhotra, V. M., Zhang, M. H., & Leaman, G. H. (2000). Long-Term performance of steel reinforcing bars in portland cement concrete incorporating moderate and high volumes of ASTM Class F Fly Ash. *American Concrete Institute, Journal Of*, *97*(4), 409–417. https://doi.org/10.14359/7401

Mattock, A. H. (1976). Design proposals for reinforced concrete corbels. *Prestressed Concrete Institute*, *21*(3), 18–42.

Ministerie van Infrastructuur en Waterstaat. (2021, March 3). *Meer laadpalen in parkeergarages*. Rijksoverheid.nl. Retrieved February 7, 2024, from https://www.rijksoverheid.nl/actueel/nieuws/2021/03/04/meer-laadpalen-in-parkeergarages#:~:text=Er%20zijn%20in%20Nederland%20zo,gemiddeld%20zo'n%20450%20parkeerplekken.

Monroe, D. C. (2001). THE STRUCTURAL MAINTENANCE OF PARKING GARAGES. *Parking: The Magazine of the Parking Industry*, *40*(9). https://trid.trb.org/view/714946

Nederlands Normalisatie Instituut. (2011). Eurocode 2: Ontwerp en berekening van betonconstructies - Deel 1-1: Algemene regels en regels voor gebouwen. In *Eurocode* (NEN-EN 1992-1-1:2005+C2:2011 nl).

Nederlands Normalisatie Instituut. (2007). *NEN 6702: Technische grondslagen voor bouwconstructies - TGB 1990 - Belastingen en vervormingen*.

Neupane, R. C., Eddy, L., & Nagai, K. (2017). Investigation on strengthening approaches adopted for poorly detailed RC corbels. *Fibers*, *5*(2), 16. https://doi.org/10.3390/fib5020016

NOS. (2017, May 27). *Deel nieuwe parkeergarage Eindhoven Airport ingestort*. https://nos.nl/artikel/2175278-deel-nieuwe-parkeergarage-eindhoven-airport-ingestort

NOS. (2018, December 17). *"Gestuntel" bij bouw van ingestorte garage Wormerveer*. Retrieved June 3, 2024, from https://nos.nl/artikel/2264007-gestuntel-bij-bouw-van-ingestorte-garage-wormerveer

NOS. (2024, May 30). *Ingestorte hellingbanen in parkeergarage Nieuwegein overgeslagen bij inspecties*. https://nos.nl/artikel/2522526-ingestorte-hellingbanen-in-parkeergarage-nieuwegein-overgeslagen-bij-inspecties

Nuiten, P. C., & Rinsma, J. (2021). DUURZAAM ONDERHOUD PARKEERGARAGES. *vlb-brance.nl*. Retrieved February 7, 2024, from https://vlb-branche.nl/pdf/7-handreiking-duurzaam-onderhoud-parkeergarages-duurzaam-ontwerp-nov-2021.7af747.pdf

Phan, L. T. (1996). *Fire performance of High-Strength Concrete: A report of the State-of-the-Art* (Vol. 5943). National Insitute of Standards and Technology.

Pradhan, B., & Bhattacharjee, B. (2011). Rebar corrosion in chloride environment. *Construction and Building Materials*, *25*(5), 2565–2575. https://doi.org/10.1016/j.conbuildmat.2010.11.099

Rabbat, B. G., & Russell, H. G. (1985). Friction coefficient of steel on concrete or grout. *Journal of Structural Engineering*, *111*(3), 505–515. https://doi.org/10.1061/(asce)0733-9445(1985)111:3(505

Rijksoverheid. (2022, April 22). Onderzoek TNO leidt tot grote versnelling in de beoordeling CC2-constructies met breedplaatvloeren. *Cementonline*. Retrieved April 5, 2024, from https://www.cementonline.nl/onderzoek-tno-leidt-tot-grote-versnelling-in-de-beoordeling-cc2-constructies-met-breedplaatvloeren

Ryou, J., & Ann, K. Y. (2008). Variation in the chloride threshold level for steel corrosion in concrete arising from different chloride sources. *Magazine of Concrete Research*, *60*(3), 177–187. https://doi.org/10.1680/macr.2008.60.3.177

Šavija, B., & Schlangen, E. (2011). Chloride ingress in cracked concrete- a literature review. In *Rilem bookseries* (pp. 133–142). https://doi.org/10.1007/978-94-007-2703-8_14

SGS Intron. (2017). *Meer constructieproblemen bij parkeergarages*. Retrieved February 5, 2024, from https://www.sgs.com/-/media/sgscorp/documents/corporate/brochures/otar-sgs-intron-problemen-parkeergarages-a4-nl-17-07.cdn.nl-BE.pdf

SGS Intron. (2019). *PARKEERGARAGES ONDERZOEK EN OPLOSSINGEN BIJ SCHADES EN CONSTRUCTIEPROBLEMEN*. Retrieved February 5, 2024, from https://www.sgs.com/-/media/sgscorp/documents/corporate/brochures/sgs-ind-parkeergarages-onderzoek-naar-schade-en-constructieproblemen-nl.cdn.nl-NL.pdf

Sheng, J., & Xia, J. (2017). Effect of simulated pitting corrosion on the tensile properties of steel. *Construction and Building Materials*, *131*, 90–100. https://doi.org/10.1016/j.conbuildmat.2016.11.037

Slowik, V., Schmidt, M., & Fritzsch, R. (2008). Capillary pressure in fresh cement-based materials and identification of the air entry value. *Cement and Concrete Composites*, *30*(7), 557–565. https://doi.org/10.1016/j.cemconcomp.2008.03.002

Somerville, G. (1973). The Behaviour and Design of Reinforced Concrete Corbels. In *Shear in Reinforced Concrete* (SP-42, pp. 477–502). American Concrete Institute.

Stergiopoulou, C., Aggour, M. S., & McCuen, R. H. (2008). Nondestructive testing and evaluation of concrete parking garages. *Journal of Infrastructure Systems*, *14*(4), 319–326. https://doi.org/10.1061/(asce)1076-0342(2008)14:4(319

StructureCare. (n.d.). *Parking Garage Deterioration Guide*. Retrieved February 5, 2024, from https://www.structurecareus.com/structurecare-blog/parking-garage-deterioration-guide/

Tazawa, E. (1999). *Autogenous shrinkage of concrete*. https://doi.org/10.1201/9781482272123

Tighe, M. R., & Van Volkinburg, D. (1989). Parking garage crisis. *Civil Engineering*, *59*(9), 70–73. https://cedb.asce.org/CEDBsearch/record.jsp?dockey=0063664

TNO. (2023, November 14). *Vernieuwing oudere infrastructuur essentieel en urgent*. tno.nl/nl. Retrieved February 7, 2024, from https://www.tno.nl/nl/newsroom/2023/11/vernieuwing-infrastructuur-essentieel/

Valenza, J. J., & Scherer, G. W. (2007). A review of salt scaling: I. Phenomenology. *Cement and Concrete Research*, *37*(7), 1007–1021. https://doi.org/10.1016/j.cemconres.2007.03.005

Van Den Broek, T. & Betonhuis. (2019, September 12). *Samenstellende onderdelen van parkeergarages*. Betonhuis. Retrieved February 6, 2024, from https://betonhuis.nl/constructief-prefab/handboek/parkeergarages/samenstellende-onderdelen

Van Mier, J. G. M. (1986). Multiaxial strain-softening of concrete. *Materials and Structures*, *19*(3). https://doi.org/10.1007/bf02472034

Velthorst, C. (2007). Ontwerpaspecten met betrekking tot scheurvorming in de constructieve druklaag op vloeren van voorgespannen kanaalplaten. *Stufib*, *15*. https://repository.tudelft.nl/islandora/object/uuid%3A622ae2b5-d3d5-4753-aa2c-d5e0846e417c

Win, P. P., Watanabe, M., & Machida, A. (2004). Penetration profile of chloride ion in cracked reinforced concrete. *Cement and Concrete Research*, *34*(7), 1073–1079. https://doi.org/10.1016/j.cemconres.2003.11.020

Yun, Y. M., Alshegeir, A., & Ramirez, J. A. (1994). Strut-Tie model design of disturbed regions in concrete structures. *Structures Congress XII*, 233–238. https://cedb.asce.org/CEDBsearch/record.jsp?dockey=0086676

Yun, Y. M., & Chae, H. S. (2019). An optimum indeterminate strut-and-tie model for reinforced concrete corbels. *Advances in Structural Engineering*, *22*(12), 2557–2571. https://doi.org/10.1177/1369433219845689

Zhao, Y., Xu, X., Wang, Y., & Dong, J. (2020). Characteristics of pitting corrosion in an existing reinforced concrete beam exposed to marine environment. *Construction and Building Materials*, *234*, 117392. https://doi.org/10.1016/j.conbuildmat.2019.117392

Appendix A

Table A- 1 Dataset of forensic files from Adviesbureau Hageman.

Dossier	Type of damge	Cause	Element	Sub-element	Year of inspection	Type of structure	Construction year
1	Cracks	Restrained deformation	Floor	Monolithic	1977	Aboveground	1977
2	Cracks	Restrained deformation	Wall	In-situ	1977	Aboveground	1975
	Cracks	Restrained deformation	Floor	Monolithic	1977	Aboveground	1975
3	Cracks	Incorrect execution	Floor	Compressive layer	1977	Aboveground	1977
4	Support end failure	Incorrect design	Beam		1980	Aboveground	1975
	Leaking cracks	Incorrect execution	Floor	Monolithic	1980	Aboveground	1975
5	Cracks	Restrained deformation	Floor	Monolithic	1979	Aboveground	1979
6	Support end failure	Continuity rebar	Corbel		1984	Aboveground	1972
7	Cracks	Incorrect design	Beam		1987	Aboveground	1988
8	Corrosion	Insufficient cover	Roof	In-situ	1989	Underground	1974
9	Cracks	Overloading	Floor	TT	1992	Aboveground	1991
10	Cracks	Restrained deformation	Floor joint	SV-slab	1989	Underground	1985
	Cracks	Insufficient bearing material	Beam		1989	Underground	1985
11	Cracks	Restrained deformation	Floor	TT	1994	Aboveground	1994
12	Cracks	Restrained deformation	Floor	Monolithic	1995	Underground	1993
13	Leaking cracks	Restrained deformation	Floor joint	TT	1995	Underground	1994
14	Support end failure	Restrained deformation	Corbel		1998	Aboveground	1995
15	Broken rebar	Improper execution	Expansion joint		2000	Aboveground	1976
16	Leaking cracks	Restrained deformation	Floor joint	Filigree slab	2001	Aboveground	2000
	Cracks	Restrained deformation	Floor	Compressive layer	2001	Aboveground	2000
	Leakage	Failed sealant	Expansion joint		2001	Aboveground	2000

17	Cracks	Restrained deformation	Floor	Compressive layer	2000	Underground	2000
18	Support end failure	Restricted rotation	Column		2001	Aboveground	2000
19	Corrosion	Insufficient cover	Beam		2001	Underground	1972
	Spalling	Fire	Floor	Monolithic	2001	Underground	1972
	Cracks	Overloading	Beam		2001	Underground	1972
20	Camber difference	Setting formwork	Parking deck		2002	Aboveground	
21	Cracks	Restrained deformation	Floor joint	Hollowcore slab	2002	Underground	2002
22	Spalling	Fire	Floor	TT	2002	Underground	1995
23	Delamination	Improper execution	Floor	Compressive layer	2002	Underground	2002
24	Cracks	Restrained deformation	Floor	VQ-slab	2003	Underground	2001
25	Spalling	Fire	Floor	TT	2003	Aboveground	2001
26	Leaking cracks	Restrained deformation	Floor	Compressive layer	2006	Underground	2001
27	Cracks	Restrained deformation	Floor	Compressive layer	2003	Underground	2002
	Cracks	Restrained deformation	Wall	In-situ	2003	Underground	2002
28	Support end failure	Continuity rebar	Beam		2004	Aboveground	2000
29	Cracks	Restrained deformation	Floor	Monolithic	2005	Underground	1989
	Cracks	Improper curing	Floor	Monolithic	2005	Underground	1989
30	Support end failure	Continuity rebar	Beam		2005	Underground	1994
31	Cracks	Restrained deformation	Floor joint	Hollowcore slab	2005	Aboveground	2003
	Cracks	Restrained deformation	Wall		2005	Aboveground	2003
	Support end failure	Improper detailing	Column		2005	Aboveground	2003
	Cracks	Restrained deformation	Beam		2005	Aboveground	2003
	Extruded sealant	Incorrect design	Expansion joint		2005	Aboveground	2003
32	Support end failure	Unknown	Beam		2006	Underground	1995
33	Leaking cracks	Restrained deformation	Floor	Filigree slab	2006	Underground	1996
	Leakage	Improper execution	Wall joint		2006	Underground	1996
34	Leaking cracks	Restrained deformation	Wall	Sheet pile wall	2006	Underground	1996

35	Cracks	Unknown	Beam		2006	Underground	2000
36	Cracks	Restrained deformation	Floor	Compressive layer	2007	Underground	2003
	Cracks	Restrained deformation	Floor joint	Hollowcore slab	2007	Underground	2003
	Cracks	Restrained rotation	Floor	Hollowcore slab	2007	Underground	2003
37	Support end failure	Unknown	Wall		2007	Underground	1988
	Camber difference	Setting formwork	Floor	Monolithic	2007	Underground	1988
	Gravel pocket	Improper execution	Column		2007	Underground	1988
	Cracks	Restrained deformation	Beam		2007	Underground	1988
	Cracks	Missing joint	Expansion joint		2007	Underground	1988
	Cracks	Restrained deformation	Wall	In-situ	2007	Underground	1988
38	Leakage	Incorrect design joint material	Expansion joint	Filigree slab	2007	Aboveground	1987
	Cracks	Missing joint	Expansion joint	Beam	2007	Aboveground	1987
	Cracks	Restrained deformation	Floor	Parking deck	2007	Aboveground	1987
	Leaking cracks	Restrained deformation	Floor	Parking deck	2007	Aboveground	1987
39	Support end failure	Restrained deformation	Half-joint	Beam	2007	Underground	2002
40	Cracks	Restrained deformation	Floor	Filigree slab	2007	Underground	2002
41	Spalling	Fire	Floor	Hollowcore slab	2007	Underground	2003
42	Leaking cracks	Restrained deformation	Floor	Monolithic	2007	Underground	2006
43	Collapse	Excentric loading during construction	Floor	Hollowcore slab	2007	Aboveground	2007
44	Cracks	Restrained deformation	Floor	Filigree slab	2007	Underground	2007
45	Cracks	Restrained deformation	Floor	Hollowcore slab	2008	Underground	2007
46	Broken rebar	Improper execution	Floor	Parking deck	2008	Aboveground	1987
47	Cracks	Restrained deformation	Floor	Monolithic	2009	Underground	2006
48	Cracks	Restrained deformation + other	Floor	Monolithic	2008	Underground	1998
	Cracks	Restrained deformation + other	Floor	Filigree slab	2008	Underground	1998
49	Spalling	Fire	Floor	TT	2008	Aboveground	2005
50	Cracks	Corrosion	Column		2008	Aboveground	1994
	Corrosion	Unknown	Column		2008	Aboveground	1994

51	Support end failure	Restricted rotation	Expansion joint	Beam	2008	Underground	2007
52	Cracks	Restrained deformation	Floor	Filigree slab	2008	Underground	2002
	Cracks	Unknown	Floor	Filigree slab	2008	Underground	2002
	Corrosion	Contaminations in concrete	Floor	Filigree slab	2008	Underground	2002
	Cracks	Restrained deformation	Wall	In-situ	2008	Underground	2002
	Cracks	Restrained deformation	Beam		2008	Underground	2002
	Support end failure	Improper bearing material	Beam		2008	Underground	2002
	Support end failure	Collision	Stairs		2008	Underground	2002
	Cracks	Restrained deformation	Floor	Hollowcore slab	2008	Underground	2002
	Cracks	Unknown	Floor	Hollowcore slab	2008	Underground	2002
	Cracks	Restrained deformation	Floor	Compressive layer	2008	Underground	2002
	Cracks	Restrained deformation	Ramp		2008	Underground	2002
	Leaking cracks	Restrained deformation	Floor joint	Hollowcore slab	2008	Underground	2002
53	Leaking cracks	Restrained deformation	Floor	Monolithic	2009	Underground	2007
54	Leakage	Incorrect design	Wall	Sheet pile wall	2009	Underground	1999
55	Cracks	Restrained deformation	Column		2009	Underground	2001
	Support end failure	Improper bearing material	Column		2009	Underground	2001
	Support end failure	Walking bearing pad	Beam		2009	Underground	2001
56	Leakage	Incorrect design	Wall	Sheet pile wall	2010	Underground	2003
	Cracks	Restrained deformation	Floor	Filigree slab	2010	Underground	2003
57	Cracks	Restrained deformation	Floor	Filigree slab	2010	Underground	2006
58	Cracks	Restrained deformation	Floor	Compressive layer	2010	Underground	2001
59	Cracks	Plastic settlement	Floor	Monolithic	2010	Underground	2007
60	Leakage	Plastic settlement	Wall	Diaphragm wall	2010	Underground	2007
61	Cracks	Restrained deformation	Floor	Compressive layer	2010	Underground	2003
	Cracks	Restrained deformation	Floor	Compressive layer	2010	Underground	2003
62	Cracks	Restrained deformation	Column		2010	Aboveground	2005

63	Cracks	Restrained deformation	Floor	Monolithic	2010	Underground	2010
64	Spalling	Fire	Floor	Filigree slab	2010	Underground	2004
65	Support end failure	Walking bearing pad	Beam		2010	Underground	2001
66	Cracks	Improper detailing	Corbel		2011	Underground	1997
67	Spalling	Fire	Floor	TT	2012	Aboveground	1974
68	Leaking cracks	Restrained deformation	Floor	Monolithic	2011	Underground	2007
	Cracks	Torsion	Expansion joint		2013	Underground	2007
	Cracks	Improper curing	Floor	Monolithic	2013	Underground	2007
69	Cracks	Restrained rotation	Column		2011	Underground	2008
70	Cracks	Restrained deformation	Floor coating	Hollowcore slab	2011	Underground	2003
71	Cracks	Restrained deformation	Floor	Filigree slab	2011	Underground	2006
	Cracks	Restrained deformation	Wall		2011	Underground	2006
	Walking bearing pad	Horizontal displacement	Expansion joint	Beam	2011	Underground	2006
	Defect	Incorrect detailing of reinforcement in half-joint	Expansion joint	Beam	2011	Underground	2006
72	Spalling	Fire	Floor	Hollowcore slab	2011	Underground	2002
73	Leaking cracks	Restrained deformation	Wall		2012	Underground	2011
74	Defect	Incorrect detailing of reinforcement in half-joint	Half-joint		2012	Underground	1970
75	Cracks	Restrained deformation	Floor	Filigree slab	2012	Aboveground	2007
	Spalling	Corrosion	Floor	Filigree slab	2012	Aboveground	2007
	Corrosion	Incorrect design	Floor	Filigree slab	2012	Aboveground	2007
76	Cracks	Restrained deformation	Floor	Hollowcore slab	2013	Underground	2006
77	Cracks	Continuity rebar	Half-joint		2013	Underground	2006
78	Spalling	Fire	Floor	Filigree slab	2013	Underground	1998
79	Cracks	Restrained deformation	Floor	Filigree slab	2013	Aboveground	2007
80	Cracks	Restrained deformation	Floor	Compressive layer	2013	Aboveground	2011
81	Cracks	Restrained deformation	Floor	Monolithic	2013	Underground	2006

	Leakage	Discontinuous expansion joint	Expansion joint		2013	Underground	2006
	Corrosion	Leakage	Sheet pile wall		2013	Underground	2006
82	Cracks	Restrained deformation	Floor joint	Hollowcore slab	2013	Underground	2011
	Cracks	Restrained deformation	Floor	Compressive layer	2013	Underground	2011
83	Cracks	Unknown	Half-joint	Beam	2013	Underground	1978
	Cracks	Unequal settlements	Floor	TT	2013	Underground	1978
	Cracks	Incorrect execution	Column		2013	Underground	1978
84	Support end failure	Continuity rebar	Column		2014	Aboveground	1991
85	Walking bearing pad	Incorrect design	Corbel		2014	Aboveground	2007
	Support end failure	Continuity rebar	Corbel		2014	Aboveground	2007
86	Cracks	Restrained deformation	Floor	Monolithic	2015	Underground	2009
87	Cracks	Restrained deformation	Floor	Filigree slab	2015	Aboveground	2002
88	Cracks	Restrained deformation	Floor	Monolithic	2014	Underground	2010
89	Leaking cracks	Restrained deformation	Floor	Hollowcore slab	2015	Underground	2002
90	Leaking cracks	Restrained deformation	Floor	Unknown	2016	Underground	1989
91	Corrosion	Water ingress in duct	Floor	Post-tensioned	2015	Aboveground	1975
	Leaking cracks	Tendon corrosion	Floor	Post-tensioned	2015	Aboveground	1975
	Corrosion	Water ingress in duct	Floor	Post-tensioned	2015	Aboveground	1972
	Support end failure	Walking bearing pad	Corbel		2015	Aboveground	1975
92	Cracks	Corrosion	Half-joint		2015	Aboveground	1980
	Corrosion	Unknown	Half-joint		2015	Aboveground	1980
93	Spalling	Fire	Floor	TT	2015	Aboveground	1986
94	Leaking cracks	Restrained deformation	Floor	Post-tensioned	2016	Aboveground	1972
	Corrosion	Existing cracks	Floor	Post-tensioned	2016	Aboveground	1972
	Exposed tendon	Degradation	Floor	Post-tensioned	2016	Aboveground	1972
95	Support end failure	Continuity rebar	Corbel		2016	Aboveground	2005
96	Corrosion	Unknown	Half-joint		2016	Underground	1999
	Spalling	Corrosion	Half-joint		2016	Underground	1999
97	Corrosion	Chloride	Floor	Monolithic	2017	Aboveground	1967

	Cracks	Corrosion	Floor	Monolithic	2017	Aboveground	1967
	Cracks	Restrained deformation	Floor	Monolithic	2017	Aboveground	1967
98	Cracks	Restrained deformation	Floor	Monolithic	2017	Underground	1970
	Delamination	Unequal deformations	Floor	Monolithic	2017	Underground	1995
99	Collapse	Incorrect design of filligree joints	Floor	Filigree slab	2017	Aboveground	2017
100	Cracks	Restrained deformation	Floor	Hollowcore slab	2018	Aboveground	2009
101	Support end failure	Restrained deformation	Half-joint		2018	Aboveground	1991
	Defect	Incorrect detailing of reinforcement in half-joint	Half-joint		2018	Aboveground	1991
	Gravel pocket	Improper execution	Half-joint		2018	Aboveground	1991
102	Spalling	Fire	Floor	Hollowcore slab	2018	Underground	1990
103	Cracks	Restrained deformation	Floor	Hollowcore slab	2019	Aboveground	2011
104	Leakage	Incorrect design	Expansion joint		2018	Underground	2006
105	Cracks	Restrained deformation	Floor	Compressive layer	2018	Aboveground	2010
	Spalling	Frozen water in shaft	Floor	Hollowcore slab	2018	Aboveground	2010
	Support end failure	Improper bearing material	Wall	In-situ	2018	Aboveground	2010
	Cracks	Incorrect design	Corbel		2018	Aboveground	2010
106	Corrosion	Water ingress in duct	Floor	Post-tensioned	2019	Aboveground	1975
	Corrosion	Water ingress in duct	Floor	Post-tensioned	2019	Aboveground	1975
107	Cracks	Restrained deformation	Column		2019	Aboveground	2000
	Spalling	Carbonation	Floor	Monolithic	2019	Aboveground	2000
108	Support end failure	Improper bearing material	Half-joint		2019	Underground	2002
	Cracks	Overloading	Half-joint		2019	Underground	2002
109	Support end failure	Improper bearing material	Corbel	Beam	2019	Aboveground	2012
110	Spalling	Fire	Floor	Hollowcore slab	2019	Underground	2003
111	Cracks	Improper detailing	Floor	Filigree slab	2019	Aboveground	2019
112	Spalling	Fire	Floor	TT	2019	Aboveground	1988
113	Cracks	Incorrect design	Half-joint	Beam	2020	Aboveground	2000
114	Spalling	Fire	Floor	TT	2019	Aboveground	
115	Support end failure	Incorrect design	Half-joint	Beam	2020	Aboveground	2005

116	Leaking cracks	Insufficient rebar	Floor	Monolithic	2020	Underground	2019
117	Leaking cracks	Restrained deformation	Floor	Monolithic	2020	Aboveground	1967
	Delamination	Wear	Floor coating	Monolithic	2020	Aboveground	1967
118	Spalling	Fire	Floor	Hollowcore slab	2020	Underground	1998
119	Corrosion	Water ingress in duct	Floor	Post-tensioned	2020	Aboveground	1977
	Spalling	Tendon corrosion	Floor	Post-tensioned	2020	Aboveground	1977
	Cracks	Tendon corrosion	Floor	Post-tensioned	2020	Aboveground	1977
	Untightening coupling rebar	Chloride	Floor joint	TT	2020	Aboveground	1981
	Spalling	Restrained deformation	Floor joint	TT	2020	Aboveground	1981
	Cracks	Continuity rebar	Half-joint		2020	Aboveground	1981
	Corrosion	Insufficient cover	Beam		2020	Aboveground	1981
120	Leaking cracks	Insufficient rebar	Wall		2020	Underground	2013
121	Cracks	Restrained deformation	Floor joint		2021	Underground	2007
122	Support end failure	Various factors	Corbel		2021	Aboveground	2006
123	Spalling	Fire	Floor	Monolithic	2021	Aboveground	1977
124	Support end failure	Continuity rebar	Corbel	Beam	2021	Aboveground	2000
	Support end failure	Continuity rebar	Half-joint	Beam	2021	Aboveground	2000
125	Cracks	Restrained deformation	Wall	In-situ	2021	Underground	2019
	Cracks	Restrained deformation	Floor	Monolithic	2021	Underground	2019
126	Support end failure	Continuity rebar	Corbel	Column	2022	Aboveground	2005
	Leaking cracks	Restrained deformation	Floor joint	Hollowcore slab	2022	Aboveground	2005
127	Spalling	Fire	Floor	Hollowcore slab	2021	Aboveground	2011
128	Support end failure	Continuity rebar	Half-joint	Beam	2022	Aboveground	2014
129	Cracks	Restrained deformation	Floor	Filigree slab	2021	Underground	2014
130	Support end failure	Incorrect design	Column		2022	Aboveground	2012
131	Cracks	Restrained deformation	Floor	Filigree slab	2022	Underground	2000
132	Leakage	Damaged sealant	Expansion joint		2022	Underground	1991
133	Delamination	Unknown	Floor coating	Unknown	2022	Aboveground	1972
134	Support end failure	Continuity rebar	Half-joint	Beam	2024	Aboveground	2012

135	Spalling	Fire	Corbel		2023	Aboveground	1972
	Spalling	Fire	Beam		2023	Aboveground	1972
136	Cracks	Restrained deformation	Column		2023	Underground	1992
	Cracks	Restrained deformation	Wall		2023	Underground	1992
137	Support end failure	Improper bearing material	Half-joint	Floor	2023	Underground	1993
138	Cracks	Restrained deformation	Floor	Monolithic	2023	Underground	1993
	Cracks	Restrained deformation	Wall	In-situ	2023	Underground	1993
	Leakage	Missing waterstop	Wall	In-situ	2023	Underground	1993
139	Cracks	Restrained deformation	Floor joint	TT	2023	Aboveground	1970
	Support end failure	Various factors	Corbel		2023	Aboveground	2013
	Support end failure	Various factors	Half-joint	TT	2023	Aboveground	2013
140	Delamination	Unknown	Floor	Compressive layer	2023	Aboveground	2007
141	Cracks	Restrained deformation	Floor	Filigree slab	2023	Aboveground	2003
142	Leaking cracks	Deformation difference	Parking deck		2023	Aboveground	1987
143	Support end failure	Improper execution	Corbel		2023	Aboveground	1986
	Untightening coupling rebar	Chloride	Floor	TT	2023	Aboveground	1986
144	Cracks	Restrained deformation	Floor	Monolithic	2023	Aboveground	1987
145	Defect	Incorrect detailing of reinforcement in half-joint	Corbel		2024	Aboveground	2014

Appendix B

The results of the causes for types of damages with less than 10 observations contain a smaller sample size, thus provide an imprecise representation of the actual causes. To reiterate, the types of damage meeting these criteria are listed in Table B- 1.

Table B- 1 Types of damage with sample size smaller than 10.

Observed damage	Number of observations (-)	Percentage of total (%)
Delamination	5	2.1
Defect	4	1.7
Collapse	2	0.9
Walking bearing pad	2	0.9
Untightening/Corrosion coupling rebar	2	0.9
Gravel pocket	2	0.9
Camber difference	2	0.9
Broken rebar	2	0.9
Exposed tendon	1	0.4
Extruded sealant	1	0.4

Delamination

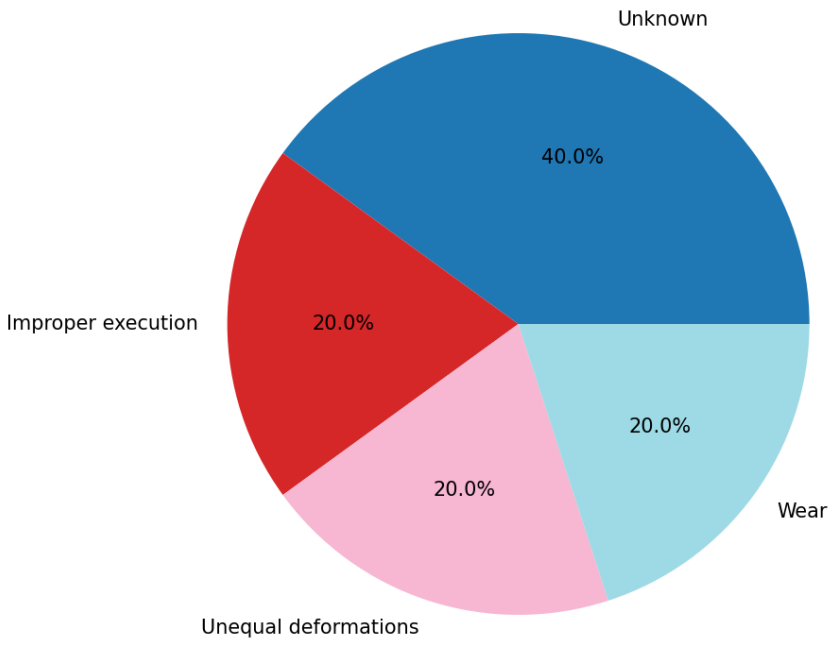

Figure B- 1 Causes of delamination of compressive layers.

Defect

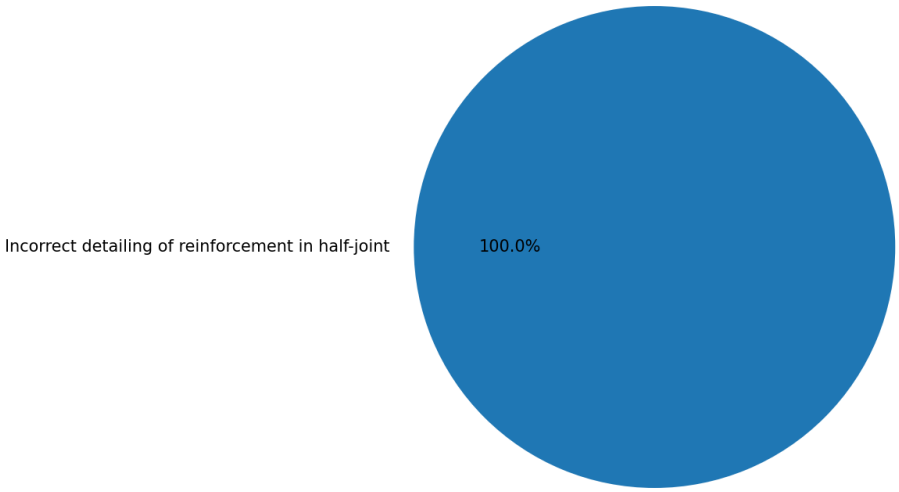

Figure B- 2 Causes of defects in parking garages.

Collapse

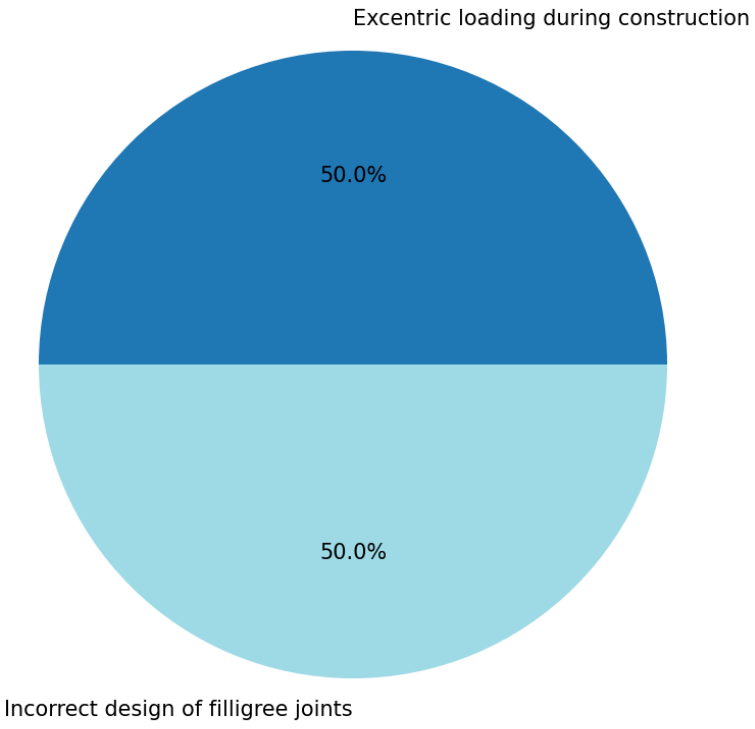

Figure B- 3 Causes of collapse in parking garages.

Broken rebar

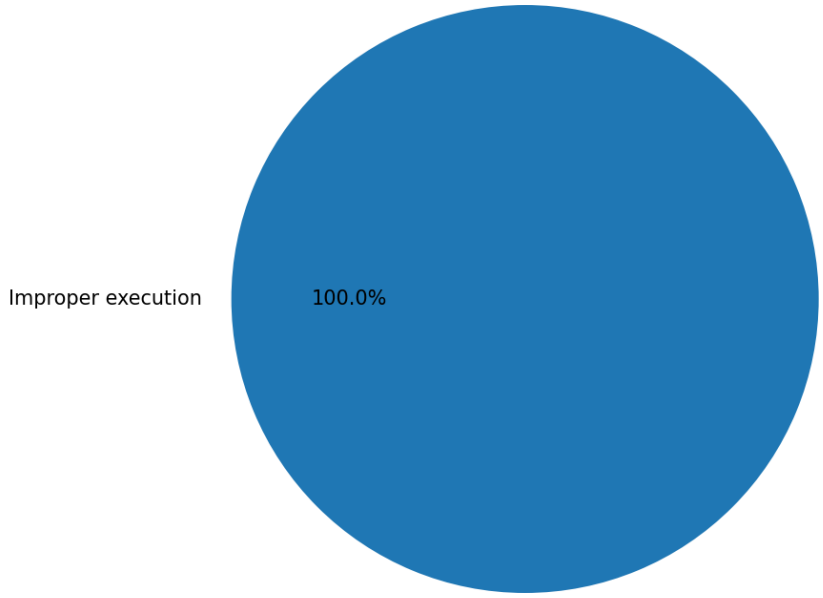

Figure B- 4 Causes of broken rebar in parking garages.

Camber difference

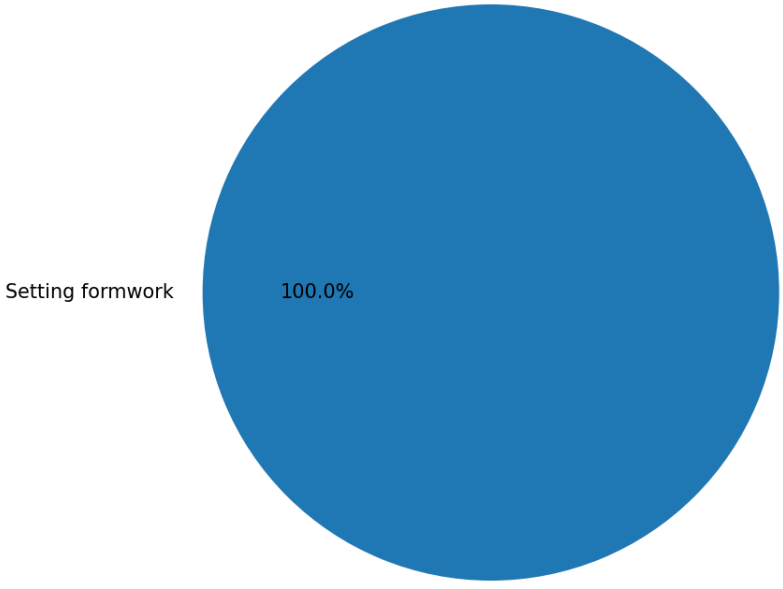

Figure B- 5 Causes of camber difference in parking garages.

Gravel pocket

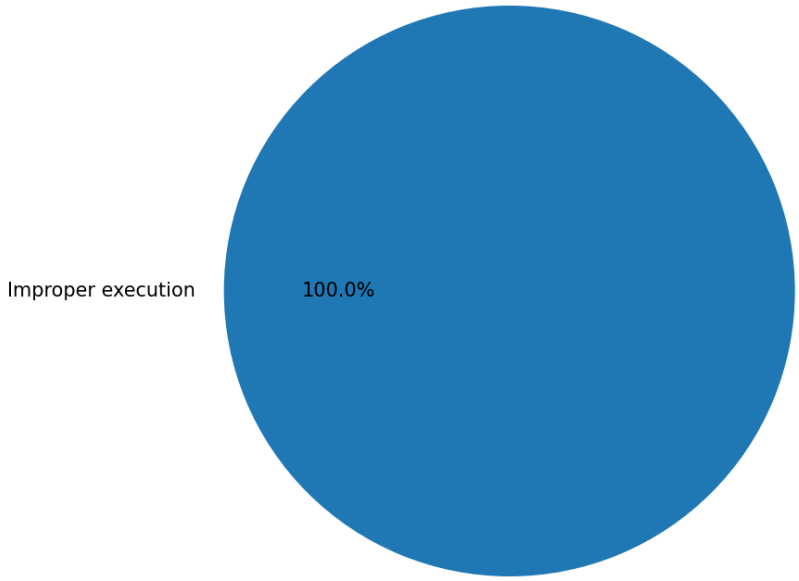

Figure B- 6 Causes of gravel pockets in parking garages.

Appendix C

The convergence of the numerical analysis describe the error in displacement, residual force, and energy which is accompanied in the calculation. Divergence or peaks in the convergence curve represent inaccuracies within the calculation at said load step. Comparison of these function give insight into the accuracy which is obtained by the numerical analysis. In Figure C- 1, Figure C- 2, and Figure C- 3, the convergence functions are plotted up to failure for mesh sizes 10x10, 15x15, and 20x20, respectively.

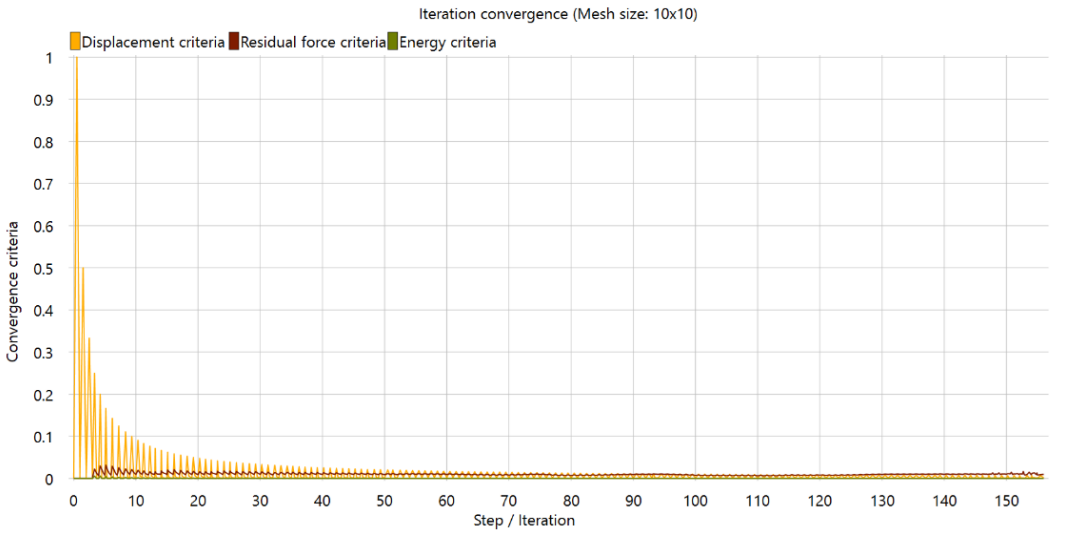

Figure C- 1 Distribution of convergence criteria of mesh size 10x10.

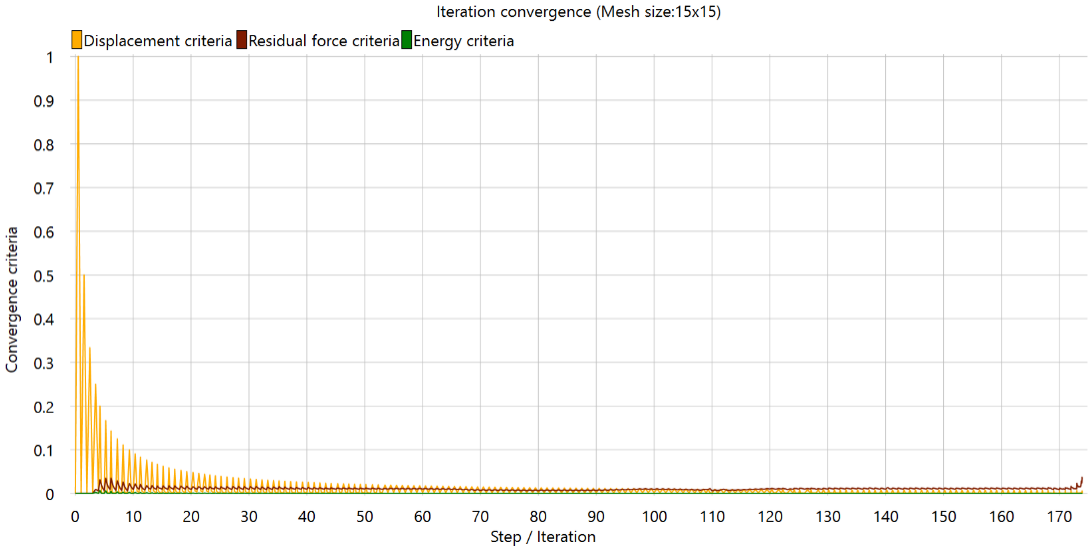

Figure C- 2 Distribution of convergence criteria of mesh size 15x15.

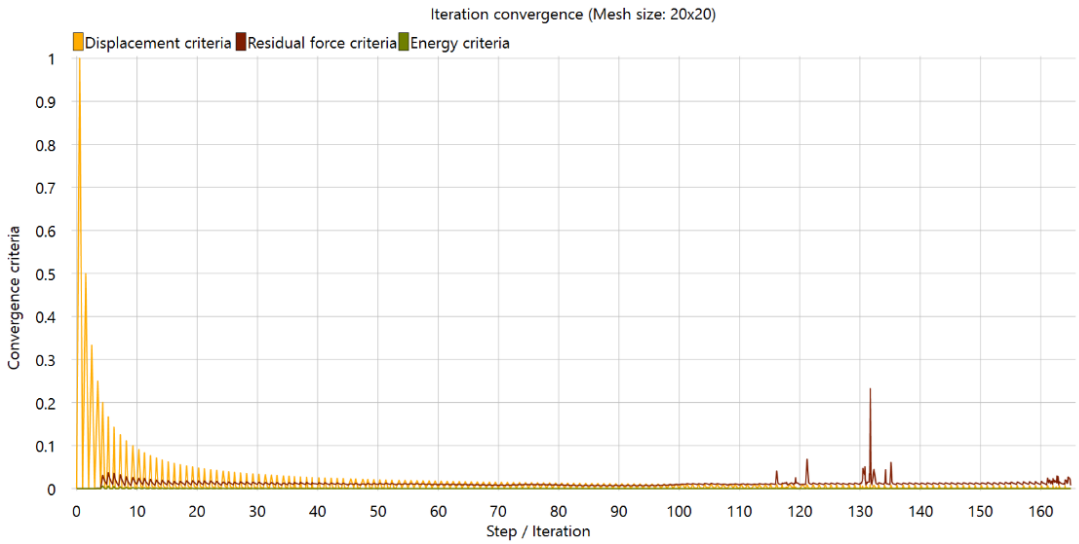

Figure C- 3 Distribution of convergence criteria of mesh size 20x20.

The failure mechanism for each mesh size is initiated at a different failure load, thus a different load step as well. The convergence function are plotted up to the initiation of the failure mechanism, as due to brittle failure larger errors in the convergence plots are expected. Moreover, numerical model is used to study the load at which the corbel end failure occurs, not its post fracture behaviour. Mesh sizes 10x10 and 15x15 present a good convergence up to initiation of failure. Between load steps 110-140 of mesh size 20x20 an exceedance in residual force error criteria is seen.

Appendix D

The dimensions of the corbel are calculated based on minimum requirements prescribed based on bearing elements or anchorage of reinforcement by NEN-EN 1992-1-1:2011 (EC2). For bearing elements the dimensions of the corbel comprises of three components: the distance from the edge of the corbel to the bearing pad ($a_2 + \Delta a_2$), the size of the bearing pad (a_1), and the distance between the bearing pad and the end of the supported element ($a_3 + \Delta a_3$), clarified in Figure D- 1.

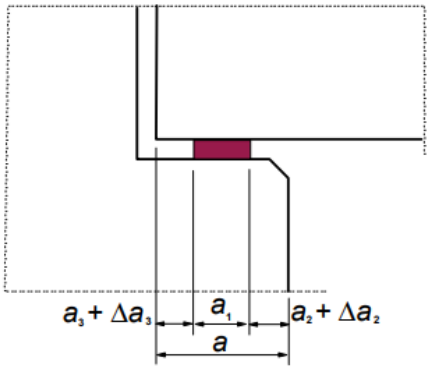

Figure D- 1 Size parameters of a support based on bearing elements- EC2 art. 10.9.4.7 (Nederlands Normalisatie Instituut, 2011).

Additionally, size requirements are prescribed for a support based on the anchorage of the tensile reinforcement of both the supporting and supported element. A schematisation is provided in Figure D- 2 on these requirements.

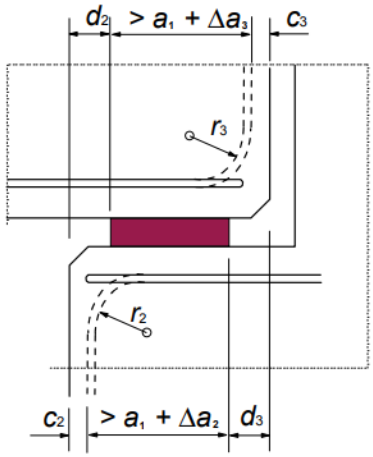

Figure D- 2 Size parameters of a support based on anchorage - EC2 art. 10.9.4.7 (Nederlands Normalisatie Instituut, 2011).

Edge distance d_2 depends on the method of anchorage of the supported element. The designed corbel uses vertically bend tensile reinforcement as anchorage measure, and thus an increased distance d_2 is required, as the additional length due to bending of the main reinforcement needs to be taken into account. Furthermore, factor d_2 consists of a tolerance factor (Δa_2) based on the dimensions of the supported element and the concrete cover (c). A concrete cover of 30 mm

and a minimum tolerance factor of 10 mm, assuming a span of the supported element of 12 m, are assumed for the corbel design (EC2 art. 10.9.5.2 table 10.5). Moreover, the diameter of the tensile reinforcement is chosen as 16 mm, resulting in the following edge distance:

$$d_2 = c + \Delta a_2 + r_2$$

$$c = 30\ mm$$

$$\Delta a_2 = \frac{span}{1200} = \frac{12000}{1200} = 10\ mm$$

$$r_2 = 2 * \phi \rightarrow r_2 = 32\ mm$$

$$d_2 = 30 + 10 + 32 = 72\ mm$$

Factor d_2 is compared to the minimum requirements of edge distance $a_2 + \Delta a_2$, which results in a governing distance. Edge distance $a_2 + \Delta a_2$ is determined based on the type of support, line- or concentrated support, the concrete strength class, and a ratio between the exerted stress and the concrete strength, Based on several assumptions factor a_2 is found as per EC2 art. 10.9.5.2 table 10.3, encompassing:

1. The corbel has a concrete strength C40/50;
2. The corbel is a concentrated support;
3. Ratio σ_{Ed} / f_{cd} exceeds 0.4.

Based on these assumptions a value for a_2 of 25 mm is found. Since edge distance d_2 is larger than $a_2 + \Delta a_2$ this becomes the governing dimension.

In a similar way the distance d_3, equal to $a_3 + \Delta a_3$, is calculated. However, for this parameter the assumption is made that the tensile reinforcement of the supported element is anchored using hairpin reinforcement. Thus, factor r_2 is left out of the equation.

$$d_3 = c + \Delta a_3$$

$$c = 30\ mm$$

$$\Delta a_3 = \frac{span}{2500} = \frac{12000}{2500} = 5\ mm\ (assuming\ a\ prefab\ element\ of\ 12\ m\ span)$$

$$d_3 = 30 + 5 = 35\ mm$$

The remaining dimensions are the size of the bearing element. As previously stated, the corbel is assumed to be a concentrated support. Additionally, the ratio between exceeding stress (σ_{Ed}) and concrete strength (f_{cd}) is assumed to exceed 0.4. Thus, the minimum length of the bearing pad is 140 mm (EC2 art. 10.9.5.2 table 10.2).

To conclude, a minimum length of the corbel is 247 mm, calculated by summation of these parameters. For further calculations a width of 300 mm is used. Furthermore, the height and width of the corbel are set at 400 and 300 mm, respectively (Figure D- 3).

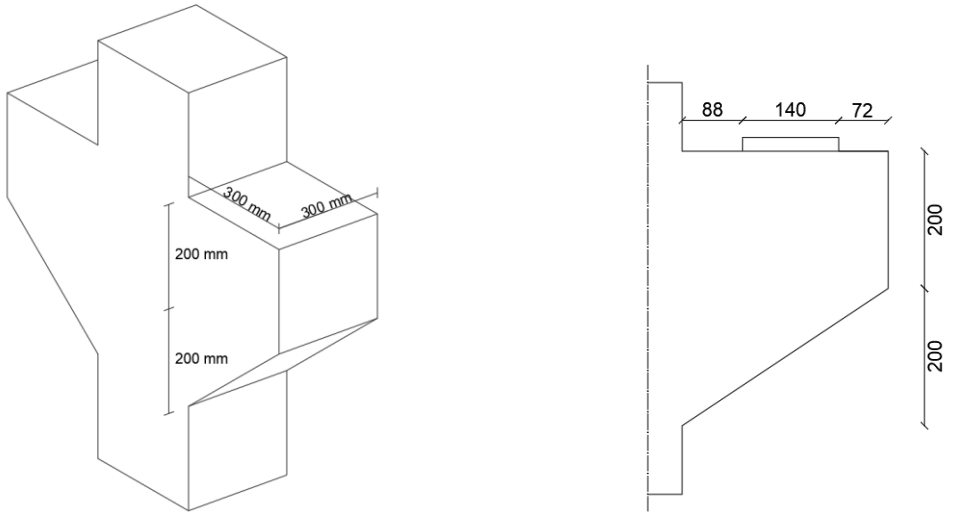

Figure D- 3 Visualisation of the corbel dimensions, 3D view (left) and side view (right) in mm.

The corbel is designed for a vertical design load (F_d) of 400 kN, without additional horizontal loading. Additionally, a concrete strength of C40/45 and reinforcement diameter of the tensile reinforcement of 16 mm are assumed for the following calculations. Various design parameters and dimensions are enumerated in Table D- 1.

Table D- 1 Design parameters and dimensions.

Parameter	Value	Unit
F_v	400	kN
F_h	0	kN
$a_3 + \Delta a_3$	88	mm
a_1	140	mm
$a_2 + \Delta a_2$	72	mm
h_c	400	mm
b	300	mm
l	300	mm

Calculating the required amount of tensile reinforcement for a corbel can be obtained using two schematisation models: a strut-and-tie model or a deep beam model. The largest difference in these calculations is the difference in internal lever arm “z”. Both methods are used to calculate the tensile reinforcement configuration to found out the difference in required reinforcement for both methods. First a strut-and-tie model is used for calculation of the corbel.

Strut-and-tie

Corbel classification

Categorization of a corbel for a strut-and-tie model (STM) depends on the ratio between the lever arm of the applied load and the height of the corbel. If the lever arm between support and start of the corbel does not exceed half its height, the corbel can be calculated as a short cantilever. Otherwise the corbel should be calculated as a long cantilever, which in case it does, requires additional vertical stirrups (Figure D- 4).

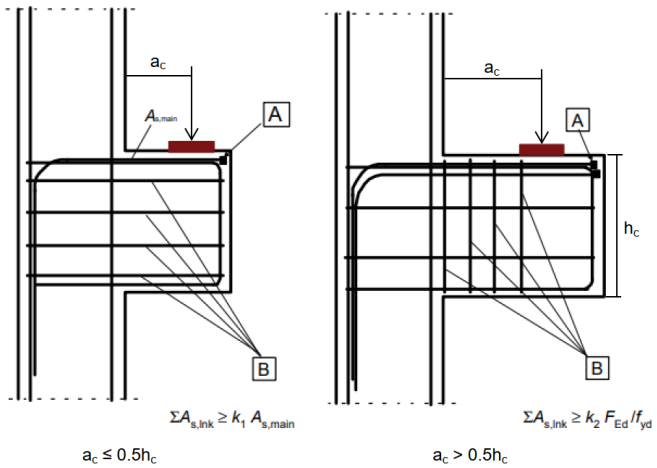

Figure D- 4 Reinforcement detailing of a corbel depending on lever arm to height ratio (Nederlands Normalisatie Instituut, 2011).

For the chosen design the lever arm, a_c, over corbel height is calculated accordingly:

$$\frac{a_c}{h_c} = \frac{a_3 + \Delta a_3 + \frac{a_1}{2}}{h_c} = \frac{88 + \frac{140}{2}}{400} = \frac{158}{400} = 0.40 \leq 0.5$$

Since the ratio between lever arm and height does not exceed 0.5, the corbel is designed as a short cantilever. The strut-and-tie calculation is derived from EC2 and Braam (2010).

Bearing stresses

The stresses transferred from the bearing pad are calculated and compared to the bearing stress capacity. The bearing stress capacity is calculated according the formula for calculating the stress of a compressive strut under lateral tension (EC2 art. 6.5.2 equation 6.5.2).

$$\sigma_{Rd,max} = 0.6 * \left(1 - \frac{f_{ck}}{250}\right) * \frac{f_{ck}}{\gamma_c}$$

$f_{ck} = 40\ MPa$
$\gamma_c = 1.5$

$$\sigma_{Rd,max} = 0.6 * \left(1 - \frac{40}{250}\right) * \frac{40}{1.5} = 13.44\ MPa$$

For a design load of 400 kN the following bearing stresses are introduced onto the corbel:

$$\sigma_{Ed} = \frac{F_D}{A} = \frac{F}{b*a_1} = \frac{400*10^3}{300*140} = 9.5\ MPa < 13.44\ MPa$$

Tensile reinforcement

An overview of the strut-and-tie model used to calculate the tensile reinforcement is given in Figure D- 5. Two nodes are identified in the strut-and-tie model: node 1 being a compression-compression-tension (CCT) node and node 2 being a compression-compression-compression (CCC) node.

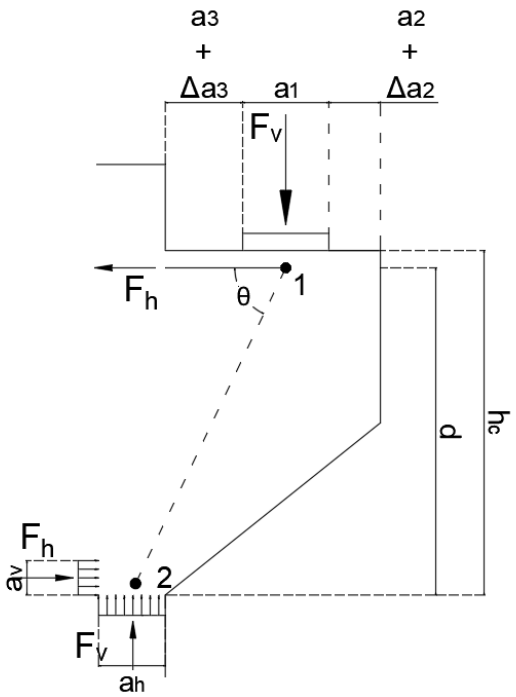

Figure D- 5 Schematisation of strut-and-tie model of the corbel.

The amount of tensile reinforcement is calculated based on the horizontal force F_h induced into the corbel due to the inclined compressive strut. To the calculate the horizontal force F_h, the assumption is made that the equilibrium in node 2 is made with the maximum allowed bearing stress in a compressive strut, rather than in a CCC node. Using force equilibrium the length a_h is determined.

$$a_h = \frac{F_v}{b*\sigma_{Rd,max}}$$

$b = width\ of\ corbel = 300\ mm$
$F_v = design\ load = 400\ kN$
$\sigma_{Rd,max} = maximum\ bearing\ stress = 13.44\ MPa$

$$a_h = \frac{F_v}{b*\sigma_{Rd,max}} = \frac{400*10^3}{300*13.44} = 99\ mm$$

Using moment equilibrium at node 2 the equation is obtained which yields force F_h.

$$\sum M_{Node\,2} = 0$$

$$\rightarrow\ F_h * \left(h_c - c - \frac{1}{2}\phi_{main} - \frac{1}{2} * a_v\right) = F_v * \left(a_3 + \Delta a_3 + \frac{1}{2} * a_1 + \frac{1}{2} * a_h\right)$$

The vertical distance in which node 2 makes equilibrium, length a_v, can be calculated in a similar fashion as length a_h by force equilibrium.

$$a_v = \frac{F_h}{b * \sigma_{Rd,max}}$$

By substitution of these formulas, the equation is obtained to calculate the horizontal force in the reinforcement.

$$\frac{1}{2} * F_h^2 - F_h * b * \sigma_{Rd,max} * d + b * \sigma_{Rd,max} * F_v * \left(a_3 + \Delta a_3 + \frac{1}{2} * a_1 + \frac{1}{2} * a_h\right) = 0$$

$$F_h = \sigma_{Rd,max} * b * d \pm \sqrt{\left(\sigma_{Rd,max} * b * d\right)^2 - \frac{4}{2} * b * \sigma_{Rd,max} * F_v * \left(a_3 + \Delta a_3 + \frac{1}{2} * a_1 + \frac{1}{2} * a_h\right)}$$

Using this equation the tensile force F_h is calculated.

$$F_h = 13.44 * 300 * \left(400 - 30 - \frac{16}{2}\right) \pm \sqrt{\left(13.44 * 300 * \left(400 - 30 - \frac{16}{2}\right)\right)^2 - 2 * 300 * 13.44 * \left(88 + \frac{140}{2} + \frac{99}{2}\right) * 400 * 10^3}$$

$$F_h = 251\ kN$$

The required tensile reinforcement as result of the horizontal component of the compression strut results in:

$$A_{tensile} = \frac{F_h}{f_{yd}} = \frac{F_h}{\frac{f_{yk}}{\gamma_s}}$$

$\gamma_s = 1.15$
$f_{yk} = Characteristic\ yield\ strength\ of\ reinforcement$

Assuming reinforcement steel grade B500B is used the following required sectional area is needed:

$$A_{tensile} = \frac{251*1000}{\frac{500}{1.15}} = 577\ mm^2$$

For a reinforcement diameter of 16 mm for the tensile reinforcement the following configuration is required:

$$A_{tensile} = 577 = \frac{1}{4} * \pi * \phi^2 * n$$

$$\rightarrow 577 = \frac{1}{4} * \pi * 16^2 * n$$
$$\rightarrow n = 2.86 \rightarrow n = 3$$

$$A_{tensile,\varphi 16} = \frac{3}{4} * \pi * 16^2 = 603\ mm^2 > 577\ mm^2$$

Compressive strut
The inclination of the compressive strut was assumed by estimating the position of node 2. Inclination struts are limited to a set range prescribed by EC2 appendix J.3.

$$EC2\ J.3\ :\ 1.0 \leq \tan(\theta) \leq 2.5$$

$$\tan(\theta) = \frac{d - \frac{1}{2}a_v}{a_3 + \Delta a_3 + \frac{1}{2} * a_1 + \frac{1}{2} * a_h} = \frac{362 - \frac{1}{2} * 62.5}{88 + \frac{140}{2} + \frac{99}{2}} = 1.59\ (57.8°)$$

Additionally, the compressive stresses in CCT-node 1 are verified. The permitted stress in the compressive strut for the CCT-node is calculated (EC2 art. 6.5.4 equation 6.61). An additional 10% of strength can be accounted for since the inclination between the compressive strut and tensile tie exceeds 55° (EC2 art. 6.5.4 Section 6.5.2 (5)).

$$\sigma_{Rd,max,node\ 2} = 1.1 * k_2 * \left(1 - \frac{f_{ck}}{250}\right) * \frac{f_{ck}}{\gamma_c}$$

$$k_2 = 0.85$$

$$\sigma_{Rd,max,node\ 2} = 1.1 * 0.85 * \left(1 - \frac{40}{250}\right) * \frac{40}{1.5} = 20.9\ MPa$$

The vertical distance between the top of the corbel and node 1 is 38 mm. Thus, the maximum surface area to make equilibrium with the horizontal force is the corbel width multiplied by 76 mm (Figure D- 6). By assuming the maximum inclination of this strut the maximum bearing capacity is estimated.

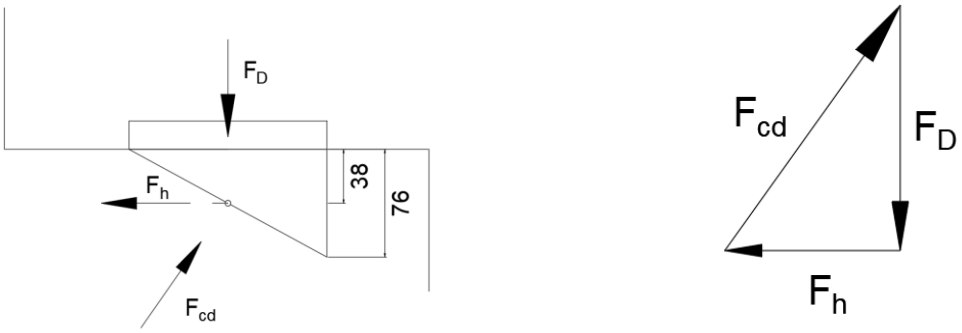

Figure D- 6 Schematisation of strut-and-tie model node 1.

The horizontal bearing capacity is calculated accordingly:

$$F_{cd,vert} = 2 * \left(c + \frac{\phi}{2}\right) * b * \sigma_{Rd,max,node\ 2}$$

$$\rightarrow\ F_{cd,vert} = 2 * \left(30 + \frac{16}{2}\right) * 300 * 20.9 = 476\ kN > 251\ kN$$

The argument could be made that right below this node, in the compressive zone, the bearing capacity would have to be calculated with the bearing stress in a compressive zone, previously calculated as 13.44 MPa, resulting in a decrease of bearing capacity. However, in a D-region the effective width of the compressive zone increases over its height, depicted in Figure D- 7.

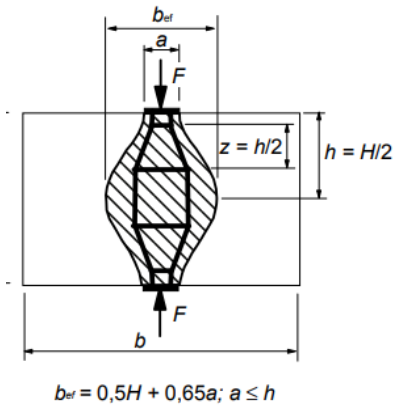

Figure D- 7 Change in effective width of a compressive strut (Nederlands Normalisatie Instituut, 2011).

The increase in effective width causes a larger surface area over which the maximum bearing stress acts. Consequently, a larger bearing capacity of the compressive strut is obtained. The effective area is calculated according to the equation provided below.

$$H = \sqrt{\left(\frac{1}{2}a_h + a_3 + \Delta a_3 + \frac{1}{2}a_1\right)^2 + \left(d - \frac{1}{2}a_v\right)^2}$$

$$H = \sqrt{\left(\frac{99}{2} + 88 + \frac{140}{2}\right)^2 + \left(362 - \frac{62.5}{2}\right)^2} = 390\ mm$$

$$b_{eff} = 0.5 * H + 0.4 * a_1$$
$$b_{eff} = 0.5 * 390 + 0.4 * 140 = 253\ mm$$

The increasing factor of the maximum bearing stress in the compressive zone can be calculated as per equation 6.63 of Section 6.7 of EC2:

$$\sqrt{\frac{A_{c1}}{A_{c0}}} = \sqrt{\frac{b_{eff} * b}{a_1 * b}} = \sqrt{\frac{253 * 300}{140 * 300}} = 1.3\ (-)$$

Finally, this results in the maximum bearing stress in the compressive zone of:

$$\sigma_{Rd,max} = 0.6 * \left(1 - \frac{f_{ck}}{250}\right) * \frac{f_{ck}}{1.5} * \sqrt{\frac{A_{c1}}{A_{c0}}}$$
$$\sigma_{Rd,max} = 0.6 * \left(1 - \frac{40}{250}\right) * \frac{40}{1.5} * 1.3 = 17.5\ MPa$$

The internal inclined compressive force can be obtained by force equilibrium, as shown in Figure D- 6. Using the inclined compressive force the internal compressive stress is calculated:

$$F_{cd} = \frac{F_{Ed}}{\sin(\theta)} = \frac{400}{\sin(1.59)} = 421\ kN$$
$$\sigma_{Ed} = \frac{F_{cd}}{b_{eff} * d} = \frac{421 * 1000}{300 * 253} = 5.54\ MPa < 17.5\ MPa$$

Shear reinforcement
The corbel element was previously categorized as a short cantilever, so only horizontal shear reinforcement is required. The minimum amount of shear reinforcement is calculated in accordance with EC2 J.3 (2).

$$A_{shear} = k_1 * A_{tensile}$$

$$k_1 = 0.25\ (NEN\ EN\ 1992 - 1 - 1)$$

$$A_{shear} = 0.25 * 603 = 150.75\ mm^2$$

For a reinforcement diameter of 8 mm for the stirrups the following configuration is required:

$$A_{shear} = 150.75 = \frac{1}{4} * \pi * \phi^2 * n$$

$$\rightarrow 150.75 = \frac{1}{4} * \pi * 8^2 * n$$
$$\rightarrow n = 3.01 \rightarrow n = 4$$

$$A_{shear,\varphi 10} = \frac{4}{4} * \pi * 8^2 = 201\ mm^2 > 150.75\ mm^2$$

Deep beam

A corbel assumed as deep beam represents a two sided corbel as a beam with direct shear distribution to its supports, as shown in Figure D- 8. Using this method the internal lever arm "z" is calculated by a set equation as per art. 6.3 of EC2. This is similar to the position of node 2 of the strut-and-tie model. However, with the deep beam model the internal lever arm is greatly reduced.

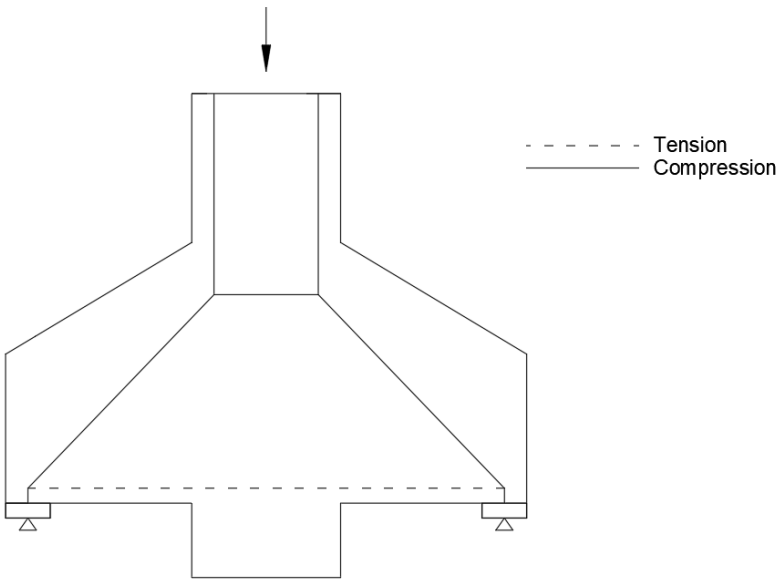

Figure D- 8 A two sided corbel schematised as deep beam.

Tensile reinforcement

The height of the internal lever arm is calculated according to art. 6.1 section (10) as per National Annex NB:2016+A1:2020 (EC2 NB).

$$z = 0.4 * a + 0.4 * h$$

$$a = \min\left(\frac{a_1}{2}; \frac{l}{4}; \frac{h}{4}\right) + \frac{1}{2}a_1 + a_3 + \Delta a_3$$

$$a = \min\left(\frac{140}{2}; \frac{300}{4}; \frac{400}{4}\right) + 70 + 88 \rightarrow a = 228\ mm$$

$$z = 0.4 * 228 + 0.4 * 400 = 251\ mm$$

The difference in internal lever arm consequently results in a difference in inclination of the compressive strut, calculated by:

$$EC2\ J.3 \quad 1.0 \leq \tan(\theta) \leq 2.5$$

$$\tan(\theta) = \frac{z}{a} = \frac{251}{228} = 1.1\ (47.7°)$$

In comparison to the strut-and-tie model the internal lever arm decreases by 80 mm. As result, the inclination of the compressive strut is shallower than in the strut-and-tie model, leading to a larger horizontal component F_h, as shown in Figure D- 9.

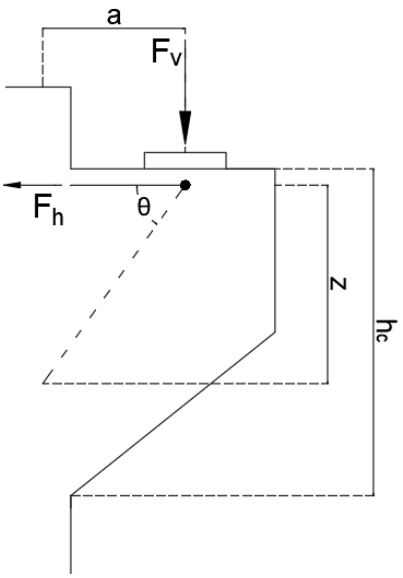

Figure D- 9 Schematisation of a deep beam corbel.

Using moment equilibrium around the node the horizontal component is obtained:

$$\sum M_{Node} = 0$$

$$\rightarrow F_h * z - F_v * a = 0$$
$$\rightarrow F_h * 251 - 400 * 228 = 0$$

$$\rightarrow F_h = 363\ kN$$

Assuming a reinforcement steel grade of B500B is used the following required sectional area is required:

$$A_{tensile} = \frac{363*1000}{\frac{500}{1.15}} = 834\ mm^2$$

Assuming a reinforcement diameter of 16 mm the following reinforcement configuration is obtained:

$$A_{tensile} = 834 = \frac{1}{4} * \pi * \phi^2 * n$$

$$\rightarrow 834 = \frac{1}{4} * \pi * 16^2 * n$$
$$\rightarrow n = 4.15 \rightarrow n = 5$$

$$A_{tensile,\varphi 16} = \frac{5}{4} * \pi * 16^2 = 1004\ mm^2 > 834\ mm^2$$

Strut-and-tie vs deep beam

A clear difference is found in the required amount of tensile reinforcement when using the strut-and-tie versus the deep beam method. Since both methods comply with EC2 both results are adequate to be used as design. Though, the large difference in required tensile reinforcement, $3\phi 16$ for STM versus $5\phi 16$ for deep beam, signify a somewhat conservative approach by the deep beam model. Tt boils down to the assumption of the height of the internal lever arm. For the final design of the corbel the results of the STM method are used. Whether the assumed internal lever arm is correct may be verified using the finite element analysis in Chapter 11.